NASW-4435

N.A.S.A. ADVANCED AERONAUTICS DESIGN SOLAR POWERED REMOTELY PILOTED VEHICLE

Major Qualifying Project
Submitted to the Faculty
of the

Worcester Polytechnic Institute

in partial fulfillment of the requirements
for the
Degree of Bachelor of Science
Submitted on April 30, 1991

by

David S. Elario
David S. Elario

Michael J. Ferreira
Michael J. Ferreira

Neal H. Guillmette
Neal H. Guillmette

G.C. Konstantakis
George C. Konstantakis

Gregory S. Lind
Gregory S. Lind

David L. Marshall
David L. Marshall

Jonathan D. Webster
Jonathan D. Webster

Cari L. Windt
Cari L. Windt

Approved By:

Prof. Andreas Alexandrou

Prof. Ralph Cohn

Prof. Vahid Motevalli

Prof. David Olinger

Prof. Joseph J. Rencis

ABSTRACT

Environmental problems such as the depletion of the ozone layer and air pollution demand a change in traditional means of propulsion that is sensitive to the ecology. Solar powered propulsion is a favorable alternative that is both ecologically harmless as well as cost effective. Integration of solar energy into designs ranging from futuristic vehicles to heating is beneficial to society. The design and construction of a Multi-Purpose Remotely Piloted Vehicle (MPRPV) seeks to verify the feasibility of utilizing solar propulsion as a primary fuel source. This task has been a year long effort by a group of ten students, divided into five teams, each dealing with different aspects of the design.

The aircraft has been designed to take-off, climb to the design altitude, fly in a sustained figure-eight flight path, and cruise for approximately one hour. This mission requires flight at Reynolds numbers between 150,000 and 200,000 and demands special considerations in the aerodynamic design in order to achieve flight in this regime. Optimal performance requires a lightweight configuration with both structural integrity and maximum power availability. The structural design and choice of solar cells for the propulsion was governed by the weight, efficiency, and cost considerations.

The final design is a MPRPV weighing 35 N which cruises 7 m/s at the design altitude of 50 m. The configuration includes a wing composed of balsa and foam NACA 6409 airfoil sections and carbon fiber spars, a tail of similar construction, and a truss structure fuselage. The propulsion system consists of 98 10% efficient solar cells donated by Mobil Solar, a NiCad battery for energy storage, and a folding propeller regulated by a lightweight and efficient control system. The airfoils and propeller chosen for the design have been researched and tested during the design process.

ACKNOWLEDGEMENTS

The members of the project group would like to thank the following for their support during this project:

Professor A. Alexandrou

Professor R. Cohn

Professor V. Motevalli

Professor D. Olinger

Professor J. Rencis

Charlotte Cody

NASA/USRA

Mobil Solar

Professor W. Durgin

Professor W. Clark

Kurt Heinzmann

Adam Szymkiewicz

Jason Makofsky

Kyle Jacobson

Special thanks go to Mark Sullivan for providing the group with its own printing facility.

TABLE OF CONTENTS

Abstract

Acknowledgements

List of Figures

List of Tables

Executive Summary

Chapter 1 - Introduction 1

Chapter 2 - Mission Definition 3

Chapter 3 - Design Procedures 4
3.1 Design Process 4
3.2 Design Description 5
3.2.1 Configuration 5
3.2.2 Dimensions 7
3.3 Testing Procedures 8

Chapter 4 - Aerodynamic Analysis 10
4.1 Introduction 10
4.2 Aerodynamic Configuration Characteristic 10
4.3 Reynold's Number Regime 11
4.4 Solar Cell Placement 12
4.5 Acquisition of Data 15
4.6 Airfoil Selection 16
4.7 Wing Sizing 20
4.8 Wing Dihedral/Wing Tip 22
4.9 Finite Effects of Wing 23
4.10 Tail Section 24
4.11 Finite Effects of Tail 27
4.12 Optimization of Excess Power Versus Angle of Attack 37

Chapter 5 - Structural Analysis 31
5.1 Introduction-Design Considerations 31
5.2 Preliminary Component Sizing 36
5.3 ANSYS Finite Element Code Analysis 40
5.3.1 Wing Analysis 40
5.3.2 Tail Analysis 43
5.3.3 Fuselage Analysis 45

5.4 Vibrational Analysis 48
5.5 Material Selection 50
5.6 Weight Breakdown 53

Chapter 6 - Aircraft Power Systems and Control 59
6.1 Solar Array 61
6.1.1 Array Constraints 63
6.1.2 Solar Irradiance Determination 67
6.1.3 Solar Cell Tests 70
6.2 Nickel Cadmium Batteries 73
6.3 Motor 76
6.4 Propeller Selection and Performance 82
6.5 Testing and Characterization of Motor/Propeller 90
6.6 Integrated Propulsion System 92
6.7 Controls and Interface System 96
6.7.1 Modes of Operation 97
6.7.2 Control Surfaces 98
6.7.3 Electro-Magnetic Interference 99

Chapter 7 - Performance 100
7.1 Level Flight Characteristics 100
7.2 Climbing Performance 103
7.3 Banking Performance 106

Chapter 8 - Stability and Control 108
8.1 Longitudinal Motions 109
8.1.1 Static Longitudinal Stability 109
8.1.2 Dynamic Longitudinal Stability 112
8.2 Lateral Motions 116
8.2.1 Static Lateral Stability 116
8.2.2 Dynamic Longitudinal Stability 119

Chapter 9 - Construction Methods 121
9.1 Wing Construction 121
9.2 Tail Construction 123
9.3 Modular Construction 124
9.4 Fuselage Construction 125
9.5 Fuselage/Wing Construction 126
9.6 Landing Gear 127

Chapter 10 - Environmental Considerations 128

Chapter 11 - Conclusions and Recommendations 129

References

Appendix A - Mission and Performance

A.1 Static Stability Equation Derivation
A.2 Multhorp's Method
A.3 Dynamic Stability Equations Derivations
A.4 Performance Program
A.5 Drag Correction Factor

Appendix B - Aerodynamics

B.1 The Nature of Low Reynolds Number Airfoils
B.2 Reliability of the Princeton Data
B.3 Glauert Method of Arbitrary Wind Loading
B.4 Determination of Configurational Lift and Drag

Appendix C - Structures

C.1 ANSYS Wing Data
- C.1.2 Wing Nodal Locations
- C.1.2 Wing Element Listing
- C.1.3 Wing Material Properties
- C.1.4 Wing Geometry Data
- C.1.5 Wing Nodal Displacements
- C.1.6 SIG1 and SIG2: Maximum and Minimum Stresses in Wing Beam Elements at End
- C.1.7 SXX and SYY: Planar Stresses in Wing Shell Elements
- C.1.8 SYY and SZZ: Planar Stresses in Wing Shell Elements
- C.1.9 SIG1, SIG2 and SIG3: Principal Stresses in Wing Shell Elements

C.2 ANSYS Tail Data
- C.2.1 Tail Nodal Locations
- C.2.2 Tail Element Listing
- C.2.3 Tail Geometry Data
- C.2.4 Tail Nodal Displacements
- C.2.5 SIG1 and SIG2: Maximum and Minimum Stresses in Tail Beam Elements at End
- C.2.6 SIG1, SIG2 and SIG3: Principal Stresses in Tail Shell Elements
- C.2.7 SIG1, SIG2 and SIG3: Principal Nodal Tail Stresses

C.3 ANSYS Fuselage Data
- C.3.1 Fuselage Element Listing
- C.3.2 STRS: Maximum and Minimum Stresses in Fuselage Truss Elements at End

C.4 Configuration 1 Top View
C.5 Configuration 2 Top View

C.6 Configuration 2 Side View
C.7 Configuration 1 Isometric
C.8 Configuration 2 Isometric
C.9 Final Configuration Top View
C.10 Final Configuration Isometric
C.11 Wing Rib Cell Placement Detail - Side View
C.12 Wing Rib/Tube Connection Detail - Side View
C.13 Tail Rib/Tube Connection Detail - Side View

Appendix D - Aircraft Power System Controls
D.1 Solar Array Data
D.2 Motor Specifications and Evaluation
D.3 Propeller Efficiency Data

LIST OF FIGURES

Figure 4.1: Proposal of a Flatback Airfoil (70% flat) 12
Figure 4.2: Inviscid Distribution of Pressure for 70% Flatback Airfoil 13
Figure 4.3: Proposal of a Flat Plate for Cell Placement 14
Figure 4.4: Comparison of Airfoil Sections (Re=200,000) 17
Figure 4.5: Coordinates and Plot of the NACA 6409 18
Figure 4.6: Inviscid Distribution of Pressure for the NACA 6409 at an Angle of Attack of 4 Degrees 19
Figure 4.7: Lift and Drag Characteristics of the NACA 6409 at Re=200,100 20
Figure 4.8: Solar Cell Placement in the NACA 6409 21
Figure 4.9: Elliptic vs. Rectangular Wing Loading for the NACA 6409 with an Aspect Ratio of 8.25 24
Figure 4.10: Elliptic vs. Rectangular Lift for the NACA 6409 with an Aspect Ratio of 8.25 25
Figure 4.11: Elliptic vs. Rectangular Drag for the NACA 6409 with an Aspect Ratio of 8.25 26
Figure 4.12: Optimization of Excess Power with Respect to Angle of Attack of the Wing 29
Figure 4.13: Configurational Lift to Drag at 8 meters per second 30

Figure 5.1: Wing Shear-Moment Diagrams 39
Figure 5.2: Tail Shear-Moment Diagrams 41
Figure 5.3: Deflected Wing Half-Model 43
Figure 5.4: Deflected Tail Half-Model 44

Figure 6.1: Powerplant Layout 59
Figure 6.2: Characteristic Solar Cell Curves 61
Figure 6.3: Voltage Change with Changing Temperature 62
Figure 6.4: Current Change with Changing Insolation 63
Figure 6.5: Standard Solar Cell Characteristics 63
Figure 6.6: Solar Cell Placement 64
Figure 6.7: Optical Properties vs. Incidence Angle 65
Figure 6.8: 5% Module Experimentation 66
Figure 6.9: Wiring Considerations 67
Figure 6.10: Solar parameters 69
Figure 6.11: Solar Cell Test Data 1-27-91 71
Figure 6.12: Current Adjustment 71
Figure 6.13: Solar Cell Evaluation - I-V Curve 73
Figure 6.14: Estimated Power from Solar Cells 74
Figure 6.15: Motor Diagram 76
Figure 6.16: Contour Plot of Astro-05 Motor Characteristics 80
Figure 6.17: 3-D Plot of Motor Efficiency vs Voltage and Current 81

Figure 6.18: Flow Through an Actuator Disk 83
Figure 6.19: Basic Propeller Geometry 85
Figure 6.20: Typical Blade Element 86
Figure 6.21: Typical Blade Element from Vortex Theory 87
Figure 6.22: Elemental Coefficient Curves for a Typical Propeller Blade... 89
Figure 6.23: Motor-Propeller Test Setup 90
Figure 6.24: Data For Wind Tunnel Testing of Aero-Haute 13" x 16.5" Folding Propeller 93
Figure 6.25: Motor-Propeller Map of Operating Ranges 93
Figure 6.26: Output Power vs. Input Power 95
Figure 6.27: Output Power vs. Input Power 97

Figure 7.1: Power Required/Power Available 104
Figure 7.2: Angle with Respect to Velocity 105
Figure 7.3: Circular Climb Pattern 105
Figure 7.4: Bank Angle Geometry 106

Figure 8.1: Axes for Aircraft Analysis 109
Figure 8.2: Freebody Diagram of a Wing/Tail Combination 110
Figure 8.3: Dihedral Angle for Helios '91 Design 118

LIST OF TABLES

Table 3-I:	Wing/Tail Dimensions	7
Table 5.I:	Stresses at Beam End	45
Table 5.II:	Principal Stresses for Shell Elements	46
Table 5.III:	Material Strength to Weight Ratios	51
Table 5.IV:	Material Densities	54
Table 5.V:	Wing Component Masses	55
Table 5.VI:	Tail Component Masses	56
Table 5.VII:	Fuselage Component Masses	56
Table 5.VIII:	Tubular Tail Strut Masses	57

EXECUTIVE SUMMARY

ABSTRACT

Environmental problems such as the depletion of the ozone layer and air pollution demand a change in traditional means of propulsion that is sensitive to the ecology. Solar powered propulsion is a favorable alternative that is both ecologically harmless as well as cost effective. Integration of solar energy into designs ranging from futuristic vehicles to heating is, therefore, beneficial to society. The design and construction of a Multi-Purpose Remotely Piloted Vehicle (MPRPV) seeks to verify the feasibility of utilizing solar propulsion as a primary fuel source. This task has been a year long effort by a group of eight students, divided into five teams, each dealing with different aspects of the design.

The aircraft has been designed to take-off, climb to the design altitude, fly in a sustained figure-eight flight path, and cruise for approximately one hour. This mission requires flight at Reynolds numbers between 150,000 and 200,000 and demands special considerations in the aerodynamic design in order to achieve flight in this regime. Optimal performance requires a lightweight configuration with both structural integrity and maximum power availability. The structural design and choice of solar cells for the propulsion was governed by weight, efficiency, and cost considerations.

The final design is a MPRPV weighing 35 N which cruises at 7 m/s at the design altitude of 50 m. The configuration includes a wing composed of balsa and foam NACA 6409 airfoil sections and carbon fiber spars, a tail of similar construction, and a truss structure fuselage. The propulsion system consists of 98 12.5% efficient solar cells donated by Mobil Solar, a NiCad battery for energy storage, and a folding propeller regulated by a lightweight and efficient control system. The airfoils and propeller chosen for the design have been researched and tested during the design process.

INTRODUCTION

Mission Requirements

This study investigates the possibilities for a remotely controlled solar powered aircraft. Ultimately the aircraft will be able to perform a sustained figure eight flight pattern at an altitude of 50 m using only solar power. The mission will be carried out in several flight stages including launch, climb to altitude, and pattern flight.

The aircraft will be launched away from the sun employing a catapult system to provide some initial altitude. Maximum power will be received when the aircraft is travelling away from the sun, resulting from the incidence of the solar array with respect to the sun. Therefore the best climb rate will be achieved when flying in this direction. A circular climbing pattern will be utilized, in order to compensate for slow climb rates and enable the aircraft to remain within a reasonable distance from the ground control. Once at altitude, a sustained figure eight pattern tests the aircraft characteristics over a variety of maneuvers.

Aircraft Configuration

The proposed vehicle is shown in Figures 1 and 2. General data and design parameters are summarized in Table 1.

The configuration consists of a non-conventional, high wing aircraft with two carbon fiber composite support struts primarily important in maintaining structural integrity. The two composite rods extend from the main spar in the wing to the spar of the horizontal stabilizer. This becomes of primary importance during both takeoff and landing, as large wing tip deflections could result in catastrophic failure.

A solar propulsion system, which includes 98 photovoltaic solar cells supplied by Mobil Solar

Weight	W_{gross}	40 N
Wing Area	S	1.48 m^2
Wing Loading	W	27.03 N/m^2
Aspect Ratio	AR	8.25
Wingspan	b	3.5 m
Cruise Altitude	h	50 m
Cruise Velocity	V	7 m/s
Design Lift Coeff	C_L	0.83
Design Lift-to-Drag	L/D	15.75
Cruise Power Reqd	P	15.9 W
Design Load Factor	n	7

Table 1: General Data

Corporation, powers the aircraft. The cells directly power an Astro-Flight Cobalt .05 motor which drives a folding Aero-Haute 13" x 6.5" pitch plastic propeller. As a safety feature, a switch is included to provide access to a NiCad battery backup system.

The electronics equipment is housed in a small fuselage, connected to the underside of the main wing. The fuselage was built utilizing a balsa truss structure covered with a mylar coating. The truss structure provided the fuselage with the necessary strength to safely house the electronics equipment under all anticipated loads, while minimizing the weight.

The wing and horizontal tail both have a prismatic planform possess aerodynamic characteristics of NACA 6409 airfoil sections. The wing has a span of 3.5 m and a chord of 0.424 m, resulting in an aspect ratio of 8.25. The wing is attached to the fuselage at an angle of attack of 4 degrees. At level flight conditions, this angle of attack produces a total wing C_L of 0.72 and downwash of -2^o. The tail has a span of 1 m and chord of 0.3 m, resulting in an aspect ratio of 3.33. The C_L of the tail is 0.22 and efficiency assumed 85%. The design at level flight conditions has a airplane lift coefficient of 0.83 and drag coefficient of 0.053 resulting in a configurational lift-to-drag ratio of L/D 15.75.

In addition, the aircraft is equipped with a variety of control devices including two ailerons, two rudders, and an elevator. These are directed with an onboard receiver which uses four electronic servos to control their motion.

DESIGN AND ANALYSIS

Aircraft Sizing and Weight Estimation

The required mission mandates the proposed vehicle be powered solely by the sun, therefore the design was optimized for maximum power and minimum weight. A model aircraft provided by a kit was constructed and flown. This aircraft was not solar powered, but did provide a reasonable initial weight estimation and power requirement for the proposed solar powered vehicle. Solar propulsion was integrated into the design and the

WING	Parts	Mass (g)	% Wing
Ribs	30	99.2	4.8
Leading Edge	1	84.2	4.1
Trailing Edge	1	104.4	5.1
Spar Webs	33	44.8	2.2
Skin (Mylar)		192.9	9.3
Solar Braces (foam)	270	33.7	1.6
Wing Tips (foam)	2	36.1	1.7
Carbon Rods	2	91.0	4.4
Solar Cells	90	856.8	41.5
Servos	2	43.0	2.1
Wiring		55.1	2.7
Reinforcing Ribs	10	340.0	16.5
Fasteners	10	82.2	4.0
Wing Total		2063	100

Table 2: Wing Component Masses

FUSELAGE	Mass (g)	% Fuse
Balsa Frame	111.6	12.5
Skin (Mylar)	12.3	2.5
Servo	21.5	2.4
Wiring	37.9	4.2
Motor & Gearbox	225.7	25.3
Propeller	32.9	3.7
Receiver Battery	97.0	10.9
Receiver	44.0	4.9
Speed Control	54.8	6.1
On/Off Switch	10.3	1.2
Emergency Batteries	234.3	26.2
Landing Gear	23.6	2.6
Fuselage Total	905.9	100

Table 3: Fuselage Component Masses

configuration was iteratively improved upon until a final and very unique vehicle was obtained. Tables 2 through 5 break down the actual masses for individual elements of the plane showing also their percent contribution to their section of the plane.

TAIL STRUT	Mass (g)	% Strut
Carbon Tubes (2)	225.1	80.9
Wiring	53.2	19.1
Strut Total	278.3	100

Table 4: Tubular Strut Masses

TAIL	Parts	Mass (g)	% Tail
Ribs	9	14.2	4.5
Leading Edge	1	20.0	6.422
Spar Webs	9	6.4	2.0
Elevator	1	34.8	10.8
Skin (Mylar)		42.0	13.4
Solar Braces (foam)	16	2.0	0.6
Carbon Rods	2	2.6	0.8
Solar Cells	8	76.2	24.3
Vertical Tail	2	20.2	6.4
Servos	2	43.0	13.7
Reinforcing Ribs	2	21.6	6.9
Fasteners	2	31.2	10.0
Tail Total		313.4	100

Table 5: Tail Component Masses

Aerodynamic Design and Analysis

The wing has been designed to have a span of 3.5 m and a chordlength of 0.424 m from its root to wing tip. A prismatic planform was selected in order to achieve the maximum amount of power per wing area. The flight regime corresponding to a Reynolds number of approximately 200,000 involves difficulty with viscous effect associated with the boundary layer and prediction of the laminar separation bubble. The computational methods at our disposal have proven inaccurate due to the physics of the flow. Reliable experimental data were obtained from Soartech 8: Airfoils at Low Speeds (Selig et al, 1989). Three airfoil sections were considered and their Lift-to-

Drag ratios vs angle of attack are shown in Figure 3. The NACA 6409 was determined to be well suited to thermal sailplane gliding due to its aerodynamic performance at the design point. This airfoil has a maximum of 9% thickness and 6% camber both located at 40% chord and generates a C_L of 0.72 at level flight with an attack angle of 4°. Using the Eppler code (developed by Eppler and Somers, 1980) the inviscid distribution of pressure for an angle of attack of 4° was determined.

The tail is similarly designed with the aerodynamic shape of the NACA 6409 and a prismatic planform of dimensions 0.3 m (chordlength) x 1 m (span). This component has an angle of attack of 0 degrees and generates a C_L of 0.2206 at level flight. Tail efficiency is assumed to be 85%.

The effects of finite wing length on the two dimensional lift and drag curves were investigated using a Fourier series representation developed by Glauert (1937). The prismatic wing design of this aircraft deviates from the elliptic wing resulting in a 4% loss in lift and an 8% increase in drag. Twist and taper of the wing could alleviate these problems, yet these options were not implemented due to construction difficulties.

In order to determine the optimum operational point for the given configuration, a study of the variation of excess power with attack angle was administered. An attack angle of 4° was chosen corresponding to a trimmed tail at -2° (an angle of attack of 0 degrees corresponding to the horizontal). The configurational lift to drag curve resulting from this study is shown in Figure 4.

Structural Design and Analysis

This configuration employs a semi-monoque (stressed skin) structure comprised of a balsa skeleton with a transparent mylar skin covering, providing a lightweight aerodynamic frame to the configuration. Carbon fiber rods running the span of the wing and tail are the major strengthening elements in the wing and tail design. This spanwise spar is comprised of a 3.3 mm diameter carbon fiber rod joined by balsa spar webs to create an I-beam structure. Structural half-models were created and analyzed using a professional version of ANSYS. Increasing levels of detail were incorporated during the course of the academic year.

Applying the maximum anticipated load (equivalent to a gust induced aerodynamic lift of seven times the aircraft weight simulating the design load factor) resulted in compressive and tensile stresses within the structure much less than those allowable for each component given its material properties. The maximum deflection and angle of twist in the wing are 0.24 m and 11.5° respectively, occurring in the wing tips. The tail is restrained at its tips by the connections to the carbon fiber supports and experiences a maximum deflection of only 0.515 mm at its midspan. The results of the ANSYS analysis substantiates the material selection and structural design by verifying the structure will not fail under the utmost anticipated loading.

Controls and Interface

The modified remote control radio system and the necessary hardware for controlling deflecting surfaces and switches via servo-motor, shown in Figure 5, is the essence of the controls and interface scheme.

A propulsion powerplant divided into three subsections is employed. This system includes 98 solar cells, 7 rechargeable Nickel-Cadium batteries, one DC motor, and one propeller, as shown in Figure 5. This power circuit enables three modes of operation. In one mode the solar array is the sole source of input power. A second scenario occurs when the motor is turned off and the NiCad batteries are in parallel with the solar array, the array will charge the batteries provided the array has a high enough voltage and produces sufficient current. The option of utilizing power from both the NiCad batteries as well as the solar array is also available.

The Sun is the only source of electrical input energy and the solar cells serve as the primary source of input power by converting the solar energy into electrical energy. The NiCad batteries serve as a safety feature, both as a secondary power source and a means of supplying short bursts of energy to the system when needed (ie. for takeoff and critical maneuvers). The solar array and NiCad batteries are connected in parallel via a remotely controlled switch in series with the DC

motor. The subsections were optimized to work together and the solar propulsion system was integrated into the final configuration.

Characteristics of solar cells were examined and several types of cells were considered. Finally, 12.5%, 3.75" x 3.75" cells were selected for the current design. The cells are of high quality and relatively good efficiency, yet their size and low power/weight ratio presents considerable constraints. The cells are placed within the wing and tail on foam supports. The supports are mounted on the rib sections to provide protection and maintain the aerodynamic quality of the configuration. Shading from the rib sections is inevitable. However, placing the cells as close to the upper surface of the airfoil shape greatly alleviated this problem.

Decrease in transmittance caused by the mylar coating was theoretically and experimentally evaluated. Using the Fresnel reflection equations (Duffie and Beckman, 1980) and data provided by the cell manufacturer, the theoretical transmittance of the mylar coating was determined to be around 80%. Experimental evaluation yielded a transmittance of 90%.

A random sample of solar cells were tested on Feb. 27, 1991 and the resulting current-voltage (I-V) and power curves were determined. A current adjustment was determined and applied the experimental results. Voltage change as a function of both cell and ambient temperature was estimated (Buresch, 1983), taking into account the effect of light intensity. The ambient temperature for the test data was adjusted by $+10^{o}$ to account for the "greenhouse effect" within the wing. Applying the current and voltage adjustments to the experimental data the I-V and power curves were estimated for a given flight date light intensity and current values, see Figure 6 and 7. The Astro Cobalt 05 electric, geared motor and a two-bladed, folding propeller with a diameter of 33 cm and pitch of 16.5 cm manufactured by Aero-Haute were chosen for their combined efficiency. A combined contour plot of electrical input power, shaft torque, shaft RPM, and motor efficiency versus voltage and current is shown in Fig 8. Three motor-propeller combinations were tested in the WPI wind tunnel under conditions similar to those in flight. Figure 9 illistrates the results of the tests performed for the chosen motor-propeller combination.

Stability

Longitudinal and lateral stability were evaluated by classical analysis methods (Nelson, 1989). The tail and support struts were sized to provide static longitudinal stability (Shevell, 1983). The effects of expected gust induced loads in the longitudinal direction, pitch, results in a rate of change of the pitching moment with the total airplane lift of -0.1415, rendering static stability to the configuration. In order to study the longitudinal dynamic stability of the configuration the long and short period oscillatory modes of motions were examined. A second order differential equation of the plane's motion was derived from Newton's second law and the damping ratio and natural frequency were determined. Results of the longitudinal dynamic stability analysis at the design point are given in Table 6.

MOTION	Frequency	Period
Long Period	0.948	2.12 s
Short Period	0.045	7.07 s

Table 6: Dynamic Longitudinal Stability

The vertical tail and dihedral were sized to provide lateral stability. The vertical tail has a volume coefficient of 0.018, which is very close to the typical value of 0.02 for a sailplane (Raymer, 1989), and furnishes directional stability. Dihedral stability is achieved by adding a small positive dihedral angle of 5^{o} at a location of 0.75 m from the wing root tending to return the aircraft to its equilibrium position once it has been disturbed by a rolling moment (Raymer, 1989).

Performance and Mode of Operation

Solar propulsion is very appealing on the basis that it is harmless to the environment and cost efficient. The performance of a vehicle, however, is very confined to the weather, time of day, location, season, and efficiency of its solar power system. The available solar cells for this aircraft configuration were not the most efficient or light

weight, yet did allow for excess power for take-off and climb. A computer code was developed to predict the performance of the aircraft in level flight, see Figure 10.

The aircraft is designed to climb in a circular flight path to an altitude of 50 m in 6.7 minutes, as shown in Figure 11. This mission requires 7 complete revolutions about a 200 m field. The climb rate is a function of the angle of incidence between the sun and the solar cell array, the aircraft climbs at a rate of 0.155 m/s away from the sun and 0.093 towards the sun.

At the design altitude, 15.9 W is required from the propulsion system to maintain flight at 7 m/s. A sustained figure eight flight pattern will be achieved with an angle of attack of 4°, banking angle of 4°, and a turning radius of 79 m. Figure 12 shows the optimization of excess power with respect to the attack angle of the wing.

Construction Procedure

The final design of the solar powered vehicle was meticulously constructed with every attempt to maintain the aerodynamic features and weight budget for each component and any additional items not initially allotted for. In order to facilitate transport, storage, and construction modular features were incorporated into the final configuration. Mindful consideration was given to the connections in order to maintain the structural integrity of the original design. Currently the aircraft is being prepared for a test flight in order to establish the effectiveness of the control system and its overall stability.

Environmental Impact

Society is faced with various self-induced environmental problems. Implementation of solar energy as a replacement to traditional energy resources provides an economical solution. The design and construction of this solar powered aircraft attempts to contribute to this cause and encourage future research into alternative energy resources.

CONCLUSIONS

A preliminary study of a solar powered MPRPV designed to operate at approximately sea level indicates that it is currently feasible to integrate solar propulsion into the design of airborne vehicles. Increased research regarding the potential of and possibilities for solar energy is encouraged.

ACKNOWLEDGEMENTS

The assistance and technical support of the NASA contacts, WPI faculty, Mobil Solar, and many other interested aircraft modelling enthusiasts were numerous and very greatly appreciated. Special thanks to Art Glassman, our NASA/USRA mentor and the advising professors, Prof. William W. Durgin, Prof. Andreas N. Alexandrou, Prof. Ralph F. Cohn, Prof. Vahid Motevalli, Prof David J. Olinger, Prof. Joseph J. Rencis, Prof. Clark, and Kurt Heinzmann for their faithful guidance. The educating assistance on low Reynolds number flight vital to the required mission provided by Don Harvey and Dan Somers, both affiliated with NASA Langley, has been invaluable. Also thanks to the many helpful students from WPI especially Adam Szymkiewicz, Jason Makofsky, and Kyle Jacobson for sharing their expertise.

REFERENCES

Buresch, M. 1983. Photovoltaic Energy Systems: Design and Installation. McGraw-Hill Inc., New York.

Eppler, R. and D. Somers. 1980. "A Computer Program for the Design and Analysis of Low-Speed Airfoils, Including Transition." NASA TM 80210.

Duffie, J. and W. Buckner. 1980. Solar Engineering of Thermal Processes. John Wiley and Sons, Inc.

Nelson, R. 1989. Flight Stability and Automatic Control. McGraw- Hill. New York.

Raymer, D. 1989. Aircraft Design: A Conceptual Approach. American Institute of Aeronautics and Astronautics, Inc. Washington D.C.

Selig, M., J. Donovan, and D. Fraser. 1989. Soartech 8: Airfoils at Low Speeds. H. A.

Shevell, R. 1983. Fundamentals of Flight. Prentice-Hall. Englewood Cliff, New Jersey.

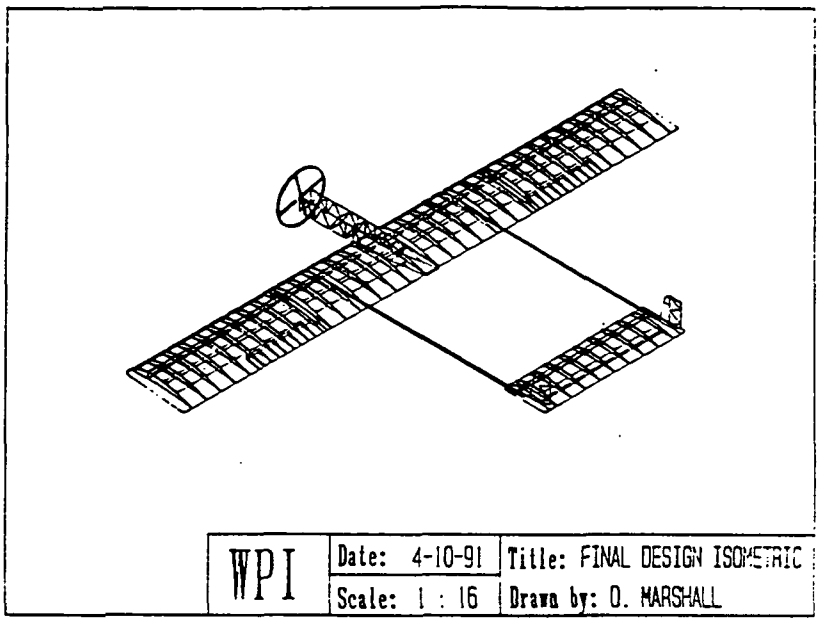

Figure 1: Final Design - Isometric View

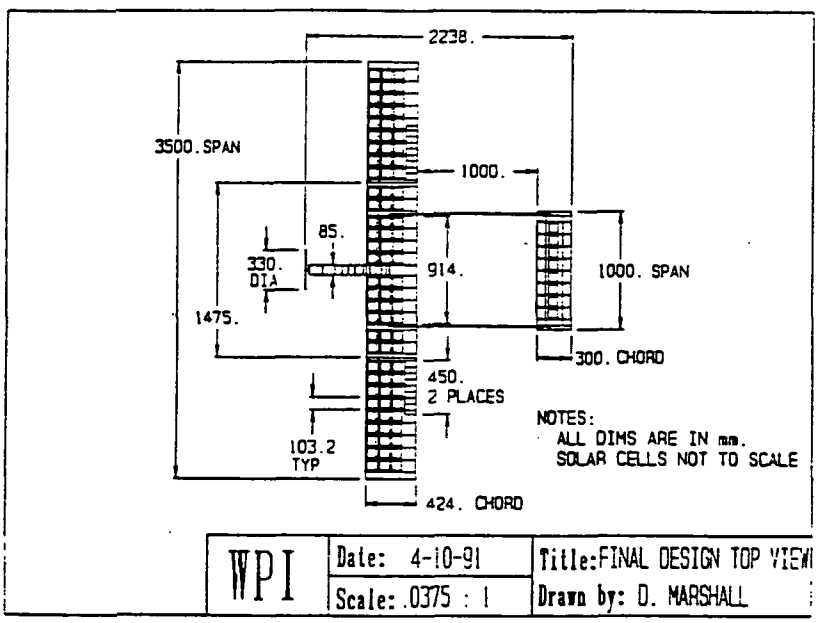

Figure 2: Final Design - Top View

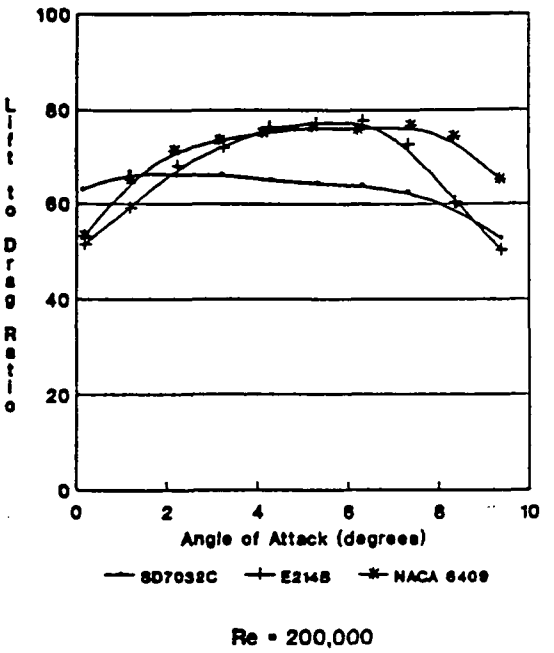

Figure 3: Comparison of Airfoil Sections

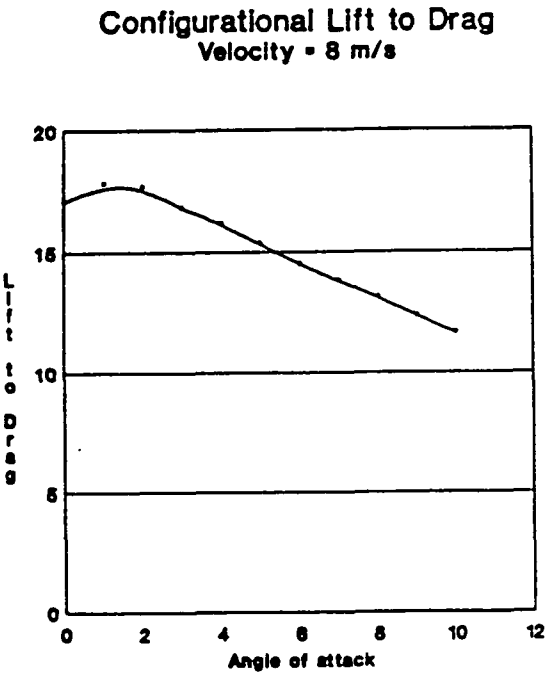

Figure 4: Configurational Lift to Drag Curve

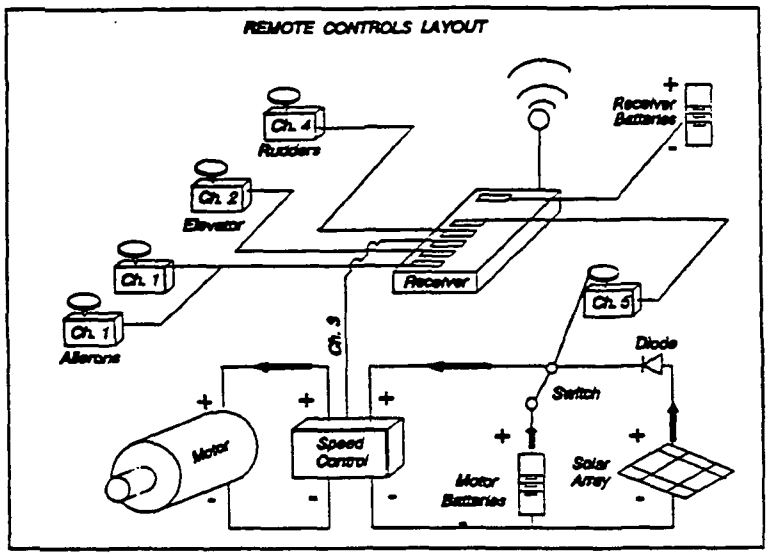

Figure 5: Controls Layout

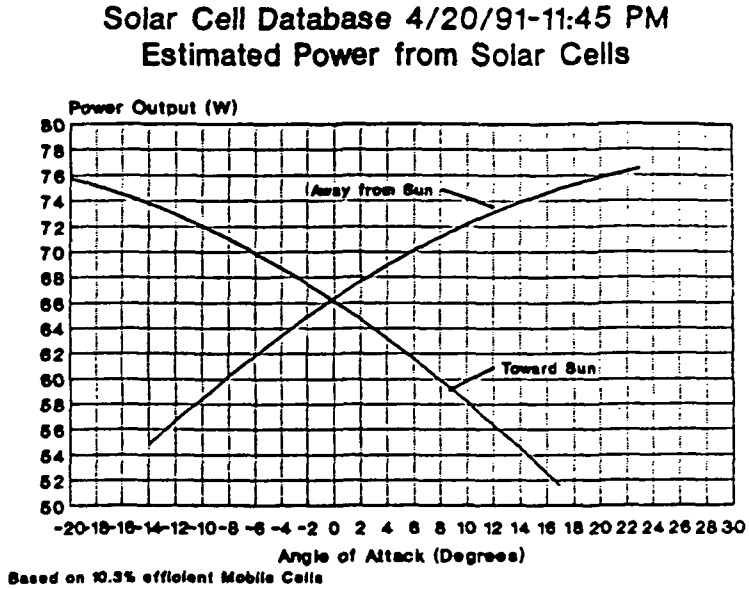

Figure 7: Estimated Power from Solar Cell Curves

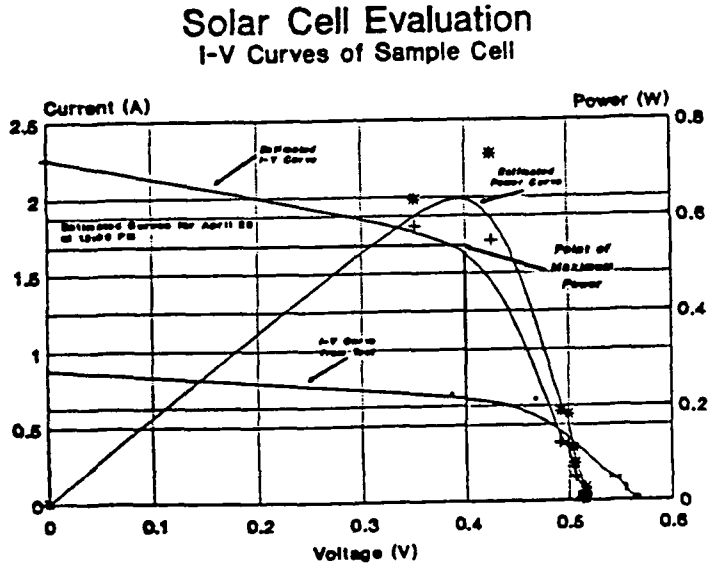

Figure 6: Solar Cell Current - Voltage Curves

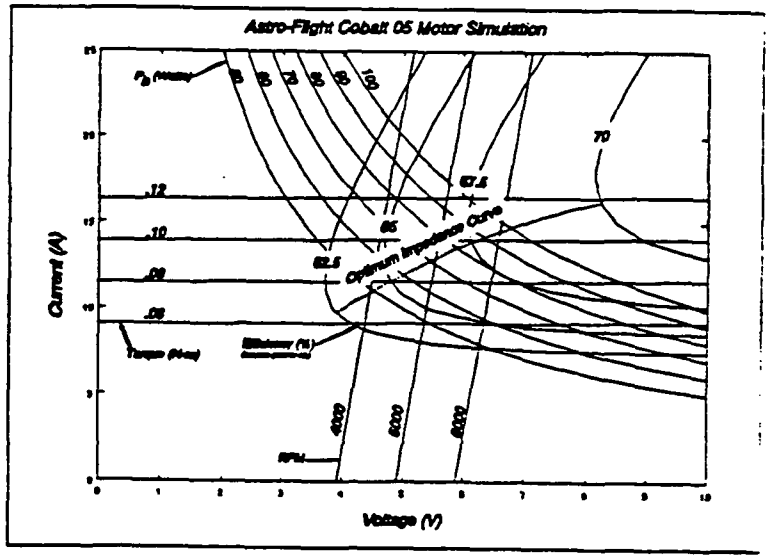

Figure 8: Combined Contour Plot for Design Motor

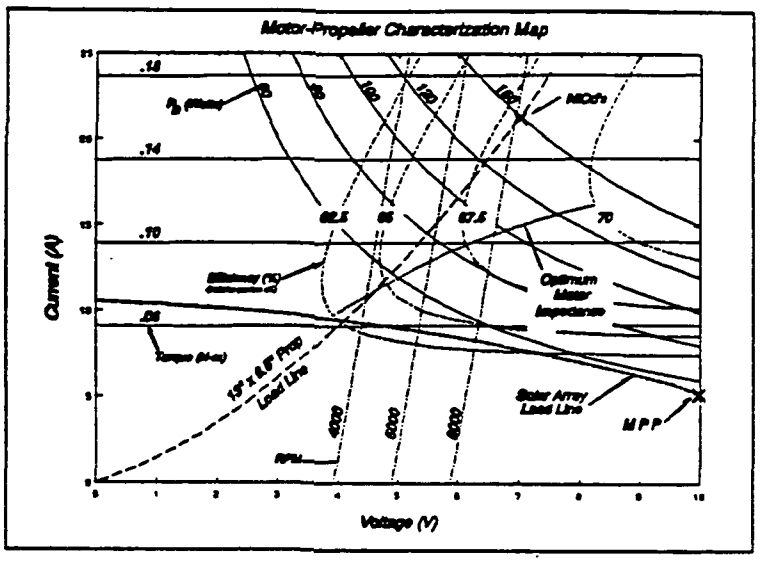

Figure 9: Combined Contour Plot for Design Motor - Propeller Setup

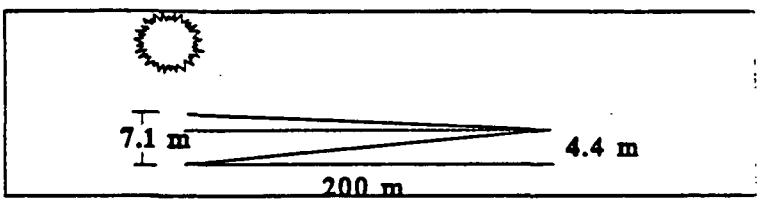

Figure 11: Circular Climb Pattern

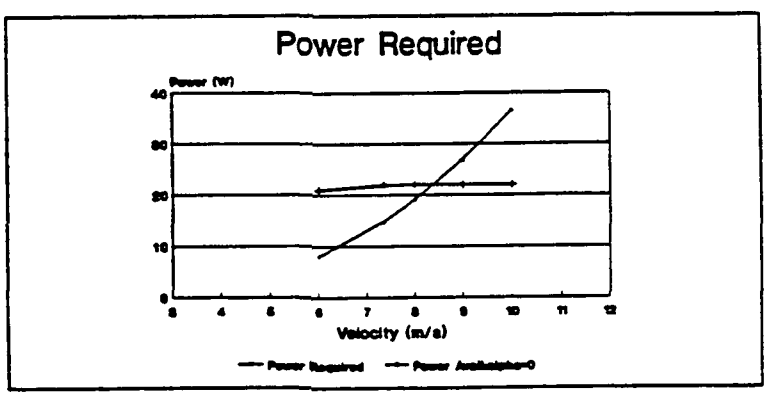

Figure 10: Design Power Curve

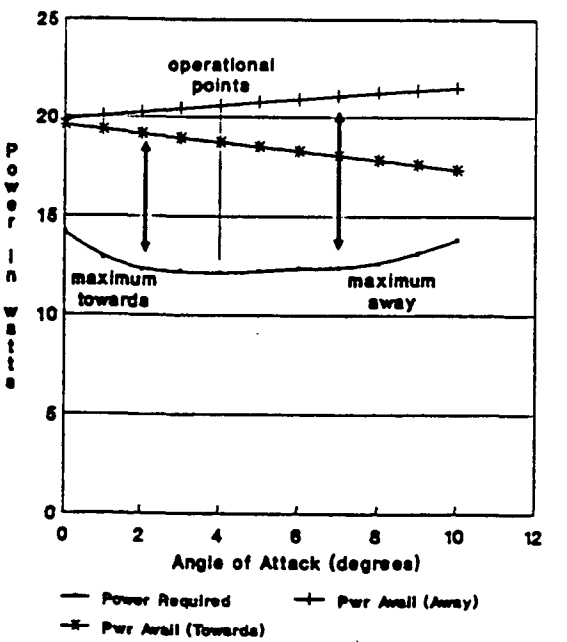

Figure 12: Optimization of Excess Power with Angle of Attack

CHAPTER 1

INTRODUCTION

The concept of solar-powered flight is not unique to the 1990's. The idea was first tested on November 4, 1974 with Sunrise I, a high altitude endurance sailplane. This plane, flown by Robert J. Boucher, proved that it was feasible to harness an inexhaustible energy source for the use of airplane propulsion. This design was not able to attain an extended solar flight, but it set a record for solar-powered vehicles that has yet to be broken (Boucher, 1984). In addition to Sunrise, other small scale aircraft have been designed utilizing solar arrays and solar charged batteries to assist on takeoff and to partially power flight. The work of Freddie To in England resulted in the Solar One, and of Larry Mauro created the Solar Riser in the United States, both of which used batteries charged off of the solar cell arrays mounted on their wings for takeoff. The next step in this progression of technology was to design and build a plane that would fly exclusively on solar power without battery assistance.

This became the goal of Paul MacCready, who was already famous for his successful manpowered aircrafts, the Gossamer Condor and the Gossamer Albatross. Working with Robert Boucher, MacCready lead his group of designers and builders to success, and on November 20, 1980 the first truly solar powered manned aircraft flew for 2 minutes and 50 seconds. After several similar flights and numerous tests, a goal was set for the first long distance flight, from Tucson to Phoenix, Arizona.

This flight began on December 3, 1980, and though it was not successfully completed, a great deal was learned about the reliability and piloting of this revolutionary plane (Cowley, 1981).

This idea of solar powered flight has even carried over into remote control sailplanes. Experts have been incorporating this new energy source into their planes for years now, and enjoying the challenge. Most of these designs utilize the solar cells to charge and maintain charge of the onboard NiCd batteries. This system is set up to provide the convenience of being able to fly at the spur of the moment, because the batteries need not be precharged, they are charged as the plane flies (Blakely, 1982). The next step, similar to the one taken by Paul MacCready, is to create sailplanes that are powered solely by the sun, without battery assistance.

Although some have had much success with the solar flight of sailplanes, the concept of utilizing only the sun's energy for power still provides an extraordinary design challenge. Standard aircraft design requires numerous trade-offs between a wide range of engineering disciplines, including aerodynamics, controls, structures, performance and propulsion. The difficulty arises in integrating the requirements of each discipline towards one common goal. The addition of a solar propulsion system creates new design requirements which further complicate this already intricate process. As part of their Advanced Aeronautics Design Program, NASA/USRA sponsored a study that challenges students with this process, the design and construction of a solar-powered remote control aircraft that is powered directly by the sun with no battery assistance.

CHAPTER 2

MISSION DEFINITION

The ultimate goal for the aircraft is to perform a sustained figure eight flight pattern at an altitude of 50 m using only solar power. The mission will be carried out in several flight stages including launch, climb to altitude, and pattern flight.

The aircraft will be launched away from the sun utilizing a catapult system to provide some initial altitude. As a result of the solar array positioning, the most power will be received when the aircraft is travelling away from the sun. Therefore the best climb rate will be achieved when flying in this direction. A circular climbing pattern will be utilized, in order to compensate for slow climb rates and enable the aircraft to remain within a reasonable distance from the ground control. Once at altitude, a sustained figure eight pattern tests the aircraft characteristics over a variety of maneuvers.

CHAPTER 3

DESIGN PROCEDURES

3.1 DESIGN PROCESS

In order to develop a design which would successfully complete the mission, the project team was divided into four design sub-groups. The four groups were Aeronautics, Structures, Mission/Performance, and Controls/Interface. Each of these groups was responsible for specific tasks relating to the overall design.

The Aeronautics group was primarily responsible for the development of the wing and horizontal tail. This included choosing a variety of airfoil sections and analyzing them to determine the lift/drag characteristics. The group also had to interact with the Controls/Interface group to ensure that the geometry of the selected airfoil section could satisfy the solar cell placement requirements. After the airfoil section was selected the wing and tail were optimized to provide the maximum lifting force with the least amount of drag.

The responsibilities of the Structures group included structural analysis and material selection. Once an original sizing estimate was obtained, the group analyzed a variety of materials to determine the lightest materials which could withstand the expected loadings. Most of the theoretical analysis was performed using ANSYS finite element modeling software.

The Mission/Performance group was responsible for determining the mission

profile that could realistically be achieved. In addition, the group was responsible for analyzing the overall effect of any design change by another group. The two primary areas investigated were stability and flight performance parameters.

The final group, Controls/Interface, was responsible for the integration of a solar propulsion system into the aircraft. This included selecting and testing not only the solar cells but also a motor/propeller combination that would yield the highest efficiency. Another essential task for the group was to determine the ideal solar array configuration.

The design process began with the Aeronautics, Structures, and Controls/Interface groups proposing an original design. This design was then analyzed by the Performance group, to determine if it could meet the stated mission objectives. If it could not, recommendations were made as to what changes were necessary to enable the aircraft to complete the mission. This process was iterative in nature and led to the optimization of the design.

3.2 DESIGN DESCRIPTION

3.2.1 Configuration

The final design consists of a non-conventional, high wing aircraft as shown in Appendix C.10. The main distinction between this design and conventional aircraft is the split fuselage aft of the main wing. This "split fuselage" actually consists of two horizontal tubes, constructed out of vinylester carbon-fiber composite material. These extend from the spar of the wing to the spar of the horizontal stabilizer. The primary

reason for utilizing the "split fuselage", is that the tubes aid in the prevention of wing tip deflection during critical operations. This becomes of primary importance during both takeoff and landing, as large wing tip deflections could cause contact resulting in catastrophic failure.

A solar propulsion system, which includes 98 photovoltaic solar cells supplied by Mobil Solar Corporation, powers the aircraft. The cells directly power an Astroflight Cobalt .05 motor which drives a folding Aero-haut 13" x 6.5" pitch plastic propeller. As a safety feature, a switch is included to provide access to a nicad battery backup system.

The electronics equipment is housed in a pod, connected to the underside of the main wing. The pod was built utilizing a balsa truss structure covered with a mylar coating. The truss structure provided the fuselage with the necessary strength to safely house the electronics equipment under all anticipated loads, while minimizing the weight.

The wing and horizontal tail are both constructed using N.A.C.A 6409 airfoil sections. The sections near the wing root are constructed out of balsa, while those sections near the wing tip utilize a composite foam construction. This was a necessary compromise, which accounts for the non-uniform load distribution over the wing. The cells are mounted on foam shelving in between the airfoil sections.

In addition, the aircraft is equipped with a variety of control devices including two ailerons, two rudders, and an

elevator. These are directed with an onboard receiver which uses four electronic

servos to control their motion.

3.2.2 Dimensions

Aircraft sizing becomes a very important process after the general configuration has been determined. Our design goals required the aircraft to be powered solely by the sun, therefore the major limiting factor was the power available from the solar cells to the propulsion system. As a result, the number of solar cells required was first optimized, which dictated the wing and tail dimensions. Once the wing/tail sizing had been determined, factors such as stability directly impacted all remaining component dimensions.

It was established that ninety-eight cells would yield the optimum power to weight ratio. Ninety 3/4" by 3/4" cells were placed in the wing and the remaining eight on the tail. On the wing, thirty rows of three cells were placed chordwise between each of the airfoil sections, while on the horizontal tail it was necessary to place only one cell between each of the airfoil sections. This configuration yielded a wing and tail with the following dimensions.

Table 3-I: Wing/Tail Dimensions

	WING	TAIL
SPAN	3.5 m	1.0 m
CHORD	.424 m	.3 m
PLANFORM AREA	1.48 m^2	.3 m^2
ASPECT RATIO	8.25	3.33

As a result of the tail providing less lift than the wing, it was required that the horizontal tail be positioned far enough aft to create a balancing moment around the center of gravity. As a result, it required that the leading edge of the horizontal tail be placed one meter behind the trailing edge of the wing.

The next component to be sized was the pod. In order that the center of gravity be located in such a position to provide stable flight, this pod needed to extend well in front of the leading edge of the wing. With the electronic components placed in the front of the pod the aircraft center of gravity is forced forward. The length of the pod is .891 m with .467 m extending in front of the wing. The width and height of the pod are .065 m and .08 m respectively.

3.3 TESTING PROCEDURES

An essential step in the design process includes a variety of testing procedures to ensure the design can achieve its goals. These tests should focus not only on the overall aircraft, but also on the individual components. For this design three main areas of testing include static structural analysis, solar propulsion system testing, and overall flight vehicle performance testing.

Static structural analysis verifies that the individual components can withstand expected loadings. These procedures can be carried out prior to component construction using finite element modeling. Once the components are constructed the theoretical results can be verified through deflection testing.

Solar propulsion system testing is necessary because solar cell performance

depends on how the cells are arrayed. By connecting the cells in different parallel and series combinations, the overall output of the array will be changed. Therefore, different combinations are tested to determine the ideal array.

To ensure that the plane is flight worthy, a test flight will be conducted prior to the addition of the solar propulsion system. The overall goal of this testing is to determine if the aircraft can carry out its mission, without risking the destruction of the solar array. The test is designed such that several flight characteristics can be evaluated. These include stability, maneuvering, and ease of control. In order for these tests to be valid without the solar array, an equivalent weight distribution must be included on the aircraft. Once the solar array has been added, a second test flight will be conducted to test the integrated system, prior to flying the intended mission.

CHAPTER 4

AERODYNAMIC DESIGN AND ANALYSIS

4.1 INTRODUCTION

The main objective of the Aerodynamics Group was to design and analyze all aerodynamic lifting surfaces while interacting with the other three project design groups. Preliminary interaction between the groups determined cell placement and set a general overall configuration. Responsibilities of the Aerodynamics Group included: Airfoil selection for the wing and tail; design of the wing and tail; determination of configurational lift and drag; and optimization of the configuration's level-flight operational point.

4.2 AERODYNAMIC CONFIGURATION CHARACTERISTICS

At completion of the design process the aerodynamic characteristics of the configuration were set as the following. The chosen wing airfoil section is the NACA 6409. The wing of the configuration has a prismatic planform with a span of 3.5 meters and a chord of 0.424 meters, resulting in a aspect ratio of 8.25. The wing is attached to the fuselage at an angle of attack of 4 degrees, relative to chord. At level flight conditions, this angle of attack generates a total wing C_L of 0.7195. The wing produces a downwash of -2 degrees. The tail section for the configuration was selected to be the NACA 6409. The tail has a span of 1 meter and a chord of 0.3

meters, resulting in a aspect ratio of 3.33. The C_L of the tail is 0.2206. The efficiency of the tail was assumed to be 85%. The configuration, at level flight conditions, has a airplane lift coefficient of 0.8301 and a airplane drag coefficient of 0.05269. The justification of aerodynamic sizing and methods of analysis will be discussed in the following sections.

4.3 REYNOLDS NUMBER REGIME

During the preliminary design process, it was determined that the Reynolds number based on chordlength of the main lifting surface would be approximately 200,000, which is a rather low Reynolds number for airfoils. In this regime, the viscous effects associated with the boundary layer, which include the complications of laminar-to-turbulent transition such as the effects of the laminar separation bubble, led to restricted airfoil performance. This posed several complications to design. Due to the difficulties of predicting viscous flow behavior within this Reynolds number range, available computational methods proved to be inaccurate. Reliable wind tunnel testing in the W.P.I. Aerodynamics Laboratory Wind Tunnel was not possible due to the presence of fairly high free stream turbulence levels within the test section. A more detailed discussion of the fluid mechanics related to low Reynolds number airfoils is found in Appendix B.1.

4.4 SOLAR CELL PLACEMENT

One important design consideration was the placement of solar cells within the configuration. This determination had significant influence over aerodynamic aspects of design, such as selection of wing and tail airfoils sections and sizing of the wing. Because of this, a preliminary task of the Aerodynamics Group was to aid in the determination of solar cell placement. With input from the other three groups, several options were considered, including the design of a flat-backed airfoil, an addition of a flat plate, and placement of cells within the lifting surfaces.

One consideration for the placement of solar cells was the design of a flat-backed airfoil. As seen in Figure 4.1,

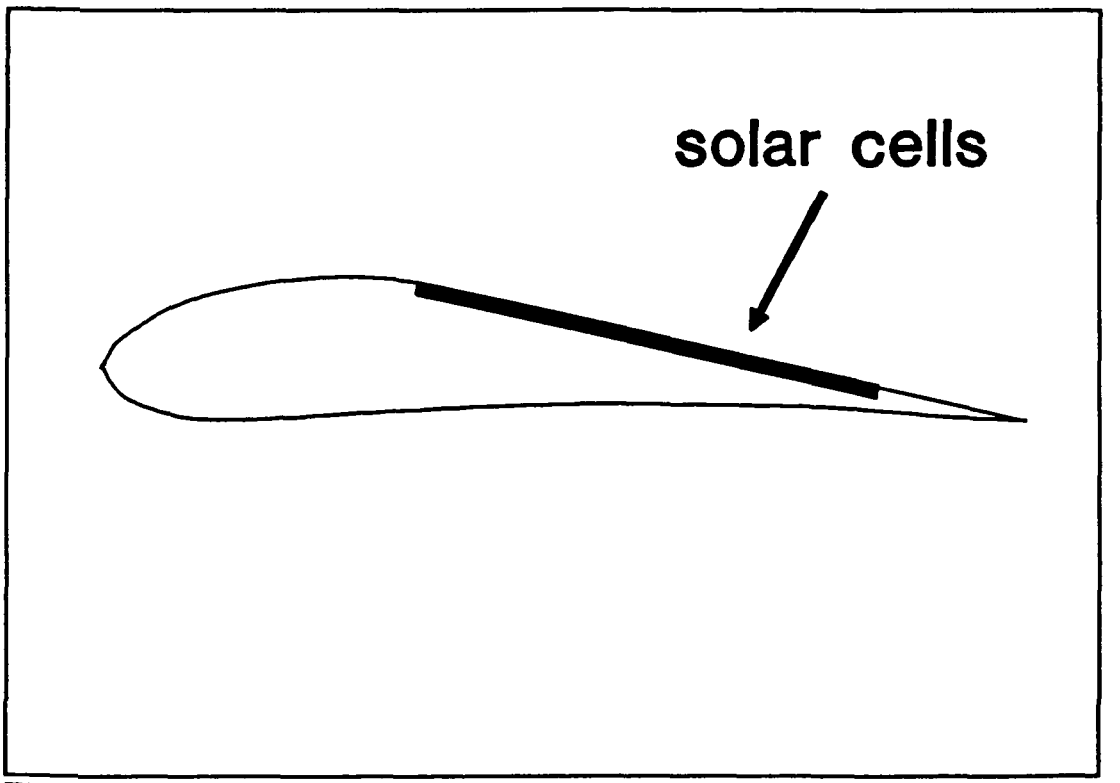

Figure 4.1: Proposal of a flatback airfoil (70 percent flat).

this would enable cell placement on the exterior of the wing and tail, however this

was discarded for several reasons. Due to the flat upper surface of such an airfoil, a smooth gradual pressure recovery could not be achieved as shown in Figure 4.2.

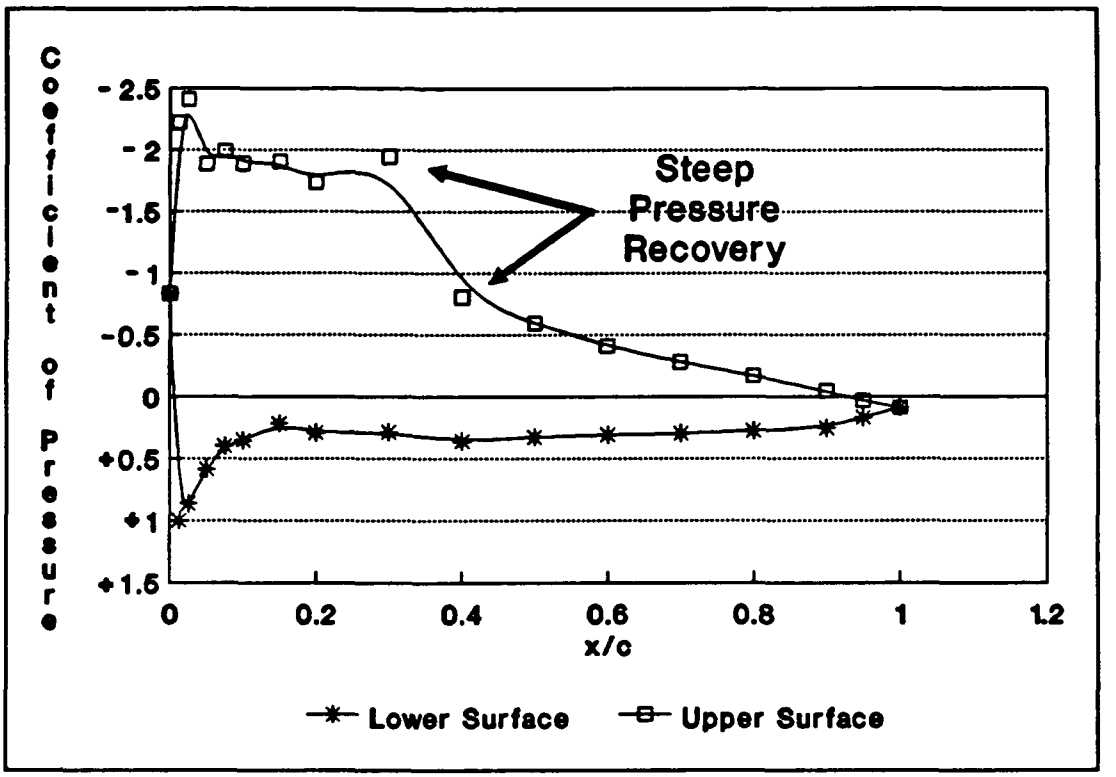

Figure 4.2: Inviscid Distribution of Pressure for 70 percent flatback airfoil.

In the laminar region, this adverse pressure recovery could result in separation, premature stall, or insufficient lift to drag ratio. In addition, the flatback airfoil, which would be rigidly placed on the airfoil's surface, would not provide adequate protection for the fragile solar cells.

Consideration was also given to the addition of a flat plate upon which cells could be placed. This flat plate would be positioned horizontally between the wing and tail, supported by the tail support booms as seen in Figure 4.3. Due to structural considerations, the optimal placement of this plate would be directly aft of the wing.

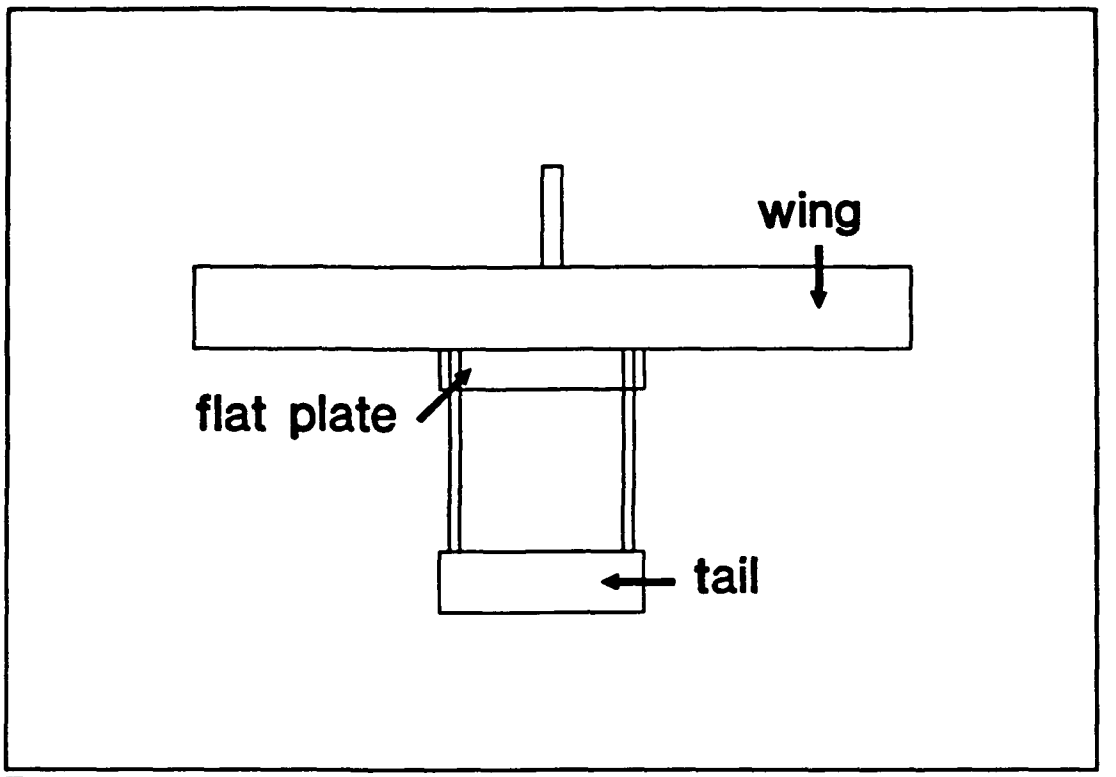

Figure 4.3: Proposal of a flat plate for cell placement.

This would enable the plate to be supported by the wing as well as the booms, thus reducing the maximum bending moment on the plate. This would also minimize excess support structures, therefore keeping additional weight to a minimum. Despite the structural advantages of the flat plate placement directly aft of the wing, this configuration would create adverse aerodynamic effects. The position of such a plate would act as an extension of the wing (such as a flap), thus effectively altering the airfoil section. This 'flap' (on the order of 30 percent of chord), which would be at a negative angle of attack with respect to the wing, would cause a decrease in lift and an increase in drag. The presence of this plate would also create an undesirable shift of the aerodynamic center during climbs, resulting in stability complications. This proposal, which did not provide adequate cell protection (similar to the flatback), also

created additional drag and structural weight.

The final consideration for cell placement, which proved to be the most advantageous, was the positioning of solar cells within the lifting surfaces. This is accomplished by placing cells on non-rigid foam supports within the wing. A clear mylar coat is used as a covering to allow for solar transmittance to the cells, as well as providing the desired airfoil shape. This option would provide adequate cell protection without the addition of structural weight or the introduction of adverse aerodynamic effects, such as those introduced by the flat plate or the flat-backed airfoil. By placing the cells within the lifting surface certain losses are incurred. These losses are due to the reflectance of the mylar coating and shading produced by the ribs. Despite these losses, this option for cell placement was chosen to be the best alternative, and implemented into the final design.

4.5 ACQUISITION OF DATA

Usually in the aerodynamic design process it is desirable to either conduct wind tunnel testing or use computational techniques in the hope of finding an optimum airfoil section. For this configuration, many complications arise due to the fact that design will be operating within the low Reynolds number region. Since experimentation was not a feasible alternative and reliable computational programs (for low Reynolds numbers) were not available, it was necessary to use published experimental data. Soartech 8: Airfoils at Low Speeds, which is a compilation of low Reynolds number airfoil tests performed by Michael Selig, John Donovan, and David

Fraser at Princeton, was the primary source of data. These experimental results have been shown to be highly reliable. (More details on the reliability of these experiments are documented in Appendix B.2.)

4.6 AIRFOIL SELECTION

An important design function of the Aerodynamics Group was the selection of a high lift, low Reynolds number airfoil for the wing. This choice was based on the lift and drag characteristics of over 150 airfoils compiled in the Princeton data. The primary criterion in selecting an airfoil section was a high lift to drag ratio for a Reynolds number of 200,000. After examining the characteristics of all the airfoils published in Soartech 8, three airfoils were chosen as possible design selections. These were the Selig-Donovan(SD) 7032-C, a modified version of the Eppler(E) 214, and the NACA 6409. The lift to drag ratios for these three airfoils are shown in Figure 4.4. The SD 7032-C, which is among the best airfoils suited for thermal sailplane gliding[1] (Selig et al., 1989), has a level lift to drag ratio over a wide range of angles of attack. This type of 'plateau' would be beneficial for a wide range of operational conditions. The E 214 (with an increased aft camber) has the highest lift to drag peak of all the sample airfoils. This made it an attractive airfoil, however its drastic decrease in lift to drag following its maximum was undesirable. The NACA 6409, which was selected as the configuration's wing section, proved to be an

[1] Sailplane gliding refers to light aircraft which take advantage of thermal air currents to provide additional lift.

excellent compromise of these two, having a long plateau similar to the SD 7032-C and a high lift to drag ratio similar to the E 214.

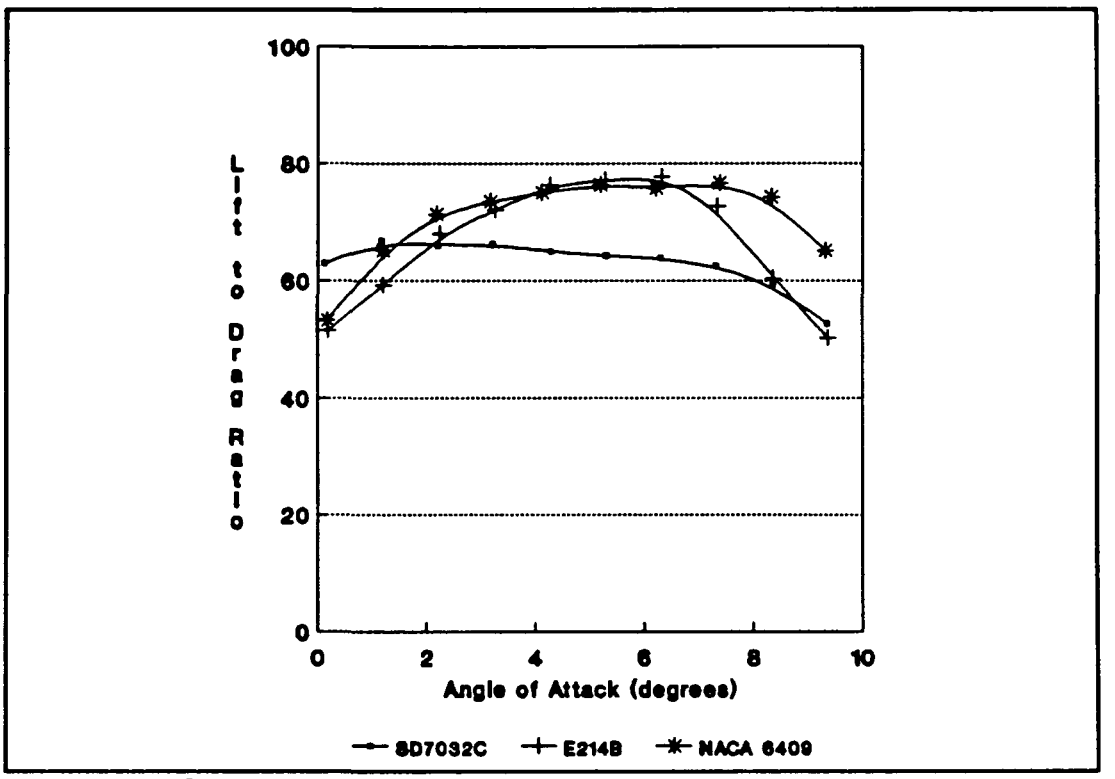

Figure 4.4: Comparison of Airfoil Sections (Re = 200,000).

Figure 4.5 shows the NACA 6409 and its coordinates relative to its chordline (which is represented by a dashed line). This airfoil is a 9 percent thickness airfoil (maximum thickness occurs at 40 percent of chord) with a maximum camber of 6 percent. It is "an excellent low speed, floater airfoil, but...the large camber severely limits the high speed performance." (Selig et al., 1989) Since the configuration will be operating at low velocities, it is believed that this is the best choice of the available airfoils. The drawback of the NACA 6409 is that separation begins around an angle of attack of 9 degrees (relative to chordline). However, the configuration will be

operating at lower angles of attack in order to avoid this phenomenon.

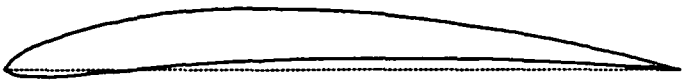

x/c	y/c	x/c	y/c	x/c	y/c
1.00000	0.00000	0.19988	0.08874	0.34730	0.01425
0.99732	0.00084	0.15830	0.07992	0.39618	0.01639
0.98930	0.00333	0.12080	0.06982	0.44707	0.01772
0.97603	0.00737	0.08780	0.05889	0.49868	0.01871
0.95760	0.01284	0.05968	0.04762	0.55040	0.01925
0.93423	0.01954	0.03677	0.03646	0.60167	0.01929
0.90615	0.02724	0.01920	0.02581	0.65193	0.01880
0.87357	0.03571	0.00720	0.01603	0.70065	0.01780
0.83690	0.04464	0.00080	0.00737	0.74728	0.01634
0.79647	0.05378	0.00000	0.00000	0.79130	0.01451
0.75272	0.06283	0.00467	-0.00573	0.83223	0.01241
0.70608	0.07153	0.01467	-0.00956	0.86957	0.01017
0.65710	0.07961	0.02973	-0.01157	0.90288	0.00791
0.60627	0.08684	0.04970	-0.01192	0.93180	0.00576
0.55413	0.09302	0.07428	-0.01080	0.95593	0.00383
0.50132	0.09796	0.10317	-0.00844	0.97503	0.00221
0.44840	0.10152	0.13607	-0.00513	0.98883	0.00101
0.39590	0.10360	0.17257	-0.00119	0.99722	0.00025
0.34367	0.10352	0.21235	0.00307	1.00000	0.00000
0.29315	0.10086	0.25498	0.00729		
0.24502	0.09584	0.30012	0.01112		

Figure 4.5: Coordinates and Plot of the NACA 6409.

Figure 4.6 shows the inviscid distribution of pressure coefficients, which was determined using the NASA numerical code (developed by Eppler and Somers, 1980), for an angle of attack of 4 degrees (which is the level-flight operating condition--See Section 4.12). The high camber produces high constant pressures over the first third of the airfoil. At maximum camber (40 percent of chord) the airfoil's somewhat steep pressure recovery begins. (The slope of this pressure recovery, which becomes larger at higher angles of attack, is the cause for the airfoil's low separation angle.) The lower surface experiences relatively constant pressures over 90 percent of the chord.

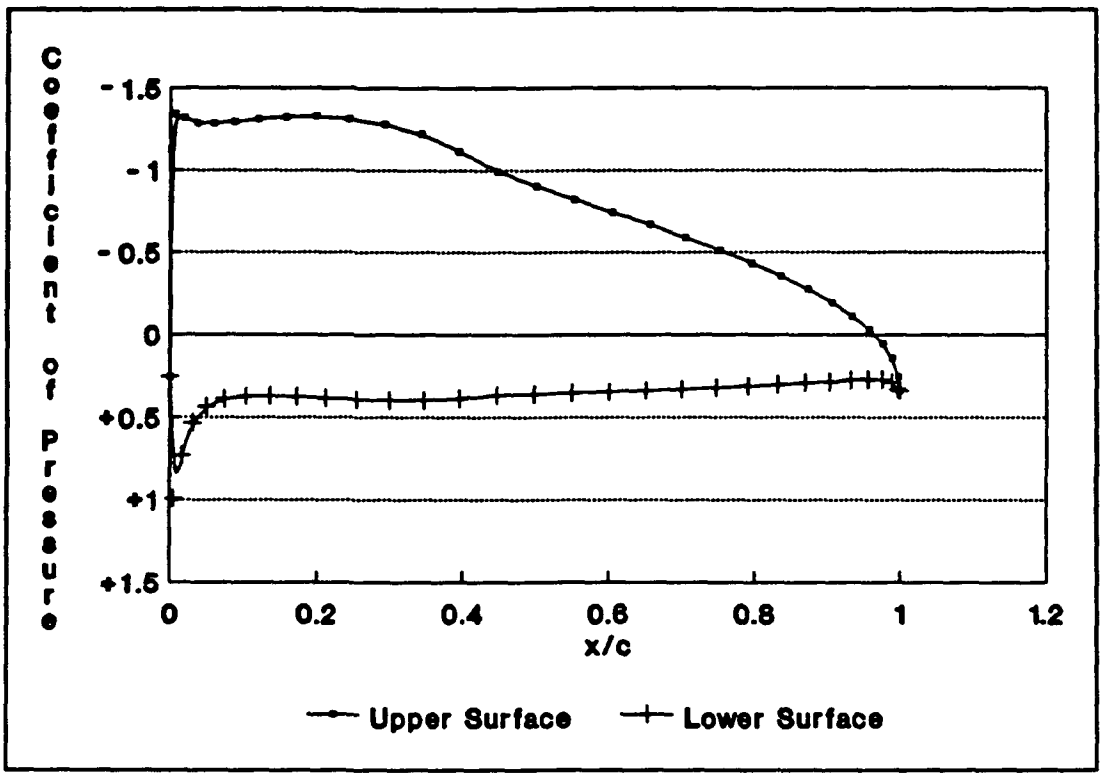

Figure 4.6: Inviscid Distribution of Pressure for the NACA 6409 at an angle of attack of 4 degrees.

Figure 4.7 shows the lift and drag characteristics of the NACA 6409 at a Reynolds number of 200,100. The airfoil's lift curve slope of 5.17 per radian is relatively constant up to an angle of attack of 8 degrees. The maximum lift coefficient of 1.34 (which is high for low Reynolds number airfoils) occurs at an angle of attack of 9 degrees with stall occurring for higher angles of attack. The drag coefficient (which is comparable with other airfoils at Reynolds numbers of approximately 200,000) varies in an approximately parabolic manner with a minimum of 0.0112 at 1 degree. These two characteristics result in a lift to drag 'plateau' of approximately 75 between the angles of 2 and 8 degrees.

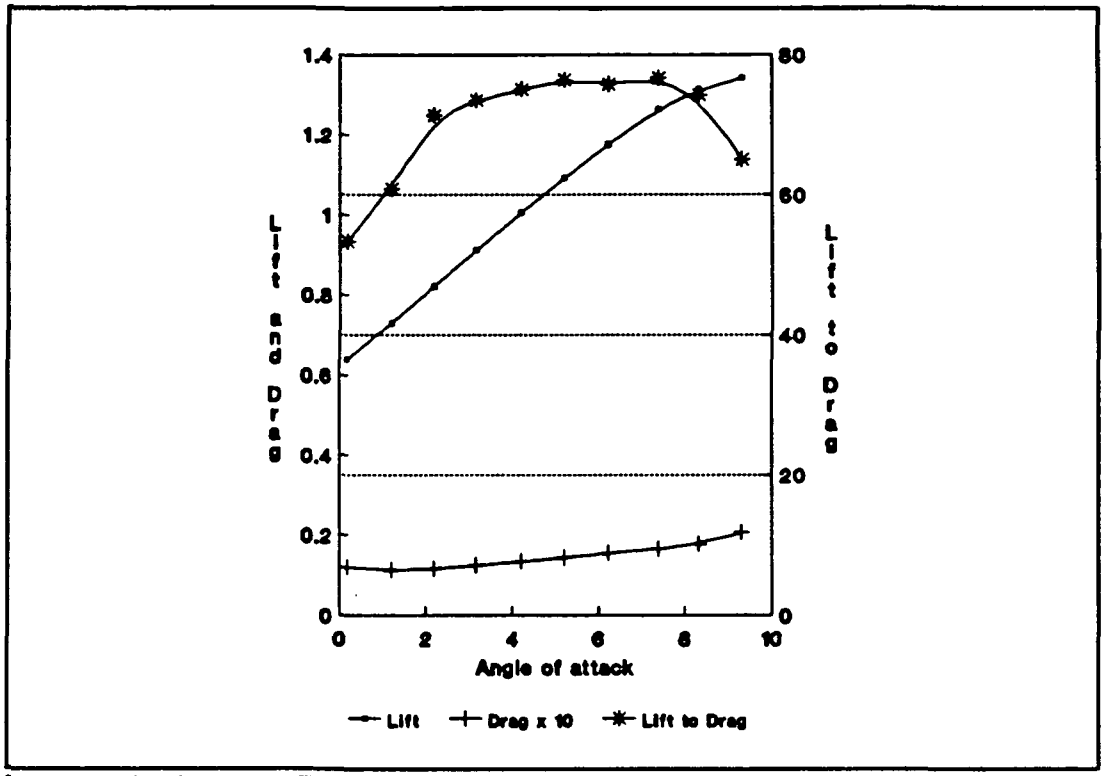

Figure 4.7: Lift and Drag Characteristics of the NACA 6409 at Re = 200,100.

4.7 WING SIZING

The wing sizing was determined based on several constraints. The primary constraint leading to chordlength optimization was the size of the solar cells, which are 9.525 centimeters square. In addition, the Controls Group required a 3.2-millimeter border about each cell (for wiring and spacing). Preliminary iterations of the Performance, Controls, and Aerodynamics Groups, determined that approximately 100 solar cells were required. These cells were to be placed close to but beneath the surface (of the wing and tail) in order to minimize the shading effect

of the ribs. The Controls Group required that the cells placed on a plane horizontal to level flight if possible in order to maintain a fairly constant solar radiation flux for all flight paths. Also, it was desired to place as many cells as possible within the same geometric plane in order to minimize voltage and current mismatches. In addition to the constraints imposed by the solar cells, there were structural constraints. As can be seen in Figure 4.8, the Structures Group dictated the location

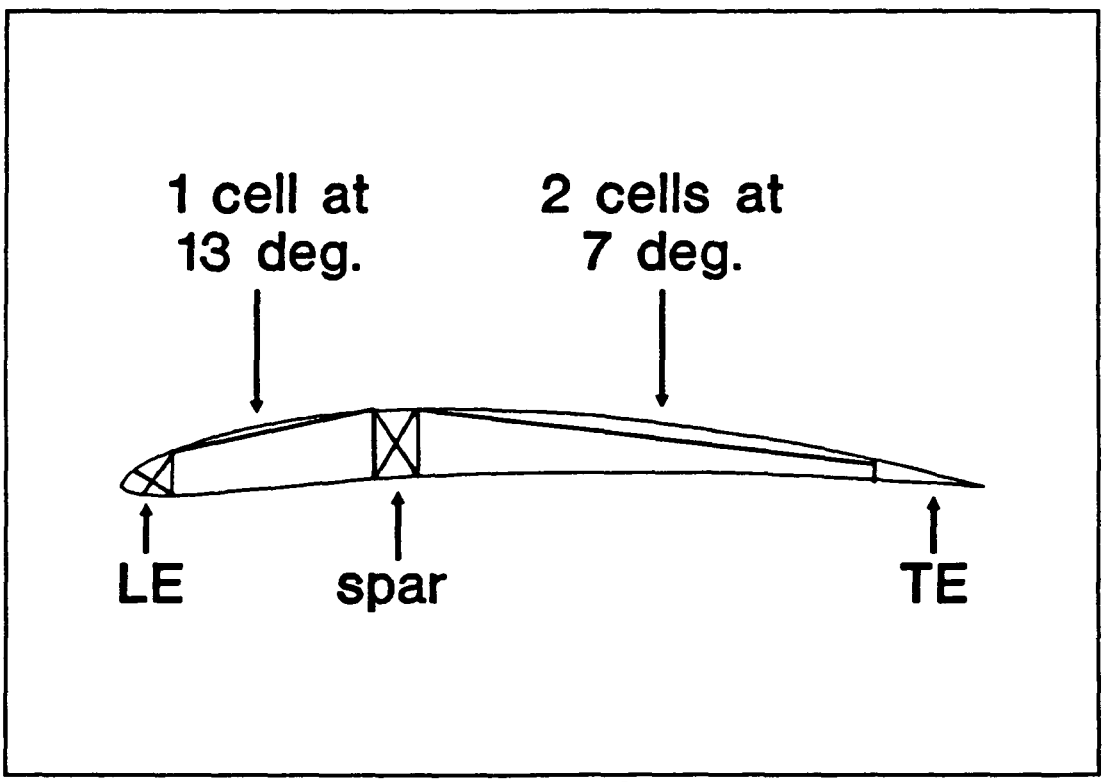

Figure 4.8: Solar cell placement in the NACA 6409.

of the main vertical support spar to be in the vicinity of the quarter-chord, preferably slightly aft. Sizing of the leading and trailing edges were dictated as well, and ample spacing was required for control devices. Based on the constraints, the chordlength of the wing was optimized for solar cell placement, minimizing the amount of unused

planform area. This resulted in an optimum chordlength of 42.4 centimeters having three chordwise-positioned solar cell arrays: One cell array positioned between the leading edge and the main support spar at 13 degrees relative to the chordline, and two cell arrays positioned between the spar and trailing edge at 7 degrees relative to the chordline. For the wing angle of attack of 4 degrees, these angles (with respect to horizontal) correspond to 9 and 11 degrees respectively.

The size and spacing of solar cells set several constraints on the wing aspect ratio. The solar cell dimensions set rib spacing at 10.2 centimeters. Based on preliminary lift and power requirements (assuming approximately 100 cells) a planform with a 3.5 meter span was selected, corresponding to an aspect ratio of 8.25. Further elongation of the span was desirable in order to reduce induced drag, however structural limitations constrained excessive span.

4.8 WING DIHEDRAL AND WING TIP

Selection on the degree and location of wing dihedral, which provides longitudinal stability, was based on a primary constraint dictated by the Structures Group. Since the construction of the wing was modular, having three separate pieces (a 1.5 meter central section and two 1 meter outer sections), dihedral was only permitted on the outer one meter sections. Empirical data was employed in the determination of exact wing dihedral. In the case of unswept civil aircraft having a mid to high wing position (as is in the configuration), typical dihedral angles are between 0 and 4 degrees over the entire span (Raymer, 1989). Since dihedral could

only be implemented on 2 meters (or 57 percent) of the span, it was determined that a 5 degree dihedral would be appropriate.

The addition of wing tips was implemented into the configuration in order to reduce vortex-generation and thus reduce induced drag. For this purpose, a sharp-edged tip tends to be the most beneficial. Of the several varieties of sharp-edged tips, the most widely used is the Hoerner wing tip. This wing tip was selected for use on the configuration. The geometry of the Hoerner wing tip consists of an upper surface which retains the airfoil section's upper camber and a lower surface which is inclined at a 30 degree angle (relative to horizontal) with a slight concavity.

4.9 FINITE EFFECTS OF WING

The effects of finite wing length on the two dimensional airfoil lift and drag curves were investigated. Using a Fourier-Series representation developed by Glauert (1937), the spanwise wing loading was determined (See Appendix B.3). The prismatic (rectangular) wing experiences a deviation from the elliptic (Fig. 4.9.), resulting in a 4 percent loss of lift (Fig. 4.10) and an 8 percent increase of induced drag (Fig. 4.11). Twist or taper of the wing could alleviate these penalties, however these options were not implemented due to construction difficulties. For the rectangular planform, the twist necessary to achieve a nearly elliptic wing would be approximately 3 degrees. Construction tolerances did not allow such small angles to be reasonably implemented into the design fabrication. For this reason twist was not utilized. Taper, which would achieve a nearly elliptic planform by varying

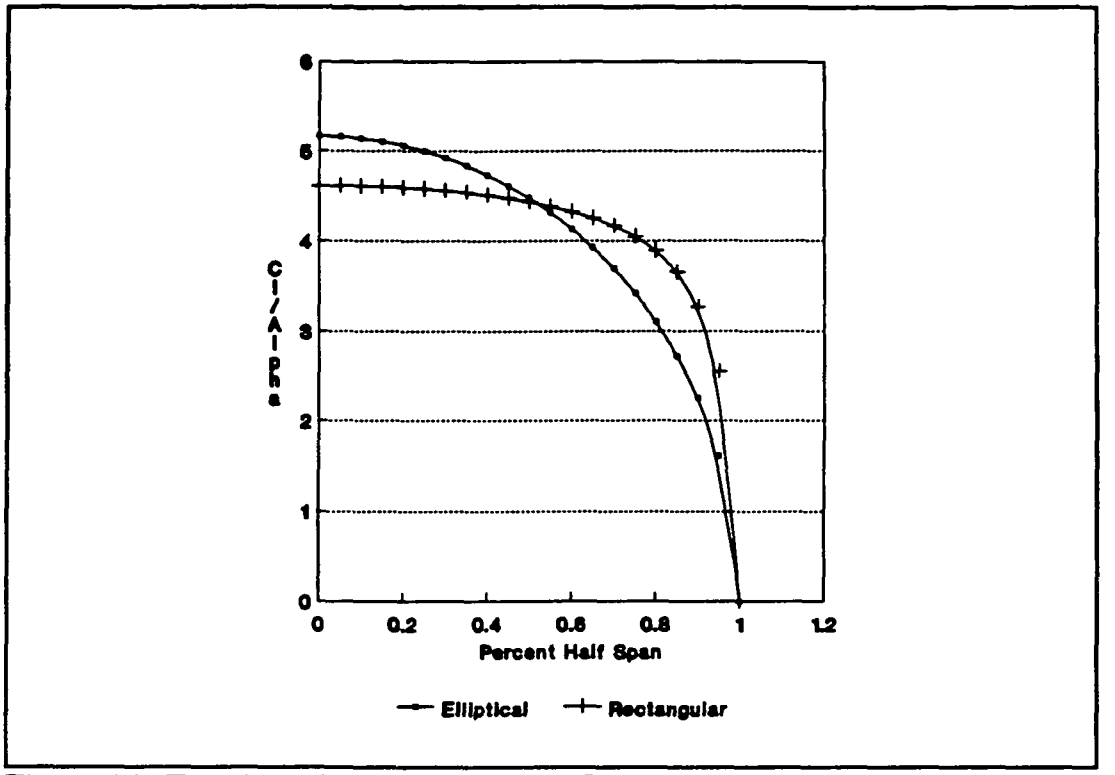

Figure 4.9: Elliptic vs. Rectangular Wing Loading for the NACA 6409 with an aspect ratio of 8.25.

chordlength along the span of the wing, was not added to the configuration due to cell placement. Since the chordlength had been optimized to contain the placement of three spanwise solar cell arrays, the spanwise reduction of chordlength could not be implemented without the reducing the number of solar cells placed in the wing.

4.10 TAIL SECTION

Selection of a tail section was based on stability requirements. For stability, the Performance Group preliminarily determined (based on typical attainable tail lift characteristics) that a 100 centimeter by 30 centimeter tail one meter aft of the

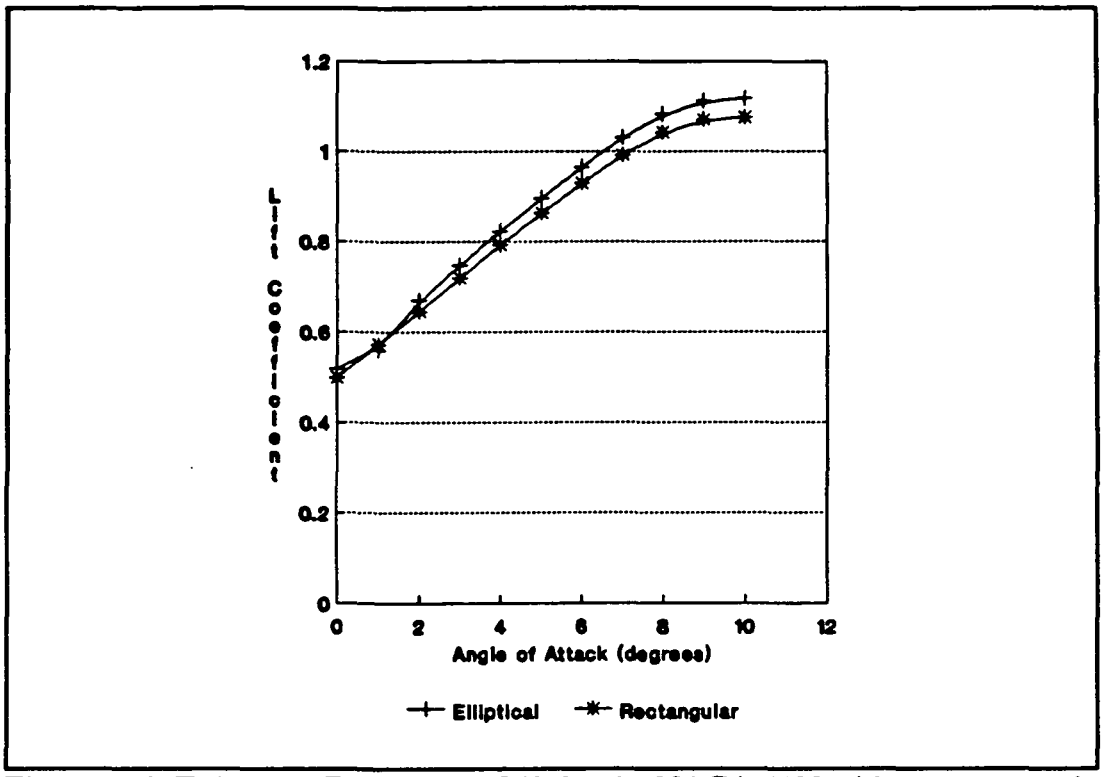

Figure 4.10: Elliptic vs. Rectangular Lift for the NACA 6409 with an aspect ratio of 8.25.

trailing edge of the wing was necessary. Based on this, an airfoil was sought to trim[2] the configuration as well as provide stability. Originally, thin symmetric airfoils were investigated for this purpose. However, the relatively large distance between the aerodynamic center of the wing and the airplane center of gravity (in excess of 15 percent of cord) resulted in a large wing moment. To counteract this moment, a high tail lift coefficient was required. By using a thin symmetric airfoil for the tail, high angles of attack would be required to produce the necessary lift coefficient, leading to the possibility of tail stall. Considerations to remedy this complication included the

[2] The process of 'trimming' refers to balancing the moment generated by the tail against all other aerodynamic moments summed about the center of gravity.

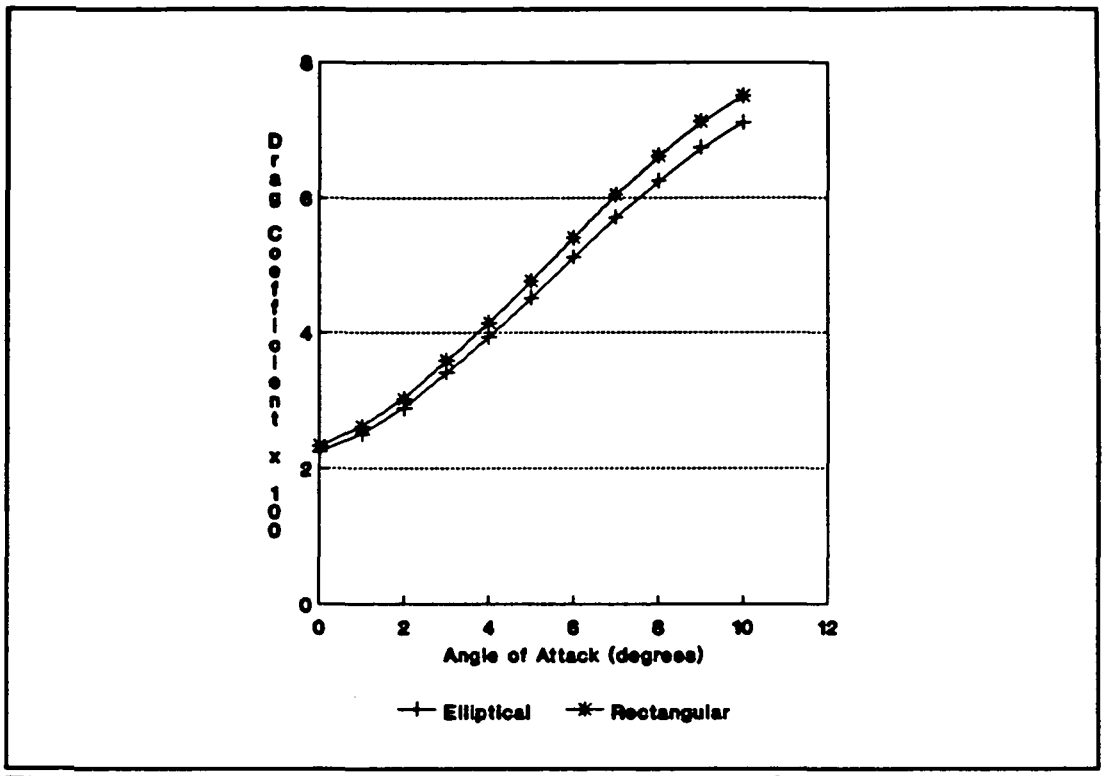

Figure 4.11: Elliptic vs. Rectangular Drag for the NACA 6409 with an aspect ratio of 8.25.

placement of the tail further aft from the wing, an increased tail planform area, or the selection of a higher lifting airfoil. An increase in the distance between the wing and tail would generate a larger bending moment on the tail booms, which was deemed undesirable by the Structures Group. Also, this movement of the tail would shift the configuration's center of gravity further from the aerodynamic center, creating a still larger wing moment. An increase of the tail planform area was determined to be unfavorable by the Performance Group due to stability complications. Selection of a higher-lifting airfoil would enable the tail to be operated at much lower angles of attack without alteration of the tail's location and size. This was determined to be the best alternative. As a result, the NACA 6409

(at Re = 150,000) was selected as the configuration's tail section. However, it is believed that a more optimal airfoil could be found for this purpose.

4.11 FINITE EFFECTS OF TAIL

The finite effects of the tail were determined similarly to the wing. For this analysis, tail loading effects due the vertical tails and support booms were neglected. A constant downwash angle (with respect to the wing) was assumed since the tail lies within the central 30 percent of the wing (where the downwash is fairly constant). A tail efficiency[3] of 85 percent was assumed. (For tails placed in the same horizontal plane as the wing axis, a tail efficiency of 85 percent may be assumed. (Shevell, 1983)). As a result of this analysis, it was determined that the tail would experience a 4 percent loss in lift compared to the elliptic planform, and a 2.5 percent increase in induced drag. This deviation from elliptic could be alleviated in the same fashion as the wing.

4.12 OPTIMIZATION OF EXCESS POWER VS. ANGLE OF ATTACK

The optimal operational point for the solar powered aircraft design was determined by optimizing excess power, P_{excess}, with respect to wing's angle of attack, α. P_{excess} is the difference between the power available from the propeller, P_{avail}, and

[3] Tail efficiency is defined as the ratio of dynamic pressure experienced by the tail to that of free stream.

the power required to propel the configuration, P_{req} at level flight. In conventionally-powered aircraft, the propulsive power available (P_{avail}) remains nearly constant over its level flight operating conditions (given constant flight speed as well as propeller and engine efficiency), thus the optimum operational point occurs where power required (P_{req}) is a minimum. This minimum P_{req} corresponds to the maximum lift to drag ratio of the configuration. However, in the case of a solar-powered aircraft, P_{avail} (as well as P_{req}) is a function of α due to the re-orientation of the solar cell arrays with respect to the sun. Therefore, it is necessary to determine P_{avail} as well as P_{req} for each operational point.

In order to determine the optimum operational point of the given configuration, the angle of attack of the wing was varied from 0 to 10 degrees. For each of these points, the tail's angle of attack with respect to the downwash of the wing, α_t, was set in order to trim the configuration at level flight. Based on these two angles of attack, P_{req} and P_{avail} were determined.

For each α, configurational coefficients of lift and drag were determined for the entire aircraft (See Appendix B.4). By equating lift to the configuration's weight, the required minimum velocity to maintain level flight was obtained. This velocity in turn determined configurational drag and finally P_{req}. P_{avail} was calculated at each angle of attack for two different cases, level flight both towards and away from the sun, with the aid of the Controls and Interfacing Group.

Figure 4.12 shows the plot of P_{avail} and P_{req} vs. α. As seen, P_{req} experienced minimal values (slightly less than 12.5 watts) for α between 2 and 7 degrees.

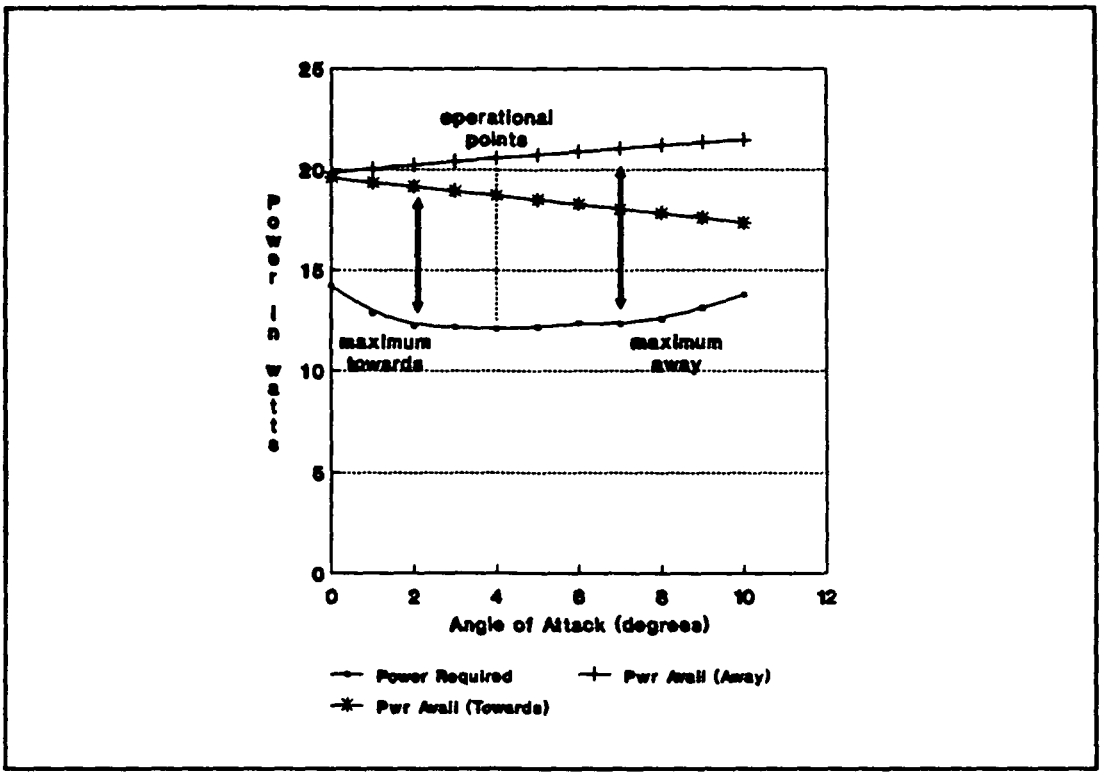

Figure 4.12: Optimization of Excess Power with respect to angle of attack the of wing.

Increasing the α while flying towards the sun resulted in lower P_{avail}. Likewise, increasing α away from the sun resulted in higher P_{avail}. For flight towards the sun, P_{excess} is maximum at 6.9 watts for α = 2 degrees. For away from the sun, P_{excess} is maximum at 8.7 watts for α = 7 degrees. A compromise of these two angles was desired, resulting in the selection of α = 4 degrees. This corresponded to a trimmed tail at an α_t = -2 degrees, which is an angle of attack of 0 degrees with respect to horizontal. For this configuration, the low angles of attack of the wing and tail are beneficial in avoiding stall, while simultaneously maintaining a high configurational lift to drag ratio. The configurational lift to drag curve resulting from this optimization is shown in Figure 4.13.

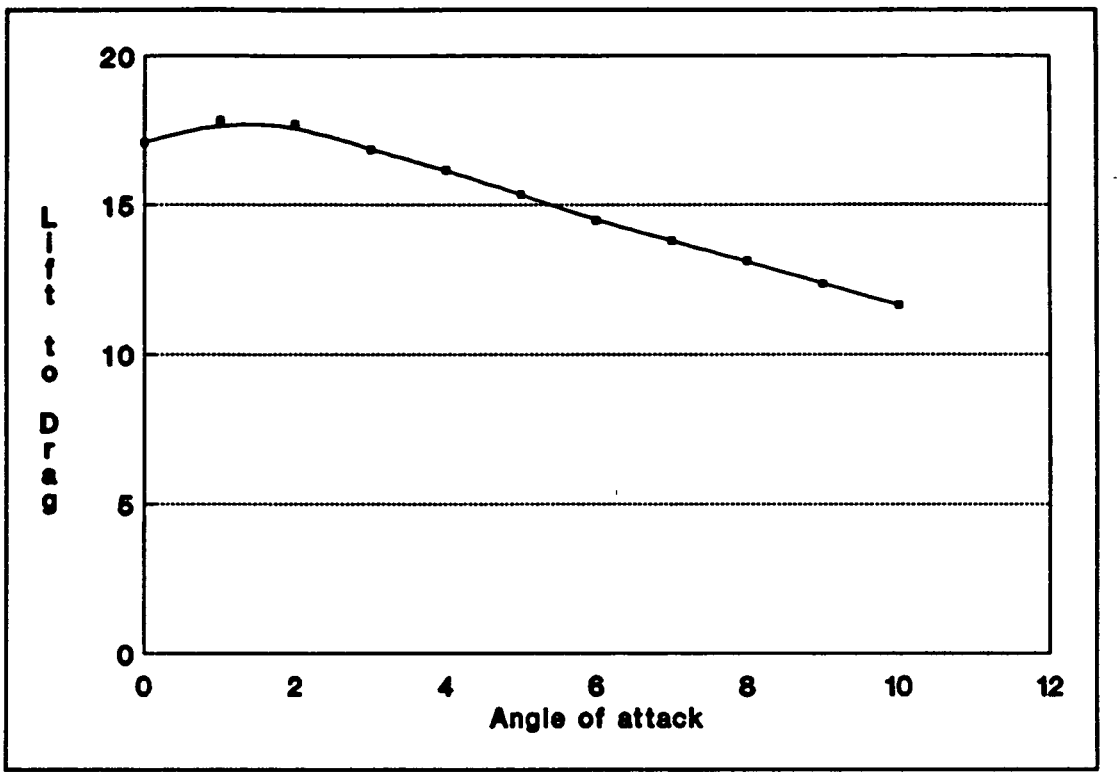

Figure 4.13: Configurational Lift to Drag at 8 meters per second.

CHAPTER 5

STRUCTURAL DESIGN AND ANALYSIS

5.1 INTRODUCTION - DESIGN CONSIDERATIONS

Aircraft structures are somewhat unique in the respect that the weight of the structure is a major consideration in the design. The structure must perform all of its supportive tasks while at the same time have the smallest possible mass. In order to design a structure one must set forth the requirements of that structure. In Rivello's text Theory and Analysis of Flight Structures, the author gives an excellent description of what the requirements of an aircraft's structure are in terms of how loads affect the structure:

1. The loads must not produce a collapse of the structure.
2. The loads must not produce a permanent deformation of the structure.
3. The loads must not produce deformations which interfere with the mission of the aircraft.

The structure of an aircraft is responsible for controlling the aerodynamic forces which are applied to the skin of the vehicle and to resist the inertial forces present during all aspects of flight. This structure is composed of several basic component parts. Each part is designed to receive different types of stresses and is designed accordingly.

A common type of aircraft structure is the semi-monocoque. Our design utilizes the structure. Semi-monocoque indicates that the skin is a stressed

member of the airframe, not just an aerodynamic covering. Underneath the skin is a supporting structure which carries part of the load because the skin is not designed to completely accept all of the loading.

The aircraft that we are designing will not necessarily include all of the component parts that a more complicated airplane would. The description of the major components that appear in the structure follows:

The skin:

1. Transmits the aerodynamic forces to the underlying frame.

2. Accepts shearing stresses in response to the torsional moments and shearing forces.

3. Resists bending and axial loads in conjunction with the longitudinal stringers.

4. Forms the aerodynamic shape of the aircraft.

The spar webs:

1. Resists the shearing stress encountered due to the applied loads.

The longitudinal members:

1. Accept the bending and axial loads in conjunction with the skin.

2. Through the division of the skin into smaller panels they increase its resistance to buckling and rupture.

The spar caps (present in the wing):

1. Resist axial and bending loads along with the skin.

2. Divide the skin into smaller sections, increasing its resistance to buckling and rupture.

The frames, rings, or bulkheads (in the fuselage), or ribs (in the wings):

1. Maintain the shape of the structure (for aerodynamic reasons).

2. Disperse any concentrated loads into other sections of the structure.

3. Function to define the column length and restrain the ends of the longitudinal stringers to increase their buckling resistance.

Simplifying assumptions are made to facilitate analysis of the structure. The usual assumptions are given as follows:

1. The longitudinal members carry only axial stresses.

2. The skin and spar webs carry only shearing stresses.

3. The axial stress is constant throughout the cross section of each longitudinal and the shearing stress is constant across the thickness of the webs.

4. The transverse frames and ribs are rigid within their own planes, maintaining their cross section during loading. However, they are assumed to possess no rigidity normal to their plane, so that they offer no restraint to warping deformations out of the plane.

To successfully accomplish the task of designing an aircraft's structure, one needs a design process, or in other words a step by step procedure to follow that results in an optimized design. Rivello's text outlines such a design process which we have adapted here to suit our aircraft:

1. Determine the critical combinations of applied loads to which the structure is subjected.

2. Layout the design tentatively specifying arrangement, size, and materials of the component parts of the structure.

    a. list other possible options
    b. justify the choice over other options

3. Determine the actual stresses and deformations in the structure due to the applied loads.

4. Determine the allowable stresses and deformations in the structure.

    a. consider safety factors

5. Compare steps four and five.

    a. determine whether or not the design is optimized
    b. if not iterate until a satisfactory design is found

6. Share information and specifications from structural design standpoint with specifications from other groups. Integrate their specifications, compromise and reiterate.

    a. controls - room for wiring, batteries, motor, etc.; method for attaching cells to wings; number of cells available (area); power available and effects on loads
    b. aero - exterior shape, loads, material weights
    c. mission and performance - stability and mission satisfaction

A central factor in the structural design process is the safety factor, or more commonly used in aircraft structural design, margin of safety. The margin of safety is defined as the ultimate stress divided by the allowable minus one. A margin of safety of 1 indicates that the loads that would cause failure of the structure are twice as great as the loads that are expected to be encountered. In the design of bridges or machinery or almost any other thing that accepts loadings margins of safety of nine or ten are not uncommon. The margins of safety that aircraft are designed for are much more demanding on the designer. Aircraft structures must be as light as possible to maximize the performance of the aircraft. Therefore it is not uncommon to use margins of safety of only zero to one. Unmanned craft such as rockets or missiles typically have margins of safety of 0 to

.2. Aircraft that carry passengers have margins of safety of about .5. In our design a margin of safety of .2 was used.

The loadings for which the solar powered airplane was designed to survive are larger than those that are experienced in horizontal, steady state flight. The aircraft's loadings are increased through the maneuvers that the plane performs and the wind gusts that strike the aircraft. The increased loadings that the structure of the aircraft must endure are expressed as a multiple of the aircraft's weight. This load factor is given the symbol n. The load factor is a function of several variables: the air density p, the wing area S, the slope of the coefficient of lift versus angle of attack a, the maximum value of the coefficient of lift Cl, the effective wind gusts that are anticipated to be experienced by the airplane KU, the airspeed of the aircraft V, and the weight of the aircraft.

The load factor that the aircraft experiences due to its maneuvering is given by (Azar and Perry, 1982):

$$n=\frac{C_l*\rho*S*V^2}{2W}$$

The load factor produced by wind gusts that strike the plane is given by the equation (Azar and Perry, 1982):

$$n=1\pm\frac{\rho*S*\beta*KU*V}{2W}$$

In these above equations the following constants are used: p = 1.204 kg/m^3, S = 1.484 m^2, B = 5.17 1/rad, KU = 7 m/s, W = 40 N, resulting in the following relationships:

$$n = .0299V^2$$

$$n = 1 \pm .8083 * V$$

These relationships give the load factors for the maneuvering and wind gust conditions that the aircraft is likely to encounter. When n is plotted as a function of V it is apparent that the wind gust induced load factor dominate the loadings, due to the fact that the airplane flies so slowly. These two sources of load multiplying factors are generally not summed, as it is assumed that the pilot will restrict maneuvers during gusty conditions. The rise of the gust load line is stopped at a value of n = 7 as a gust of seven m/s is equivalent to a fifteen mph gust. This is considered the extreme condition that the solar powered airplane will operate in. It is expected that the aircraft will only be flown on exceptionally calm days. Therefore the solar powered airplane's structure was designed to withstand loadings that correspond to a load seven times the weight of the aircraft.

5.2 PRELIMINARY COMPONENT SIZING

To choose the configuration and the sizes for the main spars that run spanwise in the wing and tail, simplified models of each were developed. A half model of the wing consisted of a cantilevered beam, the beam representing only

the main spar in the wing. For the tail a full model was devised consisting of a beam supported by pins at each end.

In these models, the main spar is assumed to be carrying all of the aerodynamic and other loads. In actuality the wing has other components which accept much of the load carrying duties. These other members include the leading and trailing edge and to a great extent, the mylar sheeting which forms the aerodynamic surfaces of the wing and tail. Although a portion of the weight of the plane is located within the wing, it was assumed that all of the weight was located in the fuselage and that the wing supported all of this weight. In the development of the simplified model of the wing, symmetry along the centerline of the plane parallel to the flight direction allowed the use of a half model. These above assumptions simplified the choice of the spar configuration and sizing. All assumptions, except the symmetry argument, produce a worst case type model, therefore these assumptions are believed to actually increase the margin of safety of the structure.

The wing was modelled as a cantilevered beam whose length equalled 1.75 meters, the half span of the wing. Vertical loads representing the aerodynamic forces were applied to the beam. These loads were calculated using the weight of the plane of forty newtons, and a gust load of seven. The loading was simplified to a constant running load, when in actuality the load drops off towards the wingtip. This assumed loading condition was corroborated by the actual aerodynamic loads obtained from the aerodynamics group. Shear and moment

diagrams were drawn, and the maximum shear and moment calculated. See Figure 5.1 for the shear and moment diagrams of the wing.

The maximum moment, 122.5 N*m Controls the design of the main spars. The normal stresses produced by this moment are given by the equation: Stress = (M*y)/I, where M is the moment, y is the distance from the neutral axis of the beam (in this case its centerline) to its upper or lower surface when viewed in a cross section, and I is the moment of inertia of the beam about its neutral axis. This normal stress must be below the maximum allowable stress for the particular material. In the above equation the stress is known, M is known, and y is known. The equation was solved for I, the goal being to achieve the required I for a particular material with the minimum weight. See the diagram which shows the optimization process for the spar cross section. Three materials, aluminum, carbon fiber/epoxy, and spruce, along with six candidate spar cross sections were considered as possible spars. The candidates were judged on several qualities, weight, ease of construction, price, availability, and connections, with weight being the overriding criterion. For the main spars in the wing 2.7mm diameter carbon fiber rods proved to be the lightest method possible, but the closest thing available was 3.3mm diameter carbon fiber rods, which were used in the construction.

A similar procedure was used to determine the carbon fiber rod sizes for the main spar in the tail. A full model of the tail consisted of a beam pin joined at both ends with a constant running load applied vertically. This load was obtained directly from the aerodynamic group's data. The load was multiplied by

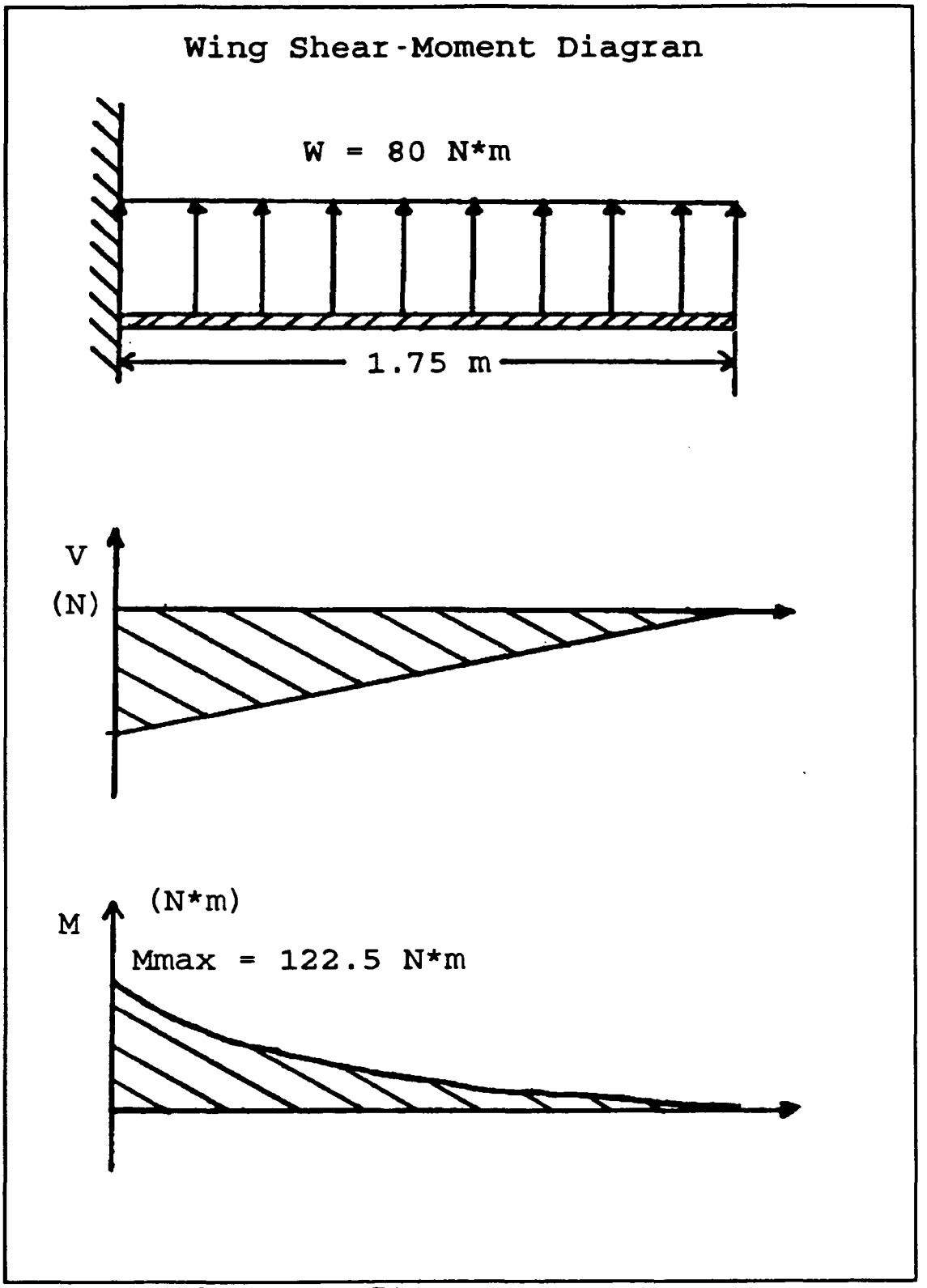

Figure 5.1 Wing Shear-Moment Diagrams

a gust load factor of seven. Shear and moment diagrams were drawn and the maximum shear and moments calculated. See Figure 5.2 for the shear-moment diagrams of the tail. The maximum normal stresses were calculated and used to calculate the minimum I needed. This I gives the proper rod dimensions for the carbon fiber. Because the tail is so small, and the carbon fiber rods so strong, the smallest rods that were available (1mm in diameter) gave a moment of inertia nine times as great as necessary.

5.3 ANSYS FINITE ELEMENT CODE ANALYSIS

5.3.1 Wing Analysis

Due to the complexity of the plane structure, the ANSYS finite element software was used to analyze each component under anticipated aerodynamic loadings. Initially, the major parts of the wing -- the leading edge, the trailing edge, and the spanwise spar -- were analyzed with their equivalent areas concentrated into a single beam. From this beam, a single area and moment of inertia representative of the entire complex wing was obtained. This beam was then analyzed with ANSYS using beam elements (STIF4) and solved for the maximum deflection due to anticipated loadings. To ensure the accuracy and reliability of ANSYS, an exact deflection analysis was carried out using simple beam theory and the numerical results were comparable.

The model became more complex as every wing component was incorporated into the analysis rather than just the major components. A half-

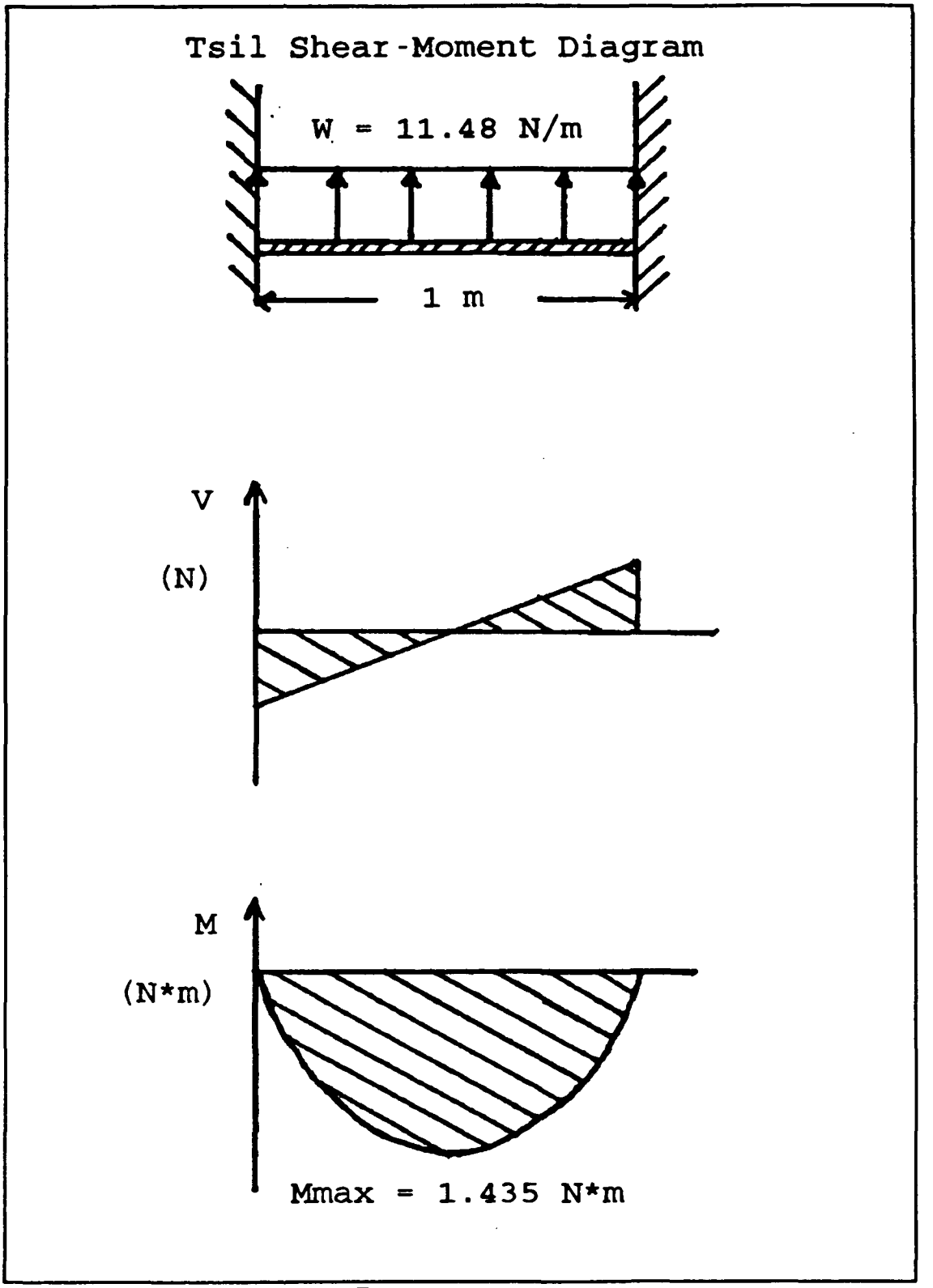

Figure 5.2 Tail Shear-Moment Diagrams

model wing was constructed consisting of 95 shell elements (STIF41) representing the mylar coating, 101 shell elements (STIF41) representing the airfoil rib sections, 15 shell elements (STIF41) representing the spar webs, 30 beam elements (STIF4) combined representing the leading and trailing edges, and 31 beam elements (STIF4) representing the spanwise spars. Applied to the half-model was a distributed load of 82.4 N/m (5.6 lbs/ft) upward on the top surface representing the maximum lift force and a downward concentrated load of 8 Newtons (1.8 lbs) at the midspan representing the weight of the fuselage. The upward lifting load is the worst case anticipated by the aerodynamics group at an airspeed of 8 m/s (17.9 miles per hour) and at an angle of attack of the plane of 3 degrees. The model was constrained in the spanwise and chordwise direction at the midspan, and in the vertical direction at the location of the tail support tube.

The maximum stress within the carbon rod, .280 GPa (40.6 ksi), occurs at node 1 and is less than the allowable stress of .9 - 1.2 Gpa (130.5 ksi) (GoodFellow, 1990). The balsa leading edge member (at node 42) experienced the maximum stresses, with a tensile stress of 20.1 MPa (2.9 ksi) and a compressive stress of 11.2 Mpa (1.6 ksi) at node 49. These stresses fell within the material limits of 35 MPa (5.1 ksi) in tension and 16 MPa (2.3 ksi) in compression (Dimwoodie, 1989). See Appendix C.1.6-C.1.9 for a complete listing of the stresses within the wing.

The maximum deflection, .24 m (9.4 in) occurs at the wing tip. The maximum angle of twist within the wing is 11.5 degrees, also occurring at the wing

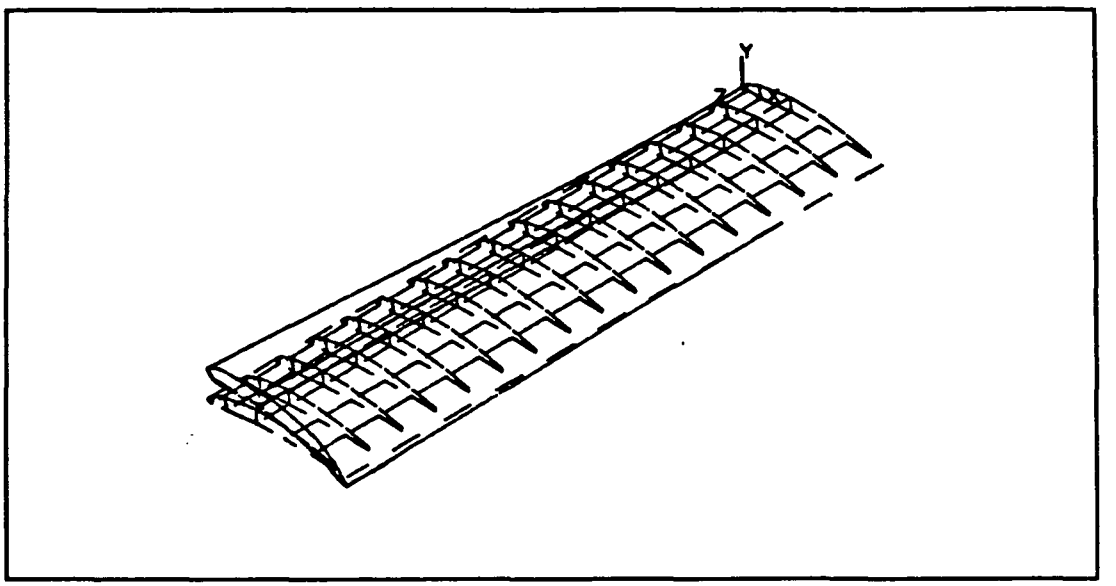

Figure 5.3 - Deflected Wing Half-Model

tip. See Appendix C.1.5 for the complete listings of deflections, and angles of twist within the wing.

The results of the ANSYS finite element analysis substantiate the material choice and structure, verifying that the structure will not fail within the materials under worst case anticipated loadings.

5.3.2. Tail Analysis

A tail analysis was carried out in a similar procedure to that of the wing. The two differ in that the tail has significantly lower applied loading than the wing does, and the tail is fixed at its tips by the carbon fiber tubes.

The tail half-model consists of 30 shell elements representing the mylar coating, 36 shell elements representing the airfoil rib sections, 5 shell elements representing the spar webs, 10 beam elements representing the leading and

trailing edges, and 10 beam elements representing the spanwise spars. See Appendix C.2.1 for node locations. The shell elements and beam elements were constructed using a stiffness matrix of STIF41 and STIF4 respectively.

This model was constrained at the wing tip representing its connection to the tail support tube. A distributed load of 6.5 N/m (.45 lb/ft) was determined to be the maximum loading on the tail. To approximate the distributed load, equivalent concentrated loads of .65 N (.15 lb) were applied at the quarter chord of the airfoil at every rib (the ribs are spaced by .1 m, or 3.94 in).

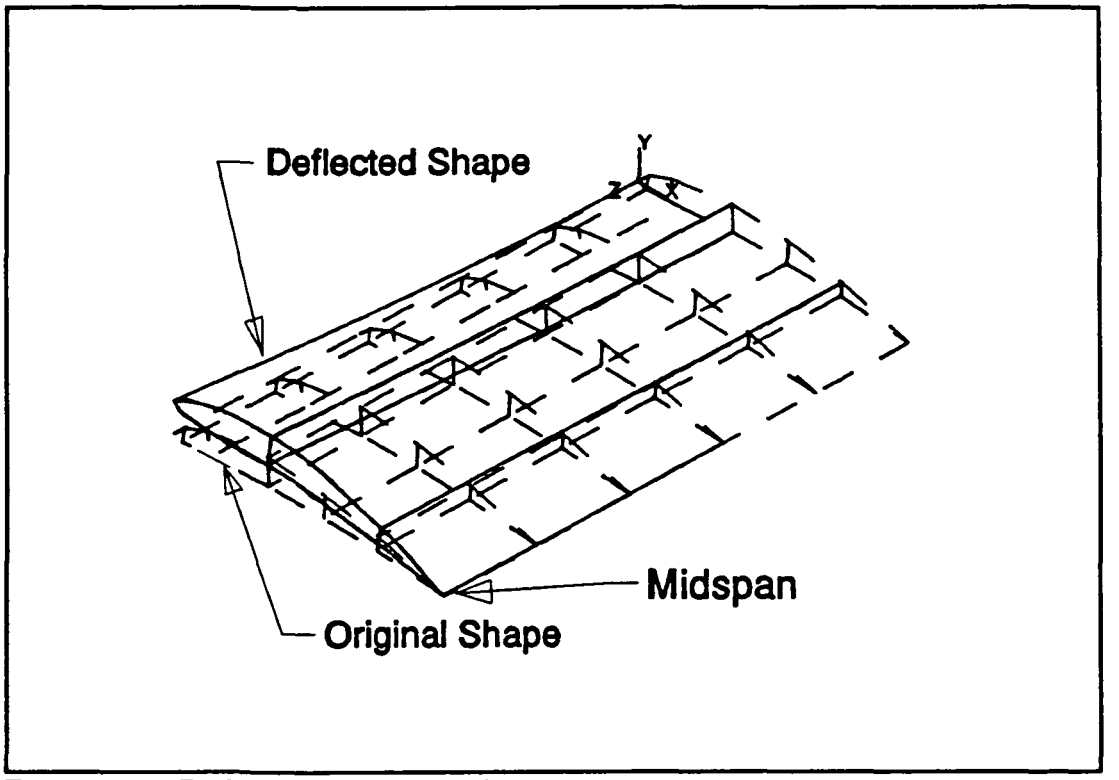

Figure 5.4 - Deflected Tail Half-Model

Under these conditions, the maximum and minimum stresses as well as the deflections were obtained for each node and element (see Appendices C.2.5 -

C.2.7). The maximum deflection of the tail occurs at node 61, the midspan of the trailing edge, and has a value of .515 mm (.020 in) in the y-direction. The deflections in the x and z direction are also negligible; their respective values are .045 mm (.002 in) and -.013 mm (-.0005 in).

Table 5.I - Stresses at Beam End

Component		Stress (MPa)	Element #	Allowable Stress (MPa)
Carbon Spar	tension	0.264228	6	900
	comp.	-0.316077	1	900
Leading Edge	tension	0.357917	16	35
	comp.	-0.322924	16	16
Trailing Edge	tension	0.026607	21	35
	comp.	-0.011209	21	16

The maximum and minimum stresses at the beam ends (SIG1 and SIG2 in ANSYS notation), are listed in Table I for each tail structural component. The minimum and maximum principal stresses (SIG1, SIG2, and SIG3) on the shell elements are listed in Table II. All the calculated stresses in Table I and II fall below the allowable stresses for each material support, confirming the in-flight integrity of the structural tail members.

5.3.3 Fuselage Analysis

The fuselage of the aircraft was designed as a balsa truss structure. To completely analyze the stresses that are produced during the flight of the plane, a three-dimensional model was constructed and analyzed on the ANSYS finite

Table 5.II - Principal Stresses for Shell Elements

Component		Stress (MPa)	Element #	Allowable Stress (MPa)
Spar Web	max	0.339340	11	35
	min	-0.015648	11	16
Mylar	max	0.206453	34	172
	min	-0.152152	57	172
Balsa Ribs	max	0.023584	75	35
	min	-0.007538	73	16

element computer software. The model consisted of thirty-four nodes representing the intersections of the truss members in the structure. Three dimensional spar elements connected the nodes in the model just as they appear in the actual fuselage. The spar elements were of two different cross sections, 1/4" * 1/4" for the four longest components of the truss structure, and 3/16" * 3/16" for the remaining shorter members of the structure. The total structure contained thirty-two elements of the larger cross section and fifty elements of the smaller cross section. The material property that was used in the computer analysis was the axial Young's Modulus for the balsa which is 6.274 GPa.

The model was loaded to simulate the actual conditions that will be present during flight. The total weight of the electronics and the motor was multiplied by the gust loading factor of seven and divided into two equal downward forces that were applied to nodes at the front edge of the fuselage. The total of these two forces was 96.2 N or 9.81 kg. Four forces were applied to the front of the fuselage to simulate the torque produced by the motor. The resultant of these

forces was zero, as they were mutually canceling. The four forces combined to produce a torque equalling .112 N*m.

The model was restrained at four nodes corresponding to the leading and trailing edges of the wing. These four nodes are the nodes which will actually be attached to the wing during the construction of the aircraft. The fuselage will also be attached to the wing through the extension of two wing ribs which will reach down alongside the fuselage and form the sides of the fuselage.

The completed model was solved using the finite element method resulting in the stresses and displacements being generated. The maximum stresses in the 1/4" * 1/4" members were 7.2 MPa in compression and 6.9 MPa in tension. The maximum stresses in the 3/16" * 3/16" members were 6.6 MPa in compression and 3.2 MPa in tension. These stresses are well within the material limits of 16 MPa in compression and 35 MPa in tension when using a margin of safety of .2 The stresses in compression were used in conjunction with Euler buckling theory and it was shown that the loadings are several orders of magnitude lower than required to produce buckling failure. These component sizes for the fuselage truss were selected because they strike a balance between being small enough to save weight and being large enough to accept the stresses without failure and also be large enough to facilitate ease of handling during construction.

When the analysis of the fuselage was performed it was also kept in mind that the deflections of the fuselage had to be minimized. In the end it appeared that the deflections of the structure did not pose a problem. The front of the

fuselage is where the maximum deflections occurred. Node one had the greatest deflection of -.006 m in the Y direction or 6 mm of deflection downward. The deflections in the other axes directions were an order of magnitude smaller than the deflection of node one. For this reason these deflections were not considered significant in the iterative process which led to the choices for the component sizes in the fuselage truss.

The computer printouts which give the model data including the nodal locations, element listing, stress results, in Appendix C.31 - C.3.2.

5.4 VIBRATION ANALYSIS

To study the effects that harmonic forces could cause vibration of the aircraft's structure and pose a threat to the structural integrity of the plane, Euler's beam equation was applied to the vibration of the aircraft's wing. Euler's beam equation starts with Newton's second Law:

$$\sum F_y = \gamma * \frac{\partial^2 y}{\partial t^2} dx$$

In which gamma represents the mass per unit length of the beam. From a free body diagram of a free element of the beam the forces on the beam are summed (V is the shear force) (James et al, 1989):

$$V - V - \frac{\partial V}{\partial x} dx = \gamma \frac{\partial^2 y}{\partial t^2} dx$$

This equation is combined with the fourth derivative of the deflection of the beam:

$$\frac{EI}{\gamma}\frac{\partial^4 y}{\partial x^4}+\frac{\partial^2 y}{\partial t^2}=0$$

to yield:

$$\frac{EI}{\gamma}\frac{\partial^4 y}{\partial x^4}+\frac{\partial^2 y}{\partial t^2}=0$$

This equation is known as Euler's beam equation (James et al,1989).

The solution of this equation yields the natural circular frequencies of the beam:

$$\omega = k^2\sqrt{\frac{EI}{\gamma}}$$

The variable k is the key to the solving for the natural circular frequencies of the beam, for it is a function of the boundary conditions imposed on the beam.

The wing model of the solar powered airplane consisted of a cantilevered beam with a length of 1.75 m, a modulus of elasticity E of 130 GPa, a moment of inertia I of $5.161*10^{-9}$ m^4, and a mass per unit length of .55 kg/m.

The values of $k_i l$ tabulated for the boundary conditions that the wing model has (fixed at one end and free at the other) are (James et al, 1989):

$$k_1 l = 1.875104$$

$$k_2 l = 4.694091$$

$$k_3 l = 7.854757$$

Given these values the corresponding k_i's are found to be:

$$k_1^2 = 10.76$$

$$k_2^2 = 67.49$$

$$k_3^2 = 189.1$$

Solving for the circular frequencies:

$$w_1 = 375.8 \text{ rad/s or } f_1 = 59.8 \text{ Hz}$$

$$w_2 = 2357 \text{ rad/s or } f_2 = 375.1 \text{ Hz}$$

$$w_3 = 6605 \text{ rad/s or } f_3 = 1051 \text{ Hz}$$

These frequencies are much higher than those that are expected to be created by the vortex shedding caused by the airflow over the rather large area of the wing. Therefore the possibility of vibration becoming a problem in terms of structural integrity is not considered.

5.5 MATERIAL SELECTION

The material selection process for use in our aircraft involved many criteria. The driving factor in the selection process was weight. Keeping the

weight of the plane a minimum was the critical goal, due to the low power upon which we are flying on. The most efficient method of minimizing the weight is to use materials with the highest possible strength to weight ratios, and/or the lowest densities:

Table 5.III - Material Strength to Weight Ratios

Material	p (kg/m^3)	(Yield Strength) tension (MPa)	shear (MPa)	tension/p (m^2/s^2)	shear/p (m^2/s^2)
steel	7860	250	145	31,807	18,448
aluminum	2800	410	220	146,429	78,571
magnesium	1800	275	-	152,778	-
titanium	4460	825	-	184,978	-
balsa wood	180	35	2.4	194,444	13,333
spruce wood	433	139	7.7	321,016	17,783
carbon/epoxy	1600	1100	130	687,500	81,250

Carbon fibers in an epoxy matrix has the highest strength to weight ratio, therefore it was the material chosen for the main load supporting members in the aircraft.

Other materials were used in the aircraft such as balsa wood, foam, and mylar. These materials were used in specialized areas of the plane to take advantage of various unique properties that each possesses.

Balsa wood was used in many components of the plane that did not require the highest strength to weight ratio material. Balsa is the lightest of all wood, having a density of only 180 kilograms per cubic meter. Its low density made it

appropriate for components that require a fixed size or dimension, such as the ribs in the wing and tail. The two dimensional outline of the ribs is given by the aerodynamics group, and the thickness dimension is determined by the structural group. In the determination of the thickness, and in essence what material, many factors come into play. First, the ribs must be lightweight. Second, they must be easily shaped. Third, they must be as thin as possible to avoid shading of the solar cells. Above all these factors, the ribs must support the aerodynamic loads applied to them through the skin of the wing. Balsa and foam satisfy the first and second factors, but only balsa could satisfy the third and last factors.

Balsa wood was used in components that carried smaller loads than the main structural components and required a large member and precise shaping, taking advantage of balsa's low density and ease of shaping. Components that used balsa for these reasons included the leading and trailing edge and the elevator and ailerons.

Components that carry little or no structural loads were made from the lowest density material to minimize the weight of the aircraft. The lowest density materials are the foams. This material was used in location such as the solar cell supports, the nose of the fuselage, and the wingtips.

Mylar was chosen for the covering for the aircraft for its unique properties. It is transparent, allowing a large portion of the sun's rays to reach the cells. Mylar is also stiff when heat shrunk over the surface of the aircraft, forming an ideal aerodynamic surface and becoming an important part of the structure.

5.6 WEIGHT BREAKDOWN

In order to predict stability characteristics accurately, the masses of each component of the aircraft had to be determined prior to their construction. Initially, weight estimates were made by multiplying published densities of the materials by their expected volume. For wooden materials, a moisture content (M.C.) of 12% is considered conventional in literature. The volume was acquired by multiplying the cross-sectional area by the thickness or length of the member. The calculated masses of sample pieces did not correspond to their measured masses, so the density of each material was recalculated based on the sample material's properties. Table 3.F.1 summarizes these results.

Table 5.IV - Material Densities

MATERIAL	Density Published (kg/m^3)	Density Measured (kg/m^3)	Percent Difference
Balsa (Dimwoodie, 1989)	188 (12% M.C.)	205.4 (block) 177.8 (sheet) 97.5 (bar)	+9.3 -5.4 -48.1
Spruce (Dimwoodie, 1989)	433 (12% M.C.)	511.8 (bar)	+18.2
Pultruded Carbon Composite (GoodFellow, 1989)	1500 - 1650	1739.8	+5.4 - +16.0
White Foam (Aircraft Spruce, 1989)	48.1	66.1	+37.4
Blue Foam (Aircraft Spruce, 1989)	32.0	35.8	+11.9

The mass estimates based on published material densities were dangerously low, which may be inferred from Table IV. The mass estimates used in this work are based on the accurate measured densities. The plane was designed and constructed with the latter estimates in mind. An inaccuracy associated with these measurements is an inability to account for additional mass due to adhesives. In one instance the cyanoacrylate glue was measured to contribute as much as 20% of the mass to a balsa segment of the plane. Likewise, the more porous foam absorbs an undetermined quantity of epoxy when covered with carbon fiber weave.

Combining the estimated component masses, the measured electrical element masses, and the approximate contribution due to glue, the plane was designed to have a mass of 4100 g, or a weight of 40 N (9.0 lbs). Since the power requirements depend on the weight, it was important that the limit weight of 40 N was not exceeded. Tables V - VII break down the actual masses for individual elements of the plane showing also their percent contribution to their section of the plane.

Table 5.V - Wing Component Masses

WING	Parts	grams	% Wing
Ribs	30	99.2	4.8
Leading Edge	1	84.2	4.1
Trailing Edge	1	104.4	5.1
Spar Webs	33	44.8	2.2
Mylar Coating		192.9	9.3
Solar Braces	270	33.7	1.6
Wing Tips	2	36.1	1.7
Carbon Rods	2	91.0	4.4
Solar Cells	90	856.8	41.5
Servos	2	43.0	2.1
Wiring		55.1	2.7
Carbon/Balsa Ribs	2	201.8	9.8
Carbon/Foam Ribs	4	51.6	2.5
Carbon/Foam/ Carbon Ribs	4	86.6	4.2
Clamps	4	31.2	1.5
Bolts/Washers	6	51.0	2.5

Table 5.VI - Tail Component Masses

TAIL	Parts	grams	% Tail
Ribs	9	14.2	4.5
Leading Edge	1	20.0	6.4
Elevator	1	34.0	10.8
Spar Webs	9	6.4	2.0
Carbon Rods	2	2.6	0.8
Solar Braces	16	2.0	0.6
Solar Cells	8	76.2	24.3
Servos	2	43.0	13.7
Mylar Coating		42.0	13.4
Vertical Tail	2	20.2	6.4
Carbon/Foam/ Carbon Ribs	2	21.6	6.9
Clamps	4	31.2	10.0

Table 5.VII - Fuselage Component Masses

FUSELAGE	grams	% Fuse
Balsa Frame	111.6	12.5
Mylar Coating	12.3	2.5
Servo	21.5	2.4
Wiring	37.9	4.2
Astro 05 & Gearbox	225.7	25.3
6.5" Blade Prop.	32.9	3.7
Receiver Battery	97.0	10.9
Receiver	44.0	4.9
Speed Control	54.8	6.1
On/Off Switch	10.3	1.2
Emergency Batteries	234.3	26.2
Landing Gear	23.6	2.6

Table 5.VIII - Tubular Tail Strut Masses

TUBE TAIL STRUT	Parts	grams	% Strut
Carbon Tubes	2	225.1	80.9
Wiring		53.2	19.1
Strut Total		278.3	100

These listed masses add up to roughly 3560 g, less than the preset limit of 4100 g. The limit should be even more closely approached when the intangibles are considered. Considered on their own, these aircraft components are of insignificant masses; however, considered collectively, the mass becomes significant. The problem lies in that their masses are often difficult or impossible to determine.

The items not listed in Tables V - VII are glue/epoxy, nylon hinges, overlapping mylar, servo rods, balsa servo bracing, balsa rib bracing, balsa/carbon dihedral braces, wing tip bracing, solar cell wiring, fuselage controls bracing, and fuselage nose foam. In some cases these items could not be weighed because there was no access to a scale between the time they were built and the time they were connected to the plane. With the glue and epoxy, it was impossible to gauge the amount used, so their mass could not be estimated. Unfortunately, it is the glue and epoxy that makes up the majority of the mass of the error in the weight estimates.

To ascertain just how much mass these items contribute, the estimated total mass is subtracted from the actual final mass. Seen from the actual final mass

(this weight was taken when the plane was almost totally constructed and includes an estimated amount to compensate for the construction remaining) of 3570 g (7.86 lbs), the mass which was unaccounted for was 10 g (.022 lbs), .28% of the final mass.

CHAPTER 6

AIRCRAFT POWER SYSTEM AND CONTROL

This aircraft utilizes a propulsion powerplant which can be divided into three

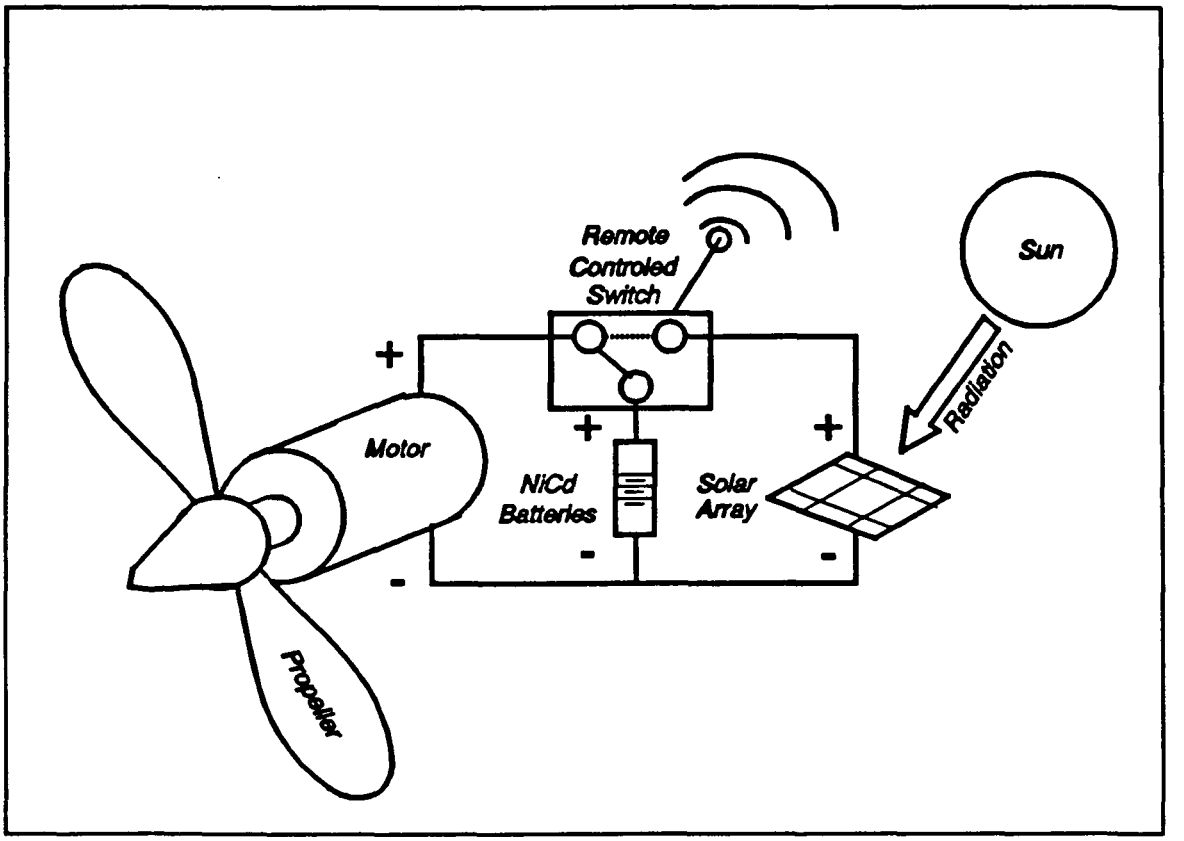

Figure 6.1: Powerplant Layout

subsections. The powerplant includes 98 solar cells, 7 rechargeable Nickel-Cadmium batteries, one DC motor, and one propeller as shown in Figure 6.1. The Sun is the only source of electrical input energy to the powerplant. The first section consists of the electrical input source; either the solar cell array alone or the NiCd batteries combined with the solar array. The solar cells serve as the primary source of input power by converting solar energy into electrical energy. The NiCd batteries have a two-fold purpose: (1) they serve as a secondary or backup power source, (2) they can supply short bursts of input energy to the system when needed, ie. for takeoff and

critical maneuvers. As we can see from Figure 6.1, the solar array and NiCd batteries are connected in parallel via a remotely controled switch in series with the DC motor. The switch selects the motor's power source, either the batteries alone or the solar array combined with the batteries. The second section consists of one geared, permanent cobalt magnet, DC motor. The DC motor converts the electrical energy supplied by the array or batteries into mechanical (rotational) energy. The third and final stage of the powerplant consists of one 13"x6.5" folding propeller. The propeller converts the rotational energy supplied by the motor into the axial energy which actually propels the aircraft.

Ultimately, the design goal was to devise the most efficient overall propulsion system. This task was not trivial because of the complexity of optimizing the three subsections to work together. Each section has its own optimal operating point or range. The objective is to integrate the three subsections so that the final power output, from the propeller, utilizes the highest possible efficiencies of each subsection.

This chapter will discuss each section separately, giving a thorough explanation of each section and its operating characteristics. Finally, the overall powerplant will be presented with its design points and characteristics. Our test data have been included in Appendix D.

6.1 SOLAR ARRAY

The advantage of using solar cells in the power plant of the airplane is that theoretically, under clear sky conditions, they will provide an inexhaustible power source. While this is true, it must be taken into account that the performance of a solar cell, as well as the power it provides, changes under varying operating conditions. These operating conditions range from temperature, time, and day of year to the cell's position and angle relative to the sun, a condition of great importance when designing an aircraft, in that the aircraft is constantly moving.

Characteristic performance curves for a silicon solar cell are shown in Figure 6.2. Plotted are current vs. voltage (I-V), and power vs. voltage. These graphs are superimposed in order to find the maximum power point for the cell. By dropping a vertical line from the apex of the power curve, the optimum operating current and voltage can be found on the I-V curve. When designing the solar array, it was configured to approach these maximum values from the individual cells.

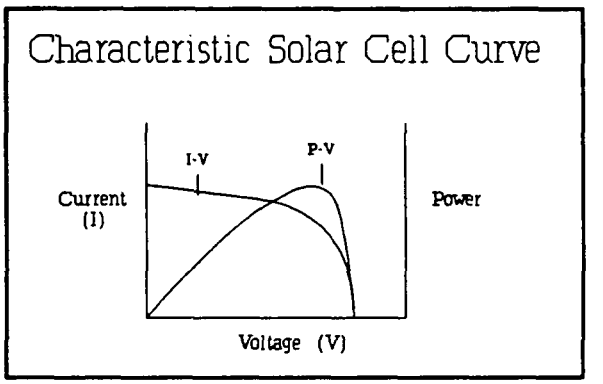

Fig. 6.2.

The shape of the I-V and Power curves for a solar cell remains fairly constant, although changes in cell operating conditions may cause overall shifts. In particular, changing temperature affects voltage magnitude and changing sunlight intensity

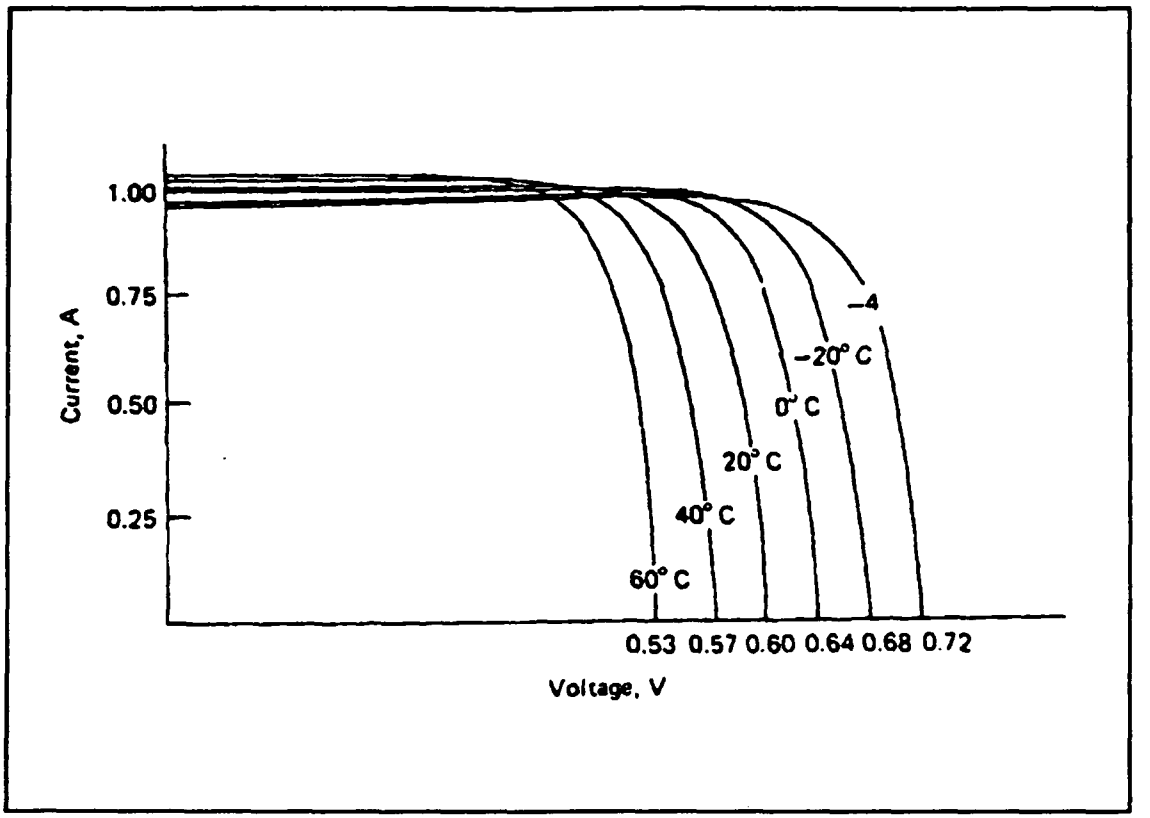

Fig. 6.3: voltage change with changing temperature

affects current magnitude. These effects are shown for a sample silicon solar cell in Figures 6.3 and 6.4 (Buresch, 1983). A cell's efficiency is normally rated at a specific temperature and solar intensity. It is therefore important to identify the operating conditions of the solar array to be designed and to apply appropriate scaling factors to the cell's voltage and current to estimate the actual achievable power output. The method for estimating actual power values will be discussed later in this chapter.

Ideally, the lightest, most efficient solar cells would be chosen for use on a project such as a solar powered plane. In the case of the WPI plane, cell selection had a role in dictating the design. Many different types of cells were looked at, with varying weights, efficiencies and cost. It was decided to go with 12.5%, 3.75"X3.75"

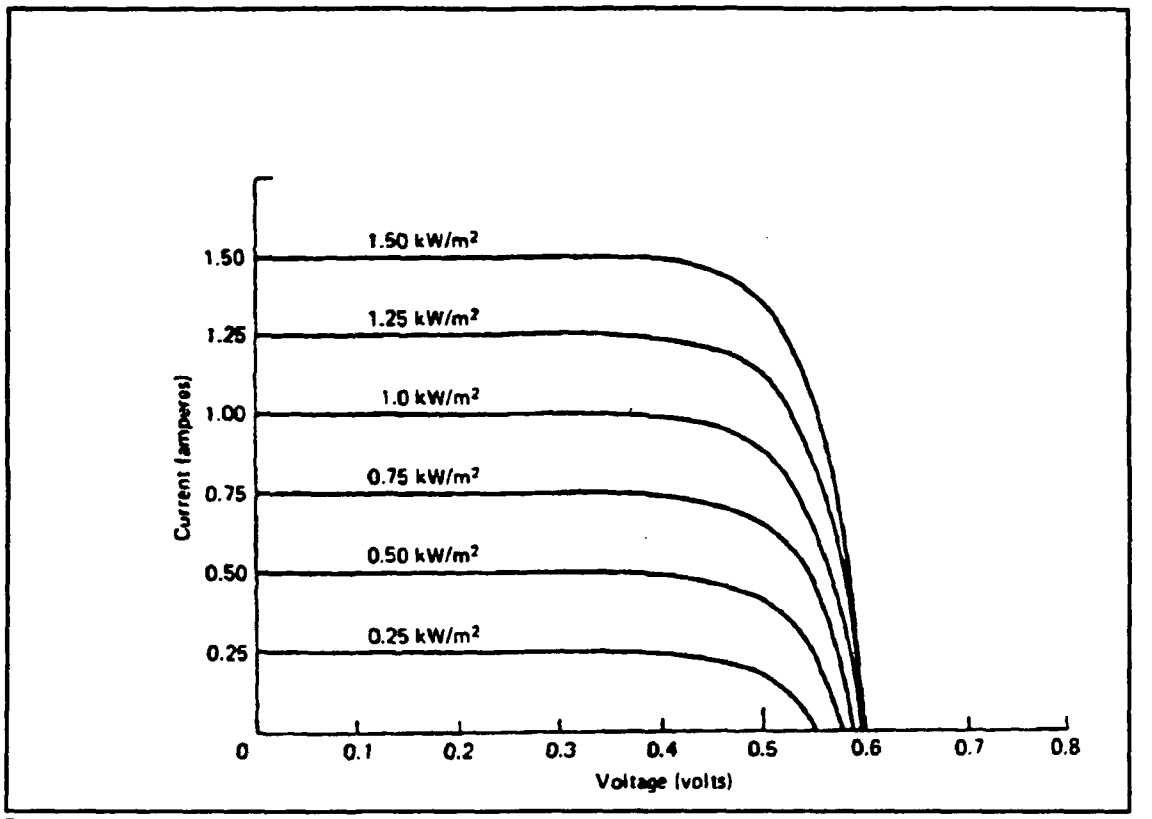

Fig. 6.4: Current change with changing insolation

cells from Mobil Solar (see Figure 6.5), because they were donated to the project at no cost. The cells are of high quality and relatively good efficiency, but their size and low power /weight ratio created notable design constraints.

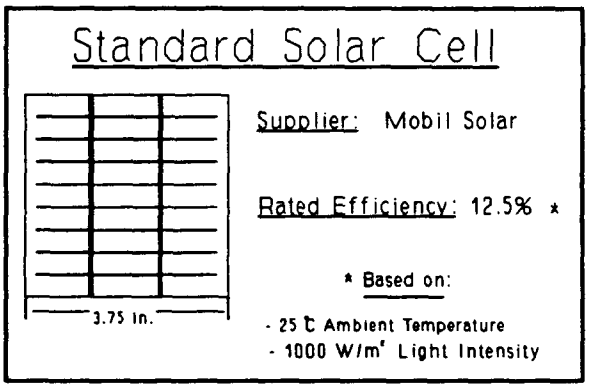

Fig. 6.5.

6.1.1 Array Constraints

In designing the airplane, the engineers had to take into account solar cell placement, because it affected aerodynamics and weight distribution. It was decided

that the majority of the cells would be placed within the wing, keeping the bulk of their weight near the plane's aerodynamic center, as well as maintaining the aerodynamic integrity of the airfoil. The wing's sizing was also dictated by cell placement. The airfoil section was made large enough to accomodate exactly three solar cells, minimizing extra structural material weight. An iteration was tried with two cells per airfoil section, but the power was insufficient for level flight. The final design called for the cells to be placed on a front and back support between ribs in the wing, one cell angled forward and two angled back. Additional cells were also added to the tail, one cell per section (see Figure 6.6).

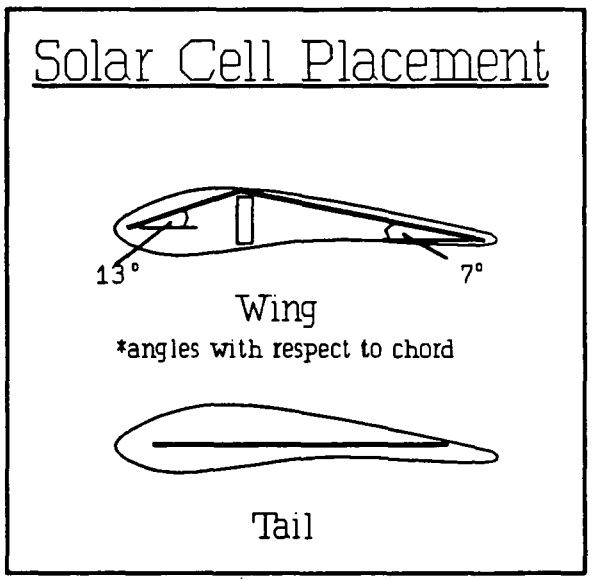

Fig. 6.6.

The advantages of placing the solar cells within the wing and tail are mostly aerodynamic. With cells of a relatively large size, it was impossible to obtain a high-lift airfoil by placing the cells on the surface. Also, having the cells on the surface would have created a greatly increased skin-friction drag, a problem for other solar powered planes (Boucher, 1985). Enclosing the cells within the wing cause three disadvantages. The first is that the angles created by filling the front and back plates within the wing had to be taken into account in many calculations and in the wiring of the array. Second, the ribs cause some shading on the cells at extreme banking angles. We tried to

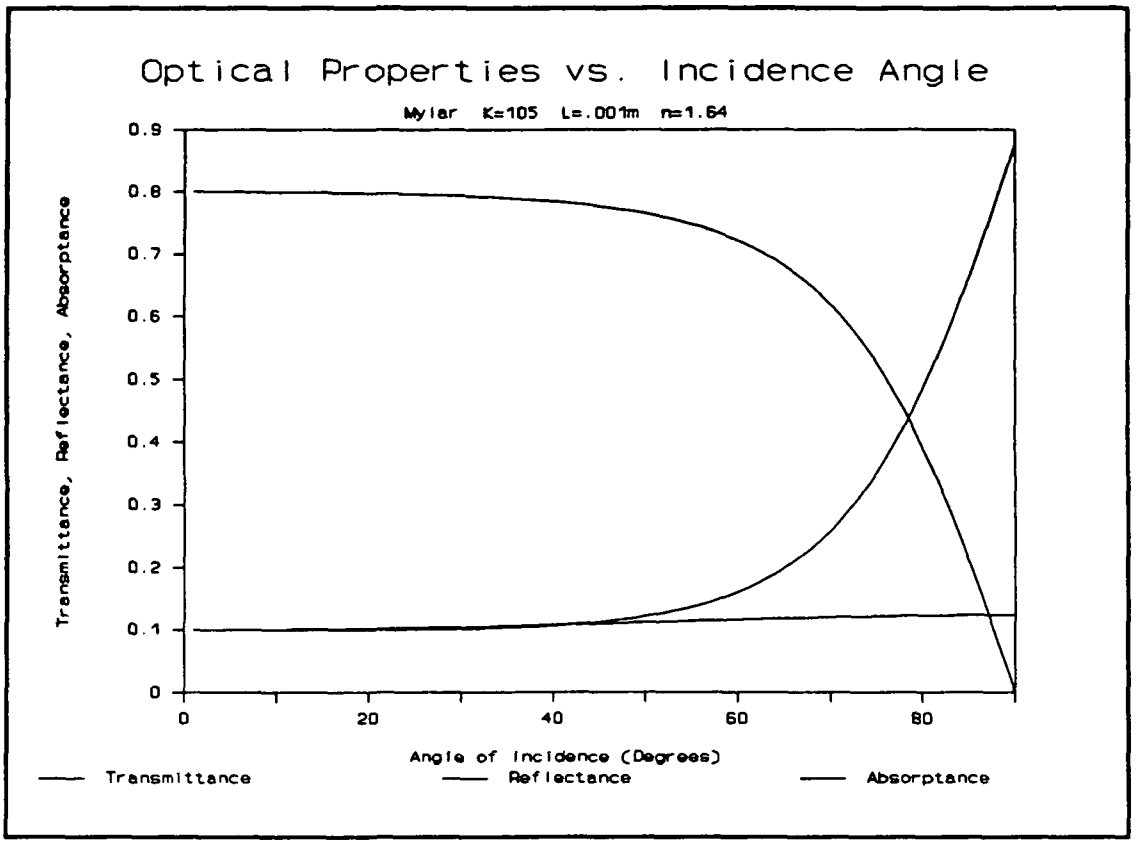

Fig. 6.7.

alleviate this problem by putting cells as close to the upper surface as possible. The final disadvantage is that the mylar coating on the wing has optical properties which inhibit the transmittence of some of the available sunlight. The mylar also creates a "greenhouse effect", increasing the temperature within the wing and thus, the solar cells. As will be seen later in the chapter, this causes a reduction in cell performance.

In evaluating the disadvantages of cell placement, it was most important to examine the optical properties of the mylar coating. Using the Fresnel reflection equations (Duffie and Beckman, 1980) and data provided by the cell manufacturer, the theoretical transmittence of the mylar coating was determined to be around 80% (see Figure 6.7). This seemed to be low, so experimental tests were conducted with

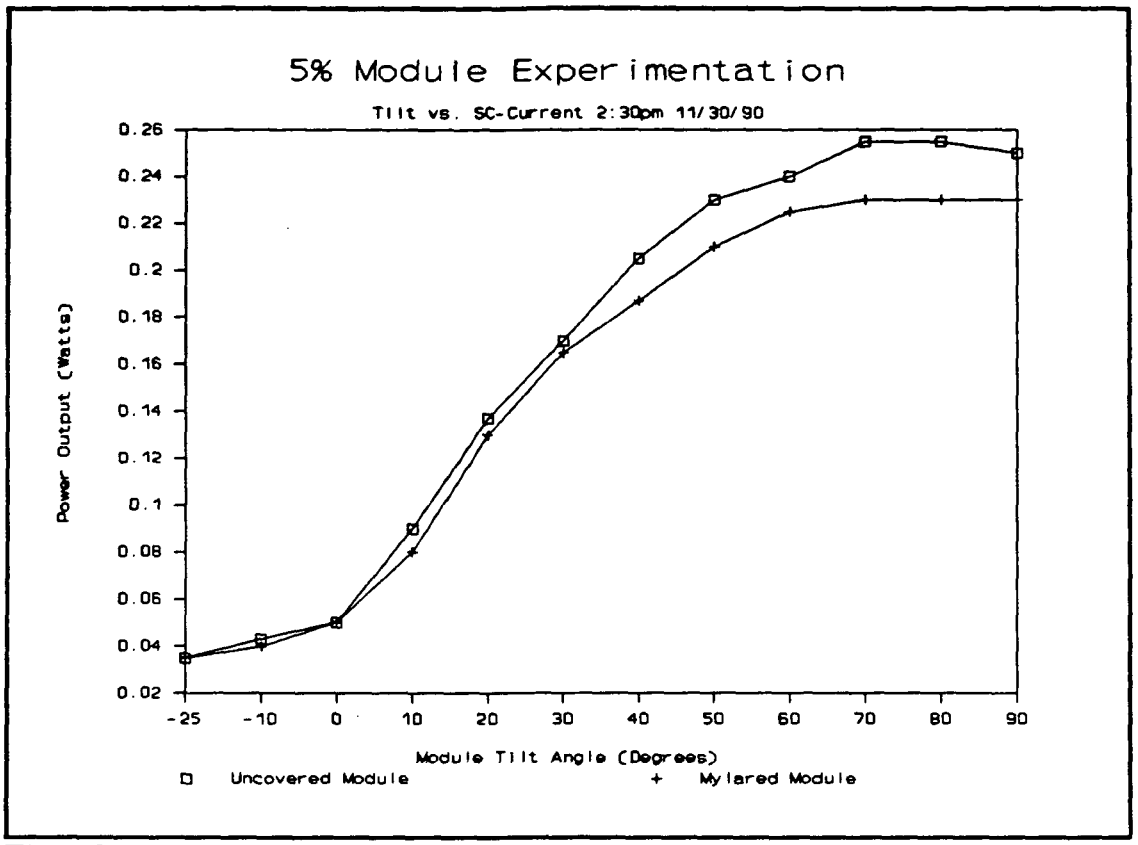

Fig. 6.8.

the mylar which would be used to construct the plane. These test yielded a transmittence of 90% (see Figure 6.8). The experimental values were determined to be the more accurate and were therefore used in the final calculations.

Other considerations that must be taken into account when designing the solar array are cell matching and wiring of the array. It is important that the solar cells being used have very similar voltage and current characteristics to prevent a "weak" cell from reducing the performance of other cells within a module of the array. In our case, the cell amperage and voltage matched up quite well under a constant light source, to two decimal places. The problem that arose, though, was that cells with identical angles to the sun must be grouped together. When wiring the cells, groups

could be either be put in series where voltages add, or parallel where currents add (see Figure 6.9). This is important because the array voltages and currents must provide the necessary input values for both the motor and the charging of the NiCad batteries, in order to operate at both the solar cell maximum power point and maximum motor efficiency. The matching of the solar array to the necessary input values is discussed later in the chapter.

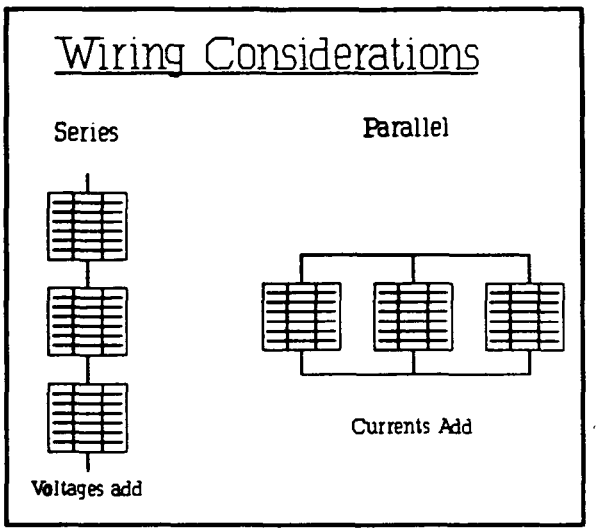

Fig. 6.9

6.1.2 Solar Irradiance Determination

In order to determine the power delivered by the solar cell array on the target flight date, the solar intensity on that date must first be calculated. Solar radiation comes in two forms, direct and diffuse radiation. Direct radiation can be directly calculated using known parameters. Diffuse radiation cannot be calculated, only estimated, because it is a function of reflectance and atmospheric conditions. When calculating available radiation, only direct radiation was taken into account. Up to 20% more solar power may be obtained from diffuse radiation, but using only direct radiation in the design computations enables diffuse radiation to be used to provide the margin of safety, balancing out any wiring or array losses that were not accounted

for.

The amount of energy reaching a solar cell on the earth is dependent on the amount of radiation reaching the earth from the sum, transmittence properties of the atmosphere, and the angle of incidence between the solar cell and direct beam radiation. The amount of extraterrestrial radiation is solely dependent on the day of the year, and can be found by the following relation:

$$G=G_{sc}(1+0.033\cos(360\frac{n}{365})) \qquad (6.1)$$

where: n = day of year
G_{sc} = solar constant

Transmittence is a function of the flight altitude of the airplane relative to sea level, as well as clear day atmospheric conditions and was estimated to be approximately 66% (Duffie and Buckner, 1980) at solar noon.

Angle of incidence depends on a number of parameters, some of which are shown in Fig. 6.10 (Duffie and Buckner, 1980). These include Worcester's latitude above the equator, the slope (β) of the solar cell with respect to the ground, the zenith angle (θ_z) or angle between the sun and the perpendicular to the ground, and azimuth angle (γ), the deviation of the projection of the normal to the cell's surface on the horizontal from the local meridian. Two other parameters are the declination angle (δ), the angular position of the sun at solar noon with respect to the equator, and hour angle (ω), the movement of the sun with respect to the local meridian, due to the rotation of the earth. These last two parameters are relative to "solar noon",

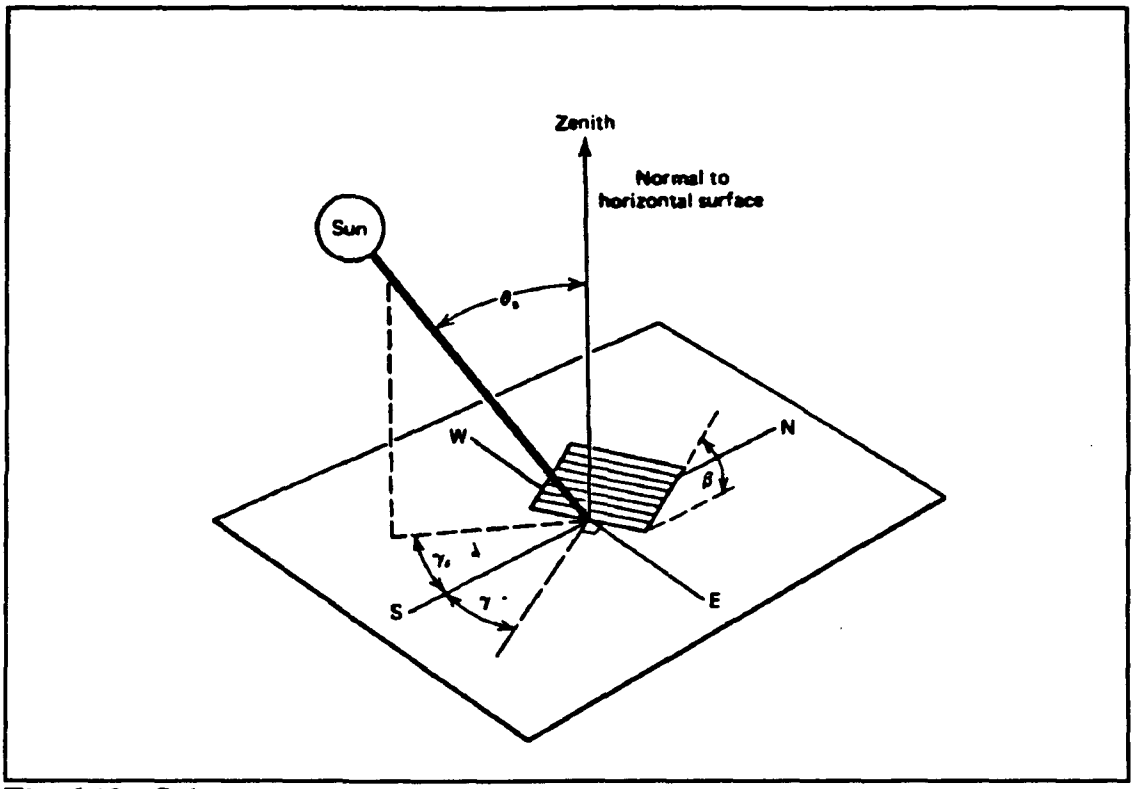

Fig. 6.10: Solar parameters

the time when the sun crosses the local meridian (Buresch, 1983).

For modeling purposes, it was assumed that takeoff for each test flight would occur at solar noon, eliminating the hour angle. Also, the plane was assumed to fly directly toward or directly away from the sun, the worst and best cases respectively due to solar cell placement, eliminating the azimuth angle and simplifying analysis. The relationship between angle of incidence,(θ) and the other angles is:

$$\cos\theta = \sin\delta\sin\phi\cos\beta - \sin\delta\cos\phi\sin\beta$$

$$+ \cos\delta\cos\phi\cos\beta + \cos\delta\sin\phi\sin\beta \qquad (6.2)$$

where: n = day of year

$$\delta = 32.45\sin(360(\frac{284+n}{365}))$$

Combining all of the equations above, we can obtain the final equation for computing the solar power delivered to a one square meter area on earth:

$$P = transmittence(G)\,(\cos^{-1}\theta) \qquad (6.3)$$

The power values for a $1m^2$ surface at various inclination angles with the horizontal, as well as a complete listing of power values can be found in Appendix D.1.

6.1.3 Solar Cell Tests

Ideally, to find out how much power is obtained from one solar cell under a given sun intensity, we would simply multiply the solar energy by the cell area and 12.5% efficiency supplied by the manufacturer. As we have shown, however, cell performance varies under changing conditions. To find the estimated power obtained from a cell on a given day, the actual operating efficiency must be calculated. The best way to do this is to start with a known set of solar cell performance data and then apply correction factors to estimate the performance on the flight date.

Solar cell tests were performed on three random solar cells from the group to be used in the plane. Tests were performed on Feb. 27, 1991 on a rooftop on the campus of WPI in order to minimize the effect of reflected diffuse radiation. The resulting I-V and power curves are shown below in Figure 6.11 for the average cell in the test group.

Once actual test data for the solar cells were obtained, adjustments could be

applied to the voltage and current values to estimate the I-V and power curves for a cell on the flight date. The current adjustment was a function of the light intensity on flight and test dates. Because current has a linear relationship with light intensity, it was possible to find a correction factor, given flight and test date light intensity and test date current values. This factor was calculated to be 2.574 (see Figure 6.12).

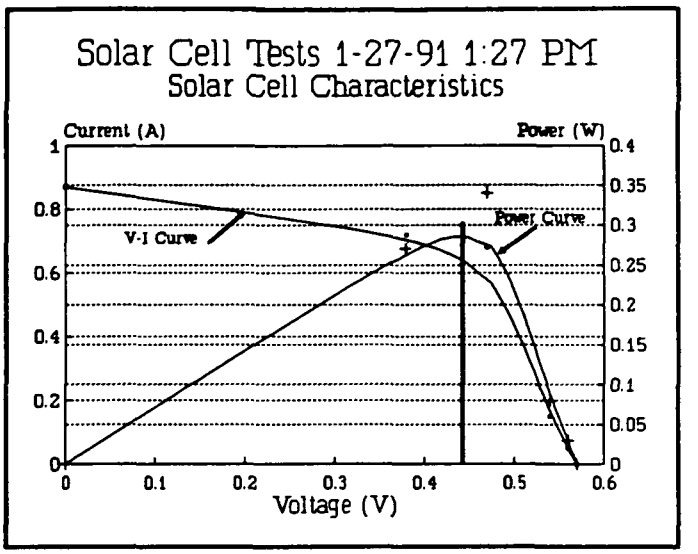

Fig. 6.11.

Cell voltage changes with temperature. Relations thus had to be applied to estimate voltage change as a function of both cell and ambient temperature, taking into account the effect of light intensity on cell surface temperature (Buresch, 1983). The first step was to calculate the cell temperature on test and flight dates using the following relation:

$$T_c = T_a + kS \qquad (6.4)$$

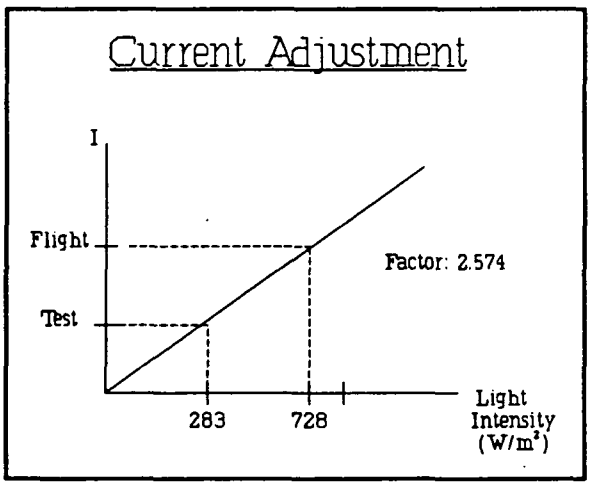

Fig. 6.12.

where:

T_c = adjusted cell temperature
T_a = ambient temperature
k = solar cell temperature coefficient, 0.2

S = solar insolation, mW/cm^2

It should be noted that the ambient temperature for the test date was adjusted by +10° F to account for the "greenhouse effect" within the wing. After cell surface temperatures were calculated, following equation was applied to find the adjusted cell voltage:

$$V_a = V_{test}[1 + \beta (T_{test} - T_a)] \qquad (6.5)$$

where:
V_a = adjusted cell voltage
V_{test} = reference cell voltage
β = solar cell output vs. temperature coefficient, 0.004
T_{test} = test cell temperature
T_a = flight date cell temperature

From these calculations, a factor of 0.8383 was applied to the cell test voltages to estimate flight operating voltages. By applying both the current and voltage adjustment factors to the test data, estimated V-I and power curves were obtained for the flight date (see Figure 6.13). Then, comparing the point of maximum power to the amount of solar energy provided to the cell surface, it was determined that the actual operating efficiency of the solar cells on the flight date would be 10.26%. This efficiency was then lessened by another 2% for I^2R losses from the wiring and 5% for array and matching losses. The final calculated operating efficiency of the cells was then used, along with the solar cell area to find total power for the array at various flight angles of attack (see Appendix D.1). Figure 14 provides the power curves for the plane, heading both toward and away from the sun.

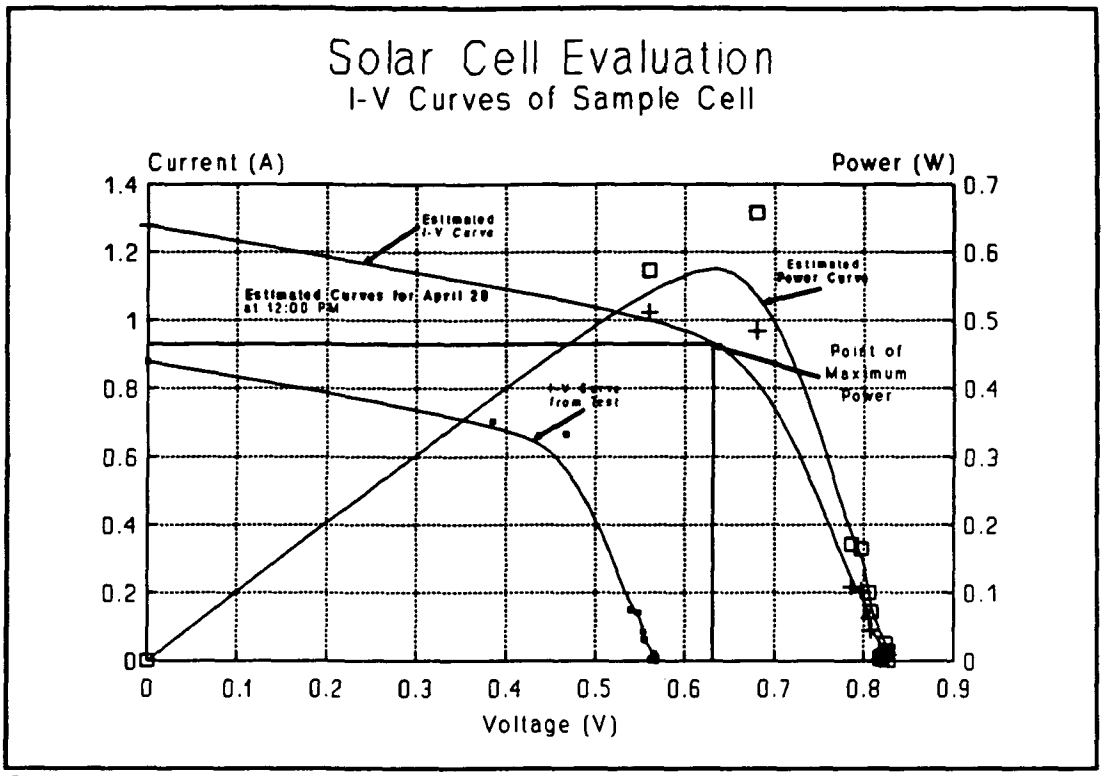

Fig. 6.13.

6.2 NICKEL-CADMIUM BATTERIES

In addition to the solar array, the power plant for the plane utilizes seven 1.2 V Nickel - Cadmium (NiCd) batteries. Batteries were used in the plane for several reasons. The most important was the fact that a moving solar plane provides a fluctuating current to the motor, an un-desirable operating condition. Batteries supply a constant voltage to the motor and let the motor draw whatever current it needs. The solar cells were set up to charge the batteries, with the fluctuating current affecting only the rate of charge. The batteries also provided a safety measure to account for any

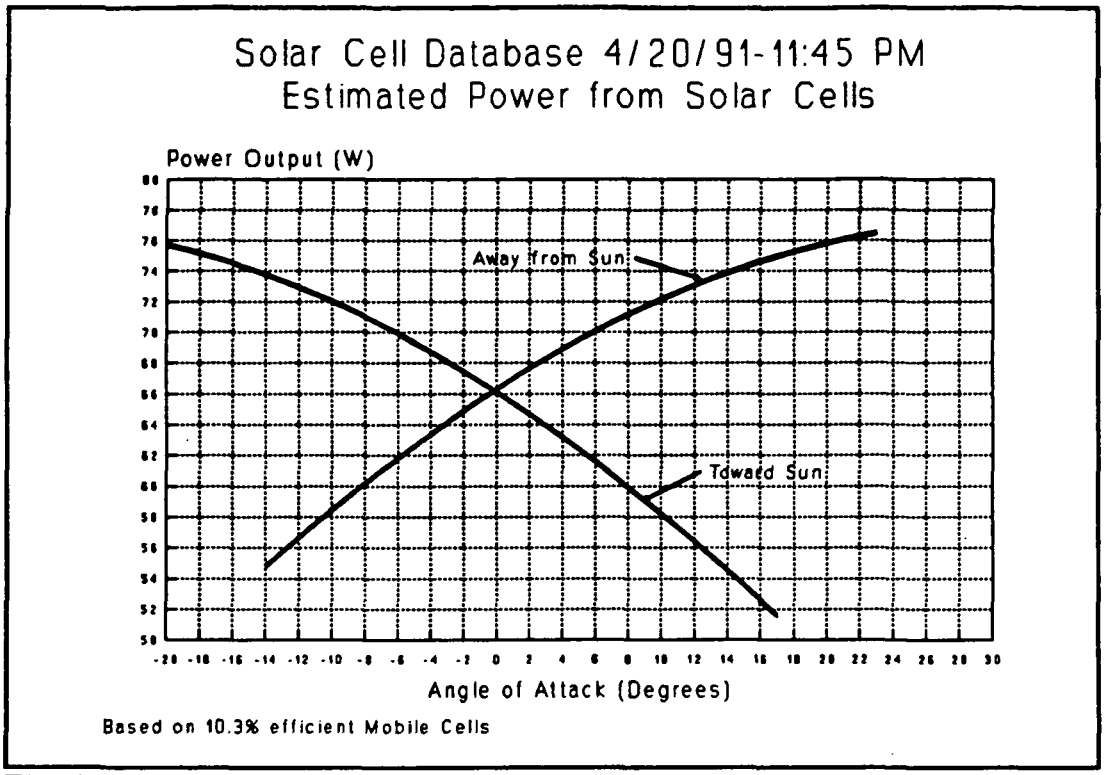

Fig. 6.14

loss of power from the solar array. Use of NiCd batteries assured easy re-charging, and durability.

The inclusion of batteries in the solar plane also provided an added advantage. When the design of the plane was near completion, a problem was discovered with its center of gravity, which was found to be too far back on the wing. Correct positioning of the batteries forward of the wing in the fuselage moved the center of gravity back to its correct place.

When using NiCd batteries, certain problems must be taken into account. It is important that when charging the batteries at high rates of charge, as in the case of the solar plane, they cannot be over-filled. This could cause damage to the batteries. Because most of the batteries' power will be used as soon as the cells get

charged, this problem proved negligible. Another problem particular to NiCd batteries is that if they are constantly being recharged only to a certain capacity, which could happen during multiple flights, a "memory effect" is induced, enabling the batteries to be charged only to that capacity in the future (Perez, 1985). This problem also proved to be negligible, due to the relatively short duration of use of the batteries, and their easy replaceability.

6.3 DC MOTOR

The second subsection of our system consists of a cobalt-magnet DC motor and reduction gearbox manufactured by Astro-Flight, Inc. We used the Astro Cobalt 05 geared motor with a 2.2:1 gear ratio (see Appendix D.2 for manufacturer's specifications). We chose this type of motor because cobalt magnet DC motors are the most efficient electric model motors available. The Astro-035 was also examined, however it could not provide the necessary power needed by our aircraft.

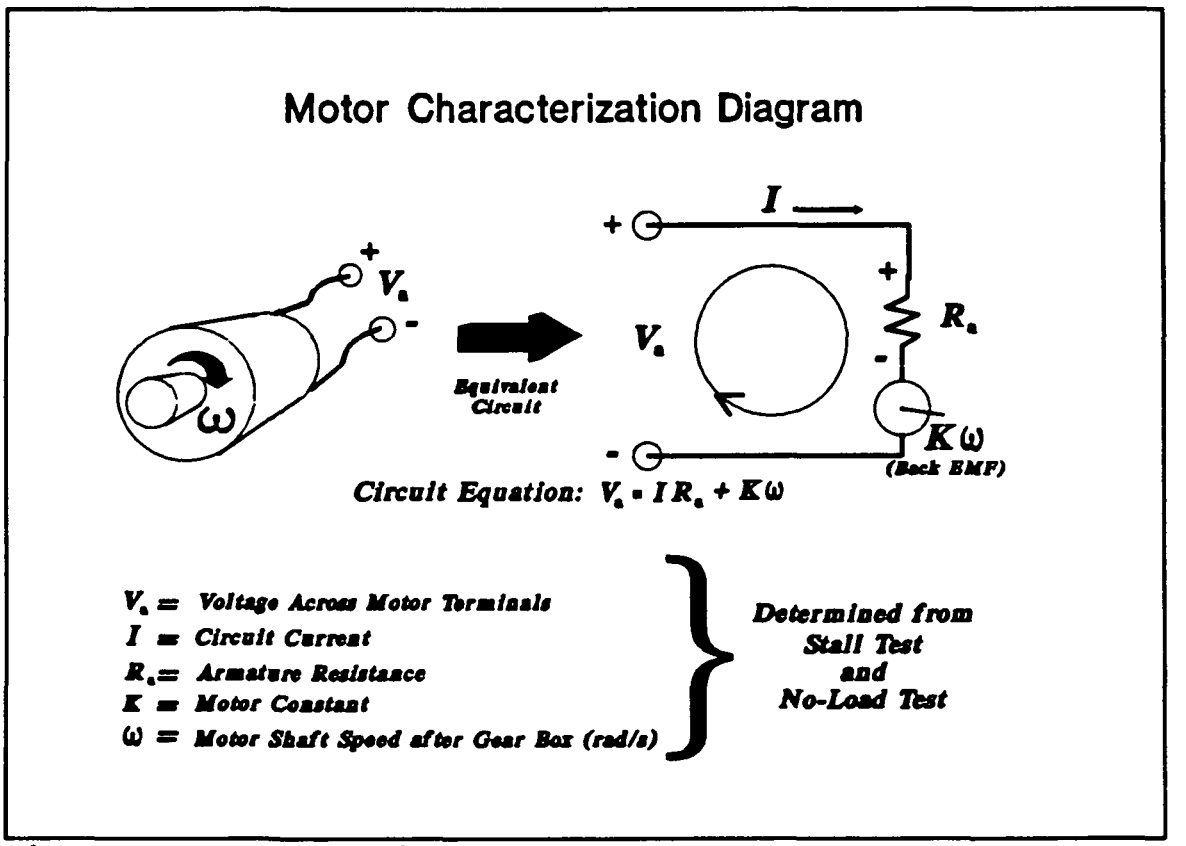

Figure 6.15: Motor Diagram

DC motor characteristics, ie. speed, torque, and efficiency can be represented as functions of both voltage and current. The motor characterization diagram in Figure 6.15 shows the equivalent circuit representing our DC motor. By applying Kirchoff's Voltage Law around this circuit:

$$\Sigma V=0 \qquad (6.6)$$

we derive with the Circuit Equation in the diagram. This method allows us to obtain a profile of the motor efficiency for optimum voltage and current inputs. The electrical input power into the motor is:

$$P_{motor}=V_a I \qquad (6.7)$$

where V_a is the voltage across the motor's armature terminals, and I is the current into the motor (Cogdell, 1990).

Two tests are performed to obtain the required parameters for calculating DC motor performance. These are the stall and the no-load tests. The stall test is executed by holding the external shaft of the motor still while applying an electrical input, V_a and I, to the motor. By recording the voltage across the motor terminals and the current into the motor, we can determine the parameter R_a, the resistance of the armature (wire coil) in the motor. Rearranging our circuit equation and solving for R_a, keeping in mind that ω is 0, yields:

$$R_a=\frac{V_a}{I}, \qquad (6.8)$$

otherwise known as Ohm's Law. The next test conducted is the no-load test which is done by applying an electrical input to an unloaded (propellerless) motor. By recording the voltage across the terminals, the current into the motor, and the shaft speed in radians/second, we can determine K, the motor constant. By rearranging our circuit equation, including R_a from the stall test, and solving for K:
which has units of Newton-meters/ampere (N-m/A). The K value used is an average value determined from five data points. The data from the no-load test are also used

$$K=\frac{V_a-IR_a}{\omega} \qquad (6.9)$$

to determine two other parameters, namely damping coefficient (**B**) and frictional torque (T_f). This is done by graphing KI versus ω and applying a linear, least squares regression, curve fit to the data. The resulting slope represents **B** and the y-axis intercept represents T_f. The damping coefficient is a mechanical property of the motor, largely dependent upon ω, and the frictional torque is the motor's torque when $\omega=0$ (Heinzmann, 1990).

The resulting parameters are: armature resistance R_a in ohms, motor constant **K** in N-m/A, frictional torque constant T_f in N-m, and damping coefficient **B** in N-m-s. For our motor, the numerical values of these parameters are as follows:

R_a:	0.05 ohms
K:	0.0095 N-m/A
T_f:	0.016 N-m
B:	1.6E-5 N-m-s.

Knowing these parameters, we can obtain an accurate estimate of the motor's performance. Expressing the motor's shaft speed using our circuit equation and solving for ω yields

$$\omega=\frac{V_a-IR_a}{K}, \qquad (6.10)$$

where V_a and I are both independent variables for our DC motor. We use the simulated motor speed along with the specified motor parameters to simulate the shaft torque (T_a), with the following relation:

C-2

$$T_s = KI - T_f - \omega B \qquad (6.11)$$

which is also a function of both V_a and I. Now the motor efficiency (output power/input power) can be expressed in terms of our dependant variables, shaft torque, motor speed, terminal voltage, and current:

$$\eta_{motor} = \frac{P_{motor-}}{P_{-motor}} = \frac{\omega T_s}{V_a I} . \qquad (6.12)$$

By making V_a an MxN matrix of M voltages x N columns and I an MxN matrix of M rows x N currents, the dependant variables also become matrices by performing **scalar** operations on the matrices. For example, each value in the motor efficiency matrix corresponds to the voltage and current values in each matrix at the same element location. Computer software greatly simplifies the process of creating these large matrices. We used PCMatLab to generate the matrices and to create plots of the simulated data versus voltage and current. These plots are contour plots of three-dimensional data showing one or more motor characteristics as functions of two independent variables: voltage and current.

A contour plot is like a relief map. There are two independent variable axes, x and y, and the lines on the plot represent constant values of some dependant variable or variables. On a relief map, the x and y axes are planar distances and the contour lines represent elevations of constant magnitude. On our contour plots, the x axis is voltage, the y axis is current, and the overlaid contour lines represent the motor's characteristics. Figure 6.16 is a combined contour plot of electrical input power, shaft torque, shaft RPM, and motor efficiency versus voltage and current.

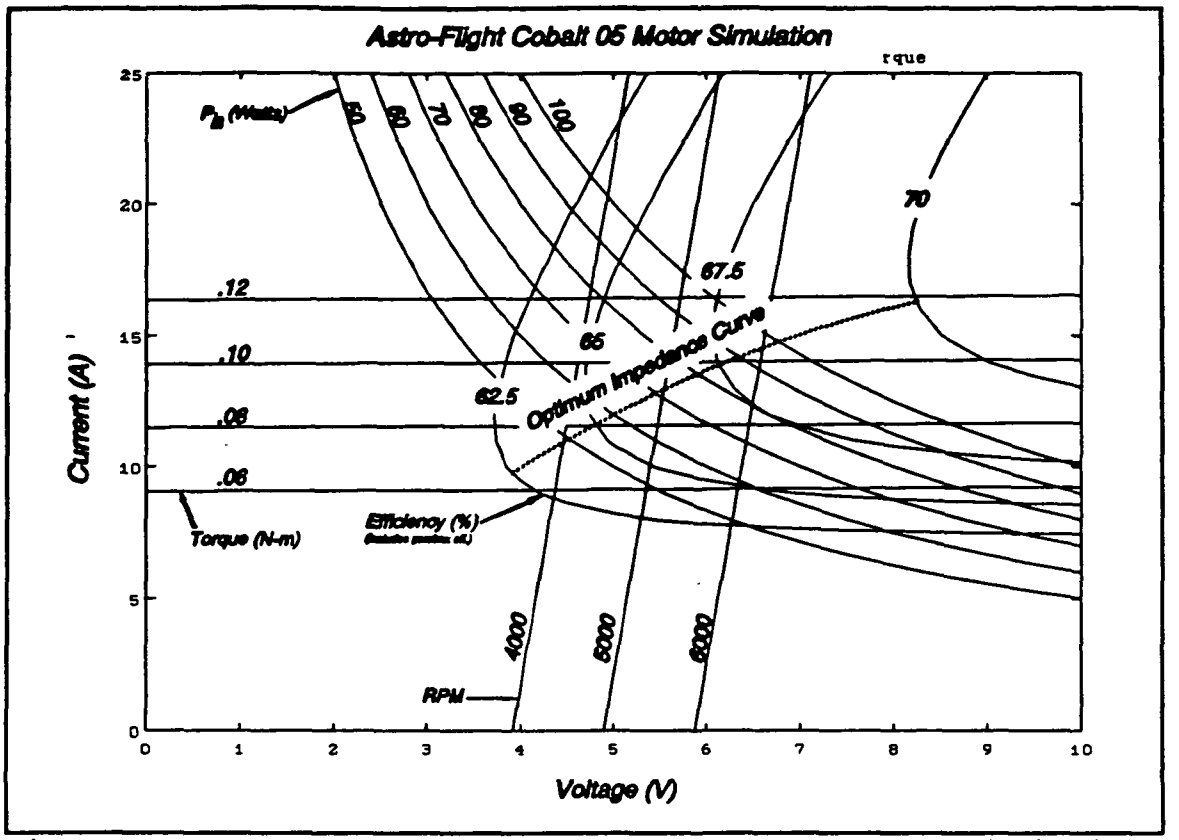

Figure 6.16: Contour Plot of Astro-05 Motor Characteristics

Note that the motor efficiency includes a gearbox efficiency of 88%.[1] The electrical input power contour lines represent the product of voltage and current along each line. For example, looking at the 60W input contour line, if we choose any point on that line and read the corresponding voltage and current values from the axes, the product of that voltage and current will be equal to 60W.

Figure 6.17 is an is an isometric 3-D mesh plot of motor efficiency vs. voltage and current, also created using PCMatLab.[2]

---

[1]This efficiency was determined from actual propeller loaded tests which will be discussed in a later section.

[2]The PCMatLab programs used to generate the matrices and plots is also included in Appendix D.2. We acknowledge Kurt Heinzmann for his help with this procedure.

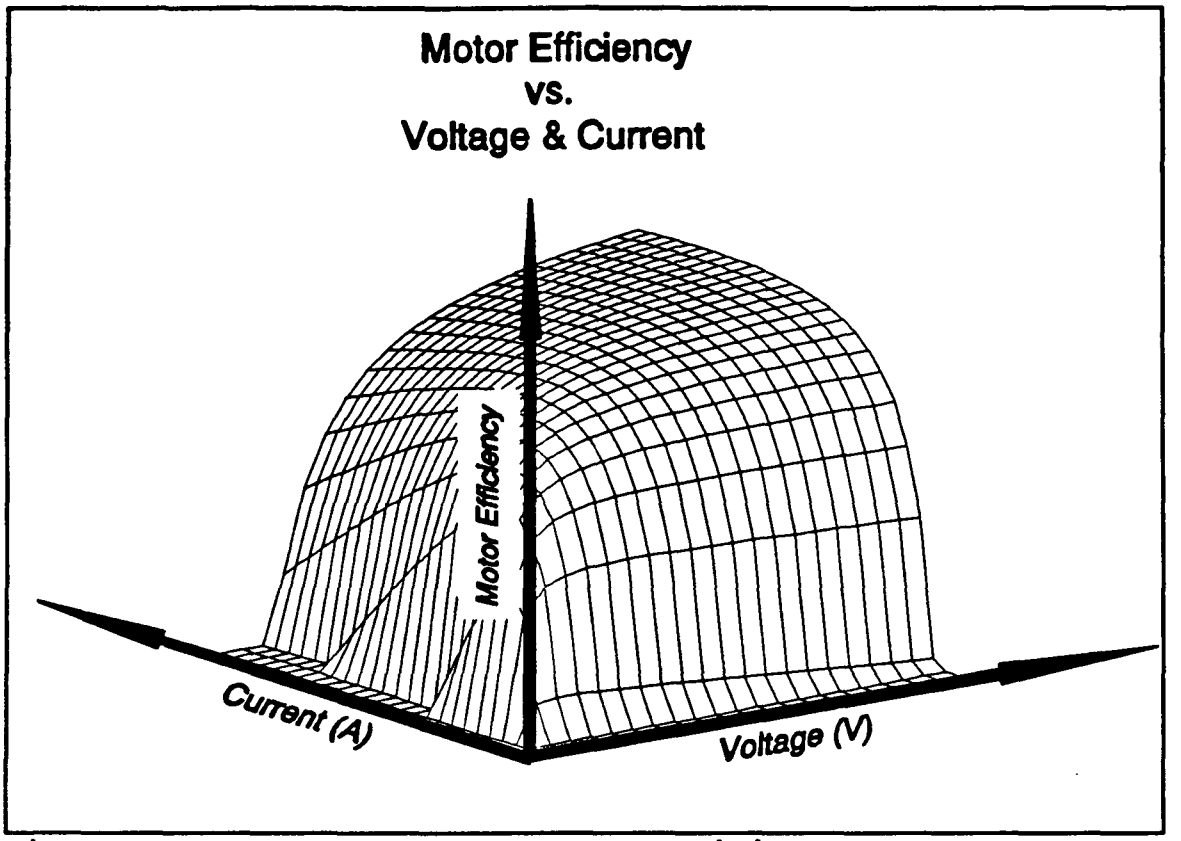

Figure 6.17: 3-D Plot of Motor Efficiency vs Voltage and Current

Our objective is to operate the motor at the highest motor efficiency possible, from a given electrical input power from either the solar array or NiCd batteries. This is done by operating the motor at a voltage and current that puts it at the intersection of the desired input power contour and highest efficiency. The highest efficiency acheiveable for a given input power contour is determined by the efficiency contour whose apex intersects the input power contour. Looking at Figure 6.16, the load line (not a contour line) passing through these apexes represents the optimum motor impedance at each electrical input power level. When running the motor from the solar array or NiCd's, we would like to set up the array or the batteries so that they would deliver the optimum voltage and current to the motor for given input power levels.

However, there are problems associated with setting up an electrical source to deliver the required current. There is an electrical power loss through the wiring that is quadradically proportional to the current through the wire. This is commonly referred to as I^2R loss:

$$P_{loss}=I^2R_{wire} \qquad (6.13)$$

where R_{wire} is the resistance of the wiring. An additional important aspect of this power loss is that the loss occurs by generating heat in the wiring. With high current loads, the heat may become intense enough to actually melt the wire casing or destroy the wire itself! This problem can be alleviated by using low resistance wire. Another problem with high current transfer is electro-magnetic interference. The remote control reception of the servo-motors can be severely affected by EMF. This problem can also be alleviated by shielding the wire from the servo-motors to the receiver in the control system (Cogdell, 1990).

This concludes our discussion of DC motor performance. Next, we will look at the third section of our powerplant; its function and characteristics.

6.4 PROPELLER SELECTION AND PERFORMANCE

The third section of this aircraft's powerplant consists of a two-bladed folding propeller manufactured by Aero-Haute, a German model airplane company. When fully expanded, the propeller has a diameter of 33 cm and a geometric pitch of 16.5 cm. We will now discuss methods of obtaining high propeller efficiency through basic propeller theory and the application of this theory to our propeller.

The roots of the most complicated propeller theory can be traced back to Newton's Second Law:

$$F=ma=\frac{mdV}{dt} \qquad (6.14)$$

which states that the force F or thrust produced is equal to the change in momentum in unit time. A propeller operates by producing a relatively small change in velocity of a relatively large mass of air. The earliest theory describing propeller action is the Rankine-Froude momentum theory. This theory assumes that the propeller disk, created when the propeller is rotating, can be replaced physically by an actuator disk that has an infinite number of blades and is capable of producing a uniform change

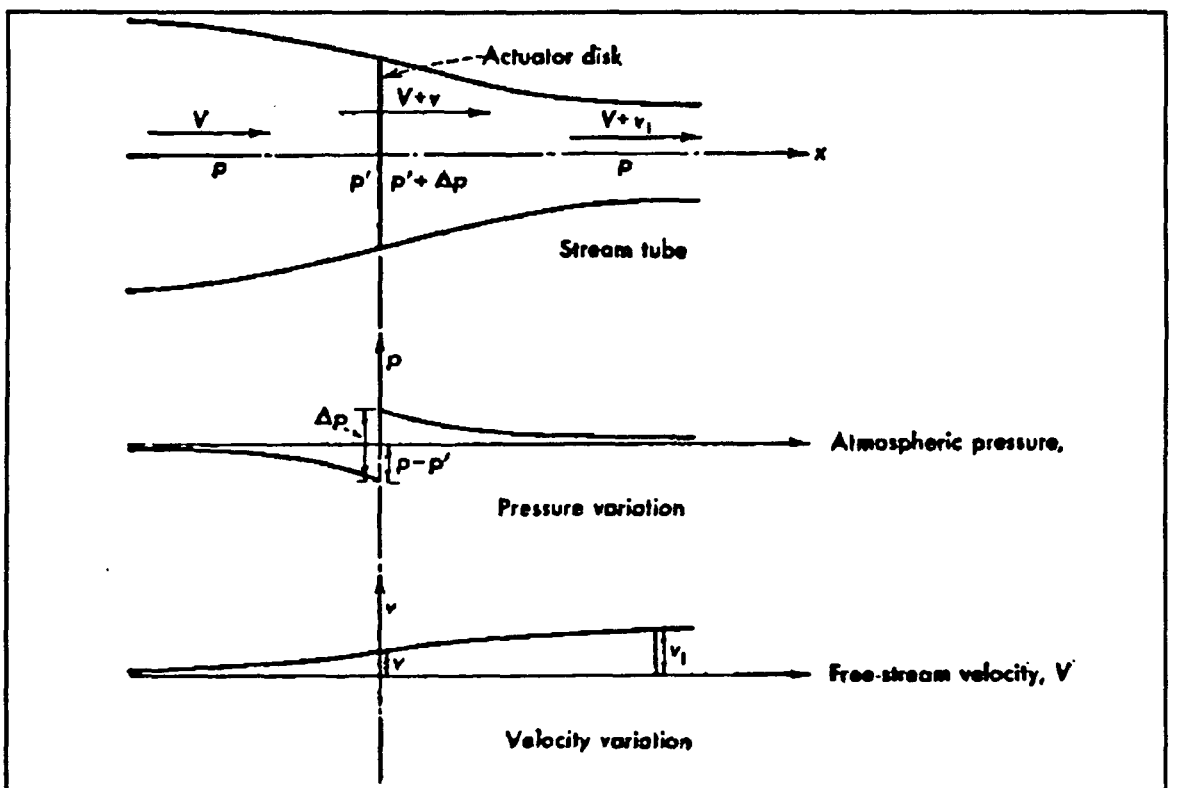

Ref: Dommasch, Sherby, Connolly, Airplane Aerodynamics, 1967.

Figure 6.18: Flow through an Actuator Disk.

in velocity of the air stream passing through the disk as shown in Figure 6.18. In developing the momentum theory, we assume that we deal with a steady-state, steady-flow (irrotational flow) and incompressible fluid. Although this theory is useful in determining theoretical ideal propeller efficiencies:

$$\eta_{ideal} = \frac{V}{V+v} \qquad (6.15)$$

where $\underline{V}$ is the free stream airspeed and $\underline{v}$ is the change in velocity through the actuator disk, momentum theory tells us nothing about the losses associated with propeller geometry: energy lost in slip-stream rotation, propeller profile drag, non-uniform thrust loading, blade-interference, increased drag and changes in flow in the compressible range. However, some of these effects are considered in blade-element theory.

As a propeller moves through the air, it also rotates so that each point on the propeller follows a helical path as shown in Figure 6.19. Because the rotational speed at the root of the blade is much less than at the tip, while the forward velocity is the same at both points, the relative wind at the root sections is almost along the propeller axis, whereas at the tip the relative wind is more nearly perpendicular to this axis. Consequently, to obtain the most efficient angles of attack for each radial blade element, it is necessary to twist the blades so that the blade angle (β), at the root approaches 90° relative to the plane of rotation, while the tip angle approaches 0°. Because a propeller is discontinuous at the hub, allowing for a spinner and pitch-changing mechanism in some cases, the blade angle at the root is less than 90° since the blade begins away from the propeller axis. Blade element theory assumes that the induced flow past a blade element is the same as that past a wing of aspect ratio

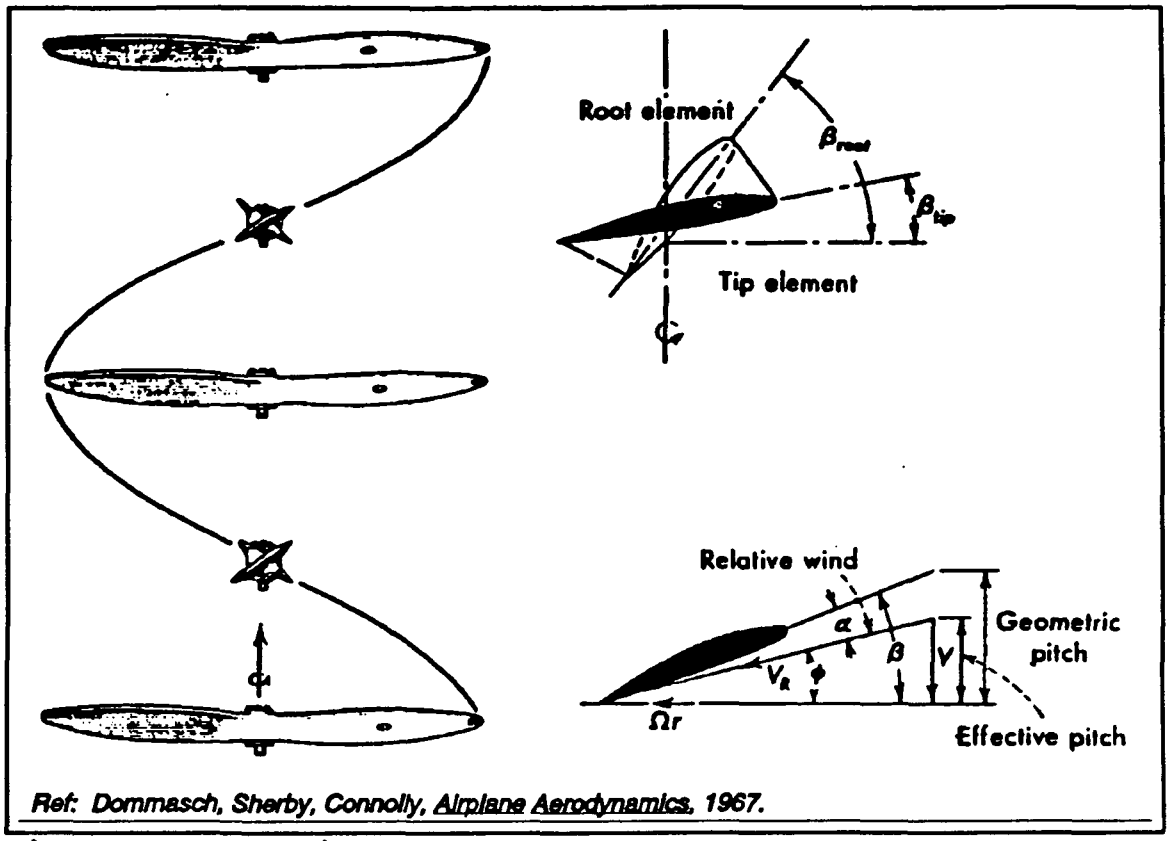

Ref: Dommasch, Sherby, Connolly, Airplane Aerodynamics, 1967.

Figure 6.19: Basic Propeller Geometry.

6. In applying this theory, the angle of attack is taken to be the difference between the geometric-pitch angle β and the effective-pitch angle ϕ as shown in Figure 6.20. The lift and drag coefficients for each blade element can be obtained from a plot of airfoil data for an aspect ratio of 6. The forces **dL** and **dD** on a blade element of width **dr** and chord **b** produce differential thrust, **Dt**, and differential torque, **dQ**, at each station **r** away from the hub of the propeller. The differential thrust created by the element is the sum of the components of the lift and drag forces perpendicular to the plane of rotation, and the differential torque is the sum of the components of the lift and drag forces parallel to the plane of rotation, multiplied by their moment arm (r),

$$dT = dL(\cos\phi) - dD(\sin\phi) = \frac{1}{2}\rho V_R^2 b[c_l(\cos\phi) - c_d(\sin\phi)]\,dr \quad (6.16)$$

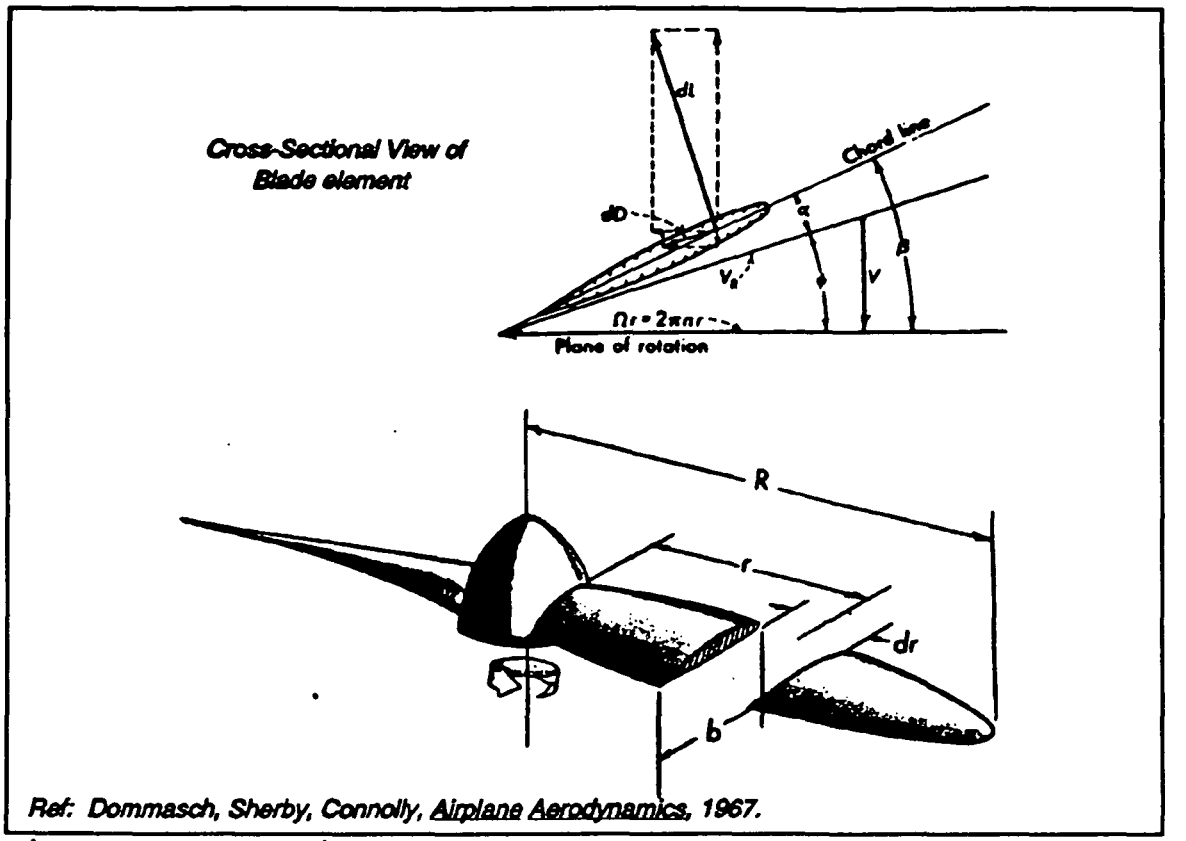

Ref: Dommasch, Sherby, Connolly, Airplane Aerodynamics, 1967.

Figure 6.20: Typical Blade Element.

$$dQ = [dL(\sin\phi) + dD(\cos\phi)]\, r = \frac{1}{2}\rho V_R^2 br\,[c_l(\sin\phi) + c_d(\cos\phi)]\,dr. \quad (6.17)$$

For a propeller with **B** blades, expressions for net thrust and torque are obtained by integration of the above differentials with respect to radial distance r

$$T = qB\int_0^R \frac{b}{\sin^2\phi}(c_l\cos\phi - c_d\sin\phi)\,dr, \quad (6.18)$$

$$Q = qB\int_0^R \frac{br}{\sin^2\phi}(c_l\sin\phi + c_d\cos\phi)\,dr \quad (6.19)$$

where **q** is the dynamic pressure based on freestream density **ρ** and velocity **V**. Although blade-element theory is useful in predicting actual propeller thrust and torque, and may produce answers within 10% of measured values, there is a more

exact method which enables us to calculate the induced flow rather than assume it to be that created by a wing with an aspect ratio of 6.

Recall from elementary aerodynamics that the induced flow about a wing was the result of the circulation created from lift. Similarly, with Vortex Theory, the induced velocity created by a rotating propeller may be considered a result of

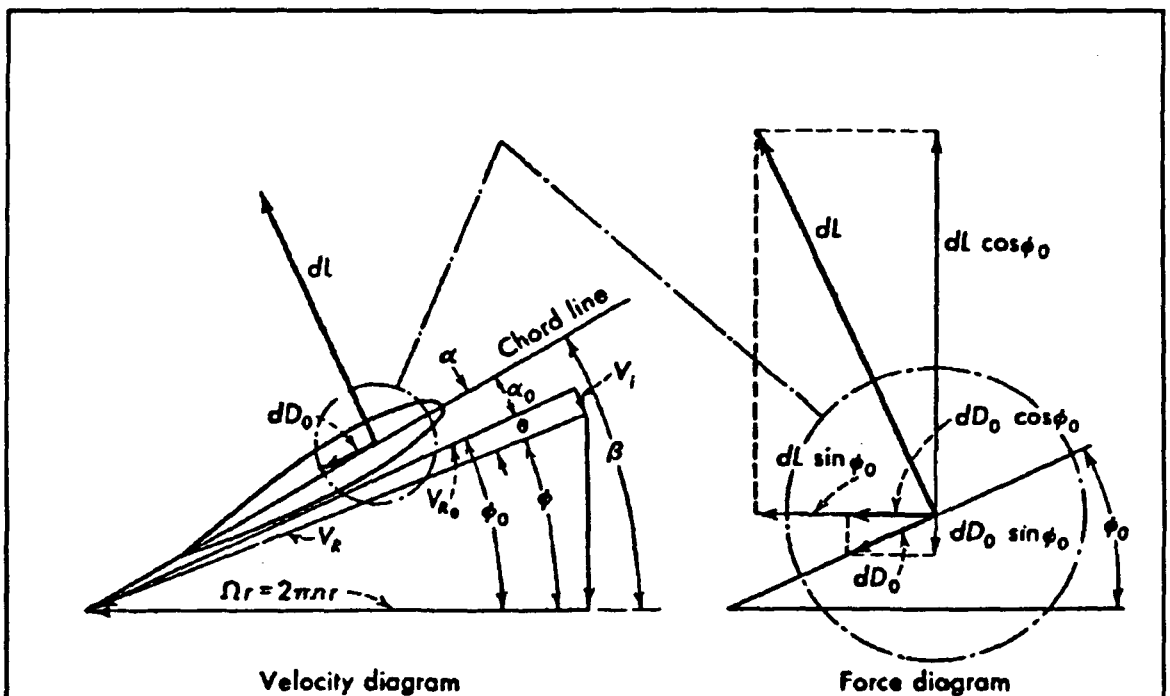

Ref: Dommasch, Sherby, Connolly, Airplane Aerodynamics, 1967.

Figure 6.21: Typical Blade Element from Vortex Theory.

circulation about a blade element. Figure 6.21 shows a blade element and the associated forces, angles, and velocities. The differential thrust and differential torque can be determined in the same way as in blade-element theory; by summing the forces perpendicular and parallel to the propeller's plane of rotation:

where dC_T and dC_Q are differential thrust and torque coefficients, and **D** is the propeller diameter (not to be confused with the D in Figure 6.21 which is blade-

$$\frac{dT}{dr}=\frac{1}{2}\rho(2\pi n)^2\frac{\cos^2\theta}{\cos^2\phi}r^2bB(c_l\cos\phi_0-c_d\sin\phi_0)=\frac{dC_T}{dr}\rho n^2D^4 \quad (6.20)$$

$$\frac{dQ}{dr}=\frac{1}{2}\rho(2\pi n)^2\frac{\cos^2\theta}{\cos^2\phi}r^3bB(c_l\sin\phi_0+c_d\cos\phi_0)=\frac{dC_Q}{dr}\rho n^2D^5 \quad (6.21)$$

element profile drag). The algebra involved in simplifying the vortex theory analysis is lengthy and will not be included here (Dommasch, Sherby, et. al, 1967). In summary, all one needs to find the elemental thrust and torque coefficients is a propeller's geometry, ie. b, R, β, and the type of airfoil. One can then determine the elemental coefficients, dC_T/dr and dC_Q/dr, for various points on a propeller span by using the vortex theory method. A spread sheet would be an ideal tool for this job. To find C_T and C_Q, as well as the distribution of loading along the propeller span for stress analysis work, graphical integration may be used. The area under each of the curves in Figure 6.22 gives us C_T and C_Q for the entire propeller, assuming each propeller blade is identical of course. From these coefficients, thrust and torque can be calculated with the equations above.

Finally, the propeller efficiency can be expressed as the ratio of power output to power input, relative to the propeller:

$$\eta_{Propeller}=\frac{P_{prop}}{P_{-prop}}=\frac{TV}{Q\omega} \quad (6.22)$$

where $\underline{T}$ is thrust, $\underline{V}$ is airspeed, $\underline{Q}$ is shaft torque, and $\underline{\omega}$ is shaft speed in rad/s. Incidently, Q and ω are the same as $\underline{T_s}$ and $\underline{\omega}$ which were introduced in our DC motor discussion. From this point on, shaft torque will again be referenced as $\underline{T_s}$. All of these variables can either be calculated analytically or found experimentally. To restate our objective in designing a propeller, or choosing a propeller , we wanted to use the most efficient propeller possible for a given operating range on the motor.

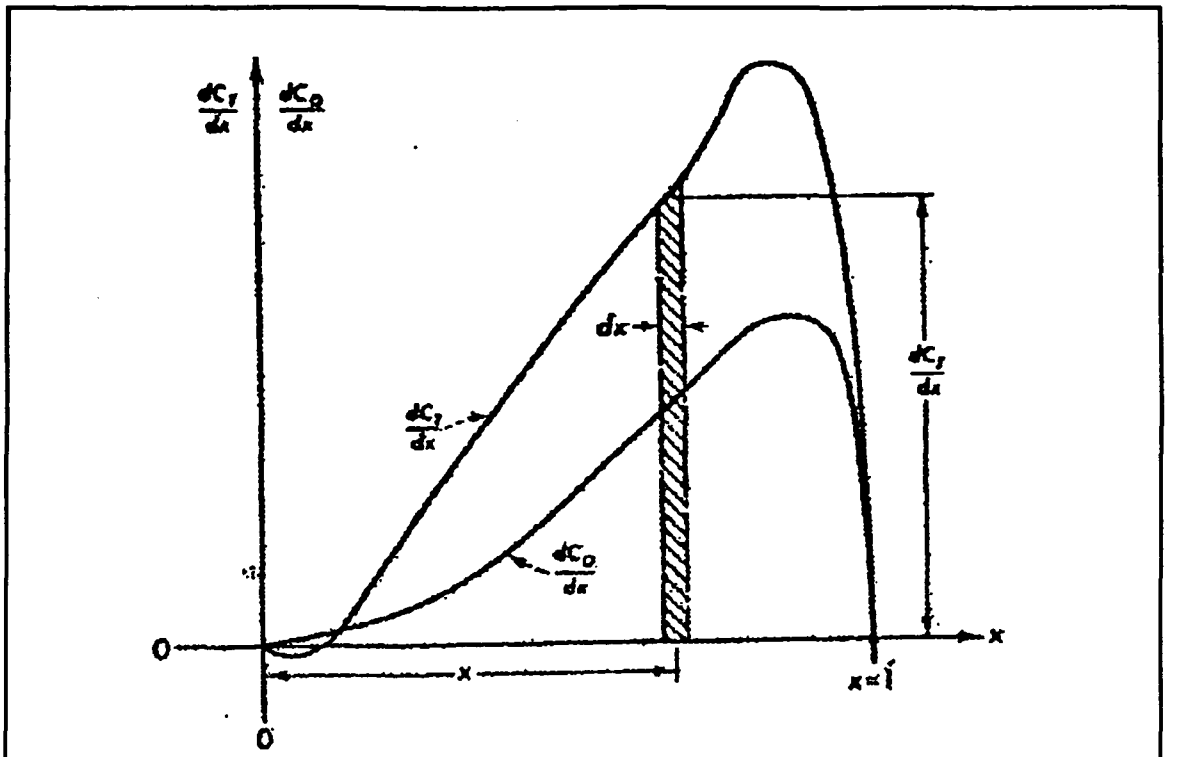

Ref: Dommasch, Sherby, Connolly, Airplane Aerodynamics, 1967.

Figure 6.22: Elemental Coefficient Curves for a Typical Propeller Blade.

It is possible to optimize propeller performance for any motor range by using a propeller with a pitch changing mechanism. This would be ideal for our project. However, it was not possible due to time constraints.

The propeller theory presented here is not complicated, yet it can produce numbers very close to actual experimental values of thrust and torque. More exact theories have been developed by Goldstein, Lock, and Theodorsen, but they are beyond the scope of this project. These theories are analytical tools which can used in the absence of experimental capability. The easiest and most obvious way to find the thrust and torque generated by a spinning propeller is through experimentation. This brings us to a discussion of our methods of testing and characterizing the motor-propeller combination as a single system.

6.5 TESTING AND CHARACTERIZATION OF MOTOR-PROPELLER

The motor-propeller combination was tested in a wind tunnel under conditions similar to those that the airplane would experience in actual flight. The equipment used for testing the Astro-05 motor with a variety of propellers is illustrated in Figure 6.23. The function of this equipment is as follows:

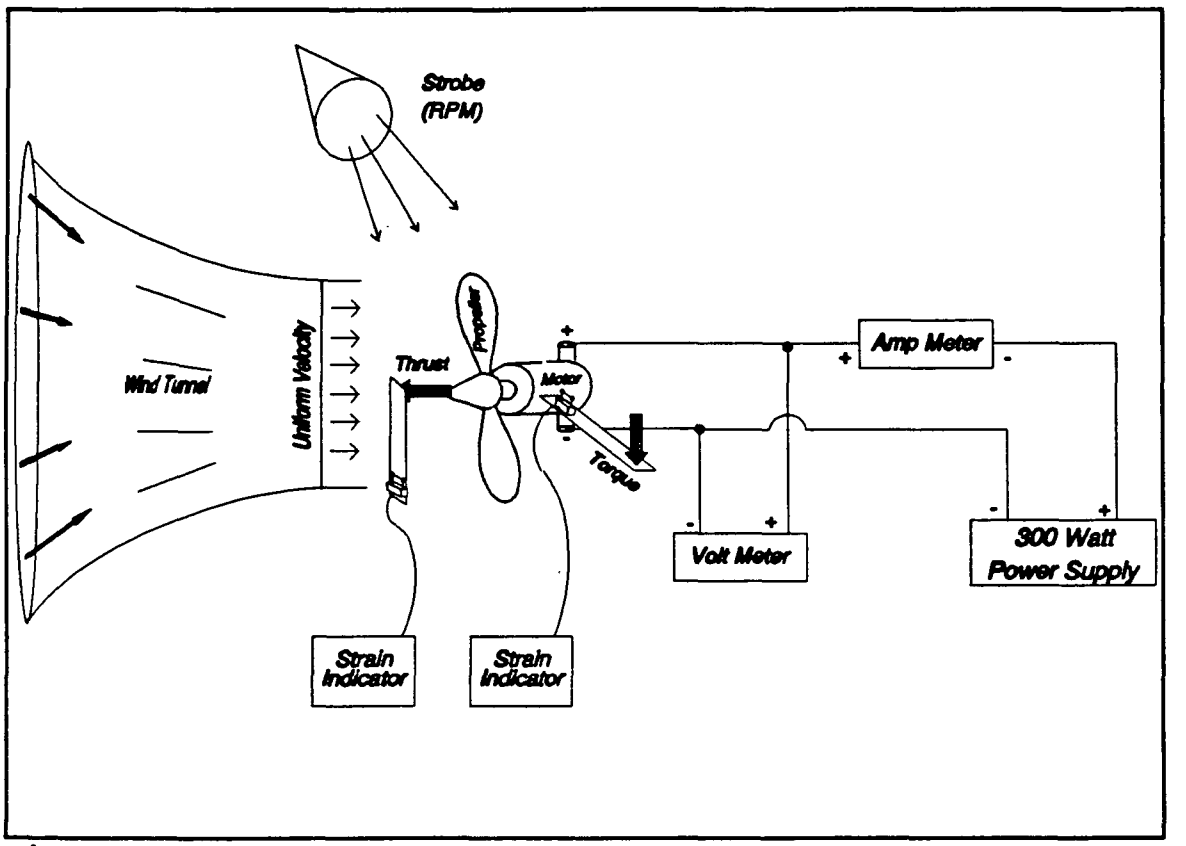

Figure 6.23: Motor-Propeller Test Setup.

Subsonic wind tunnel with an isolated 18inx18inx22in test section - used to generate airspeeds ranging from 3 to 9 m/s. This wind tunnel was equipped with a pitot tube which measures the static pressure in the test section. This allows us to calculate the freestream velocity in the test section.

1 Variable frequency strobe light - used to accurately measure propeller RPM which was converted into rad/s (ω).

1 300-Watt DC power supply - used to generate the required voltage and current for the DC motor.

2 Digital multimeters - used to measure terminal voltage (V_a) and current (I) into the DC motor.

1 Thrust/Torque stand - custom made test fixture which the motor-propeller system was mounted to, which in turn was mounted inside of the wind tunnel. This fixture used strain gauges to measure the bending deflection of two aluminum strips. The deflection of the two strips was directly proportional to the forces, Thrust and Torque, acting on these strips in the elastic regime (Young's Modulus).

2 Strain indicators - used to measure the strain of the thrust and torque strips on the test stand.

All mechanical and electrical losses associated with the motor-propeller system were taken into account by this test, especially the aerodynamic propeller losses. Of course, there is error associated with the equipment, but our equipment was calibrated after each individual propeller test. The strain gauges and indicators, which were our primary concern, were tested using known masses, and the errors were no more than one or two grams, which is well within reason. Another source of error was the wind tunnel velocity. The tunnel used for our experiments is designed to run at speeds up to 70 m/s so that one or two m/s error would not be significant. In our case, such an error would be significant. Based on information from the operators of the wind tunnel we added an additional 1 m/s to our calculated tunnel airspeeds.

The test was done by holding the wind tunnel at a constant airspeed, setting the power supply at maximum current draw, and incrementing the voltage from 0 to 8 V, in 1-V steps. Readings of voltage, current, RPM, thrust, torque, and airspeed (velocity) were recorded per increment. By setting the power supply's current at maximum, the motor was allowed to draw as much current as needed, as its terminal voltage was varied, thereby simulating the way the motor would work when powered

by the batteries alone, or batteries and solar array in parallel. Incidently, the Astro 05 motor is rated for 8.5 V, which was not exceeded during testing. Four or five trials per propeller were conducted, changing the tunnel airspeed each for trial and holding it constant throughout.

This test was conducted with three different propellers in order to determine the most efficient motor-propeller combination. The first test was done with an Aero-Haute 12"x7" folding propeller, the second with the Aero-Haute 13"x6.5" folding propeller, and the third with a 14"x8" fixed wooden propeller. The tabulated data for these propellers are found in Appendix D.3. The fixed wooden propeller, which is designed primarily for gas-powered model engines, was too heavy for our motor, and the 8" pitch also severely over-torqued the motor. The two Aero-Haute propellers, which are extremely light and are designed for electric motors, performed much better than the wooden propeller. The 13" Aero-Haute proved to be best suited to our motor; it was the most efficient propeller.

The following pages contain graphs of overall and individual motor and propeller performance based on our test, and they are all referenced as Figure 6.24. The wind tunnel was set at two airspeeds: 7.0 m/s and 8.7 m/s. This range of airspeeds was used because the velocity for level flight, determined by the Mission and Performance Group, falls between these two airspeeds at 7.2 m/s.

6.6 INTEGRATED PROPULSION SYSTEM

Let us look at the graph of shaft torque vs. RPM of Figure 6.24. Originally, the relationship of torque and RPM from the test did not correlate to that from the

Data for Aero-Haute 13"x6.5" Folding Propeller
Wind Tunnel Tested on 2/17/91

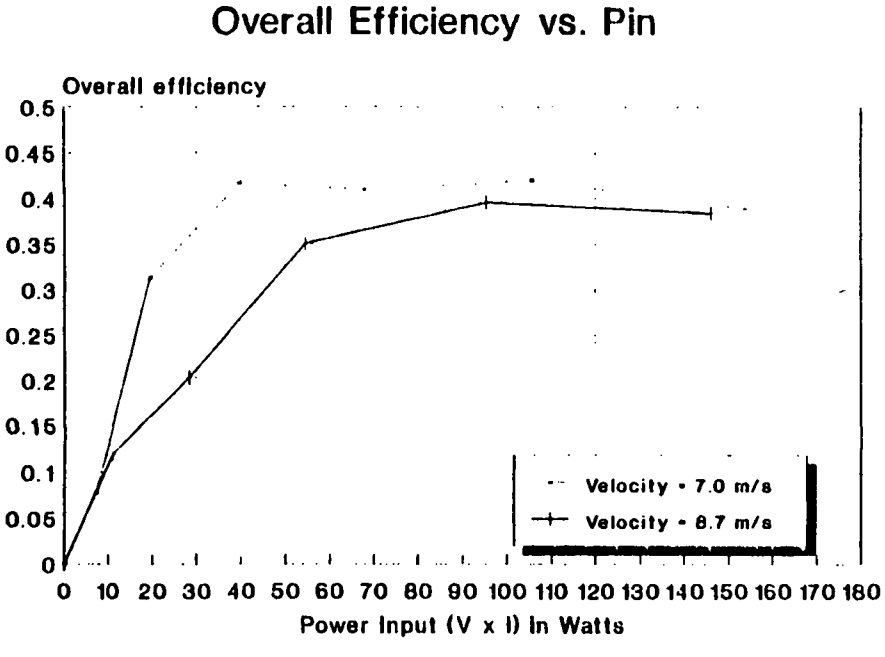

Figure 24a

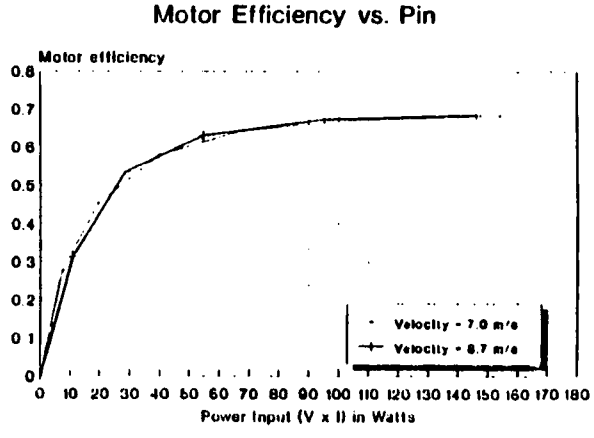

Figure 24b

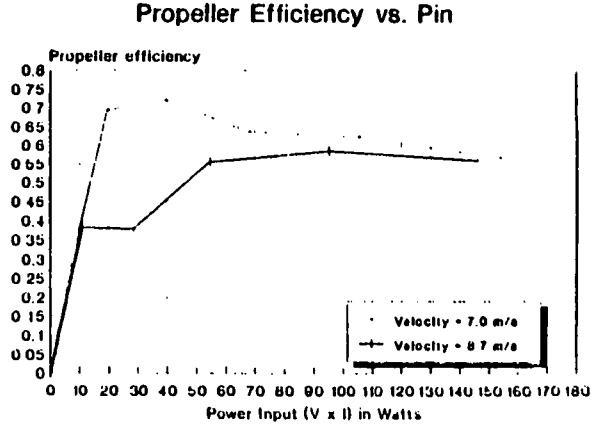

Figure 24c

Aero-Haute 13"x6.5" Folding Propeller (cont.)

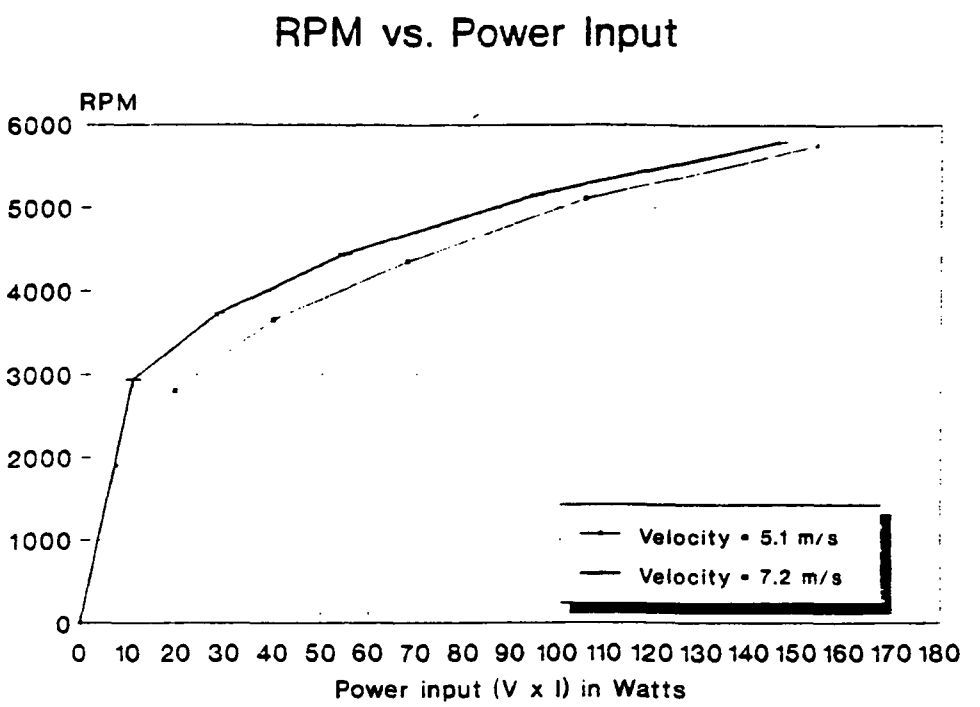

Figure 24d

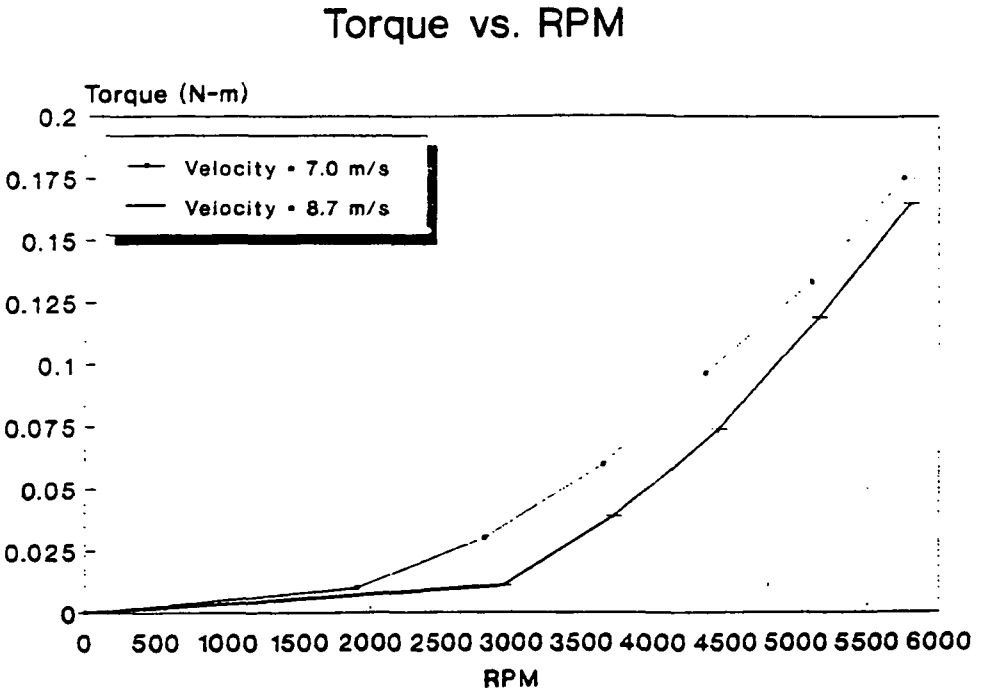

Figure 24e

motor characterization method. This is due to the fact that when the bearing on the motor's external reduction gearbox is put under the axial load from the propeller's thrust, the gearbox becomes inefficient by not transmitting all of the shaft torque to the propeller. The proportional difference of torque was taken, with respect to P_{in}, between the test data and motor simulation. That ratio, which was 0.88 (88 %), was applied to the shaft torque in the motor simulation program. Since motor efficiency is directly proportional to shaft torque, the motor's efficiency is also reduced by 12% in the simulation. This improved the correlation between the overall contour plot in Figure 6.16 with all of the information in the motor test plots. For example, if we compare a point on the plot of motor efficiency versus P_{in} with the intersection of the corresponding motor efficiency and input power contours of Figure 6.25, the two

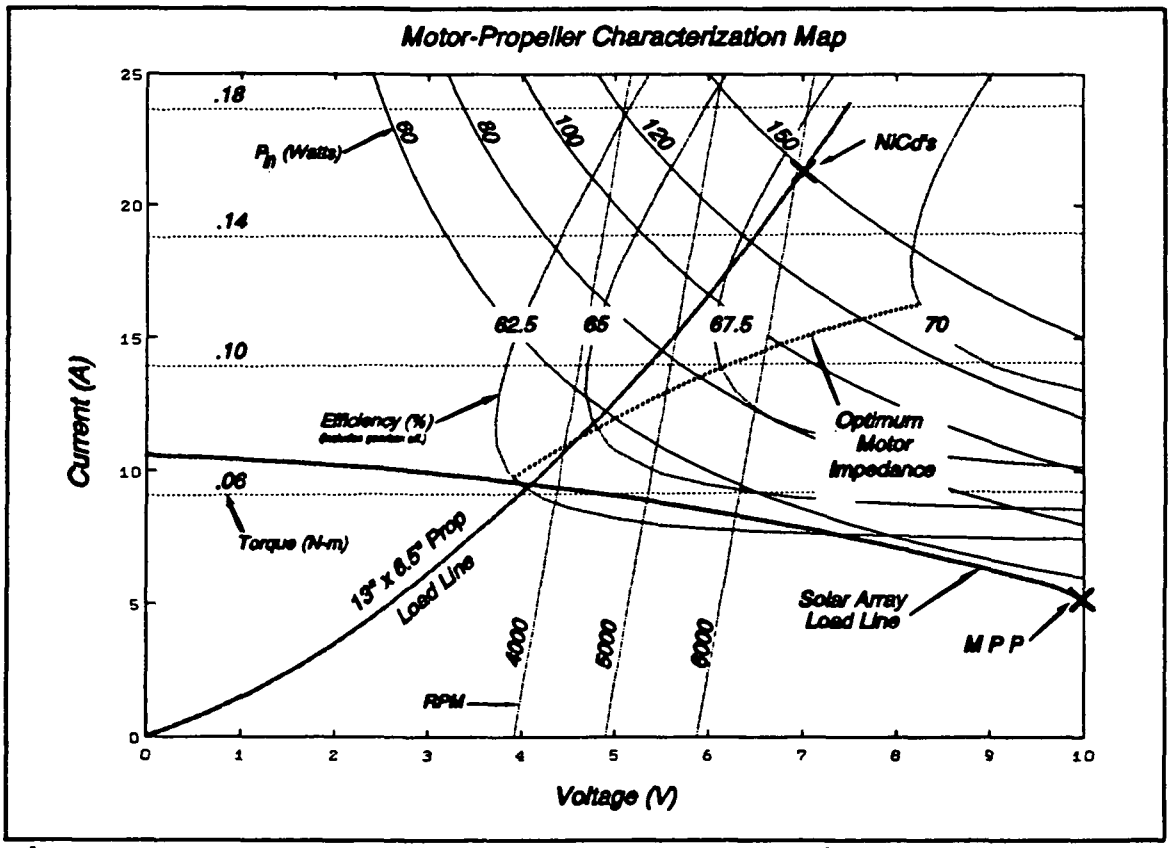

Figure 6.25: Motor-Propeller Map of Operating Ranges.

contours will intersect at the propeller load line. This load line represents the actual

voltage and current (impedance) of the motor recorded during our test of the motor-propeller system. This load line is dependant upon the type of propeller being used and the airspeed.

The objective is to choose a propeller that renders a load line that best correlates with the optimum impedance of the motor. Of course, it is almost impossible to find a propeller that will give a load line superimposed on the optimum impedance, but it is possible to select a propeller which minimizes the load line deviation for a selected motor. If a pitch changing mechanism were used, propeller performance could then be optimized through either active or passive control. By designing a propeller such that its maximum efficiencies occur at RPM's that correspond with the motor's optimum efficiencies, the propeller load line would more closely follow the optimum impedance curve for that motor.

Our aircraft's entire powerplant can be represented by one plot of the motor characteristics with the load lines of our propeller and solar array overlaid on this plot, as shown in Figure 6.25. When operating at a selected electrical input power, which can be controled with a speed control (section 6.7), we can use Figure 6.25 to find the values of RPM, shaft torque, and motor efficiency at the intersection of the desired input power contour and motor load line. The motor will follow this load line at any input power, while the plane is flying between 7.0 and 8.7 m/s with the Aero-Haute 13"x6.5" propeller. The other propeller characteristics, i.e. thrust and efficiency, and the overall performance of the motor-propeller system can only be found in the test plots of Figure 6.24.

Finally, the overall output power from the propeller, for two airspeeds, as a function of electrical input power into the motor is shown in Figure 6.26. This graph

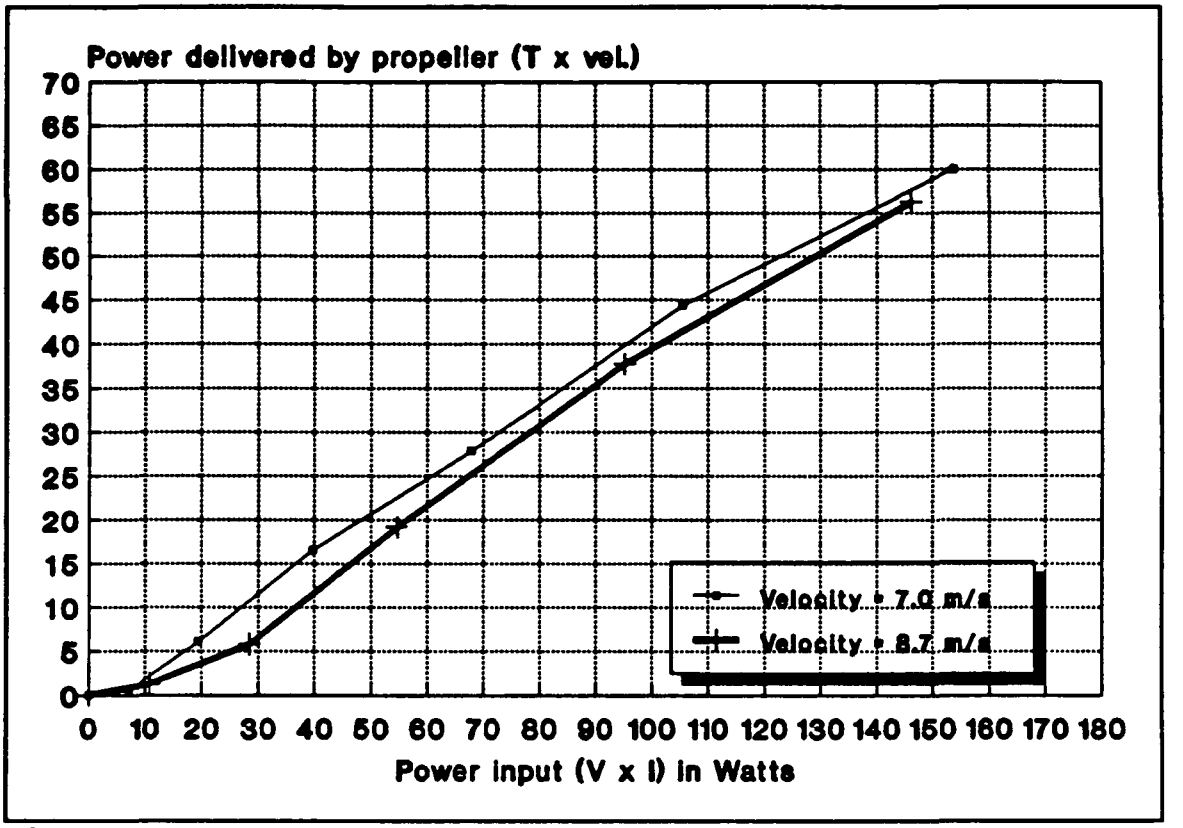

Figure 6.26: Output Power vs. Input Power.

uses the test data described in the previous section. Given the power required to fly the airplane (thrust x airspeed) at level flight or at any climb rate, this plot tells us the electrical input power required to generate that output power.

The motor's voltage and current requirements for the required input power can be extrapolated from Figure 6.25, and with that input power, one can find the flying power from Figure 6.26. The maximum power that the propeller can deliver is 58 W, using a fully charged NiCd battery pack. While powered soley by the NiCd pack, the powerplant can sustain 58 W output for aproximately two minutes. The solar array is set up with 3 sets of 25 solar cells in series and 1 set of 23 in series, with the four sets parallel to each other, so that the array's maximum power point (MPP) will provide a high enough voltage to charge the 8.4-V NiCd battery pack. The current into the battery pack will vary, of course, due to changes in incidence

angles. The solar load line in Figure 6.25 is a well estimated curve of array performance for a certain orientation of the aricraft and a certain solar day and time: the aircraft is climbing away from the sun, at 6° relative to the horizontal, on April 27, 1991 at 12:00 PM. This curve will vary continuously as the aircraft changes orientation. Using direct solar power to drive the motor, with the NiCd's open circuited, will provide a maximum flying power of 19 W. This corresponds to the point where the solar array load line and the propeller load line intersect in Figure 6.25.

This concludes our discussion of the airplane's powerplant. Our goal was to devise the most efficient overall propulsion system. This task was not trivial because of the complexity of optimizing the three subsections to work together. Each section had its own optimal operating points. The ultimate objective was to integrate the three subsections so that the final power output, from the propeller, utilized the highest efficiencies of each subsection.

6.7 CONTROLS AND INTERFACE SYSTEM

The Controls and Interface System of our airplane consists of a slightly modified remote control radio system and the necessary hardware for controlling deflecting surfaces and switches via servo-motor. The radio transmitter, receiver and servo-motors used are manufactured by Futaba, Inc. The Futaba Model FP-T7UAP 7-Channel radio and receiver were used. Of the 7 open channels, only 5 were needed in this airplane; one for switching input power modes and four for the control surfaces. The controls layout is shown, with some detail, in Figure 6.27. The receiver

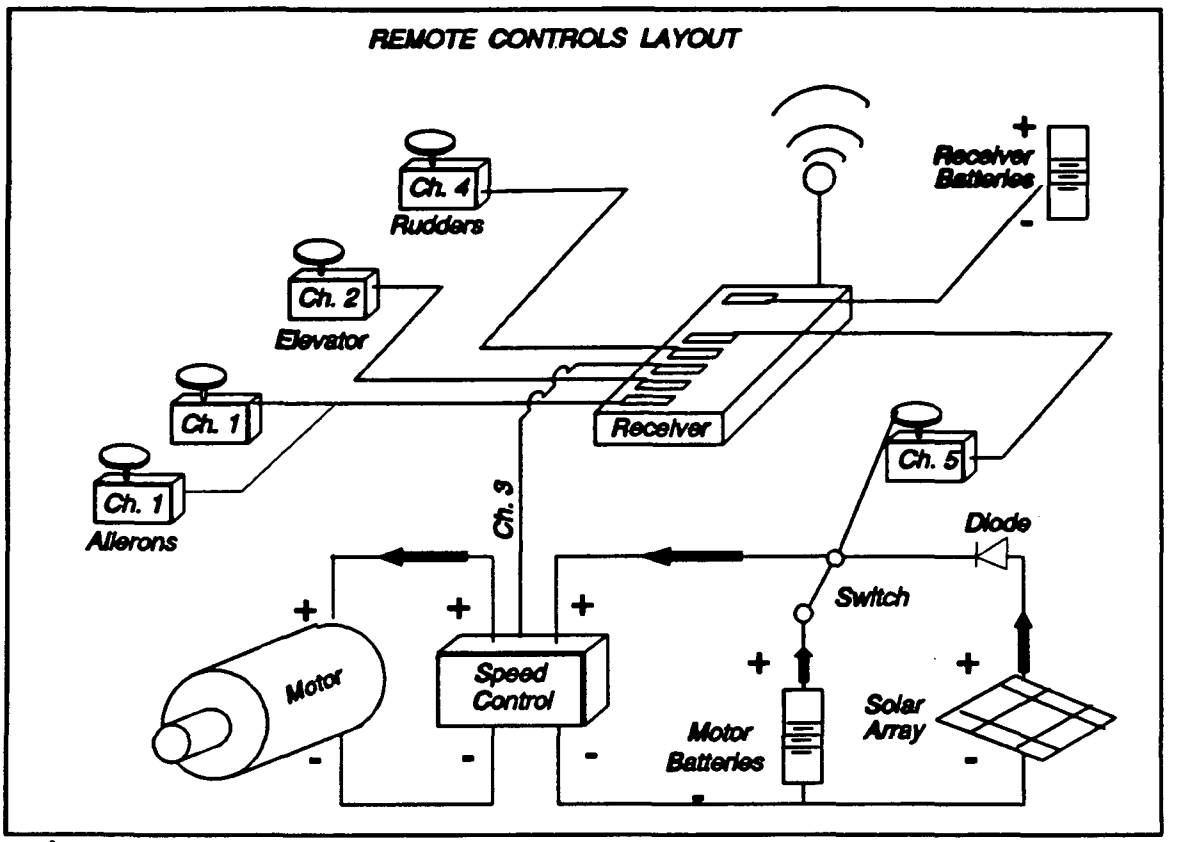

Figure 6.27: Controls Layout.

batteries are not in the solar circuit due to the possibility of complications in controlling the aircraft.

6.7.1 Modes of Operation

Let us first discuss the power circuit involving the solar array, NiCd's, speed control, and DC motor. The speed control is a device that regulates the amount of current that is allowed into the motor. In effect, it is an electronic throttle. The speed control used in the airplane is manufactured by Rhobart, Inc. and is rated to be 98% efficient. When the speed control is at "full throttle," it allows all available current from the input power source, batteries alone or batteries and array, pass into the motor. When it is at "0 throttle," it doesn't allow any current pass.

This power circuit enables three modes of operation. The solar cell array has a diode in series with the rest of the power circuit which prevents current from passing back into the array. In addition to this, the speed control disallows current to pass into the motor when it is shut off. Therefore, when the remote switch in the circuit is manually activated so that the NiCd's are parallel to the solar cells, the solar array will attempt to charge the NiCd's, provided that the array has a high enough voltage and produces sufficient current to effectively charge them in the few minutes required. This is one mode. A second scenario occurs when the NiCd's are in the circuit parallel with the array with the speed control directing electricity into the motor. The solar cells are still charging the batteries somewhat, but they also directly supply the motor with electricity. Both the array and the NiCd's now power the plane. This constitutes a solar-assisted operating mode. Thirdly, when the connection to the NiCd's is open, by remotely actuating the switch, and the solar array is the only input power source, the airplane is in the truly solar-powered mode.

6.7.2 Control Surfaces

The aircraft configuration uses two rudders, an elevator and ailerons. The very basic control surface requirements for a small scale remote control sailplane are one rudder and an elevator. Our configuration, being of larger scale than normal, required two rudders for controlling yaw stability, an elevator for climb and descent, and ailerons for roll stability and banking. The receiver can handle up to two servos per channel, however, the more servos used, the faster the receiver batteries discharge. We can see from the diagram that there is one servo for the two rudders,

two servos for the ailerons, and one for the elevator. Each of the aileron servos is mounted in the location of the aileron itself to ensure that the maximum servo torque is transmitted directly to the aileron and not dissipated by complex linkages. Similarilly, the elevator and rudder servos are mounted in the horizontal stabilizer to deliver maximum torque to the surfaces. No tests were conducted to determine the amount of control surface deflection and torque was required for maneuvering the airplane. However, with previous expertise in radio-controled aviation, the control system designers used their intuition to determine the amount of surface deflection required to maneuver the aircraft effectively.

6.7.3 Electro-Magnetic Interference

There are signal interferance problems associated with having extended wire leads from the receiver to the servos. When these leads are longer than 25 or 30 cm, the servos may pick up noisy signals from the surroundings, motor or speed control. If large enough, this interferance may cause uncontrollable oscilation, resonance or "glitching" by the servo. Shielding the leads from electro-magnetic interferance (emi) is one way to avoid problems. Another option is to place capacitors across the motor terminals and/or the speed control to avoid voltage spikes while the motor is running. Before flight testing the airplane, without solar cells, the airplane's controls and motor were ground tested several times according to the specifications given by Futaba, Inc., for the radio we used. With the transmitter antena fully retracted, the controls' response was tested from 30 meters away. There was no glitching or lag in servo response.

CHAPTER 7

PERFORMANCE

7.1 LEVEL FLIGHT

When an airplane is in steady level flight, all of the forces acting on the craft are in a state of equilibrium. This requires the lifting force to be equal to the weight of the aircraft, as shown in Equation 7.1.

$$L=C_l\frac{\rho}{2}V^2S=W \tag{7.1}$$

where:
- L = Total aircraft lift
- W = Aircraft Weight
- C_l = Wing lift Coefficient
- V = Velocity
- S = Wing Planform Area
- ρ = Air density

This force is a combination of the lifting contributions of the wing, tail, and fuselage. For the analysis of the solar plane design, the minimal lift provided by the pod fuselage section has been excluded. By manipulating Equation 7.1 and accounting for both the wing and tail lift contributions, we can calculate the absolute minimum velocity required for level flight, which is shown in Equation 7.2.

$$V_{min}=\sqrt{\frac{2L}{\rho\,(C_{l_w}S_w+C_{l_t}S_t)}} \tag{7.2}$$

where:
- C_{lw} = Wing lift coefficient
- C_{lt} = Tail lift coefficient

S_w = Wing planform area
S_t = Tail planform area

This minimum velocity can only be achieved when the airfoil lift coefficient is at its maximum design value. Substituting the appropriate values from the solar aircraft design, yields an absolute minimum flight velocity of 6.38 m/s

Equation 7.3 shows that in addition to the lift-weight relationship, the thrust of the aircraft must be equal to the overall aircraft drag.

$$D=C_d\frac{\rho}{2}V^2S=Thrust \qquad (7.3)$$

where:
D = Aircraft Drag
C_d = Airplane Drag Coefficient

The aircraft drag coefficient, Equation 7.4, is a

combination of the induced drag due to lift and the "parasitic" skin friction drag.

$$C_d=\frac{C_l^2}{\Pi Ae}+C_{d_p} \qquad (7.4)$$

where: A = Aspect Ratio
e = Oswald Airplane Efficiency Factor
C_{dp} = Parasitic Drag Coefficient

The first term of this equation shows that as the lift coefficient increases, the drag also increases. In order to keep the induced drag to a small level while still providing lift, one can employ an aircraft with a high aspect ratio as in the design of the solar powered aircraft.

Parasitic drag is caused primarily from skin friction resulting from the air flow over the exposed aircraft surfaces. To calculate the parasitic drag coefficient, it is

necessary to sum each component's drag contribution to the overall parasitic drag as shown in Equation 7.5.

$$C_{d_p} = \sum \frac{K_i C_{f_i} S_{wet_i}}{S_{wing}} \qquad (7.5)$$

where: K_i = a correction factor which is a function of length to diameter, which takes into account pressure drag and increased local velocities (Shevell, 1983).

S_{wet} = the component surface area which air flows over.

S_{wing} = the wing planform surface area, which is used as a reference area.

C_{fi} = Skin Friction Coefficient

In order to determine the skin friction coefficient, it is necessary to establish the air flow as either laminar or turbulent over the exposed surfaces. In the solar aircraft design, the flow over most aircraft surfaces can be considered turbulent due to separation over the wing and tail surfaces. The turbulent skin friction coefficient is given by Equation 7.6.

$$C_f = 0.455 (\log_{10} Re_x)^{-2.58} \qquad (7.6)$$

where: Re_x = Reynold's Number

The previous equations demonstrate a precarious balance between lift and drag in aircraft design. Increasing the lift coefficient to lift excess weight, or increasing the aircraft velocity, will result in much higher drag. To overcome this increased drag more thrust will then be required to maintain steady level flight. The design for the solar plane needed to keep the thrust required to a minimum while

still providing the necessary lifting force. In order to accomplish this, the aircraft operating velocity, of 7 m/s, remained very close to the minimum flight speed. This yielded the slow, glider-type configuration. To reduce the minimum flight speed to 6.38 m/s, the structural design was trimmed to its lowest feasible weight. In addition, a high aspect ratio of 8.25 was used to further reduce the induced drag. The aspect ratio is the ratio of the aircraft wingspan to the wing chord length. In order to assist in the iteration process, the performance group developed a program to calculate minimum flight speed, and required power for a variety of operating conditions. This program can be found in Appendix A.4. In order to execute the performance program, it is necessary to input several aircraft dimensional parameters in addition to the general operating conditions. The program will then calculate the minimum flight velocity, along with the necessary power for a range of aircraft velocities. Superimposing the required power with the available power from the propulsion system, yields a power curve as shown in Figure 7.1 below. By cross-referencing the desired velocity with the power curve the required power can be determined. For the desired operating velocity of 7 m/s the aircraft will need 15.9 W of power for level flight. Figure 7.1 also shows that a small increase in operating velocity substantially increases the required power.

7.2 CLIMB PERFORMANCE

Once it was established that the aircraft could perform the basic steady level flight, climb was examined. Our design goals specified that we attain an

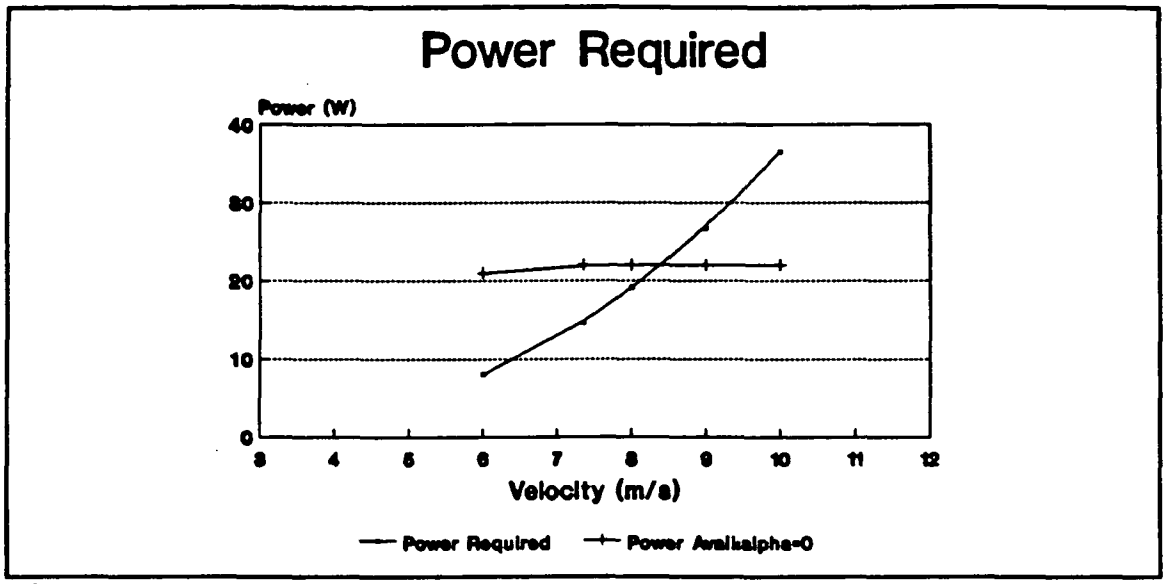

Figure 7.1
Power Required/Power Available

operating altitude of 50 m. The general equation for climb rate is the difference between the available engine power and the power required for level flight divided by the weight of the aircraft as shown in Equation 7.7.

$$\frac{dh}{dt} = \frac{P_{avail} - P_{req}}{W} \qquad (7.7)$$

The maximum excess power and thus the maximum climb rate would occur at the minimum aircraft velocity. Adding a 10% safety factor on the minimum velocity we determine that the appropriate climbing velocity is 7 m/s. From the power calculations in the above section, we determined that the required level flight power is 15.9 W. Because of the solar cell arrangement on the wings, the plane receives different levels of available power depending if it is flying towards or away from the sun. When the plane is flying away from the sun there are 20.6 W of power yielding a possible climb rate of .155 m/s. If however, the aircraft is flying towards the sun

there are 18.73 W of power yielding a possible climb rate of .093 m/s. Knowing both the forward airspeed as well as the possible climb rate we can determine the pitch-up angle with respect to the given climb rate, shown in Figure 7.2.

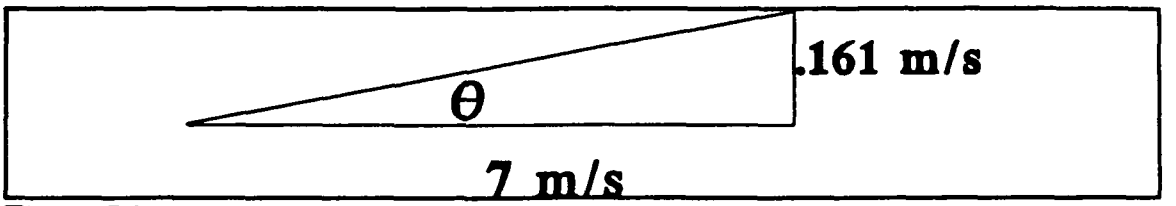

Figure 7.2
Angle with respect to velocity

Because of the solar array, it is then necessary to determine if the pitch up angle will increase or reduce available power. Because of the very small angles involved for the solar plane there was a negligible power change in both cases.

The small climb rates posed a problem. If the plane were to reach altitude through a straight line climb from takeoff it would take 2333.1 m. Because of this,

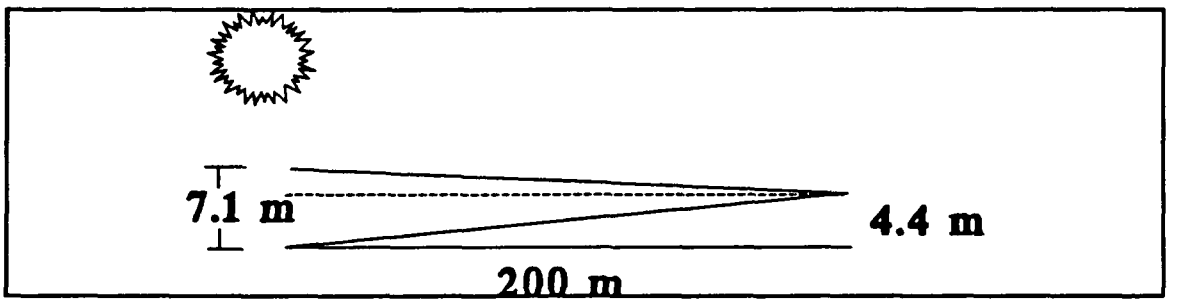

Figure 7.3
Circular Climb Pattern

we chose to use a circular climbing pattern, Figure 7.3, which would enable the plane to operate in a much smaller area. Utilizing this climbing method, one complete pass over a 200 m field, will result in a vertical climb of 7.1 m and takes 57 s. In

summary, to reach the design altitude of 50 m it takes 7.0 passes and a total time of 6.7 minutes. In the case of a battery assisted takeoff, the available power would be much greater, thereby reducing the time to climb substantially.

7.3 BANKING PERFORMANCE

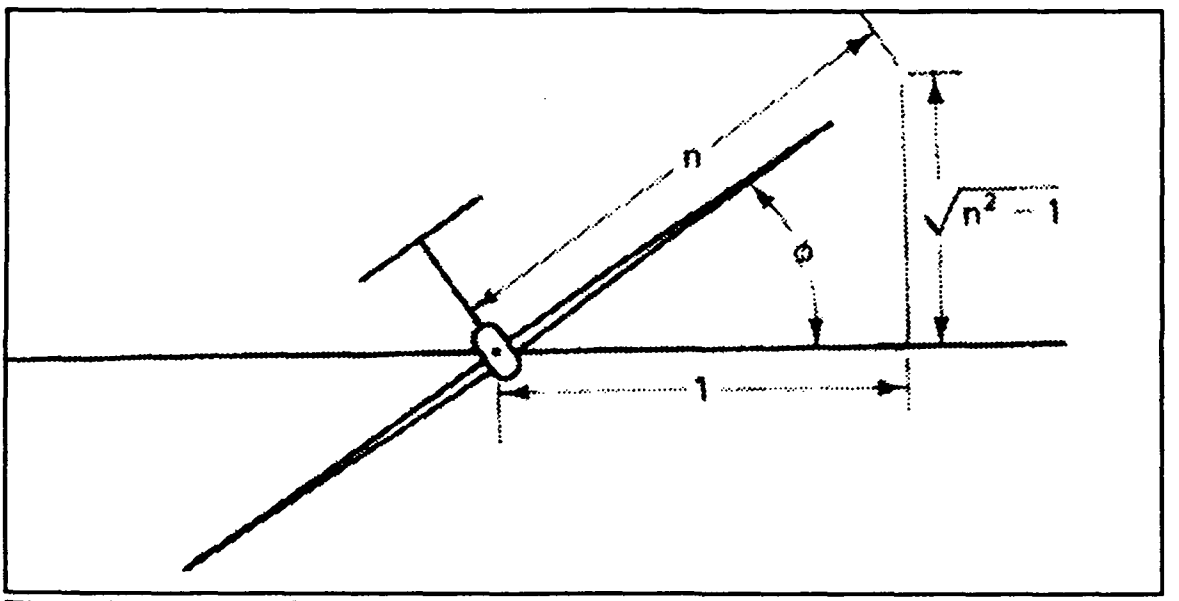

Figure 7.4 Banking Geometry

In addition to level flight and climbing performance it is essential to examine the banking performance of our solar powered aircraft. The mission definition specifies that the aircraft must be able to perform a sustained figure eight pattern at the design altitude. The geometry of a banking aircraft can be seen in Figure 7.4. In a turn, the lateral force must balance the centrifugal force on the plane. In a level turn the aircraft weight must be equal to the vertical lift component.

From this relation,

$$L\sin\phi = \frac{\left[\frac{L\cos\phi}{g}\right] V^2}{R} \qquad (7.8)$$

where : ϕ = bank angle
R = turning radius

we can specify a turning radius given both the aircraft velocity as well as the banking angle. One important factor, is the relationship between lift and weight. Since for a level flight turn,

$$W = L\cos\phi \qquad (7.9)$$

the required lift for a specified turning radius follows the relation,

$$\frac{L}{W} = \frac{1}{\cos\phi} = n \qquad (7.10)$$

which requires that the lift be greater than the weight by the ratio n. For this to occur the minimum aircraft velocity must increase. Because of this, it was essential that the designed banking angles remain as small as possible to allow the plane to maintain its slow flight speed. For our design we chose a banking angle of 4 degrees which yielded a turning radius of 79 m and did not increase operating velocity.

CHAPTER 8

STABILITY AND CONTROL

Once a design for an aircraft has been developed that will accomplish the prescribed mission statement, the stability of the design must be analyzed. This stability refers to the ability of the aircraft to return to its original equilibrium position, without pilot assistance, after its flight path has been disturbed. It is important to the future pilot that the plane is stable and has good handling qualities so that it can be easily controlled. Airplanes that require constant pilot control are not safe to fly and are tiring to the pilot, regardless if he is controlling the plane as a passenger or from the ground.

There are two types of airplane stability, static and dynamic. Static stability is achieved if the forces created by the disturbance return the craft to its original position. The plane will be statically unstable if these forces are too strong and cause the craft to overshoot this position. Dynamic stability deals with the entire history of a motion and is achieved if the motion is "damped," returning the craft to its original equilibrium, or trim, position. Though, designers strive to create stable airplanes, slight dynamic instability is acceptable as long as the control mechanisms, such as the aileron, elevator, and rudders, can correct the motion.

Free motion of an aircraft is very complicated, so to simplify the analysis, the airplane will be considered a rigid body with six degrees of freedom. An XYZ coordinate system is fixed at the center of gravity of the airplane and moves with it.

The craft can experience small deviations in roll about the x-axis, in pitch about the y-axis, and in yaw about the z-axis as seen in Figure 8.1. These motions are divided into two groups, lateral motions and longitudinal motions. The lateral motions include pitching motions, while longitudinal motions include rolling and yawing. These two groups can be analyzed separately because changes in the longitudinal motions have no effect on the lateral motions and vice-versa.

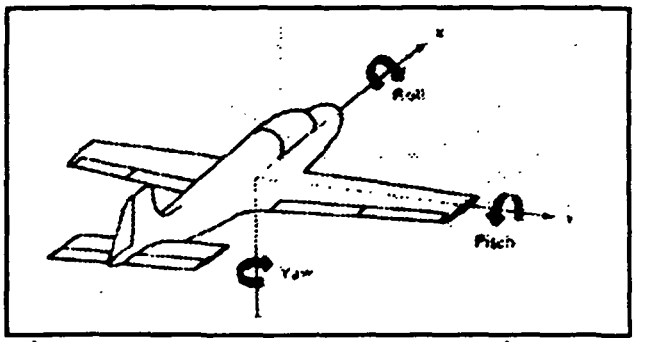

Figure 8.1: Axes for Aircraft Analysis.

8.1 LONGITUDINAL MOTIONS

8.1.1 Static Longitudinal Stability

While an airplane is in flight, it is subjected to wind gusts in every direction. If it is hit by a gust that effects its motion in the longitudinal direction, the angle of attack of the aircraft will change. As the angle of attack of an aircraft changes, the lifting forces and the moment about the center of gravity also changes, causing the craft to deviate from its trim position. If this moment increases with the increase of angle of attack and lift, the nose of the plane will begin to pitch up. As these values continue to increase, the nose will continue to pitch up because no restoring force is present to return it to the trim position. This in an example of an unstable airplane. For the plane to be stable, the rate of change of the pitching moment with the lift

must be negative. This means that as the lift increases, the pitching moment decreases providing the necessary restoring force.

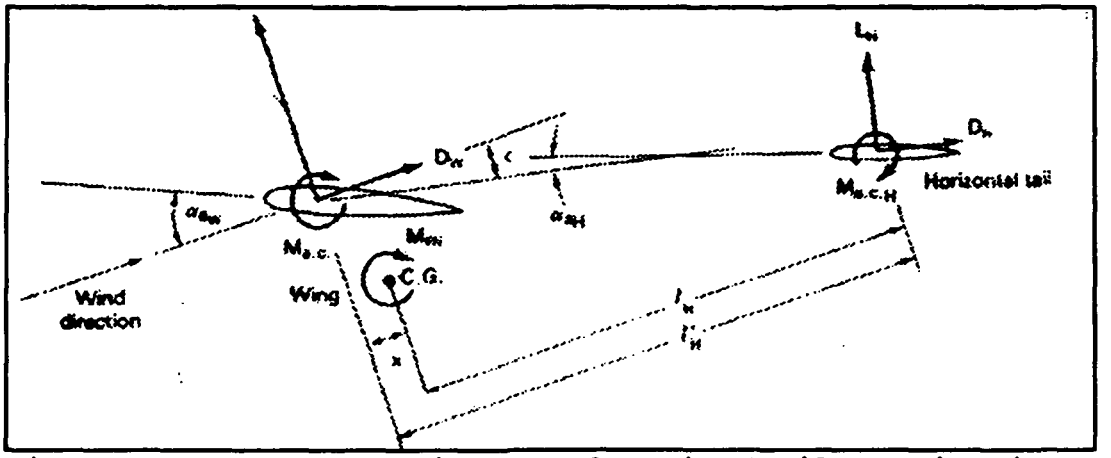

Figure 8.2: Freebody Diagram of a Wing/Tail Combination.

To evaluate the rate of change of the pitching moment with lift, the moments about the center of gravity must be summed. Examining Figure 8.2, the equation becomes:

$$M_{cg}=M_{ac}+L_W x-L_H l_H+M_F$$

Converting this equation into coefficient form and differentiating it with respect to the coefficient of lift of the wing gives the rate of change of the pitching moment coefficient with coefficient of lift of the wing. This equation is then expanded to give the rate of change of the pitching moment with the total airplane lift (Shevell, 1983):

$$\left(\frac{dC_m}{dC_l}\right)_{cg}=\frac{x}{c}-\left[\frac{(dC_l/d\alpha)_H}{(dC_l/d\alpha)_W}\left(1-\frac{d\varepsilon_H}{d\alpha}\right)\frac{S_H}{S_W}\frac{l_H}{c}\eta_H+\left(\frac{dC_M}{dC_{l_W}}\right)_F\right]\times$$

where:

$(dC_M/dC_L)_{cg}$ = rate of change of the moment coefficient

$$\left[\frac{1}{1+\frac{(dC_L/d\alpha)_H}{(dC_L/d\alpha)_W}(1-\frac{d\epsilon_H}{d\alpha})\frac{S_H}{S_W}\eta_H}\right]$$

with lift coefficient about the center of gravity.

x/c = location of the center of gravity with respect to the aerodynamic center.

$(dC_L/d\alpha)_H$ = lift curve slope of horizontal tail.

$(dC_L/d\alpha)_W$ = lift curve slope of wing.

$(d\epsilon_H/d\alpha)$ = rate of change of the downwash with angle of attack.

S_H = wetted area of the horizontal tail.

S_W = planform area of the wing.

l'_H = distance from the aerodynamic center of the wing to the aerodynamic center of the tail.

c = mean chord of the wing.

η_H = tail efficiency, the ratio of the effective dynamic pressure over the horizontal tail to the freestream dynamic pressure.

$(dC_M/dC_{Lw})_F$ = contribution of the fuselage to the rate of change of the moment coefficient with lift coefficient: value is calculated in Appendix A.2.

The derivation of Equation 8.2 can be found in Appendix A.1.

In the design of the solar powered plane, the variables that can change in each iteration are x/c, the location of the center of gravity with respect to the aerodynamic center; S_H and S_W, the areas of the wing and tail; and l'_H, the distance from the wing

aerodynamic center to the tail aerodynamic center. The other variables are characteristics of the wing, tail or the fuselage, and these elements of the plane are used as the basis for the design.

Of these four variables, the area of the wing is determined first. This value is dependant on the aerodynamics of the chosen airfoil and on the characteristics of the solar cells that are to be used as the power source. Using an initial weight estimate, power calculations are used to determine how much power is necessary for flight, and this is compared to the amount of power available from various solar cell arrangements that will fit within the airplane design. Once the size of the wing is set, the three other variables are determined simultaneously through iteration. The area of the tail and the distance that it was away from the wing determine the location of the center of gravity. Values are assumed, and then Equation 8.2 is used to determine if the corresponding configuration has static longitudinal stability. If the equation results in an negative number, the configuration is stable, and the stability analysis is continued.

Using the appropriate values for the solar powered plane, Equation 8.2 yields -.1415 as can be seen in Appendix A.1. This value shows that the design has static longitudinal stability.

8.1.2 Dynamic Longitudinal Stability

To study the dynamic longitudinal stability, all of the longitudinal motions of the airplane must be analyzed.

These motions, created by a disturbance of the equilibrium flight path, are characterized by two oscillatory modes of motion, the long period, also called the phugoid period, and the short period. These two modes are studied by modeling the airplane's motions as ordinary second order differential equations. These are then solved to find the damping ratio and frequency of each mode. From these values, the stability and controllability of the plane can be determined.

The damping ratio and the damped natural frequency are the two values that determine the amount of stability of the airplane. The damping ratio is a measure of the dissipation of the energy of the motion caused by the disturbance. A highly damped system returns quickly to the equilibrium position and is called the short period. The long period mode is only slightly damped and returns very slowly, oscillating about the equilibrium position. The damped natural frequency can be found using the damping ratio and the natural frequency as follows:

$$\omega = \omega_n \sqrt{1-\zeta^2}$$

where:

ω = Damped natural frequency.

ω_n = Undamped natural frequency.

ζ = damping ratio.

The damped natural frequency is then used to determine the time period of each oscillation.

For a design to be dynamically stable it must have positive damping, and it must return to its equilibrium position within the required time period. This period

varies for different types of planes, depending on the necessary performance levels. Negative damping causes the energy of the motion of increase, and therefore causes the motion to grow until the plane goes out of control.

The second order differential equation of the plane's motion is derived from Newton's second law. By summing the pitching moments about a constrained center of gravity, and then expanding the moments in terms of the variables of the disturbance the equation becomes:

$$\lambda^2-(M_q+M_{\dot{\alpha}})\lambda-M_\alpha=0$$

where:

M_q = Moments due to the dynamic pressure.

$M_{\dot{\alpha}}$ = Moments due to the rate of change of the angle of attack.

M_α = Moments due to the angle of attack.

The derivation of this equation can be found in Appendix A.3.

This equation can be compared to a standard second order differential equation,

$$\lambda^2+2\zeta\omega_n\lambda+\omega_n^2=0$$

and the damping ratio and the natural frequency can be found,

resulting in:

$$\omega_n=\sqrt{-M_\alpha}$$

$$\zeta = \frac{-(M_q + M_{\dot{\alpha}})}{2\sqrt{-M_\alpha}}$$

where:

ω_n = damped natural frequency

ζ = damping ratio

These three equations are the general equations that govern the dynamic longitudinal stability analysis. To analyze the two modes of motion, the long and the short periods, the equations are rederived using the appropriate assumptions as can be seen in Appendix A.3.

The resulting equations for both modes are as follows:

$$\omega_{n_p} = \sqrt{\frac{-Z_u g}{u_0}}$$

$$\zeta_p = \frac{-X_u}{2\omega_{n_p}}$$

Long Period Equations

$$\omega_{n_{sp}} = \sqrt{\frac{Z_\alpha M_q}{u_0} - M_\alpha}$$

$$\zeta_{sp} = -\frac{M_q + M_{\dot{\alpha}} + \frac{Z_\alpha}{u_0}}{2\omega_{n_{sp}}}$$

Short Period Equations

where:

u_o = Velocity of the plane.

Z_u, $Z_{\dot{\alpha}}$, X_u, M_q, $M_{\dot{\alpha}}$, M_α = Motion derivatives.

These derivatives are functions of motions coefficients and the characteristics of the airplane. The variables that can change with each iteration in these equations are the distance from the wing to the tail and the location of the center of gravity. If the results of an iteration determine the plane to be dynamically unstable, these values are adjusted, and then the analysis is run again. This is repeated until the design is stable, and then the new values are analyzed for static stability.

The design of the solar powered plane has dynamic longitudinal stability as is shown by the following values:

Long Period: ζ = .948 Period = 2.12 seconds

Short Period: ζ = .045 Period = 7.07 seconds

8.2 LATERAL MOTIONS

8.2.1 Static Lateral Stability

Lateral motion analysis is similar to the longitudinal analysis except that it includes motions in two directions, the yaw and the roll. For static lateral stability, the directional stability and dihedral stability of the airplane must be considered.

The directional stability of an airplane is its tendency to point into the oncoming airstream and is provided by the vertical tail (Shevell, 1983). A plane will rotate in the yaw direction, deviating from a straight path into the oncoming

airstream, if it is subjected to a lateral lifting force. This lift can be caused by the vertical tail, a deflection of the rudder, or by a lateral wind gust. In the design process, the tail must be designed to have the ability to control the airplane in such situations.

The vertical tail controls the airplane by generating a moment about the center of gravity in the yawing direction. The moments that need to be countered by the vertical tail are those created by the wing. These two types of moments are related by the tail and wing areas and by the moment arm of the tail. The tail effectiveness becomes a function of the tail area times its moment arm. This is then related to the span of the wing and leads to the vertical tail volume coefficient.

$$C_{vt}=\frac{L_{vt}S_{vt}}{b_w S_w}$$

where:

L_{vt} = distance from the wing quarter chord to the vertical tail quarter chord.

S_{vt} = area of the vertical tail.

b_w = wing span.

S_w = area of the wing.

For the solar powered plane, the vertical tail volume coefficient is .018. This is close to .02 which is the typical value for a sailplane (Raymer, 1989). This is a good approximation because the solar power design is being modeled after a sailplane to provide extra gliding capabilities.

Dihedral stability is achieved by adding a small positive dihedral angle to the wing, where a positive angle is formed when the tip of the wing is higher than the

root of the wing. This dihedral tends to return the airplane to its equilibrium position once it has been disturbed in the roll direction. As the plane begins to roll, the angle of attack of the section of the wing that is at the dihedral angle increases while the angle of attack of the rest of the wing decreases. This creates added lift on the tip which returns the craft to its equilibrium position.

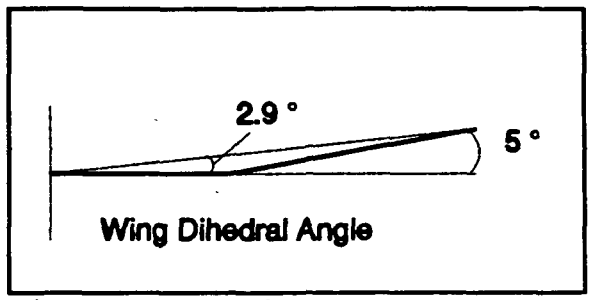

Figure A.3: Dihedral Angle for Helios'91 Design.

It is difficult to take everything into account when determining the necessary dihedral angle for a design. For a wing that is flat in the middle and has the dihedral only on the outer sections the dihedral angle should be estimated so that it places the wing tips as high as they would be for a dihedral angle that starts at the root of the wing. The solar powered airplane is designed with this type of wing, with a the flat center section of one and a half meters and two wing tips of one meter in length that are angled up 5 degrees on each side. This five degree angle places the tip of the wing at the same height that a straight line drawn from the root of the wing to its tip at a 2.9 degrees angle would, as can be seen in Figure A.3. A guideline for airplanes whose wing is aligned with the rest of the plane, not above or below it, is a dihedral angle of 2 to 4 degrees (Raymer, 1989). This makes the solar powered plane's dihedral angle a good estimation.

8.2.2 Dynamic Lateral Stability

Dynamic lateral stability can be dealt with in the same manner that longitudinal stability is in the preceding section. The rolling and yawing motions can be modeled as second order differential equations, but a problem arises with the force and moment derivatives. In the lateral case, there are fewer derivatives that can be safely neglected from the equations. This in coupled with the fact that reliable values for these derivatives can only be obtained through special experiments which require a complete model of the airplane design (Von Mises, 1959). Due to these circumstances a complete analysis of the dynamic lateral stability is difficult to perform. The two types of lateral dynamic motions, the spiral mode and the Dutch Roll, can be controlled, though, using control surfaces such as the ailerons and the vertical tail.

The spiral mode occurs when the aircraft gets caught in a turn where the banking angle increases, turning the airplane tighter and tighter each time. This is a slow process though, so the pilot has sufficient time to correct the motion before all control is lost.

The Dutch Roll is a condition where the plane yaws and rolls to one side then to the other side, each time overshooting the equilibrium position. This motion is controlled using the vertical tail. To ensure that the vertical tail has the ability to provide this control, it's size should not be reduced below the size determined using the vertical tail volume coefficient unless wind tunnel tests can be performed to obtain reliable dynamic derivatives (Raymer, 1989). The vertical tail volume

coefficient of the solar powered plane has not be changed, so the airplane should have the necessary dynamic stability in this direction.

CHAPTER 9

CONSTRUCTION PROCEDURE

9.1 WING CONSTRUCTION

The construction of the wing is crucial to the completion of our objectives, since a majority of the plane's lift originates at the wing. Also, it is important that the wing construction be as light as possible since it is the largest component of the aircraft. Additionally, the wing must be and stiff to prevent large deflections and subsequent damage to the imbedded solar cells.

Considering these requirements, the wing is comprised of a balsa skeleton with a transparent mylar skin covering. Carbon fiber rods (spar caps) running the span of the wing are the major strengthening element in the wing. This spanwise spar is comprised of a 3.3 mm diameter carbon fiber composite rod inlaid on the top and bottom of the ribs at the quarter chord. Spar webs joining the two rods are made of balsa sheets 3.2 mm (1/8 inch) thick. The spar webs are cut in 101.6 mm (4 inch) lengths so that they may be placed between the ribs.

The ribs of the wing are cut from balsa 1.6 mm (1/16 inch) thick in the shape of the NACA 6409 airfoil. Balsa proved to be lightest while also being the easiest to form when compared to composite options. The ribs are spaced at 103.2 mm (4 1/16 inch) intervals allowing 101.6 mm (4 inches) of room for the solar cells.

The solar cells are 95.25 x 95.25 mm^2 (3.75 x 3.75 $inch^2$) wide, and 3.2 mm (1/8

inch) thick. They rest between the ribs and are braced from vertical deflection by foam strips glued to the ribs. Due to the delicate nature of the cells, they are not glued to the wing structure, thus allowing more freedom in the case of unexpected deformations. The cells lie on foam shelving which is glued to the surrounding ribs, and a smaller piece of foam is glued above the solar cell to prevent bouncing. Three cells lie between each rib, with one in the front and two towards the trailing edge. The front cell is separated from the rear two at the quarter chord by the spanwise spar and the spar webs.

The balsa leading edge of the wing is a store bought piece that was roughly a semicircle with a 15 mm (.6 inch) diameter extruded to a certain length. This piece is sanded by hand to a fine detail by intermittently running a template, from which the correct cross-section was cut, over the length and sanding smooth any discrepancies.

Similarly, a balsa trailing edge of the approximate desired dimensions was purchased at a local hobby store and sanded using the same techniques. The trailing edge is interrupted from running the span of the wing by two ailerons on the tips of the wing. The ailerons are each 450 mm (17.7 inches) in length and they rest flush against the tips of the wings. One micro servo controls each aileron.

The wing tips are made of foam since they are not integral to the strength of the wing, and the foam was measured to be approximately one sixth the density of the balsa. The foam is easily carved with a sharp knife and more finely detailed with sandpaper.

The entire wing is covered with the transparent mylar skin. The mylar is heated with an iron and a hot air blower so that the mylar shrinks to a tight fit. The mylar becomes taut between the airfoil ribs, thus keeping the shape of the airfoil while also adding to the structural integrity of the wing.

9.2 TAIL CONSTRUCTION

The tail has much in common with the wing. The tail, like the wing, consists of a balsa skeleton covered in transparent mylar, solar cells resting between the ribs, carbon fiber reinforcing spar caps, foam wing tips, and a NACA 6409 airfoil shape. However, the tail is smaller in scale than the wing.

Although the methods of construction for the wing and tail are identical, the sizing remains different. The tail experiences significantly lower loadings than the wing does, hence, it does not have to be built as strong as the wing.

The tail has a span of 1 meter (39.4 inches) and a chord of .3 meter (11.8 inches), as opposed to the wing's span of 3.5 meters (11.5 feet) and chord of .424 meters (16.7 inches). The tail has only one solar cell that rests between the ribs, as opposed to three for the wing. The solar cells in the tail, eight in all, lie behind the carbon spanwise spar and before the elevator. Also, the carbon spars for the wing are 3.3 mm (.13 inches) in diameter compared with 1 mm (.04 inches) in diameter in the tail. The spar webs connecting the carbon spars are 1.6 mm (1/16 inch) thick in the tail, half the thickness of those in the wing.

Instead of a trailing edge, the tail has an elevator which is 75 mm (3.0 inches)

thick and one meter (39.4 in) in length. To keep the weight of the elevator to a minimum, the elevator has its own leading and trailing edges, with balsa ribs keeping the airfoil shape every 101.6 mm (4 inches). This configuration cancels the need for a solid elevator. The elevator is controlled by two servos placed in the back of the tail.

A unique element to the tail are the vertical rudders. They rise 175 mm (6.9 inches) above the tail, occupy the aft 148 mm (5.8 inches) of the tail chord, and are situated at the tips of the tail. The frame of the rudders are 4.8 x 4.8 mm (3/16 inches)^2 balsa pieces. Within the pivoting portion of the rudder, the balsa pieces are also used to form a truss, thus helping the rudder maintain its shape. Foam fills the stationary segment of the rudder to keep the shape intact. Two balsa pieces from the stationary portion of the rudder extend downward and are sandwiched between two tail ribs, thus securing the rudder to the tail. Each rudder has a servo to control its motion.

9.3 MODULAR CONSTRUCTION

The plane has been designed in a modular fashion in order to facilitate transport, storage, and construction. The wing is separated into three sections; the middle section spans 1.5 m (4.9 ft), while the outer two sections are each 1 m (3.3 ft) long. The middle section is bolted to the outer sections through reinforced composite ribs. The NACA 6409 airfoil shaped ribs are cut from foam and covered on one side with composite carbon fiber weave. At the surface of contact of the two ribs, the

foam was cut at an angle of 5 degrees so the outer sections would act as dihedral for added stability. Three intermittently spaced bolts connect the ribs and also provide for easy disassembly. The bolts are fastened at the head by epoxy resin, because the solar cell placement will prevent access to one side of the ribs. Space was set aside on the other side of the rib joint to allow for tightening and loosening of the nuts. The force of the nuts and screw heads on the outer carbon surface of the ribs is dispersed partially by washers to avoid overly concentrated stresses at the bolt hole.

The ribs are connected to the wing structure at the leading edge, the trailing edge, and at the main spanwise spar. This ensures that while the ribs are attached to each other, that they are also secured to the wing structure.

The plane can be further broken down by removing the tubular tail supports from the wing and tail. These two carbon tubes are clamped to carbon reinforced ribs in the wing and tail. The clamps are plastic and have rubber inserts which provide sufficient friction to prevent the tube from any motion within the clamps. The clamps are bolted to composite ribs which are cut from foam and covered on both sides with carbon fiber weave.

9.4 FUSELAGE CONSTRUCTION

The fuselage was designed with several considerations in mind. The fuselage had to be long enough to position the center of gravity far enough forward to make the aircraft stable in flight. The fuselage was required to be large enough inside to

accommodate all of the necessary electronics, including motor batteries to power the plane during pre-solar testing and for back-up in case of solar power failure. The fuselage also had to be designed with the problem of how to connect it to the wing in constant consideration.

The fuselage of the aircraft was constructed from square balsa rods measuring 1/4" * 1/4" and 3/16" * 3/16". The longest rods were used for the longest members that span all the way from the trailing edge of the wing to the very front of the fuselage. These four larger rods form the corners of the fuselage. Zig-zagging in between the corner rods are the smaller rods. The angle between the smaller and the larger rods is approximately 45 degrees and the two sides of the fuselage. On the top and the bottom the smaller rods simply connect to the same points as the rods on the sides do in a zig-zag fashion. The fuselage floor was constructed from 1/8" balsa sheeting as it must support the weight of the electronics and the batteries. The sides and top of the fuselage were covered in the same mylar as the wing and tail. The top incorporated a balsa trap door making the electronics accessible. The motor was mounted in a solid block of balsa wood which formed the nose of the fuselage.

9.5 FUSELAGE/WING CONNECTION

The fuselage to wing connection is one of the critical joint areas of the aircraft. The fuselage not only carries considerable weight cantilevered almost a half meter from the wing, all of the critical components are contained inside. Therefore the fuselage to wing connection was conceived with strength being foremost in mind. The

fuselage will be connected permanently to the wing at three locations; the wing's leading edge, the main spar of the wing, and the trailing edge of the wing. These three connection points will be especially strengthened to withstand the moment created by the weight of the electronics being cantilevered. Along with these three connection points, the fuselage will be continuously supported along the entire chord of the wing by two wing ribs that will extend downward to form the sheeting on the aft portion of the fuselage.

9.6 LANDING GEAR

The Solar Powered Model Airplane has a single wheel located near the center of gravity to aid in the landing of the aircraft. This wheel is composed of a plastic wheel/hub surrounded by a foam rubber and plastic tire. The tire is somewhat flexible to absorb the bumps present on the grassy surface of the runway. The axle of the landing gear is a carbon fiber rod 3.3 mm (.130 in.) in diameter. The supporting structure of the wheel is built from balsa rods, hardwood dowels, and balsa sheeting. This structure is connected to the structure that comprises the underside of the fuselage.

They propeller of the aircraft is a folding type, to prevent damage during landings, since the landing wheel only will protrude from the aircraft approximately 10 cm (3.94 in.). The folding prop will also lower the aircraft's drag during gliding flight.

CHAPTER 10

ENVIRONMENTAL IMPACT

Recognition of environmental problems facing society, such as polluted air and water, the depleting ozone layer, and shortage of natural resources demands some consideration for the future. First, the causes must be considered, and next, various possible solutions must be developed, weighing the pros and cons of each.

Fuel sources such as gas and oil are harmful to the environment and rapidly decrease our natural resources, yet these fuels are used every day by many members of society. Currently research is being done in the areas of solar and nuclear energy. Solar energy is a very attractive and safe source of energy for various reasons, it is both cost efficient and ecologically harmless. Implementation of solar power into daily life is therefore beneficial to society.

The design of the Solar Powered Multi-Purpose Remotely Piloted Vehicle focused mainly on the feasibility of utilizing solar energy as a primary fuel source for an airborne vehicle and the environmental and economical advantages. The construction and flight testing seeks to verify the accuracy of the design procedure as well as provide inspiration and a model for futuristic aircraft.

Additional research and development into solar energy and other possible fuels is definitely a positive step for the environment, the development of science, and the future of the planet Earth.

CHAPTER 11

CONCLUSIONS & RECOMMENDATIONS

During the design and construction of the solar plane, Helio '91, various engineering problems were encountered. This provided the entire group with various tasks, sometimes extremely challenging, and others time consuming, but for the most part enjoyable. Every group dealt with different challenges, the most dominant being the design, selection, and construction of the various aircraft components and the aerodynamic, structural, and performance analysis.

The final design is a Multi-Purpose Remotely Piloted Vehicle (MPRPV) weighing 35 N which cruises 7 m/s at the design altitude of 50 m. The configuration includes a wing composed of balsa and foam NACA 6409 airfoil sections and carbon fiber spars, a tail of similar construction, and a truss structure fuselage. The propulsion system consists of 98 10% efficient solar cells donated by Mobil Solar, a NiCad battery for energy storage, and a folding propeller regulated by a lightweight and efficient control system. The airfoils and propeller chosen for the design have been researched and tested during the design process.

The design and construction of an aircraft requires many iterations, time and available resources limited the development of this project. With further research, development, and effective testing many of the obstacles encountered may be overcome. As in every design, improvements are always possible. The performance of a solar powered aircraft relies heavily on the efficiency of the propulsion system,

aerodynamic design, structural integrity, material selection, and overall weight. The current aircraft was restricted in the magnitude and development of the take-off and landing procedures as well. The efficiency of the propulsion system is dictated by its individual components, the solar cells, motor, and propeller. Selection of solar cells was limited to the solar cells donated by Mobil Solar due to both the availability of and demand for cells with higher efficiencies as well as budget constraints. Efficient, lightweight cells are now available at a considerable cost, and development of solar cells with even higher efficiencies is continually under research. A motor and propeller with a higher overall efficiency is another possible improvement to this design, additional wind tunnel tests on these components will help to determine the most efficient system. It is desirable to increase the performance parameters of this plane, such as the climb rate and velocity. Aerodynamically, an elliptical wing distribution would be ideal for this aircraft. While the current wing satisfies the design requirements, a wing with increased aerodynamic performance is a possibility. The available airfoil design codes were determined unreliable for the design flight regime. Very little experimental data for airfoils with Reynolds numbers between 150,000 and 200,00 was found and the few reliable test facilities were unaccessible. Additional study of low Reynold's number flow and airfoil design would benefit the overall configuration.

The final design includes a small wheel for landing, closer consideration to landing procedures is recommended in order to protect the aircraft from a destructive landing. This vital component of the plane was limited in extensiveness

by the weight budget. Alternative procedures for take-off are another possibility, currently take-off is limited to locations with smaller areas than desired and without a runway to speak of.

The size of the final design demanded that the plane be modular. This requirement added additional engineering challenges, constructing the plane modular without adding much weight became a feat in itself due to the fact that gross weight is a major performance factor. Connections were carefully developed using composite materials and fasteners which did not sacrifice the structural integrity while remaining within the weight budget.

The possibilities for a solar powered remote controlled airplane are limitless. The recommendations mentioned note the areas the project group felt most restricted during their design process, further study in these areas are encouraged. Hopefully this project will allow others the opportunity to utilize the results of this MQP to develop other designs.

REFERENCES

Abbott, I. and A. Von Doenhoff. 1959. Theory of Wing Sections. Dover Publications, Inc. New York.

Allen, D. and W. Haisler. 1959. Introduction to Aerospace Structural Analysis. John Wiley and Sons. WPI TL671.6 A38.

Blakely, L. January 1982. "Flying High With Solar Power." Model Aviation.

Boucher, R. July 10, 1985. Starduster: A Solar Powered High Altitude Airplane. AIAA-85-1449. AIAA/SAE/ASME 21st Joint Propulsion Conference, Monterey, CA.

Boucher, R. 1985. "Sunrise, the World's First Solar-Powered Airplane." Journal of Aircraft. Vol. 22, No. 10.

Buresch, M. 1983. Photovoltaic Energy Systems: Design and Installation. McGraw-Hill Inc., New York.

Cowley, M. June 18 1981. "Wings in the Sun: the evolution of Solar Challenger." Flight International.

Dommash, Sherby, and Connolly. 1969. Airplane Aerodynamics.

Duffie, J. and W. Buckner. 1980. Solar Engineering ofThermal Processes. John Wiley and Sons, Inc.

Eppler, R. and D. Somers. 1980. "A Computer Program for the Design and Analysis of Low-Speed Airfoils, Including Transition." NASA TM 80210.

Eppler, R. 1990. Airfoil Design and Data. Springer-Verlag. Berlin.

Hall, D. and S. Hall. (Lockheed Missiles & Space Co.). April 1984. StructuralSizing of a Solar Powered Aircraft. NASA-CR-172313. NASA Langley Research Center. Hampton, VA. Contract NAS1-16975.

Hoerner, S. 1958. Fluid Dynamic Drag. Published by author.

James, M. et. al. 1989. Vibrations of Mechanical and Structural Systems. Harper and Row. New York.

Kuethe, A. & C. Chow. 1986. Foundations of Aerodynamics 4th ed. John Wiley & Sons. New York.

Lissaman, P. 1983. Low-Reynolds-Number Airfoils. "Annual Review of Fluid Mechanics", Vol. 15.

Nelson, R. 1989. Flight Stability and Automatic Control. McGraw-Hill. New York.

Peery, D. and J. Azar. 1982. Aircraft Structures. McGraw-Hill. New York. WPI TL671.6 P4 1982

Perez, R. 1985. The Complete Battery Book. TAB Books, Inc. Blue Ridge Summit, PA.

Raymer, D. 1989. Aircraft Design: A Conceptual Approach. American Institute of Aeronautics and Astronautics, Inc. Washington D.C.

Rivello, R. 1969. Theory and Analysis of Flight Structures. McGraw-Hill. New York. WPI TL671.6 R53

Schlichting, H. 1979. Boundary-Layer Theory. McGraw-Hill. New York.

Selig, M., J. Donovan, and D. Fraser. 1989. Soartech 8: Airfoils at Low Speeds. H. A. Stokely Publisher. Virginia Beach, Virginia.

Shevell, R. 1983. Fundamentals of Flight. Prentice-Hall. Englewood Cliff, New Jersey.

Von Mises, R. 1959. Theory of Flight. Dover Publications, Inc. New York.

White, F. 1986. Fluid Mechanics. McGraw-Hill. New York.

NASA/USRA

SOLAR POWERED MODEL AIRCRAFT

APPENDICES

APPENDIX A

MISSION & PERFORMANCE

A.1 STATIC STABILITY EQUATION DERIVATION

For static stability, the rate of change of the pitching moment coefficient with coefficient of lift must be determined, and the result must be a negative number. The equation that will solve for this value is found by first summing moments about the center of gravity of the airplane. This results in Equation 8.1 from Chapter 8:

$$M_{cg}=M_{ac}+L_W x-L_H l_H+M_F \tag{1}$$

Expanding this into coefficient form gives:

$$M_{cg}=C_{M_{ac}} qS_W c+C_{L_W} qS_W x-C_{L_H} qS_H l_H \eta_H+C_{M_F} qS_W c \tag{2}$$

where:

q = dynamic pressure

S_W = wing planform area

c = mean chord of the wing

x = distance between the aerodynamic center and the center of gravity

S_H = wetted area of the horizontal tail

l_H = distance between the center of gravity of the plane and the aerodynamic center of the tail

η_H = tail efficiency

Dividing by $qS_W c$ results in:

$$C_{M_{cg}}=C_{M_{ac}}+C_{L_W}\frac{x}{c}-C_{L_H}\frac{S_H}{S_W}\frac{l_H}{c}\eta_H+C_{M_F} \tag{3}$$

Next, the equation needs to be differentiated with respect to the coefficient of lift of the wing:

$$\frac{dC_{M_{cg}}}{dC_{L_W}} = \frac{x}{c} - \frac{dC_{L_H}}{dC_{L_W}} \left(\frac{S_H}{S_W}\right) \frac{l_H}{c} \eta_H + \left(\frac{dC_M}{dC_{l_W}}\right)_F \tag{4}$$

Relating dC_{LH}/dC_{LW} to the change in downwash at the tail gives:

$$\frac{dC_{L_H}}{dC_{L_W}} = \frac{(dC_L/d\alpha)_H}{(dC_L/d\alpha)_W} \left(1 - \frac{d\epsilon_H}{d\alpha}\right) \tag{5}$$

Which is then substituted into Equation 8.2, it becomes:

$$\left(\frac{dC_M}{dC_{L_W}}\right)_{cg} = \left[\frac{x}{c} - \frac{(dC_L/d\alpha)_H}{(dC_L/d\alpha)_W} \left(1 - \frac{d\epsilon_H}{d\alpha}\right) \frac{S_H}{S_W} \frac{l_H}{c} \eta_H + \left(\frac{dC_M}{dC_{L_W}}\right)_F\right] \tag{6}$$

This equation calculates the rate of change of the pitching moment with respect to wing lift coefficient. To determine stability, the rate of change of the pitching moment with respect to total airplane lift coefficient is needed. This can be done using the following relation:

$$\left(\frac{dC_M}{dC_L}\right)_{cg} = \left(\frac{dC_M}{dC_{L_W}}\right)_{cg} \left[\frac{(dC_L/d\alpha)_W}{(dC_L/d\alpha)}\right]$$

$$= \left(\frac{dC_M}{dC_{L_W}}\right)_{cg} \left[\frac{(dC_L/d\alpha)_W}{(dC_L/d\alpha)_W + (dC_L/d\alpha)_H \left(1 - \frac{d\epsilon_H}{d\alpha}\right) \frac{S_H}{S_W} \eta_H}\right]$$

$$= \left(\frac{dC_M}{dC_{L_W}}\right)_{cg} \left[\frac{1}{\left[1 + \frac{(dC_L/d\alpha)_H}{(dC_L/d\alpha)_W} \left(1 - \frac{d\epsilon_H}{d\alpha}\right) \frac{S_H}{S_W} \eta_H\right]}\right] \tag{7}$$

Substituting $(dC_M/dC_{Lw})_F$ from Equation 6 into Equation 7 gives:

$$\left(\frac{dC_M}{dC_L}\right)_{cg} = \left[\frac{x}{c} - \frac{(dC_L/d\alpha)_H}{(dC_L/d\alpha)_W}\left(1-\frac{d\epsilon_H}{d\alpha}\right)\frac{S_H}{S_W}\frac{l_H}{c}\eta_H + \left(\frac{dC_M}{dC_{L_W}}\right)_P\right] \times \qquad (8)$$

$$\left[\frac{1}{\left[1+\frac{(dC_L/d\alpha)_H}{(dC_L/d\alpha)_W}\left(1-\frac{d\epsilon_H}{d\alpha}\right)\frac{S_H}{S_W}\eta_H\right]}\right]$$

One more substitution must be made to get the final equation. The variable l_H is the distance from the center of gravity to the quarter chord of the tail and therefore is dependant on x/c, the location of the center of gravity divided by the chord of the wing. The l_H can be replaced by defining a new variable l'_H, the longitudinal distance from the aerodynamic center of the wing to the aerodynamic center of the tail. Examining Figure 8.2 in Chapter 8,

$$l'_H = l_H + x$$

therefore:

$$l_H = l'_H - x \qquad (9)$$

Substituting for l_H and rearranging terms gives the final equation (Shevell, 1983):

$$\left(\frac{dC_M}{dC_L}\right)_{cg} = \frac{x}{c} - \left[\frac{(dC_L/d\alpha)_H}{(dC_L/d\alpha)_W}\left(1-\frac{d\epsilon_H}{d\alpha}\right)\frac{S_H}{S_W}\frac{l_H}{c}\eta_H + \left(\frac{dC_M}{dC_{L_W}}\right)_P\right] \qquad (10)$$

$$\left[\frac{1}{\left[1+\frac{(dC_L/d\alpha)_H}{(dC_L/d\alpha)_W}\left(1-\frac{d\epsilon_H}{d\alpha}\right)\frac{S_H}{S_W}\eta_H\right]}\right]$$

This value was calculated for the solar powered plane using the following values:

$x/c = .15$

$(dC_L/d\alpha)_H = 3.43$

$(dC_L/d\alpha)_W = 4.15$

$(d\epsilon_H/d\alpha) = .32$

$S_H = .3\ m^2$

$S_W = 1.48\ m^2$

$l'_H = 1.4\ m$

$c = .424\ m$

$\eta_H = .85$

$(dC_M/dC_{Lw})_F = .0000363$

where $(dC_M/dC_{Lw})_F$ is computed in Appendix A.2

Substituting them all into the equation gives:

$$\left(\frac{dC_M}{dC_L}\right)_{cg} = .15 - \left[\frac{3.43}{4.15}(1-.32)\frac{.3m^2}{1.48m^2}\frac{1.4m}{.42m}.85 + .000036\right] \times \left[\frac{1}{\left[1+\frac{3.43}{4.15}(1-.32)\frac{.3m^2}{1.48m^2}.85\right]}\right]$$

$$\left(\frac{dC_M}{dC_L}\right)_{cg} = -.14$$

Therefore, the design has static longitudinal stability.

A.2 MULTHORP'S METHOD

The $(dC_M/dC_{Lw})_F$ term of Equation 8.2 in Chapter 8 accounts for the contribution of the airplane fuselage to the rate of change of the pitching moment with the wing lift coefficient. This value is found by first calculating the rate of change of the moment coefficient of the fuselage with the angle of attack, $C_{M\alpha F}$, and then dividing this number by the rate of change of the wing lift coefficient with the angle of attack. The first value, $C_{M\alpha F}$, is found using Multhorp's method of analyzing the aerodynamic characteristics of the fuselage (Nelson, 1989).

To use this method, the fuselage of the airplane is divided into segments, and then the contribution of each segment is determined. These contributions are then added together to get the total change of the pitching moment with angle of attack as can be seen in the following equation:

$$C_{M_{\alpha_F}} = \frac{1}{36.5Sc}\sum_{0}^{l_f} w_f^2 \frac{d\epsilon_u}{d\alpha} dx \qquad (1)$$

where:

S = wing reference area

c = wing mean aerodynamic chord

w_f = the width of the segement of the fuselage

$d\epsilon_u/d\alpha$ = the change in local flow angle with angle of attack for each section

For the solar powered plane, there is no fuselage section behind the wing, only the two slender carbon fiber tubes. Because of this, the main contribution to the pitching moment comes from the pod section that sticks out in front of the

wing. For analysis, the plane is divided into three sections to take both the pod and the tubes into account, as can be seen in Figure A.1. The first section is the small, tapered nose block, the second the rest of the pod that is in front of the wing, and the third is the two carbon fiber tubes. The width of each section is known, and $d\epsilon_u/d\alpha$ for each section is found by using Figures A.2.12 and A.3, which can be found at the end of the Appendix.

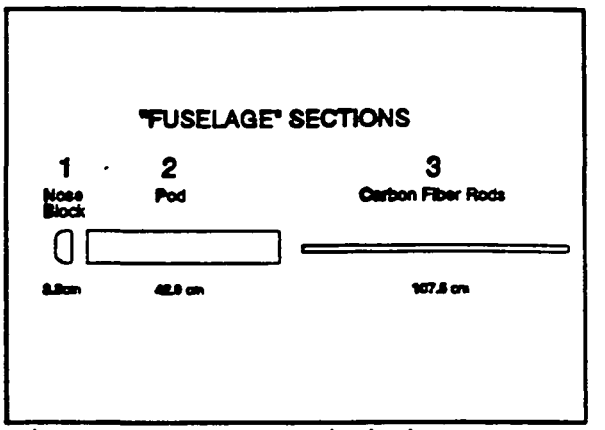

Figure A.1: Divisions for Multhorp's Method

The $d\epsilon_u/d\alpha$ term is determined in a different way for each section because the wing causes the airflow to change as it passes over the body. The locations in front of the wing are subjected to upwash which creates large local angles of attack. Therefore, $d\epsilon_u/d\alpha$ will be greater than one. For those locations aft of the wing, the flow is in downwash and the angle of attack of the fuselage is reduced.

The width of the nose block is 6.5 centimeters, and its $d\epsilon_u/d\alpha$ is found on Figure A.2.12a using x_i, the distance from the wing to the middle of the block. This value is 44.8 centimeters, and dividing it by the chord length of the wing gives:

$$\frac{x_i}{c}=\frac{44.8cm}{42.4cm}=1.057$$

Using this value to read $d\epsilon_u/d\alpha$ off of Figure A.2.12 yields:

$$\frac{d\epsilon_u}{d\alpha}=1.1$$

Section 2, the pod in front of the wing, is also 6.5 centimeters in width, and the $d\epsilon_u/d\alpha$ is found on Figure A.2.12b using x, the length of section 2. This value is 42.9 centimeters, and dividing this by the chord length of the wing gives:

$$\frac{x}{c}=\frac{42.9\,cm}{42.4\,cm}=1.012$$

This is then used to read $d\epsilon_u/d\alpha$:

$$\frac{d\epsilon_u}{d\alpha}=1.8$$

The width of the two carbon fiber rods is very small, only 5 millimeters. For this section, $d\epsilon_u/d\alpha$ is found using the following equation:

$$\frac{d\epsilon_u}{d\alpha}=\frac{x_i}{l_h}\left[1-\frac{d\epsilon}{d\alpha}\right] \qquad (2)$$

where:

l_h = the distance from the trailing edge of the wing to the center of the tail

$d\epsilon/d\alpha$ = the downwash angle of the wing

Substituting the appropriate values gives:

$$\frac{d\epsilon_u}{d\alpha}=\frac{.5m}{1.075m}[1-.32]$$

$$\frac{d\epsilon_u}{d\alpha}=.3163$$

All of these values are then substituted into Equation 1 yielding:

$$C_{m_{\alpha f}} = \frac{1}{(36.5)(1.48m^2)(.424m)} \times [2[(.005m)^2(.3163)(1.0m)] +$$

$$+(.065m)^2(1.1)(.038m) + (.065m)^2(1.8)(.429m)]$$

$$C_{m_{\alpha f}} = .0001508$$

The value for $(dC_M/dC_L)_F$ is then found by dividing $C_{M\alpha F}$ by the wing lift coefficient, dC_{LW}:

$$\left(\frac{dC_M}{dC_L}\right)_F = \frac{.0001508}{4.15} = .0000363$$

This is a very small number, which means that the "fuselage" in our design contributes very little to the rate of change of the pitching moment with the coefficient of lift, as can be seen in the calculation in Appendix A.1.

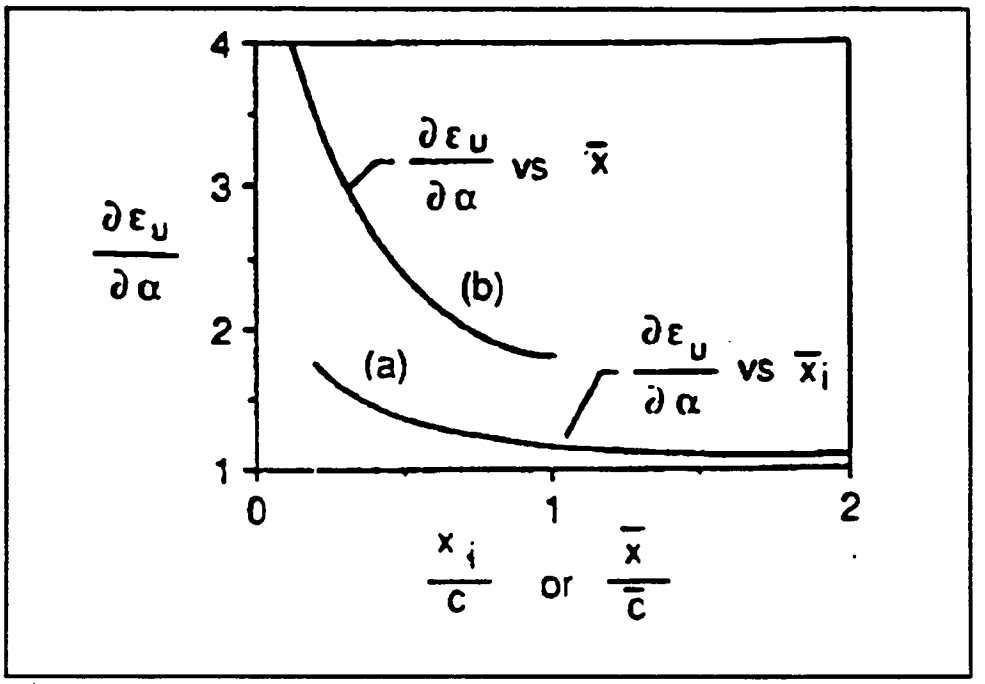

Figure A.2.12: Graph of $d\varepsilon_u$ versus x/c.

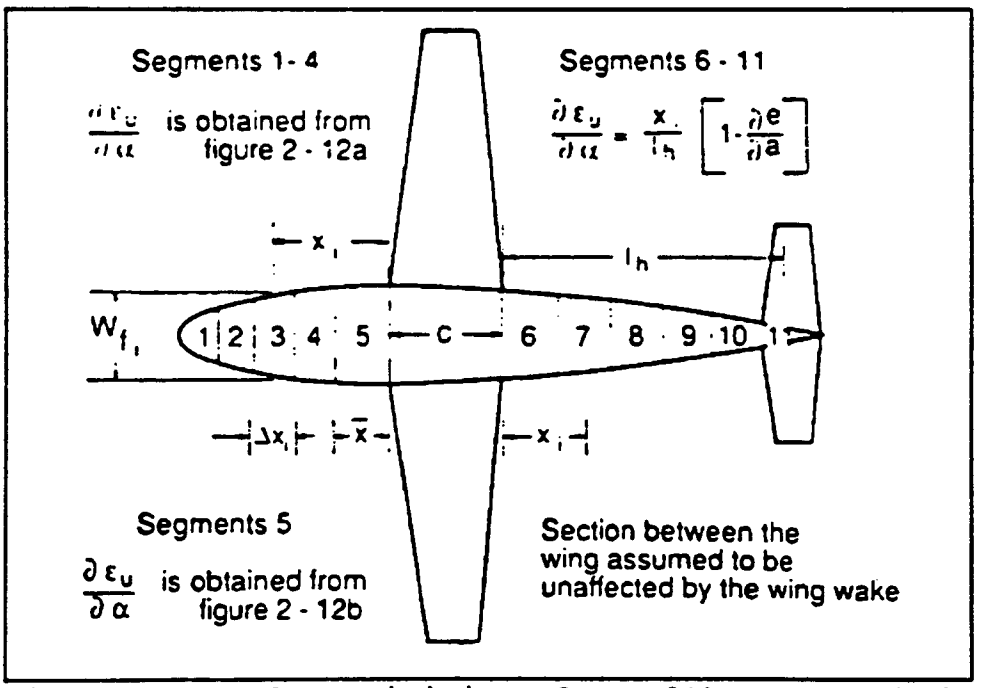

Figure 3: Fuselage Divisions for Multhorp's Method.

$$\lambda_p = \frac{X_u \pm \sqrt{X_u^2 + 4\frac{Z_u g}{u_o}}}{2.0} \tag{9}$$

Solving for the frequency and damping ratio gives,

$$\omega_{n_p} = \sqrt{-Z_u \frac{g}{u_o}} \tag{10}$$

$$\eta_p = \frac{-X_u}{2\omega_{n_p}} \tag{11}$$

the equations used in Chapter 8 to calculate the long period stability of the solar powered airplane.

More details on the derivations of these equations and the derivations of an aircraft's equations of motions can be found in Chapters 2, 3 and 4 of Flight Stability and Control, by Robert C. Nelson.

A homogeneous solution can be found for Equation 1 by assuming a solution in the form:

$$\boldsymbol{x}=\boldsymbol{x}_r e^{\lambda_r t}$$

Substituting this into Equation 1 gives:

$$[\lambda_r \boldsymbol{I}-\boldsymbol{A}]\boldsymbol{x}_r=0$$

where:

I = the identy matrix

To solve for the nontrivial solution,

$$[\lambda_r \boldsymbol{I}-\boldsymbol{A}]=0$$

must be true, where λ_r gives the characteristic roots or the eigenvalues of the system. Once λ_r has been found the frequency and damping ratio can be determined and used to analyze the dynamic stability of the design.

For each of the modes of motion, long and short, certain assumptions can be made to simplify Equation 2. For the short period, Δu is assumed to be zero and the X-force equation can be dropped. The state-space equation then becomes:

$$\begin{bmatrix}\Delta\dot{w}\\ \Delta\dot{q}\end{bmatrix}=\begin{bmatrix}Z_w & u_0\\ M_w+M_{\dot{w}}Z_w & M_q+M_{\dot{w}}u_0\end{bmatrix}\begin{bmatrix}\Delta w\\ \Delta q\end{bmatrix} \qquad (3)$$

This is then written in terms of the angle of attack using:

$$\Delta\alpha=\frac{\Delta w}{u_o}$$

The derivatives due to w must also be replaced with derivatives due to the angle of attack. This is done using

the following equations:

$$Z_{\dot{\alpha}} = \frac{1}{I_y}\frac{dZ}{d\dot{\alpha}} = \frac{1}{I_y}\frac{dZ}{d(\Delta w/u_o)} = \frac{u_o}{I_y}\frac{dZ}{dw} = u_o Z_w$$

$$M_{\dot{\alpha}} = \frac{1}{I_y}\frac{dM}{d\dot{\alpha}} = \frac{1}{I_y}\frac{dM}{d(\Delta \dot{w}/u_o)} = \frac{u_o}{I_y}\frac{dM}{d\dot{w}} = u_o M_{\dot{w}}$$

$$M_{\alpha} = \frac{1}{I_y}\frac{dM}{d\alpha} = \frac{1}{I_y}\frac{dM}{d(\Delta w/u_o)} = \frac{u_o}{I_y}\frac{dM}{dw} = u_o M_w$$

Making all of the substitutions, the state equation becomes:

$$\begin{bmatrix}\Delta\dot{\alpha}\\ \Delta\dot{q}\end{bmatrix} = \begin{bmatrix}\frac{Z_\alpha}{u_0} & 1\\ M_\alpha + M_{\dot{\alpha}}\frac{Z_\alpha}{u_0} & M_q + M_{\dot{\alpha}}\end{bmatrix}\begin{bmatrix}\Delta\alpha\\ \Delta q\end{bmatrix} \qquad (4)$$

Solving for the eigenvalues gives the determinant:

$$\begin{vmatrix}\lambda - \frac{Z_\alpha}{u_0} & -1\\ -M_\alpha - M_{\dot{\alpha}}\frac{Z_\alpha}{u_0} & \lambda - (M_q + M_{\dot{\alpha}})\end{vmatrix} = 0$$

Expanding the determinant yields the characteristic equation:

$$\lambda^2 - (M_q + M_{\dot{\alpha}} + \frac{Z_\alpha}{u_o})\lambda + M_q\frac{Z_\alpha}{u_o} - M_\alpha = 0$$

Solving for the short period roots, λ_{sp}, gives:

$$\lambda_{sp} = \frac{(M_q + M_{\dot{\alpha}} + \frac{Z_\alpha}{u_o}) \pm [(M_q + M_{\dot{\alpha}} + \frac{Z_\alpha}{u_o})^2 - 4(M_q\frac{Z_\alpha}{u_o} - M_\alpha)]^{1/2}}{2.0} \qquad (5)$$

then, solving for the frequency and damping ratio gives:

$$\omega_{n_{sp}} = [\,(M_q \frac{Z_\alpha}{u_o} - M)\,]^{1/2} \tag{6}$$

$$\zeta_{sp} = \frac{-[M_q + M_{\dot{\alpha}} + \frac{Z_\alpha}{u_o}]}{(2\omega_{n_{sp}})} \tag{7}$$

These are the equations necessary to determine the airplane's stability in the short mode in Chapter 8.

The long period is characterised by a very slow oscillating motion and can be considered a gradual interchange of potential and kinetic energy about the equilibrium position. This motion includes changes in the pitch attitude, altitude, and velocity with a fairly constant angle of attack. Assuming this angle to be zero and also neglecting the pitching moment equation, the state equation becomes:

$$\begin{bmatrix} \Delta u \\ \Delta\theta \end{bmatrix} = \begin{bmatrix} X_u & -g \\ \frac{-Z_u}{u_0} & 0 \end{bmatrix} \begin{bmatrix} \Delta u \\ \Delta\theta \end{bmatrix} \tag{8}$$

The characteristic roots, the frequency and the damping ratio can be solved for using the determinant:

$$\begin{vmatrix} \lambda - X_u & g \\ \frac{Z_u}{u_0} & \lambda \end{vmatrix} = 0$$

Expanding this gives:

$$\lambda^2 - X_u\lambda - \frac{Z_u g}{u_o} = 0$$

Solving for λ_p, the long period root, yields:

A.4 PERFORMANCE PROGRAM

The following pages contain the performance program along with sample runs for a variety of operating conditions. The first few trial runs are for the design weight of 29 N. These are followed by runs of the actual aircraft weight of 35 N.

```
10 REM ************************************************************
20 REM ****************** CONSTANTS ****************************
30 REM ************************************************************
40 PI = 3.14159265#                              :REM VALUE OF PIE
50 TA = 288.16                        :REM TEMPERATURE AT SEA LEVEL (K)
60 PA = 101230!                        :REM PRESSURE AT SEA LEVEL (N/m^2)
70 R = 287                            :REM GAS CONSTANT (N*m/Kg*K)
80 C = .0065                         :REM ATMOSPHERIC LAPSE RATE
90 KV = 1.4607E-05                    :REM KINEMATIC VISCOSITY
100 REM ***********************************************************
110 REM ****************** INPUTS ********************************
115 LPRINT " PROGRAM INPUTS"
120 INPUT "GROSS WEIGHT (N)";W
125 LPRINT "GROSS WEIGHT (N)";W
130 INPUT "FLIGHT ALTITUDE (m)";Z
135 LPRINT "FLIGHT ALTITUDE (m)";Z
140 INPUT "WING SPAN (m)";B
145 LPRINT "WING SPAN (m)";B
150 INPUT "WING MEAN CHORD LENGTH (m)";LW
155 LPRINT "WING MEAN CHORD LENGTH (m)";LW
160 INPUT "OPERATING WING LIFT COEFFICIENT";CL
165 LPRINT "OPERATING WING LIFT COEFFICIENT";CL
170 INPUT "OPERATING WING DRAG COEFFICIENT";CDW
175 LPRINT "OPERATING WING DRAG COEFFICIENT";CDW
180 INPUT "WETTED VERTICAL TAIL AREA (m^2)";SVT
185 LPRINT "WETTED VERTICAL TAIL AREA (m^2)";SVT
190 INPUT "VERTICAL TAIL MEAN CHORD LENGTH (m)";LVT
195 LPRINT "VERTICAL TAIL MEAN CHORD LENGTH (m)";LVT
200 INPUT "OPERATING HORIZONTAL TAIL DRAG COEFFICIENT";CDT
205 LPRINT "OPERATING HORIZONTAL TAIL DRAG COEFFICIENT";CDT
210 INPUT "OPERATING HORIZONTAL TAIL LIFT COEFFICIENT";CLT
215 LPRINT "OPERATING HORIZONTAL TAIL LIFT COEFFICIENT";CLT
220 INPUT "HORIZONTAL TAIL PLANFORM AREA(M^2)";HT
225 LPRINT "HORIZONTAL TAIL PLANFORM AREA(M^2)";HT
230 INPUT "WETTED FUSALAGE AREA (m^2)";SF
235 LPRINT "WETTED FUSALAGE AREA (m^2)";SF
240 INPUT "FUSALAGE LENGTH (m)";LF
245 LPRINT "FUSALAGE LENGTH (m)";LF
250 INPUT "WETTED BOOM AREA (1)(m^2)";SB
255 LPRINT "WETTED BOOM AREA (1)(m^2)";SB
260 INPUT "BOOM LENGTH (m)";LB
265 LPRINT "BOOM LENGTH (m)";LB
270 INPUT "FUSALAGE CORRECTION FACTOR";KF
275 LPRINT "FUSALAGE CORRECTION FACTOR";KF
276 INPUT "BOOM CORRECTION FACTOR";KB
280 LPRINT "BOOM CORRECTION FACTOR";KB
290 INPUT "VERTICAL TAIL CORRECTION FACTOR";KVT
295 LPRINT "VERTICAL TAIL CORRECTION FACTOR";KVT
300 REM ***********************************************************
310 REM ****************** ATMOSPHERIC CALCULATION ******************
320 REM ***********************************************************
330 PZ=0:TZ=0
340 TZ=TA-(C*Z)                       :REM TEMPERATURE AT ALTITUDE
350 PZ= PA*(1-(C*Z)/TA)^5.26          :REM PRESSURE AT ALTITUDE
360 RO= (PZ)/(R*TZ)                   :REM AIR DENSITY
370 REM ***********************************************************
380 AR =B/LW
390 S=B*LW
400 REM ***********************************************************
410 REM ****************** REYNOLD'S # CALCULATION*******************
420 REM ***********************************************************
425 LPRINT
```

```
430 VM=SQR((2*W)/(RO*(CL*S)+(CLT*HT)))
440 V=1.1*VM
450 LPRINT "MINIMUM OPERATING VELOCITY";V
460 RVT = (V*LVT)/KV
470 RF = (V*LF)/KV
480 RB = (V*LB)/KV
490 REM*************************************************************************
*
500 REM*******************FRICTIONAL COEFFICIENTS*************************
**
510 CVT=1.328/SQR(RVT)
530 CF= .455*(LOG(RF)/LOG(10))^-2.58
550 CB= .455*(LOG(RB)/LOG(10))^-2.58
570 REM*************************************************************************
****
580 CDP = (CDW)+(((2*HT)/S)*CDT)+2*(KB*CB*(SB/S))+2*(KVT*CVT*(SVT/S))+(KF
*CF*(SF
/S))
630 E = 1/((.38*PI*AR*CDP)+1.103)
640 PREQ=.5*((CL^2/(PI*AR*E))+CDP)*RO*V^3*S
645 LPRINT "THE REQUIRED POWER FOR LEVEL FLIGHT ";PREQ "W"
650 PRINT PREQ
```

```
 PROGRAM INPUTS
GROSS WEIGHT (N) 29.8
FLIGHT ALTITUDE (m) 50
WING SPAN (m) 3.5
WING MEAN CHORD LENGTH (m) .42
OPERATING WING LIFT COEFFICIENT .7922
OPERATING WING DRAG COEFFICIENT .0132
WETTED VERTICAL TAIL AREA (m^2) .0805
VERTICAL TAIL MEAN CHORD LENGTH (m) .2
OPERATING HORIZONTAL TAIL DRAG COEFFICIENT .0148
OPERATING HORIZONTAL TAIL LIFT COEFFICIENT .2595
HORIZONTAL TAIL PLANFORM AREA(M^2) .3
WETTED FUSALAGE AREA (m^2) .2055
FUSALAGE LENGTH (m) .89
WETTED BOOM AREA (1)(m^2) .0414
BOOM LENGTH (m) 1
FUSALAGE CORRECTION FACTOR 1.07
BOOM CORRECTION FACTOR 1
VERTICAL TAIL CORRECTION FACTOR 1.04

RESULTS
FOR FLIGHT VELOCITY OF 7.1 m/s
THE REQUIRED POWER FOR LEVEL FLIGHT  16.72864 W
 PROGRAM INPUTS



GROSS WEIGHT (N) 29.8
FLIGHT ALTITUDE (m) 50
WING SPAN (m) 3.5
WING MEAN CHORD LENGTH (m) .42
OPERATING WING LIFT COEFFICIENT .7922
OPERATING WING DRAG COEFFICIENT .0132
WETTED VERTICAL TAIL AREA (m^2) .0805
VERTICAL TAIL MEAN CHORD LENGTH (m) .2
OPERATING HORIZONTAL TAIL DRAG COEFFICIENT .0148
OPERATING HORIZONTAL TAIL LIFT COEFFICIENT .2595
HORIZONTAL TAIL PLANFORM AREA(M^2) .3
WETTED FUSALAGE AREA (m^2) .2055
FUSALAGE LENGTH (m) .89
WETTED BOOM AREA (1)(m^2) .0414
BOOM LENGTH (m) 1
FUSALAGE CORRECTION FACTOR 1.07
BOOM CORRECTION FACTOR 1
VERTICAL TAIL CORRECTION FACTOR 1.04

RESULTS
FOR FLIGHT VELOCITY OF 7.4 m/s
THE REQUIRED POWER FOR LEVEL FLIGHT  18.93163 W
```

```
 PROGRAM INPUTS
GROSS WEIGHT (N) 29.8
FLIGHT ALTITUDE (m) 50
WING SPAN (m) 3.5
WING MEAN CHORD LENGTH (m) .42
OPERATING WING LIFT COEFFICIENT .7922
OPERATING WING DRAG COEFFICIENT .0132
WETTED VERTICAL TAIL AREA (m^2) .0805
VERTICAL TAIL MEAN CHORD LENGTH (m) .2
OPERATING HORIZONTAL TAIL DRAG COEFFICIENT .0148
OPERATING HORIZONTAL TAIL LIFT COEFFICIENT .2595
HORIZONTAL TAIL PLANFORM AREA(M^2) .3
WETTED FUSALAGE AREA (m^2) .2055
FUSALAGE LENGTH (m) .89
WETTED BOOM AREA (1)(m^2) .0414
BOOM LENGTH (m) 1
FUSALAGE CORRECTION FACTOR 1.07
BOOM CORRECTION FACTOR 1
VERTICAL TAIL CORRECTION FACTOR 1.04

RESULTS
FOR FLIGHT VELOCITY OF 7.6 m/s
THE REQUIRED POWER FOR LEVEL FLIGHT  20.50269 W
```

```
 PROGRAM INPUTS
GROSS WEIGHT (N) 29.8
FLIGHT ALTITUDE (m) 50
WING SPAN (m) 3.5
WING MEAN CHORD LENGTH (m) .42
OPERATING WING LIFT COEFFICIENT .7922
OPERATING WING DRAG COEFFICIENT .0132
WETTED VERTICAL TAIL AREA (m^2) .0805
VERTICAL TAIL MEAN CHORD LENGTH (m) .2
OPERATING HORIZONTAL TAIL DRAG COEFFICIENT .0148
OPERATING HORIZONTAL TAIL LIFT COEFFICIENT .2595
HORIZONTAL TAIL PLANFORM AREA(M^2) .3
WETTED FUSALAGE AREA (m^2) .2055
FUSALAGE LENGTH (m) .89
WETTED BOOM AREA (1)(m^2) .0414
BOOM LENGTH (m) 1
FUSALAGE CORRECTION FACTOR 1.07
BOOM CORRECTION FACTOR 1
VERTICAL TAIL CORRECTION FACTOR 1.04

RESULTS
FOR FLIGHT VELOCITY OF 8 m/s
THE REQUIRED POWER FOR LEVEL FLIGHT  23.90054 W
```

```
 PROGRAM INPUTS
GROSS WEIGHT (N) 35
FLIGHT ALTITUDE (m) 50
WING SPAN (m) 3.5
WING MEAN CHORD LENGTH (m) .42
OPERATING WING LIFT COEFFICIENT .7922
OPERATING WING DRAG COEFFICIENT .0132
WETTED VERTICAL TAIL AREA (m^2) .0805
VERTICAL TAIL MEAN CHORD LENGTH (m) .2
OPERATING HORIZONTAL TAIL DRAG COEFFICIENT .0148
OPERATING HORIZONTAL TAIL LIFT COEFFICIENT .2595
HORIZONTAL TAIL PLANFORM AREA(M^2) .3
WETTED FUSALAGE AREA (m^2) .2055
FUSALAGE LENGTH (m) .89
WETTED BOOM AREA (1)(m^2) .0414
BOOM LENGTH (m) 1
FUSALAGE CORRECTION FACTOR 1.07
BOOM CORRECTION FACTOR 1
VERTICAL TAIL CORRECTION FACTOR 1.04

RESULTS
MINIMUM OPERATING VELOCITY 7.523355
THE REQUIRED POWER FOR LEVEL FLIGHT  19.89075 W


 PROGRAM INPUTS
GROSS WEIGHT (N) 30
FLIGHT ALTITUDE (m) 50
WING SPAN (m) 3.5
WING MEAN CHORD LENGTH (m) .42
OPERATING WING LIFT COEFFICIENT .7922
OPERATING WING DRAG COEFFICIENT .0132
WETTED VERTICAL TAIL AREA (m^2) .0805
VERTICAL TAIL MEAN CHORD LENGTH (m) .2
OPERATING HORIZONTAL TAIL DRAG COEFFICIENT .0148
OPERATING HORIZONTAL TAIL LIFT COEFFICIENT .2595
HORIZONTAL TAIL PLANFORM AREA(M^2) .3
WETTED FUSALAGE AREA (m^2) .2055
FUSALAGE LENGTH (m) .89
WETTED BOOM AREA (1)(m^2) .0414
BOOM LENGTH (m) 1
FUSALAGE CORRECTION FACTOR 1.07
BOOM CORRECTION FACTOR 1
VERTICAL TAIL CORRECTION FACTOR 1.04

RESULTS
MINIMUM OPERATING VELOCITY 6.965274
THE REQUIRED POWER FOR LEVEL FLIGHT  15.79757 W
```

```
 PROGRAM INPUTS
GROSS WEIGHT (N) 35
FLIGHT ALTITUDE (m) 50
WING SPAN (m) 3.5
WING MEAN CHORD LENGTH (m) .42
OPERATING WING LIFT COEFFICIENT .7922
OPERATING WING DRAG COEFFICIENT .0132
WETTED VERTICAL TAIL AREA (m^2) .0805
VERTICAL TAIL MEAN CHORD LENGTH (m) .2
OPERATING HORIZONTAL TAIL DRAG COEFFICIENT .0148
OPERATING HORIZONTAL TAIL LIFT COEFFICIENT .2595
HORIZONTAL TAIL PLANFORM AREA(M^2) .3
WETTED FUSALAGE AREA (m^2) .2055
FUSALAGE LENGTH (m) .89
WETTED BOOM AREA (1)(m^2) .0414
BOOM LENGTH (m) 1
FUSALAGE CORRECTION FACTOR 1.07
BOOM CORRECTION FACTOR 1
VERTICAL TAIL CORRECTION FACTOR 1.04

RESULTS
FOR FLIGHT VELOCITY OF 7.75 m/s
THE REQUIRED POWER FOR LEVEL FLIGHT  21.73632 W



 PROGRAM INPUTS
GROSS WEIGHT (N) 35
FLIGHT ALTITUDE (m) 50
WING SPAN (m) 3.5
WING MEAN CHORD LENGTH (m) .42
OPERATING WING LIFT COEFFICIENT .7922
OPERATING WING DRAG COEFFICIENT .0132
WETTED VERTICAL TAIL AREA (m^2) .0805
VERTICAL TAIL MEAN CHORD LENGTH (m) .2
OPERATING HORIZONTAL TAIL DRAG COEFFICIENT .0148
OPERATING HORIZONTAL TAIL LIFT COEFFICIENT .2595
HORIZONTAL TAIL PLANFORM AREA(M^2) .3
WETTED FUSALAGE AREA (m^2) .2055
FUSALAGE LENGTH (m) .89
WETTED BOOM AREA (1)(m^2) .04143
BOOM LENGTH (m) 1
FUSALAGE CORRECTION FACTOR 1.07
BOOM CORRECTION FACTOR 1
VERTICAL TAIL CORRECTION FACTOR 1.04

RESULTS
FOR FLIGHT VELOCITY OF 7.9 m/s
THE REQUIRED POWER FOR LEVEL FLIGHT  23.01853 W
```

```
 PROGRAM INPUTS
GROSS WEIGHT (N) 35
FLIGHT ALTITUDE (m) 50
WING SPAN (m) 3.5
WING MEAN CHORD LENGTH (m) .42
OPERATING WING LIFT COEFFICIENT .7922
OPERATING WING DRAG COEFFICIENT .0132
WETTED VERTICAL TAIL AREA (m^2) .0805
VERTICAL TAIL MEAN CHORD LENGTH (m) .2
OPERATING HORIZONTAL TAIL DRAG COEFFICIENT .0148
OPERATING HORIZONTAL TAIL LIFT COEFFICIENT .2595
HORIZONTAL TAIL PLANFORM AREA(M^2) .3
WETTED FUSALAGE AREA (m^2) .2055
FUSALAGE LENGTH (m) .89
WETTED BOOM AREA (1)(m^2) .0414
BOOM LENGTH (m) 1
FUSALAGE CORRECTION FACTOR 1.07
BOOM CORRECTION FACTOR 1
VERTICAL TAIL CORRECTION FACTOR 1.04

RESULTS
FOR FLIGHT VELOCITY OF 8
THE REQUIRED POWER FOR LEVEL FLIGHT  23.90054 W


 PROGRAM INPUTS
GROSS WEIGHT (N) 35
FLIGHT ALTITUDE (m) 50
WING SPAN (m) 3.5
WING MEAN CHORD LENGTH (m) .42
OPERATING WING LIFT COEFFICIENT .7922
OPERATING WING DRAG COEFFICIENT .0132
WETTED VERTICAL TAIL AREA (m^2) .0805
VERTICAL TAIL MEAN CHORD LENGTH (m) .2
OPERATING HORIZONTAL TAIL DRAG COEFFICIENT .0148
OPERATING HORIZONTAL TAIL LIFT COEFFICIENT .2595
HORIZONTAL TAIL PLANFORM AREA(M^2) .3
WETTED FUSALAGE AREA (m^2) .2055
FUSALAGE LENGTH (m) .89
WETTED BOOM AREA (1)(m^2) .0414
BOOM LENGTH (m) 1
FUSALAGE CORRECTION FACTOR 1.07
BOOM CORRECTION FACTOR 1
VERTICAL TAIL CORRECTION FACTOR 1.04

RESULTS
FOR FLIGHT VELOCITY OF 8.5 m/s
THE REQUIRED POWER FOR LEVEL FLIGHT  28.65006 W
```

A.5 CORRECTION FACTORS

Equation 7.5 discussed a correction factor used for determining the "parasitic" drag coefficient. The following chart can be used to determine the form factor k. To determine k, read vertically from the fineness ratio to the curve and then across to the value for k.

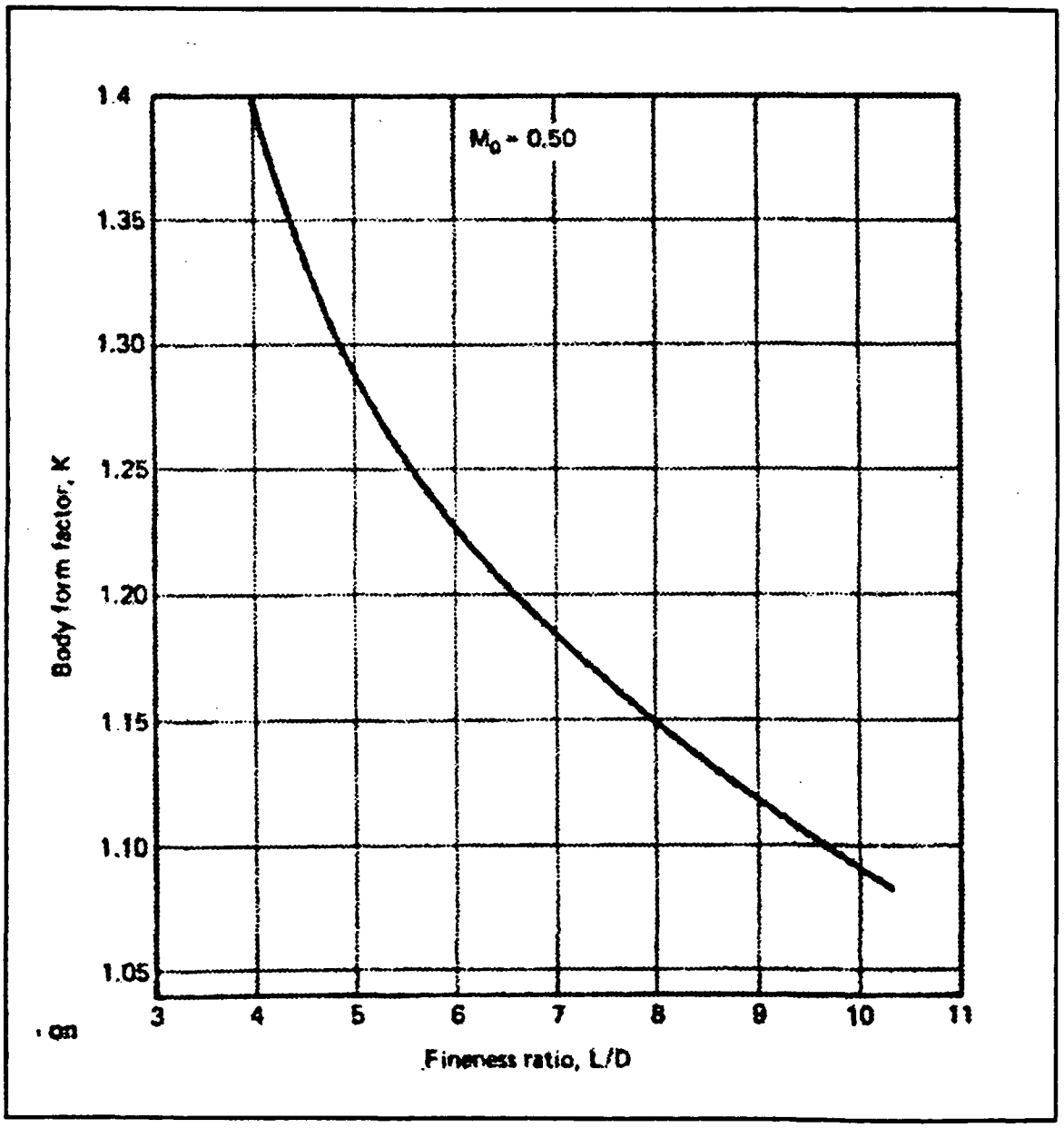

APPENDIX B

AERODYNAMICS

B.1 THE NATURE OF LOW REYNOLDS NUMBER AIRFOILS

B.1.1 Nature of the Reynolds Number

Through observation, it can be seen that identical airfoils can exhibit drastically different characteristics at various operating conditions. For example, the airfoil section of a bird's wing, which performs adequately for the operating conditions of the bird, would result in poor performance on a jet aircraft. This effect on performance, due to extreme differences of size and velocity, implies some dependance on a scaling effect. This scaling effect is quantified as the Reynolds number.

The Reynolds number for flow over an airfoil (often referred to as the Reynolds number based on chordlength) is defined as:

$$Re = \frac{\rho V c}{\mu}$$

where ρ is the density of the flow medium and μ is its viscosity, V is the velocity of free stream, and c is the chordlength of the airfoil. This non-dimensional parameter quantifies the relationship between inertial (fluid momentum) and viscous effects associated with flow about an airfoil.

Figure B.1.1 shows the full spectrum of Reynolds numbers for atmospheric flight. Here, the flight speed for various

objects is plotted versus the Reynolds number based on chordlength. Below a Reynolds number of $7x10^4$, conventional airfoil performance is highly unlikely due to severe viscous effects. Above this limit, viscosity plays a significant role in the behavior of airfoils up to a Reynolds number of 10^6. Airfoils operating in this region are commonly referred to as low Reynolds number airfoils.

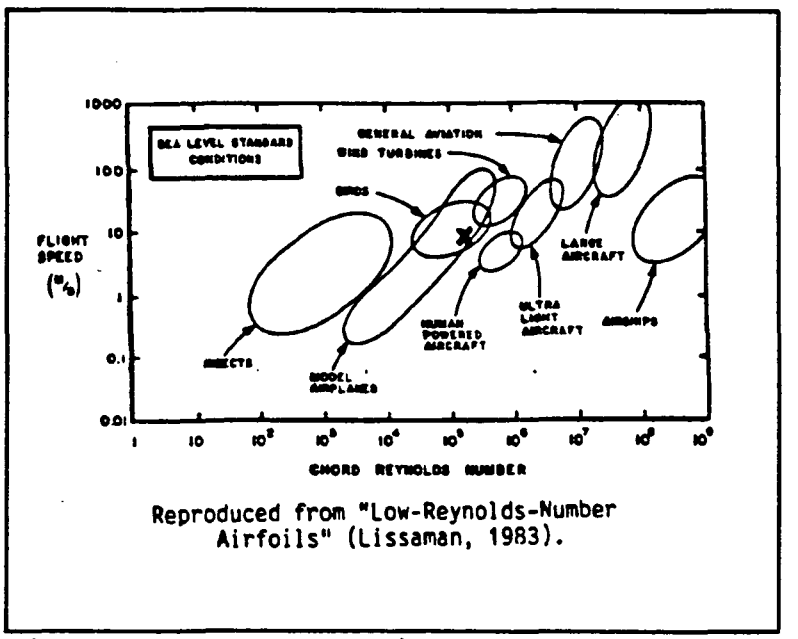

Reproduced from "Low-Reynolds-Number Airfoils" (Lissaman, 1983).

Figure B.1.1: The Flight Reynolds Number Spectrum.

The dynamics of flight are governed by the two types of flow: laminar and turbulent. In the case of a smooth flat plates, transition normally occurs between Reynolds numbers of $5x10^5$ and $3x10^6$ (White, 1986,). However, this may be prematurely induced by perturbations within the flow, such as rough surfaces or adverse pressure gradients. Thus, most low Reynolds number airfoils encompassed within a laminar flow

experience a transition to turbulent between their leading and trailing edges. The position of this transition plays a significant role in the aerodynamic performance of airfoils. This is primarily due to differences in laminar and turbulent boundary layers.

Laminar boundary layers create less drag than turbulent boundary layers. At first glance, this would make laminar flow about an airfoil more desirable. However, laminar boundary layers are less capable of negotiating adverse pressure gradients than turbulent boundary layers. This causes laminar boundary layers to be more susceptible to separation. The occurrence of laminar separation results in a dramatic deterioration of airfoil performance, thus a turbulent flow tends to be more desirable over the surface of airfoils in these regions of adverse pressure gradients.

B.1.2 Fluid Mechanics of Low Reynolds Number Airfoils

An airfoil's upper (or suction) surface experiences pressures lower than that of free stream. These low pressures, which are associated with accelerated flow, must return to approximate free stream conditions at the trailing edge. Through this process, the flow is decelerated, experiencing a positive pressure gradient known as a pressure recovery or pressure ramp. The occurrence of such a pressure recovery creates favorable conditions for boundary layer separation. At Reynolds numbers in excess of 10^6, transition occurs upstream of this adverse gradient, causing the pressure

recovery to be negotiated by a turbulent boundary layer. However, for low Reynolds number airfoils, the boundary layer may still be laminar at the onset of the pressure recovery. In this case, performance is strongly dictated by the boundary layer's poor resistance to separation.

For airfoils having Reynolds numbers on the order of 10^4 and relatively low lift coefficients, the pressure recovery is gradual, allowing laminar flow over the entire airfoil surface without separation. However, as lift increases, the pressure ramp becomes steeper, resulting in laminar separation. At Reynolds numbers below 10^5, this separation may occur over nearly the entire airfoil. However this separated boundary layer, which is extremely susceptible to transition, rapidly becomes turbulent. The turbulent boundary layer, which is more capable of negotiating the adverse pressure gradient, may reattach itself to the airfoil, creating a laminar separation bubble.

Figure B.1.2 shows the general geometry of the laminar separation bubble. Following laminar separation, the boundary layer rapidly undergoes transition and reattaches itself to the surface, forming an approximately normal turbulent profile. This process produces a region of recirculation on the airfoil's surface which results in the drastic deterioration of lift to drag. The presence of this laminar separation bubble is predominant for Reynolds numbers below $2x10^5$, however its behavior is not well understood. This poses difficulties to design and numerical analyses of low

Reynolds number airfoils.

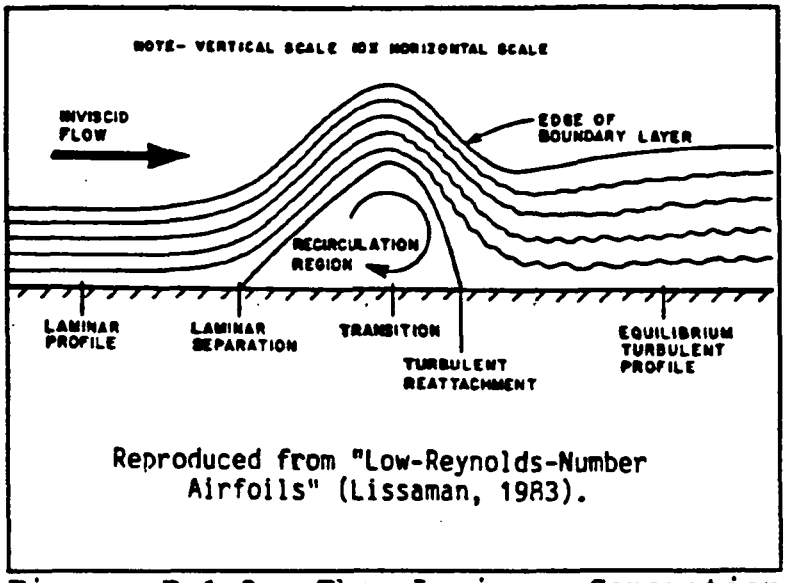

Figure B.1.2: The Laminar Separation Bubble.

B.1.3 Experimental Testing of Low Reynolds Number Airfoils

One problem in the study of low Reynolds number airfoils is the acquisition of reliable section data obtained through experimental testing. In the past, doubt was expressed about the validity of data from many low Reynolds number experimental tests. Many facilities often could not reproduce data yielded for a particular airfoil. This was due to the susceptibility of low Reynolds number airfoils to various influences in the flow. These include boundary layer effects, initial turbulence levels, and perturbations generated either acoustically or by test apparatus. To yield accurate data, a wind tunnel design must take these effects into account.

Currently in the world there are several wind tunnels which have yielded published reproducible data for low

Reynolds number airfoils. These tunnels include the NASA Langley Low Turbulence Pressure Tunnel, the Low-Turbulence Tunnel at Delft, and the Model Wind Tunnel at Stuttgart. As shown in Appendix B.2, the Princeton 3' x 4' smoke tunnel is a fourth tunnel whose data correlates well with the other three aforementioned tunnels.

B.1.4 Numerical Airfoil Analysis

At chord Reynolds numbers above 10^6 there has been much research conducted on understanding flow behavior. Subsequently, computational methods have become well developed in this range. Currently computational methods can accurately predict airfoil behavior, even in the region of stall, separation and post stall. Unfortunately, in the low Reynolds number regime, computational methods are not as well developed. This is primarily due to the appearance of unusual flow characteristics, which are not apparent at higher Reynolds numbers. These characteristics are all related to transition, laminar separation or the laminar separation bubble. At chord Reynolds numbers under $5x10^5$, the laminar separation bubble has a dominant influence on airfoil performance. Currently the mechanism of the bubble is not completely understood, even though considerable amount of work has been conducted to try to accurately predict its development. Until the process of the laminar bubble is better understood, or a way of approximating the complete two-dimensional Navier-Stokes equations is found, a complete

numerical method can not be designed. Currently, methods for predicting transition and laminar bubble behavior are being developed, and some are just becoming available for use in aerodynamic analysis.

B.1.5 Relationship to Current Design

The wing airfoil section on the configuration has a chord Reynolds number of approximately 180,000. (The location of this operational point within the flight Reynolds number spectrum is indicated in Figure B.1.1 by an 'x'.) This lies well in the region of low Reynolds number airfoils. As previously mentioned, there are difficulties in airfoil design, when dealing with these low Reynolds numbers. To design an optimum airfoil section for the configuration, it would have been desirable to use a low turbulence wind tunnel to yield performance data. Unfortunately, the W.P.I. wind tunnel was not designed to minimize the effects that are crucial at low Reynolds numbers. Time and distance constraints did not allow tests using a reliable low turbulence wind tunnel.

Although reliable computational methods have been developed and become available for design analysis, none could be obtained due to monetary constraints. Because of these reasons, it was necessary to use the data yielded from the Princeton smoke tunnel in the design procedure.

B.2 RELIABILITY OF THE PRINCETON DATA

As discussed in Appendix B.1, there are many complications associated with experimental testing of low Reynolds number airfoils. It is therefore desirable to verify data in order to ensure reasonably accurate aerodynamic characteristics. To do this, yielded results may be compared with data from other facilities. As an additional check, airfoil characteristics may be approximated using numerical and empirical methods.

B.2.1 Experimental Verification

Figure B.2.1 shows a comparison of Princeton data for the

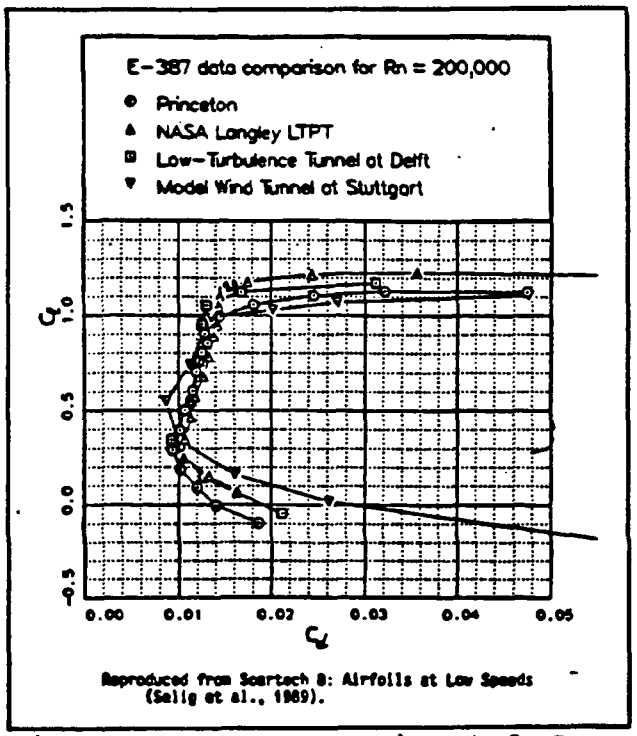

Figure B.2.1: Experimental Drag Polars of the Eppler 387 (Re = 2×10^6) for Princeton and three Low Turbulence Tunnels.

Eppler 387 at a Reynolds number of 200,000 with experimental results from NASA Langley, Delft, and Stuttgart. Here, the Princeton data is in close agreement with the three low turbulence wind tunnels. However, the Princeton drag polar is slightly lower than the other polars. This was due to the errors in fabrication of the Princeton airfoil, which had a camber 0.4 percent less than the actual E 387.

B.2.2 Verification Using Inviscid Lift and Empirical Drag

In order to validate the experimental lift and drag characteristics of the Princeton data, lift and drag were approximated using numerical and empirical methods. The lift for the NACA 6409 was calculated inviscidly, and the drag was calculated empirically.

B.2.2.1 Inviscid Lift

Since available viscous numerical codes could not accurately calculate lift within the low Reynolds number regime (as discussed in Appendix B.1), lift was determined inviscidly using a NASA-developed numerical code (Eppler and Somers, 1980), in order to confirm the validity of the Princeton data. Given the pressure distribution (C_p) form this code, the sectional lift coefficient could be determined through the following relationship:

$$C_l = \frac{1}{c} \int_{L.E.}^{T.E.} (C_{p_l} - C_{p_u})\, dx \qquad \text{(B.2.1)}$$

Here, Cp_u and Cp_l represent the coefficients of pressure (which vary in the chordwise, or x, direction) on the upper and lower surfaces respectively. The airfoil's chordlength is represented by c. T.E. and L.E. represent the x-positions of the trailing and leading edges. This integral expression for the airfoil section lift coefficient is geometrically interpreted as the area between the Cp_u and Cp_l curves as shown in Figure B.2.2.

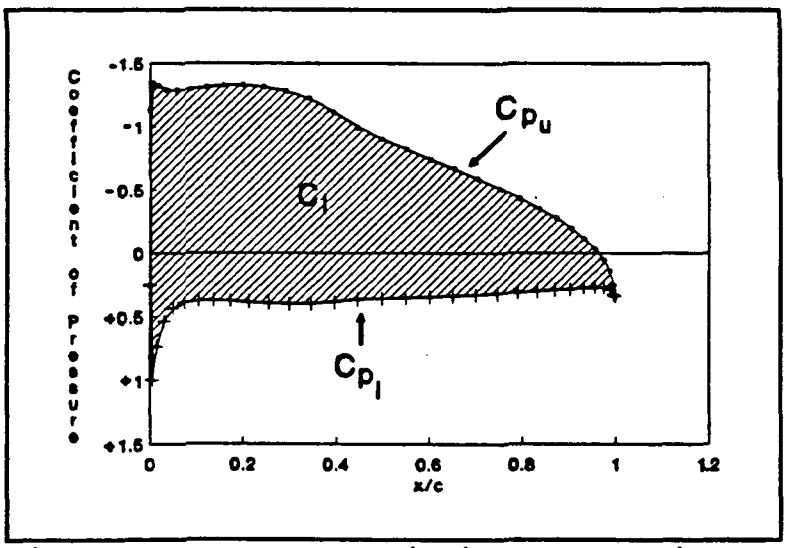

Figure B.2.2: Geometric interpretation of inviscid lift coefficient for the NACA 6409 at an angle of attack of 4 degrees.

The C_l expression may be approximated by a numerical integration, such as the following Riemann summation based on average pressure coefficients:

$$C_l = \sum_{i=1}^{i=n-1} (\overline{C_{p_{l_i}}} \Delta x_i) - \sum_{j=1}^{j=m-1} (\overline{C_{p_{u_j}}} \Delta x_j) \qquad \text{(B.2.2)}$$

Here, m and n represent the number of known coefficients on the upper and lower surface respectively. The values of (i = 1) and (j = 1) correspond to the leading edge and the values of (i = n) and (j = m) correspond to the trailing edge. The C_p expressions represent the average coefficients of pressure of the i^{th} (and j^{th}) value and its corresponding consecutive term and, Δx represents the chordwise distance between these points:

$$\overline{C_{p_{l_i}}} = \frac{1}{2} (C_{p_{l_i}} + C_{p_{l_{i+1}}}) \qquad \text{(B.2.3)}$$

$$\Delta x_i = x_{i+1} - x_i \qquad \text{(B.2.4)}$$

$$\overline{C_{p_{u_j}}} = \frac{1}{2} (C_{p_{u_j}} + C_{p_{u_{j+1}}}) \qquad \text{(B.2.5)}$$

$$\Delta x_j = x_{j+1} - x_j \qquad \text{(B.2.6)}$$

A simple computer program was written to apply Equation B.2.2. This was then applied to the Eppler output of the NACA 6409 using approximately 30 points on each surface. These results were compared to experimental results as shown in Figure B.2.3. As seen, the inviscid lift characteristics

correlate reasonably well with the data, suggesting that the Princeton data is reliable. Disagreement of the two is attributed to the negligence of viscosity in the calculated values.

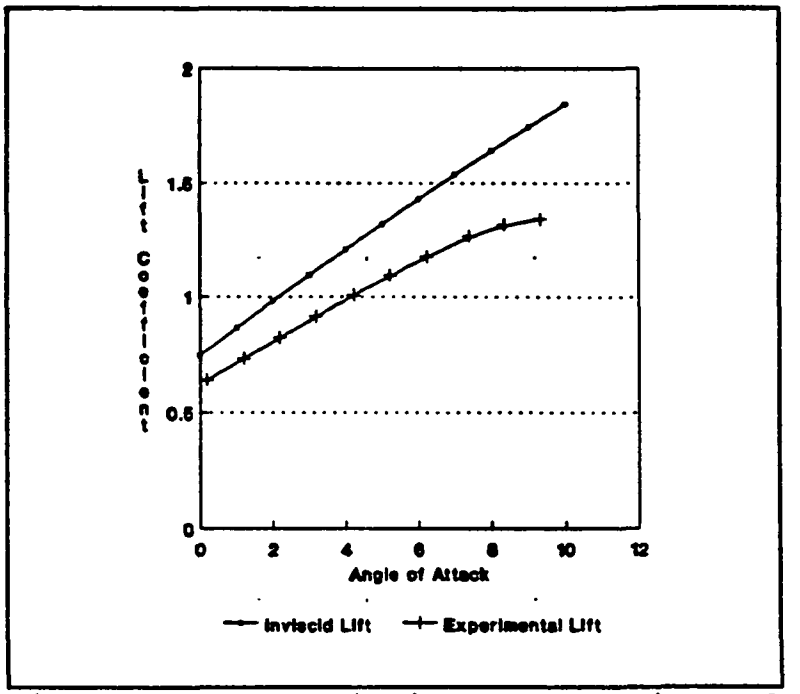

Figure B.2.3: Inviscid vs. Experimental Lift for the NACA 6409.

B.2.2.2 Empirical Drag

In order to verify the experimental data, it was necessary to determine drag empirically. This was calculated by expressing drag as a parabolic function of lift, or

$$C_d = C_{d_p} + kC_l^2 \qquad \text{(B.2.7)}$$

Here, Cd_p represents the sectional parasitic drag, C_l is the sectional lift coefficient, and k is an empirical constant.

For most thin airfoil sections, this value is around $0.38Cd_p$ (Shevell, 1983), thus Equation B.2.7 becomes:

$$C_d = C_{d_p}(1 + 0.38C_l^2) \qquad \text{(B.2.8)}$$

Sectional parasitic drag (Cd_p), which is defined as the portion of drag independent of lift, includes pressure and skin friction drag. For thin airfoils, this may be expressed as the drag over a flat plate corrected for pressure drag and fineness effects (Shevell, 1983), such as

$$C_{d_p} = KC_f\left(\frac{S_{WET}}{S_{REF}}\right) \qquad \text{(B.2.9)}$$

Here, K represents the empirical correction factor, C_f is the skin friction coefficient from flat plate theory, and (S_{wet}/S_{ref}) is the ratio of the section's wetted area to its reference (planform) area. For thin airfoils, this ratio is typically 2.04 due to curvature of the airfoil (Shevell, 1983).

For airfoils, the empirical correction factor K may be expressed as

$$K = \left[1 + Z\left(\frac{t}{c}\right) + 100\left(\frac{t}{c}\right)^4\right] \qquad \text{(B.2.10)}$$

where t/c is the airfoil's maximum thickness as a percentage of chord, and Z (which is equal to $(2 - M^2)/(1 - M^2)^{0.5}$) quantifies the compressibility effects as a function of free-stream Mach number. For operational velocities of the

configuration (less than 10 meters per second), the square of Mach number may be neglected, resulting in a compressibility factor of 2. For the NACA 6409, the maximum thickness is 9 percent of chord. These values result in an 18.7 percent correction to flat plate theory (K = 1.187).

The skin friction coefficient (C_f) in Equation B.2.9 may be expressed as a function of Reynolds number (Re) using flat plate theory (Schlichting, 1979) for both laminar and turbulent flow:

$$C_f = \frac{1.328}{\sqrt{Re}} \qquad \text{laminar (B.2.11)}$$

$$C_f = 0.027 Re^{-\frac{1}{7}} \qquad \text{turbulent (B.2.12)}$$

At Re = 200,100, this corresponds to a laminar C_f of 0.00297 and a turbulent C_f of 0.00472. These values resulted in a laminar parasitic drag coefficient of 0.007186 and a turbulent parasitic drag coefficient 0.01173, resulting in two drag curves as functions of lift:

$$C_l = 0.00719(1+0.38C_l^2) \qquad \text{lam (B.2.13)}$$

$$C_d = 0.01143(1+0.38C_l^2) \qquad \text{turb (B.2.14)}$$

Since the flow over a low Reynolds number airfoil experiences transition (as discussed in Appendix B.1), it follows that the experimental sectional drag should occur between the empirical

laminar and turbulent curves (provided that separation does not occur).

Using calculated inviscid lift coefficients, the plots of Equations B.2.13 and B.2.14 were compared with the experimental data. As seen in Figure B.2.4, the experimental sectional drag coefficients fell between the empirical curves for laminar and turbulent flow, indicating the reliability of the Princeton data.

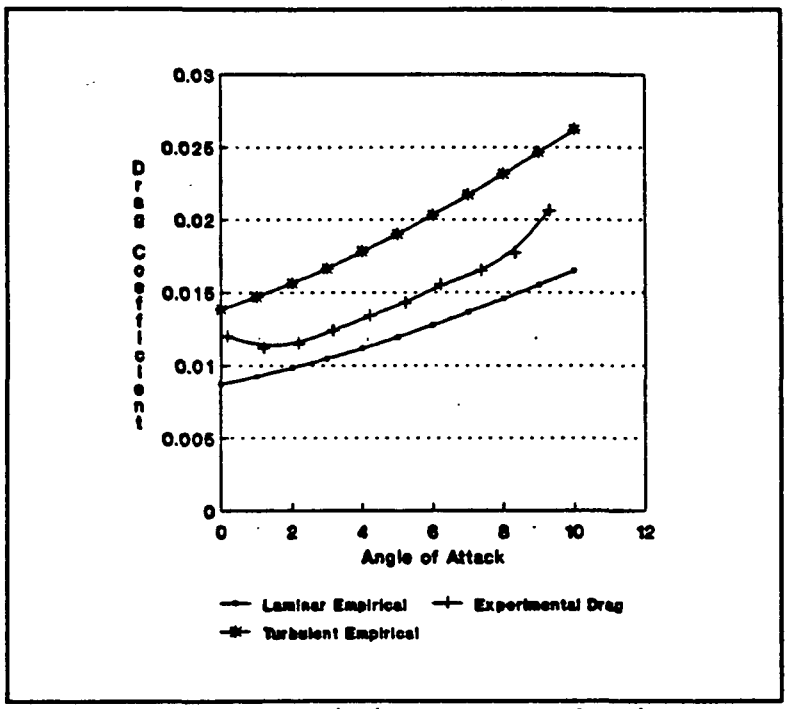

Figure B.2.4: Empirical Drag (laminar and turbulent) vs. Experimental Drag for the NACA 6409 at Re = 200,100.

B.3 GLAUERT METHOD OF ARBITRARY WING LOADING

In a method developed by H.A. Glauert in 1937, a Fourier series approximation may be used to express an arbitrary symmetrical circulation distribution about a wing. Combining this series with finite wing theory, the absolute angle of attack (α_a) for an arbitrary wing can be expressed as

$$\alpha_a(\theta) = \frac{m_{os}C_s}{m_o C}\sum_{n=1}^{\infty} A_n \sin(n\theta) + \frac{m_{os}C_s}{4b}\sum_{n=1}^{\infty} nA_n \frac{\sin(n\theta)}{\sin\theta} \quad \text{(B.3.1)}$$

Here, the A_n terms represent constants of the Glauert Fourier summation. These constants quantify the planform geometry, twist and the angle of attack of a particular wing configuration. The term m_o represents the sectional lift curve slope, c is the sectional chordlength and, b is the wing span. The subscript 's' represents the section characteristics at the wing's plane of symmetry (y = 0). The quantity θ represents a trigonometric transformed position along the wing span as shown in Figure B.3.1.

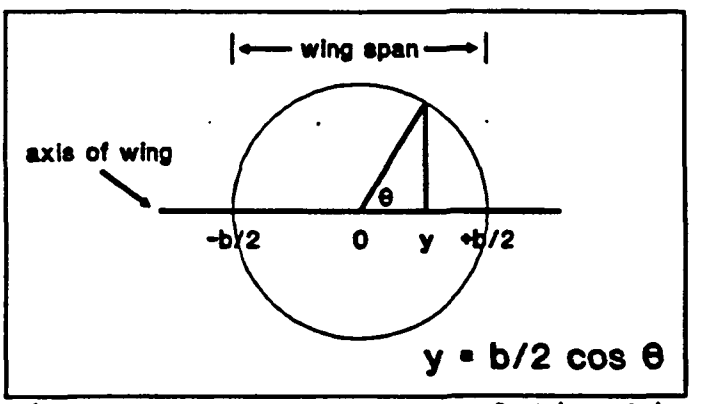

Figure B.3.1: The relationship between spanwise position y and the angle θ.

Using the Glauert constants, finite lift and induced drag may be determined for any given symmetric wing. through the following relationships:

$$C_L = \frac{m_{os} c_s \pi b}{4S} A_1 \qquad \text{(B.3.2)}$$

and

$$C_{D_i} = (C_{D_i})_{el} (1+\sigma) \qquad \text{(B.3.3)}$$

where:

$$\sigma = \sum_{n=2}^{\infty} \left(\frac{n A_n^{\,2}}{A_1^{\,2}} \right) \qquad \text{(B.3.4)}$$

$$(C_{D_i})_{el} = \frac{C_L^{\,2}}{\pi (AR)} \qquad \text{(B.3.5)}$$

Equation B.3.2 is the expression for the finite lift coefficient of the wing. S represents the planform area and A_1 represents the first constant of the Glauert series. Equation B.3.3 expresses the induced drag as a deviation of elliptical induced drag ($(C_{Di})_{el}$) through the quantity σ. For a given wing geometry the only unknowns, as can be seen in the above relationships, are the A_n terms. Thus, to calculate finite lift and induced drag it is necessary to solve for the unknown Glauert constants.

In the case of a rectangular wing, Equation B.3.1 simplifies to

$$\alpha_a = \sum_{n=1}^{\infty} A_n \sin(n\theta) \left(1 + \frac{m_o}{4(AR)} \frac{n}{\sin\theta}\right) \qquad \text{(B.3.6)}$$

It can be shown for a symmetric wing that the even A_n terms drop out, leaving only the odd terms. In addition, these Glauert constants decrease in value by approximately an order of magnitude between consecutive odd terms. Therefore the first four odd A_n terms are sufficient for solving lift and drag of an untwisted rectangular wing. This may be accomplished by selecting four arbitrary points along the wing. For an untwisted wing the absolute angle of attack remains constant for all θ. By selecting four points along the span of the wing (corresponding to four θ values) four simultaneous equations may be written. Using these, the first four odd values of A_n may then be solved to determine the finite lift and induced drag.

B.4 DETERMINATION OF CONFIGURATIONAL LIFT AND DRAG

B.4.1 Configurational Lift

In calculating total configurational lift, all contributions were referenced to the wing's planform area. It was assumed that the lifting effects of the fuselage pod, support booms, and vertical tails were negligible. The expression used to determine the total configurational lift is:

$$C_L = C_{L_w} + \eta_t \left(\frac{S_{tail}}{S_{wing}} \right) C_{L_t} \qquad \text{(B.4.1)}$$

where C_{L_w} and C_{L_t} represent the finite lift coefficients of the wing and tail (with respect to their own planforms) and (S_{tail}/S_{wing}) is the ratio of the tail planform area to the wing planform area. The (η_t) represents the efficiency of the tail (defined as the ratio of dynamic pressure at the tail to that of free stream), which is assumed to be 0.85.

B.4.2 Configurational Drag

In determining total configurational drag,

$$C_D = C_{D_p} + \frac{C_L^2}{\pi (AR)\, e} \qquad \text{(B.4.2)}$$

where C_{D_p} represents the configuration's parasitic drag, C_L is

the total configurational lift, AR is the wing's aspect ratio, and e is the Oswald airplane efficiency.

The total configurational parasitic drag (C_{D_p}), which is drag independent of finite lift, can be expressed as a summation of individual component contributions using an empirical modification of flat plate theory:

$$C_{D_p} = \sum_i K_i C_{f_i} \left(\frac{S_{WET_i}}{S_{REF}} \right) \qquad \text{(B.4.3)}$$

Here, K represents an empirical modification of flat plate theory (due to pressure drag and finite effects over a body), C_f represents the skin friction coefficient from flat plate theory, and (S_{wet}/S_{ref}) is the ratio of the wetted area of the component to the reference (or planform) area. In the case of the presented configuration, the expression for parasitic drag becomes

$$C_{D_p} = K_w C_{f_w} + K_{HT} C_{f_{HT}} \left(\frac{S_{HT}}{S_w} \right) + K_{VT} C_{f_{VT}} \left(\frac{S_{VT}}{S_w} \right) + \ldots$$

$$\ldots + K_b C_{f_b} \left(\frac{S_b}{S_w} \right) + K_p C_{f_p} \left(\frac{S_p}{S_w} \right) \qquad \text{(B.4.4)}$$

where w denotes the wing; HT the horizontal tail; VT the vertical tail; b the booms; and p the pod (or shortened fuselage). Since C_{D_p} is the drag independent of finite lift, KC_f for aerodynamic surfaces is merely the sectional drag

coefficients, thus:

$$C_{D_p} = C_{d_w} + C_{d_{HT}} \left(\frac{S_{HT}}{S_w} \right) + K_{VT} C_{f_{VT}} \left(\frac{S_{VT}}{S_w} \right) + \ldots$$

$$\ldots + K_b C_{f_b} \left(\frac{S_b}{S_w} \right) + K_p C_{f_p} \left(\frac{S_p}{S_w} \right) \qquad \text{(B.4.5)}$$

For non-lifting surfaces, the correction factor K may be obtained empirically as a function of the fineness ratio (component length to diameter)(Shevell, 1983). The skin friction coefficient C_f may be determined from flat plate theory. Since transition would occur over the configuration, turbulent skin friction is assumed for all components:

$$C_f = 0.027 Re_l^{-\frac{1}{7}} \qquad \text{(B.4.6)}$$

where the Reynolds number is based on the component length. This assumption yielded conservative (over-predicted) drag estimates, creating a marginal error which was beneficial to the design process.

The Oswald airplane efficiency, e, may be determined using the following relationship:

(B.4.7)

where σ represents a correction factor due to the deviation from elliptic (as determined by the Glauert Method in Appendix

B.3), s is an empirical correction factor for wing loading interference due to the fuselage, and k represents the empirical effects of configurational parasitic drag on induced drag. For the case of unswept wings, this value is typically $0.38C_{D_p}$ (Shevell, 1983). For a fuselage-diameter to wingspan ratio of approximately 0.03, the fuselage interference correction factor s is approximately 0.99 (Shevell, 1983). The correction factor for deviation from elliptic drag, σ, is approximately 0.08 for the configuration's wing. These values result in an Oswald airplane efficiency of approximately 76 percent for a velocity of 8 meters per second. (This value varies with velocity due to the Reynolds number dependency of C_f and C_{D_p}.) These calculations were used to determine the configurational lift to drag curve in Section 4.12.

APPENDIX C

STRUCTURAL ANALYSIS

C.1 ANSYS WING DATA

C.1.1 Wing Nodal Locations

LIST ALL SELECTED NODE DSYS= 0

NODE	X	Y	Z	THXY	THYZ	THXZ
1	.00000E+00	.00000E+00	.00000E+00	.00	.00	.00
2	.15590E-01	.15460E-01	.00000E+00	.00	.00	.00
3	.51220E-01	.29600E-01	.00000E+00	.00	.00	.00
4	.14572	.43890E-01	.00000E+00	.00	.00	.00
5	.23495	.39440E-01	.00000E+00	.00	.00	.00
6	.31915	.26640E-01	.00000E+00	.00	.00	.00
7	.42400	.00000E+00	.00000E+00	.00	.00	.00
8	.31685	.69300E-02	.00000E+00	.00	.00	.00
9	.23337	.81600E-02	.00000E+00	.00	.00	.00
10	.14726	.60400E-02	.00000E+00	.00	.00	.00
11	.57690E-01	-.21800E-02	.00000E+00	.00	.00	.00
12	.12610E-01	-.49100E-02	.00000E+00	.00	.00	.00
13	.00000E+00	.00000E+00	.10320	.00	.00	.00
14	.15590E-01	.15460E-01	.10320	.00	.00	.00
15	.51220E-01	.29600E-01	.10320	.00	.00	.00
16	.14572	.43890E-01	.10320	.00	.00	.00
17	.23495	.39440E-01	.10320	.00	.00	.00
18	.31915	.26640E-01	.10320	.00	.00	.00
19	.42400	.00000E+00	.10320	.00	.00	.00
20	.31685	.69300E-02	.10320	.00	.00	.00

NODE	X	Y	Z	THXY	THYZ	THXZ
21	.23337	.81600E-02	.10320	.00	.00	.00
22	.14726	.60400E-02	.10320	.00	.00	.00
23	.57690E-01	-.21800E-02	.10320	.00	.00	.00
24	.12610E-01	-.49100E-02	.10320	.00	.00	.00
25	.00000E+00	.00000E+00	.20640	.00	.00	.00
26	.15590E-01	.15460E-01	.20640	.00	.00	.00
27	.51220E-01	.29600E-01	.20640	.00	.00	.00
28	.14572	.43890E-01	.20640	.00	.00	.00
29	.23495	.39440E-01	.20640	.00	.00	.00
30	.31915	.26640E-01	.20640	.00	.00	.00
31	.42400	.00000E+00	.20640	.00	.00	.00
32	.31685	.69300E-02	.20640	.00	.00	.00
33	.23337	.81600E-02	.20640	.00	.00	.00
34	.14726	.60400E-02	.20640	.00	.00	.00
35	.57690E-01	-.21800E-02	.20640	.00	.00	.00
36	.12610E-01	-.49100E-02	.20640	.00	.00	.00
37	.00000E+00	.00000E+00	.30960	.00	.00	.00
38	.15590E-01	.15460E-01	.30960	.00	.00	.00
39	.51220E-01	.29600E-01	.30960	.00	.00	.00
40	.14572	.43890E-01	.30960	.00	.00	.00

NODE	X	Y	Z	THXY	THYZ	THXZ
41	.23495	.39440E-01	.30960	.00	.00	.00
42	.31915	.26640E-01	.30960	.00	.00	.00
43	.42400	.00000E+00	.30960	.00	.00	.00
44	.31685	.69300E-02	.30960	.00	.00	.00
45	.23337	.81600E-02	.30960	.00	.00	.00
46	.14726	.60400E-02	.30960	.00	.00	.00
47	.57690E-01	-.21800E-02	.30960	.00	.00	.00
48	.12610E-01	-.49100E-02	.30960	.00	.00	.00
49	.00000E+00	.00000E+00	.41280	.00	.00	.00
50	.15590E-01	.15460E-01	.41280	.00	.00	.00
51	.51220E-01	.29600E-01	.41280	.00	.00	.00

52	.14572	.43890E-01	.41280	.00	.00	.00
53	.23495	.39440E-01	.41280	.00	.00	.00
54	.31915	.26640E-01	.41280	.00	.00	.00
55	.42400	.00000E+00	.41280	.00	.00	.00
56	.31685	.69300E-02	.41280	.00	.00	.00
57	.23337	.81600E-02	.41280	.00	.00	.00
58	.14726	.60400E-02	.41280	.00	.00	.00
59	.57690E-01	-.21800E-02	.41280	.00	.00	.00
60	.12610E-01	-.49100E-02	.41280	.00	.00	.00

NODE	X	Y	Z	THXY	THYZ	THXZ
61	.00000E+00	.00000E+00	.51600	.00	.00	.00
62	.15590E-01	.15460E-01	.51600	.00	.00	.00
63	.51220E-01	.29600E-01	.51600	.00	.00	.00
64	.14572	.43890E-01	.51600	.00	.00	.00
65	.23495	.39440E-01	.51600	.00	.00	.00
66	.31915	.26640E-01	.51600	.00	.00	.00
67	.42400	.00000E+00	.51600	.00	.00	.00
68	.31685	.69300E-02	.51600	.00	.00	.00
69	.23337	.81600E-02	.51600	.00	.00	.00
70	.14726	.60400E-02	.51600	.00	.00	.00
71	.57690E-01	-.21800E-02	.51600	.00	.00	.00
72	.12610E-01	-.49100E-02	.51600	.00	.00	.00
73	.00000E+00	.00000E+00	.61920	.00	.00	.00
74	.15590E-01	.15460E-01	.61920	.00	.00	.00
75	.51220E-01	.29600E-01	.61920	.00	.00	.00
76	.14572	.43890E-01	.61920	.00	.00	.00
77	.23495	.39440E-01	.61920	.00	.00	.00
78	.31915	.26640E-01	.61920	.00	.00	.00
79	.42400	.00000E+00	.61920	.00	.00	.00
80	.31685	.69300E-02	.61920	.00	.00	.00

NODE	X	Y	Z	THXY	THYZ	THXZ
81	.23337	.81600E-02	.61920	.00	.00	.00
82	.14726	.60400E-02	.61920	.00	.00	.00
83	.57690E-01	-.21800E-02	.61920	.00	.00	.00
84	.12610E-01	-.49100E-02	.61920	.00	.00	.00
85	.00000E+00	.00000E+00	.72240	.00	.00	.00
86	.15590E-01	.15460E-01	.72240	.00	.00	.00
87	.51220E-01	.29600E-01	.72240	.00	.00	.00
88	.14572	.43890E-01	.72240	.00	.00	.00
89	.23495	.39440E-01	.72240	.00	.00	.00
90	.31915	.26640E-01	.72240	.00	.00	.00
91	.42400	.00000E+00	.72240	.00	.00	.00
92	.31685	.69300E-02	.72240	.00	.00	.00
93	.23337	.81600E-02	.72240	.00	.00	.00
94	.14726	.60400E-02	.72240	.00	.00	.00
95	.57690E-01	-.21800E-02	.72240	.00	.00	.00
96	.12610E-01	-.49100E-02	.72240	.00	.00	.00
97	.00000E+00	.00000E+00	.82560	.00	.00	.00
98	.15590E-01	.15460E-01	.82560	.00	.00	.00
99	.51220E-01	.29600E-01	.82560	.00	.00	.00
100	.14572	.43890E-01	.82560	.00	.00	.00

NODE	X	Y	Z	THXY	THYZ	THXZ
101	.23495	.39440E-01	.82560	.00	.00	.00
102	.31915	.26640E-01	.82560	.00	.00	.00
103	.42400	.00000E+00	.82560	.00	.00	.00
104	.31685	.69300E-02	.82560	.00	.00	.00
105	.23337	.81600E-02	.82560	.00	.00	.00

106	.14726	.60400E-02	.82560	.00	.00	.00
107	.57690E-01	-.21800E-02	.82560	.00	.00	.00
108	.12610E-01	-.49100E-02	.82560	.00	.00	.00
109	.00000E+00	.00000E+00	.92880	.00	.00	.00
110	.15590E-01	.15460E-01	.92880	.00	.00	.00
111	.51220E-01	.29600E-01	.92880	.00	.00	.00
112	.14572	.43890E-01	.92880	.00	.00	.00
113	.23495	.39440E-01	.92880	.00	.00	.00
114	.31915	.26640E-01	.92880	.00	.00	.00
115	.42400	.00000E+00	.92880	.00	.00	.00
116	.31685	.69300E-02	.92880	.00	.00	.00
117	.23337	.81600E-02	.92880	.00	.00	.00
118	.14726	.60400E-02	.92880	.00	.00	.00
119	.57690E-01	-.21800E-02	.92880	.00	.00	.00
120	.12610E-01	-.49100E-02	.92880	.00	.00	.00

NODE	X	Y	Z	THXY	THYZ	THXZ
121	.00000E+00	.00000E+00	1.0320	.00	.00	.00
122	.15590E-01	.15460E-01	1.0320	.00	.00	.00
123	.51220E-01	.29600E-01	1.0320	.00	.00	.00
124	.14572	.43890E-01	1.0320	.00	.00	.00
125	.23495	.39440E-01	1.0320	.00	.00	.00
126	.31915	.26640E-01	1.0320	.00	.00	.00
127	.42400	.00000E+00	1.0320	.00	.00	.00
128	.31685	.69300E-02	1.0320	.00	.00	.00
129	.23337	.81600E-02	1.0320	.00	.00	.00
130	.14726	.60400E-02	1.0320	.00	.00	.00
131	.57690E-01	-.21800E-02	1.0320	.00	.00	.00
132	.12610E-01	-.49100E-02	1.0320	.00	.00	.00
133	.00000E+00	.00000E+00	1.1352	.00	.00	.00
134	.15590E-01	.15460E-01	1.1352	.00	.00	.00
135	.51220E-01	.29600E-01	1.1352	.00	.00	.00
136	.14572	.43890E-01	1.1352	.00	.00	.00
137	.23495	.39440E-01	1.1352	.00	.00	.00
138	.31915	.26640E-01	1.1352	.00	.00	.00
139	.42400	.00000E+00	1.1352	.00	.00	.00
140	.31685	.69300E-02	1.1352	.00	.00	.00

NODE	X	Y	Z	THXY	THYZ	THXZ
141	.23337	.81600E-02	1.1352	.00	.00	.00
142	.14726	.60400E-02	1.1352	.00	.00	.00
143	.57690E-01	-.21800E-02	1.1352	.00	.00	.00
144	.12610E-01	-.49100E-02	1.1352	.00	.00	.00
145	.00000E+00	.00000E+00	1.2384	.00	.00	.00
146	.15590E-01	.15460E-01	1.2384	.00	.00	.00
147	.51220E-01	.29600E-01	1.2384	.00	.00	.00
148	.14572	.43890E-01	1.2384	.00	.00	.00
149	.23495	.39440E-01	1.2384	.00	.00	.00
150	.31915	.26640E-01	1.2384	.00	.00	.00
151	.42400	.00000E+00	1.2384	.00	.00	.00
152	.31685	.69300E-02	1.2384	.00	.00	.00
153	.23337	.81600E-02	1.2384	.00	.00	.00
154	.14726	.60400E-02	1.2384	.00	.00	.00
155	.57690E-01	-.21800E-02	1.2384	.00	.00	.00
156	.12610E-01	-.49100E-02	1.2384	.00	.00	.00
157	.00000E+00	.00000E+00	1.3416	.00	.00	.00
158	.15590E-01	.15460E-01	1.3416	.00	.00	.00
159	.51220E-01	.29600E-01	1.3416	.00	.00	.00
160	.14572	.43890E-01	1.3416	.00	.00	.00

NODE	X	Y	Z	THXY	THYZ	THXZ
161	.23495	.39440E-01	1.3416	.00	.00	.00
162	.31915	.26640E-01	1.3416	.00	.00	.00
163	.42400	.00000E+00	1.3416	.00	.00	.00
164	.31685	.69300E-02	1.3416	.00	.00	.00
165	.23337	.81600E-02	1.3416	.00	.00	.00
166	.14726	.60400E-02	1.3416	.00	.00	.00
167	.57690E-01	-.21800E-02	1.3416	.00	.00	.00
168	.12610E-01	-.49100E-02	1.3416	.00	.00	.00
169	.00000E+00	.00000E+00	1.4448	.00	.00	.00
170	.15590E-01	.15460E-01	1.4448	.00	.00	.00
171	.51220E-01	.29600E-01	1.4448	.00	.00	.00
172	.14572	.43890E-01	1.4448	.00	.00	.00
173	.23495	.39440E-01	1.4448	.00	.00	.00
174	.31915	.26640E-01	1.4448	.00	.00	.00
175	.42400	.00000E+00	1.4448	.00	.00	.00
176	.31685	.69300E-02	1.4448	.00	.00	.00
177	.23337	.81600E-02	1.4448	.00	.00	.00
178	.14726	.60400E-02	1.4448	.00	.00	.00
179	.57690E-01	-.21800E-02	1.4448	.00	.00	.00
180	.12610E-01	-.49100E-02	1.4448	.00	.00	.00

NODE	X	Y	Z	THXY	THYZ	THXZ
181	.00000E+00	.00000E+00	1.5480	.00	.00	.00
182	.15590E-01	.15460E-01	1.5480	.00	.00	.00
183	.51220E-01	.29600E-01	1.5480	.00	.00	.00
184	.14572	.43890E-01	1.5480	.00	.00	.00
185	.23495	.39440E-01	1.5480	.00	.00	.00
186	.31915	.26640E-01	1.5480	.00	.00	.00
187	.42400	.00000E+00	1.5480	.00	.00	.00
188	.31685	.69300E-02	1.5480	.00	.00	.00
189	.23337	.81600E-02	1.5480	.00	.00	.00
190	.14726	.60400E-02	1.5480	.00	.00	.00
191	.57690E-01	-.21800E-02	1.5480	.00	.00	.00
192	.12610E-01	-.49100E-02	1.5480	.00	.00	.00
193	.00000E+00	.00000E+00	1.6512	.00	.00	.00
194	.15590E-01	.15460E-01	1.6512	.00	.00	.00
195	.51220E-01	.29600E-01	1.6512	.00	.00	.00
196	.14572	.43890E-01	1.6512	.00	.00	.00
197	.23495	.39440E-01	1.6512	.00	.00	.00
198	.31915	.26640E-01	1.6512	.00	.00	.00
199	.42400	.00000E+00	1.6512	.00	.00	.00
200	.31685	.69300E-02	1.6512	.00	.00	.00

NODE	X	Y	Z	THXY	THYZ	THXZ
201	.23337	.81600E-02	1.6512	.00	.00	.00
202	.14726	.60400E-02	1.6512	.00	.00	.00
203	.57690E-01	-.21800E-02	1.6512	.00	.00	.00
204	.12610E-01	-.49100E-02	1.6512	.00	.00	.00

C.1.2 Wing Element Listing

50	2	1	5	0	13	25	0	
51	2	1	5	0	25	37	0	
52	2	1	5	0	37	49	0	
53	2	1	5	0	49	61	0	
54	2	1	5	0	61	73	0	
55	2	1	5	0	73	85	0	
56	2	1	5	0	85	97	0	
57	2	1	5	0	97	109	0	
58	2	1	5	0	109	121	0	
59	2	1	5	0	121	133	0	
60	2	1	5	0	133	145	0	

ELEM	MAT	TYP	REL	ESYS	NODES			
61	2	1	5	0	145	157	0	
62	2	1	5	0	157	169	0	
63	2	1	5	0	169	181	0	
64	2	1	5	0	181	193	0	
65	2	1	6	0	7	19	0	
66	2	1	6	0	19	31	0	
67	2	1	6	0	31	43	0	
68	2	1	6	0	43	55	0	
69	2	1	6	0	55	67	0	
70	2	1	6	0	67	79	0	
71	2	1	6	0	79	91	0	
72	2	1	6	0	91	103	0	
73	2	1	6	0	103	115	0	
74	2	1	6	0	115	127	0	
75	2	1	6	0	127	139	0	
76	2	1	6	0	139	151	0	
77	2	1	6	0	151	163	0	
78	2	1	6	0	163	175	0	
79	2	1	6	0	175	187	0	
80	2	1	6	0	187	199	0	

ELEM	MAT	TYP	REL	ESYS	NODES			
81	2	2	3	0	1	2	12	12
82	2	2	3	0	2	3	11	12
83	2	2	3	0	3	4	10	11
84	2	2	3	0	4	5	9	10
85	2	2	3	0	5	6	8	9
86	2	2	3	0	6	7	8	8
87	2	2	3	0	13	14	24	24
88	2	2	3	0	14	15	23	24
89	2	2	3	0	15	16	22	23
90	2	2	3	0	16	17	21	22
91	2	2	3	0	17	18	20	21
92	2	2	3	0	18	19	20	20
93	2	2	3	0	25	26	36	36
94	2	2	3	0	26	27	35	36
95	2	2	3	0	27	28	34	35
96	2	2	3	0	28	29	33	34
97	2	2	3	0	29	30	32	33
98	2	2	3	0	30	31	32	32
99	2	2	3	0	37	38	48	48
100	2	2	3	0	38	39	47	48

ELEM	MAT	TYP	REL	ESYS	NODES

101	2	2	3	0	39	40	46	47
102	2	2	3	0	40	41	45	46
103	2	2	3	0	41	42	44	45
104	2	2	3	0	42	43	44	44
105	2	2	3	0	49	50	60	60
106	2	2	3	0	50	51	59	60
107	2	2	3	0	51	52	58	59
108	2	2	3	0	52	53	57	58
109	2	2	3	0	53	54	56	57
110	2	2	3	0	54	55	56	56
111	2	2	3	0	61	62	72	72
112	2	2	3	0	62	63	71	72
113	2	2	3	0	63	64	70	71
114	2	2	3	0	64	65	69	70
115	2	2	3	0	65	66	68	69
116	2	2	3	0	66	67	68	68
117	2	2	3	0	73	74	84	84
118	2	2	3	0	74	75	83	84
119	2	2	3	0	75	76	82	83
120	2	2	3	0	76	77	81	82

ELEM	MAT	TYP	REL	ESYS	NODES			
121	2	2	3	0	77	78	80	81
122	2	2	3	0	78	79	80	80
123	2	2	3	0	85	86	96	96
124	2	2	3	0	86	87	95	96
125	2	2	3	0	87	88	94	95
126	2	2	3	0	88	89	93	94
127	2	2	3	0	89	90	92	93
128	2	2	3	0	90	91	92	92
129	2	2	3	0	97	98	108	108
130	2	2	3	0	98	99	107	108
131	2	2	3	0	99	100	106	107
132	2	2	3	0	100	101	105	106
133	2	2	3	0	101	102	104	105
134	2	2	3	0	102	103	104	104
135	2	2	3	0	109	110	120	120
136	2	2	3	0	110	111	119	120
137	2	2	3	0	111	112	118	119
138	2	2	3	0	112	113	117	118
139	2	2	3	0	113	114	116	117
140	2	2	3	0	114	115	116	116

ELEM	MAT	TYP	REL	ESYS	NODES			
141	2	2	3	0	121	122	132	132
142	2	2	3	0	122	123	131	132
143	2	2	3	0	123	124	130	131
144	2	2	3	0	124	125	129	130
145	2	2	3	0	125	126	128	129
146	2	2	3	0	126	127	128	128
147	2	2	3	0	133	134	144	144
148	2	2	3	0	134	135	143	144
149	2	2	3	0	135	136	142	143
150	2	2	3	0	136	137	141	142
151	2	2	3	0	137	138	140	141
152	2	2	3	0	138	139	140	140
153	2	2	3	0	145	146	156	156
154	2	2	3	0	146	147	155	156

155	2	2	3	0	147	148	154	155
156	2	2	3	0	148	149	153	154
157	2	2	3	0	149	150	152	153
158	2	2	3	0	150	151	152	152
159	2	2	3	0	157	158	168	168
160	2	2	3	0	158	159	167	168

ELEM	MAT	TYP	REL	ESYS	NODES			
161	2	2	3	0	159	160	166	167
162	2	2	3	0	160	161	165	166
163	2	2	3	0	161	162	164	165
164	2	2	3	0	162	163	164	164
165	2	2	3	0	169	170	180	180
166	2	2	3	0	170	171	179	180
167	2	2	3	0	171	172	178	179
168	2	2	3	0	172	173	177	178
169	2	2	3	0	173	174	176	177
170	2	2	3	0	174	175	176	176
171	2	2	3	0	181	182	192	192
172	2	2	3	0	182	183	191	192
173	2	2	3	0	183	184	190	191
174	2	2	3	0	184	185	189	190
175	2	2	3	0	185	186	188	189
176	2	2	3	0	186	187	188	188
177	2	2	3	0	193	194	204	204
178	2	2	3	0	194	195	203	204
179	2	2	3	0	195	196	202	203
180	2	2	3	0	196	197	201	202

ELEM	MAT	TYP	REL	ESYS	NODES			
181	2	2	3	0	197	198	200	201
182	2	2	3	0	198	199	200	200
183	3	2	4	0	1	12	24	13
184	3	2	4	0	12	11	23	24
185	3	2	4	0	11	10	22	23
186	3	2	4	0	10	9	21	22
187	3	2	4	0	9	8	20	21
188	3	2	4	0	8	7	19	20
189	3	2	4	0	13	24	36	25
190	3	2	4	0	24	23	35	36
191	3	2	4	0	23	22	34	35
192	3	2	4	0	22	21	33	34
193	3	2	4	0	21	20	32	33
194	3	2	4	0	20	19	31	32
195	3	2	4	0	25	36	48	37
196	3	2	4	0	36	35	47	48
197	3	2	4	0	35	34	46	47
198	3	2	4	0	34	33	45	46
199	3	2	4	0	33	32	44	45
200	3	2	4	0	32	31	43	44

ELEM	MAT	TYP	REL	ESYS	NODES			
201	3	2	4	0	37	48	60	49
202	3	2	4	0	48	47	59	60
203	3	2	4	0	47	46	58	59
204	3	2	4	0	46	45	57	58
205	3	2	4	0	45	44	56	57

206	3	2	4	0	44	43	55	56
207	3	2	4	0	49	60	72	61
208	3	2	4	0	60	59	71	72
209	3	2	4	0	59	58	70	71
210	3	2	4	0	58	57	69	70
211	3	2	4	0	57	56	68	69
212	3	2	4	0	56	55	67	68
213	3	2	4	0	61	72	84	73
214	3	2	4	0	72	71	83	84
215	3	2	4	0	71	70	82	83
216	3	2	4	0	70	69	81	82
217	3	2	4	0	69	68	80	81
218	3	2	4	0	68	67	79	80
219	3	2	4	0	73	84	96	85
220	3	2	4	0	84	83	95	96

ELEM	MAT	TYP	REL	ESYS	NODES			
221	3	2	4	0	83	82	94	95
222	3	2	4	0	82	81	93	94
223	3	2	4	0	81	80	92	93
224	3	2	4	0	80	79	91	92
225	3	2	4	0	85	96	108	97
226	3	2	4	0	96	95	107	108
227	3	2	4	0	95	94	106	107
228	3	2	4	0	94	93	105	106
229	3	2	4	0	93	92	104	105
230	3	2	4	0	92	91	103	104
231	3	2	4	0	97	108	120	109
232	3	2	4	0	108	107	119	120
233	3	2	4	0	107	106	118	119
234	3	2	4	0	106	105	117	118
235	3	2	4	0	105	104	116	117
236	3	2	4	0	104	103	115	116
237	3	2	4	0	109	120	132	121
238	3	2	4	0	120	119	131	132
239	3	2	4	0	119	118	130	131
240	3	2	4	0	118	117	129	130

ELEM	MAT	TYP	REL	ESYS	NODES			
241	3	2	4	0	117	116	128	129
242	3	2	4	0	116	115	127	128
243	3	2	4	0	121	132	144	133
244	3	2	4	0	132	131	143	144
245	3	2	4	0	131	130	142	143
246	3	2	4	0	130	129	141	142
247	3	2	4	0	129	128	140	141
248	3	2	4	0	128	127	139	140
249	3	2	4	0	133	144	156	145
250	3	2	4	0	144	143	155	156
251	3	2	4	0	143	142	154	155
252	3	2	4	0	142	141	153	154
253	3	2	4	0	141	140	152	153
254	3	2	4	0	140	139	151	152
255	3	2	4	0	145	156	168	157
256	3	2	4	0	156	155	167	168
257	3	2	4	0	155	154	166	167
258	3	2	4	0	154	153	165	166
259	3	2	4	0	153	152	164	165

260	3	2	4	0	152	151	163	164

ELEM	MAT	TYP	REL	ESYS	NODES			
261	3	2	4	0	157	168	180	169
262	3	2	4	0	168	167	179	180
263	3	2	4	0	167	166	178	179
264	3	2	4	0	166	165	177	178
265	3	2	4	0	165	164	176	177
266	3	2	4	0	164	163	175	176
267	3	2	4	0	169	180	192	181
268	3	2	4	0	180	179	191	192
269	3	2	4	0	179	178	190	191
270	3	2	4	0	178	177	189	190
271	3	2	4	0	177	176	188	189
272	3	2	4	0	176	175	187	188
273	3	2	4	0	181	192	204	193
274	3	2	4	0	192	191	203	204
275	3	2	4	0	191	190	202	203
276	3	2	4	0	190	189	201	202
277	3	2	4	0	189	188	200	201
278	3	2	4	0	188	187	199	200

C.1.3 - Wing Material Properties

Material	Young's Modulus (EX) (GPa)
Pultruded Carbon65 Fiber Composite (GoodFellow, 1990)	
Balsa (Dimwoodie, 1989)	6.274
Mylar Monocoat (TopFlite, 1969)	3.630

C.1.4 - WING GEOMETRY DATA

STIF4; 3-Dimensional Beam Elements:

Part	NSET	Area (m^2) R1	I_{zz} (m^4) R2	I_{yy} (m^4) R3	Z-thk. (m) R4	Y-thk. (m) R5
Carbon Spar Cap	1	$8.55e^{-6}$	$5.82e^{-12}$	$5.82e^{-12}$	.0033	.0033
Leading Edge	5	$8.84e^{-5}$	$1.24e^{-9}$	$1.24e^{-9}$	.015	.015
Trailing Edge	6	$9.45e^{-5}$	$3.82e^{-9}$	$3.82e^{-9}$	.027	.007

STIF41; 4 Node Shell Element:

Part	NSET	Thickness (m) R1
Spar Web	2	.00318
Ribs	3	.00158
Mylar	4	.00003

C.1.5 Wing Nodal Displacements

PRINT NODAL DISPLACEMENTS

***** POST1 NODAL DISPLACEMENT LISTING *****

LOAD STEP 1 ITERATION= 1 SECTION= 1
TIME= .00000E+00 LOAD CASE= 1

THE FOLLOWING X,Y,Z DISPLACEMENTS ARE IN GLOBAL COORDINATES

NODE	UX	UY	UZ	ROTX	RO
1	.00000000E+00	.00000000E+00	.00000000E+00	.00000000E+00	.0000
2	.00000000E+00	.00000000E+00	.00000000E+00	.00000000E+00	.0000
3	.00000000E+00	.00000000E+00	.00000000E+00	.00000000E+00	.0000
4	.00000000E+00	.00000000E+00	.00000000E+00	.00000000E+00	.0000
5	.00000000E+00	.00000000E+00	.00000000E+00	.00000000E+00	.0000
6	.00000000E+00	.00000000E+00	.00000000E+00	.00000000E+00	.0000
7	.00000000E+00	.00000000E+00	.00000000E+00	.00000000E+00	.0000
8	.00000000E+00	.00000000E+00	.00000000E+00	.00000000E+00	.0000
9	.00000000E+00	.00000000E+00	.00000000E+00	.00000000E+00	.0000
10	.00000000E+00	.00000000E+00	.00000000E+00	.00000000E+00	.0000
11	.00000000E+00	.00000000E+00	.00000000E+00	.00000000E+00	.0000
12	.00000000E+00	.00000000E+00	.00000000E+00	.00000000E+00	.0000

***** POST1 NODAL DISPLACEMENT LISTING *****

LOAD STEP 1 ITERATION= 1 SECTION= 1
TIME= .00000E+00 LOAD CASE= 1

THE FOLLOWING X,Y,Z DISPLACEMENTS ARE IN GLOBAL COORDINATES

NODE	UX	UY	UZ	ROTX	RO
13	.12520343E-04	.16983654E-02	.72736173E-04	-.32635314E-01	-.8239
14	.75068716E-04	.16348626E-02			
15	.13680980E-03	.14834871E-02			
16	.20528913E-03	.10535320E-02	-.40215910E-03	-.19753906E-01	.3797
17	.18473500E-03	.61162026E-03			
18	.11809620E-03	.17575225E-03			
19	-.26179677E-04	-.37708870E-03	.32825189E-04	.72832489E-02	-.4893
20	.13938944E-04	.18759382E-03	.10047757E-03		
21	.24690337E-04	.61999921E-03	.17389684E-03		
22	.24718776E-04	.10419640E-02	.32894111E-03	-.19584847E-01	.3211
23	-.10952096E-05	.14558434E-02	.29104237E-03		
24	-.78616414E-05	.16471752E-02	.26148763E-03		

***** POST1 NODAL DISPLACEMENT LISTING *****

LOAD STEP 1 ITERATION= 1 SECTION= 1
TIME= .00000E+00 LOAD CASE= 1

THE FOLLOWING X,Y,Z DISPLACEMENTS ARE IN GLOBAL COORDINATES

NODE	UX	UY	UZ	ROTX	RO
25	-.42147360E-04	.66466805E-02	.14404209E-03	-.62676202E-01	-.8956
26	.23399500E-03	.63677418E-02			
27	.49237263E-03	.57230340E-02			
28	.76441943E-03	.39716768E-02	-.75374150E-03	-.36440098E-01	.7032
29	.68577543E-03	.22646185E-02			
30	.43947081E-03	.60587288E-03			
31	-.99893828E-04	-.15015663E-02	.65183654E-04	.14517188E-01	-.9466

32	.43384787E-04	.65173972E-03	.20070124E-03		
33	.77813250E-04	.22952008E-02	.34469572E-03		
34	.51310974E-04	.39393523E-02	.60808590E-03	-.36176666E-01	.2071
35	-.87057849E-04	.56050435E-02	.57021793E-03		
36	-.13054876E-03	.64213810E-02	.50632010E-03		

***** POST1 NODAL DISPLACEMENT LISTING *****

LOAD STEP 1 ITERATION= 1 SECTION= 1
TIME= .00000E+00 LOAD CASE= 1

THE FOLLOWING X,Y,Z DISPLACEMENTS ARE IN GLOBAL COORDINATES

NODE	UX	UY	UZ	ROTX	RO
37	-.16336341E-03	.14506398E-01	.21289535E-03	-.88986418E-01	-.1447
38	.46686449E-03	.13870689E-01			
39	.10490188E-02	.12410595E-01			
40	.16490972E-02	.84963667E-02	-.10582704E-02	-.50847174E-01	.1004
41	.14698453E-02	.47442544E-02			
42	.93118612E-03	.11502085E-02			
43	-.22167207E-03	-.33743179E-02	.96615101E-04	.21776753E-01	-.1407
44	.80854082E-04	.12490977E-02	.29659208E-03		
45	.14433262E-03	.48111152E-02	.49802947E-03		
46	.69291145E-04	.84287965E-02	.84356311E-03	-.50441993E-01	.1459
47	-.25770305E-03	.12144616E-01	.81718201E-03		
48	-.36406835E-03	.13992531E-01	.72729997E-03		

***** POST1 NODAL DISPLACEMENT LISTING *****

LOAD STEP 1 ITERATION= 1 SECTION= 1
TIME= .00000E+00 LOAD CASE= 1

THE FOLLOWING X,Y,Z DISPLACEMENTS ARE IN GLOBAL COORDINATES

NODE	UX	UY	UZ	ROTX	RO
49	-.33863464E-03	.24883732E-01	.27839641E-03	-.11152496	-.1931
50	.76825022E-03	.23767417E-01			
51	.17857517E-02	.21209625E-01			
52	.28242263E-02	.14389638E-01	-.13195164E-02	-.63018925E-01	.1267
53	.25074879E-02	.79011380E-02			
54	.15765437E-02	.17319551E-02			
55	-.38929190E-03	-.59935727E-02	.12670287E-03	.28957381E-01	-.1837
56	.12446545E-03	.19010953E-02	.38357776E-03		
57	.22418015E-03	.80164482E-02	.63055031E-03		
58	.82128708E-04	.14275036E-01	.10397072E-02	-.62511295E-01	.1048
59	-.49952944E-03	.20744503E-01	.10312203E-02		
60	-.69067447E-03	.23981071E-01	.92168512E-03		

***** POST1 NODAL DISPLACEMENT LISTING *****

LOAD STEP 1 ITERATION= 1 SECTION= 1
TIME= .00000E+00 LOAD CASE= 1

THE FOLLOWING X,Y,Z DISPLACEMENTS ARE IN GLOBAL COORDINATES

NODE	UX	UY	UZ	ROTX	RO
61	-.55910078E-03	.37408542E-01	.33979643E-03	-.13067374	-.2330
62	.11302146E-02	.35704940E-01			
63	.26796797E-02	.31805764E-01			
64	.42536839E-02	.21434990E-01	-.15408380E-02	-.73199894E-01	.1497

65	.37686507E-02	.11603112E-01			
66	.23581466E-02	.22892049E-02			
67	-.59987914E-03	-.93430543E-02	.15508235E-03	.35903504E-01	-.2237
68	.17162332E-03	.25440919E-02	.46027243E-03		
69	.31524612E-03	.11777622E-01	.74247946E-03		
70	.91325824E-04	.21262848E-01	.12005429E-02	-.72595728E-01	.7529
71	-.80138260E-03	.31097295E-01	.12141735E-02		
72	-.10960636E-02	.36030786E-01	.10916907E-02		

***** POST1 NODAL DISPLACEMENT LISTING *****

LOAD STEP 1 ITERATION= 1 SECTION= 1
TIME= .00000E+00 LOAD CASE= 1

THE FOLLOWING X,Y,Z DISPLACEMENTS ARE IN GLOBAL COORDINATES

NODE	UX	UY	UZ	ROTX	RO
73	-.81765633E-03	.51751097E-01	.39651922E-03	-.14680813	-.2671
74	.15454755E-02	.49368045E-01			
75	.37105491E-02	.43916805E-01			
76	.59048635E-02	.29435671E-01	-.17255938E-02	-.81566181E-01	.1697
77	.52253219E-02	.15731061E-01			
78	.32593084E-02	.27718101E-02			
79	-.84953362E-03	-.13391490E-01	.18145412E-03	.42484335E-01	-.2593
80	.22098599E-03	.31261371E-02	.52665528E-03		
81	.41602816E-03	.15974135E-01	.83540821E-03		
82	.97915712E-04	.29196882E-01	.13298581E-02	-.80880368E-01	.5292
83	-.11542810E-02	.42926691E-01	.13688286E-02		
84	-.15685679E-02	.49823710E-01	.12387234E-02		

***** POST1 NODAL DISPLACEMENT LISTING *****

LOAD STEP 1 ITERATION= 1 SECTION= 1
TIME= .00000E+00 LOAD CASE= 1

THE FOLLOWING X,Y,Z DISPLACEMENTS ARE IN GLOBAL COORDINATES

NODE	UX	UY	UZ	ROTX	RO
85	-.11088941E-02	.67616364E-01	.44814550E-03	-.16022810	-.2964
86	.20069170E-02	.64474338E-01			
87	.48598144E-02	.57289200E-01			
88	.77477828E-02	.38214360E-01	-.18771365E-02	-.88307754E-01	.1869
89	.68512030E-02	.20179099E-01			
90	.42640151E-02	.31405248E-02			
91	-.11334267E-02	-.18095971E-01	.20558813E-03	.48604409E-01	-.2900
92	.27198989E-03	.36061789E-02	.58330879E-03		
93	.52514888E-03	.20498837E-01	.91125387E-03		
94	.10234860E-03	.37901037E-01	.14313054E-02	-.87551063E-01	.3344
95	-.15510632E-02	.55984375E-01	.14977359E-02		
96	-.20988007E-02	.65075034E-01	.13644542E-02		

***** POST1 NODAL DISPLACEMENT LISTING *****

LOAD STEP 1 ITERATION= 1 SECTION= 1
TIME= .00000E+00 LOAD CASE= 1

THE FOLLOWING X,Y,Z DISPLACEMENTS ARE IN GLOBAL COORDINATES

NODE	UX	UY	UZ	ROTX	RO
97	-.14280869E-02	.84737481E-01	.49439462E-03	-.17118597	-.3213

NODE	UX	UY	UZ	ROTX	RO
133	-.25098433E-02	.14133648	.59963217E-03	-.19162751	-.3715
134	.41850168E-02	.13458541			
135	.10309707E-01	.11915416			
136	.16501159E-01	.78219943E-01	-.22178087E-02	-.10261084	.2309
137	.14574102E-01	.39559518E-01			
138	.90285631E-02	.30720079E-02			
139	-.25181834E-02	-.42371201E-01	.27720386E-03	.67387673E-01	-.3709
140	.48606278E-03	.40687685E-02	.72775598E-03		
141	.10204696E-02	.40244332E-01	.10810879E-02		
142	.10368830E-03	.77551580E-01	.16272104E-02	-.10167265	-.2060
143	-.34550233E-02	.11635214	.18029044E-02		
144	-.46362413E-02	.13587588	.16824900E-02		

***** POST1 NODAL DISPLACEMENT LISTING *****

LOAD STEP 1 ITERATION= 1 SECTION= 1
TIME= .00000E+00 LOAD CASE= 1

THE FOLLOWING X,Y,Z DISPLACEMENTS ARE IN GLOBAL COORDINATES

NODE	UX	UY	UZ	ROTX	RO
145	-.28985169E-02	.16130520	.62348006E-03	-.19514839	-.3813
146	.47839350E-02	.15355827			
147	.11811744E-01	.13585130			
148	.18916132E-01	.88881196E-01	-.22530733E-02	-.10389235	.2367
149	.16705215E-01	.44521077E-01			
150	.10342251E-01	.26533413E-02			
151	-.29070997E-02	-.49491621E-01	.28860158E-03	.70491152E-01	-.3821
152	.53996585E-03	.37971196E-02	.74793297E-03		
153	.11532647E-02	.45306773E-01	.10998320E-02		
154	.10110125E-03	.88114712E-01	.16400518E-02	-.10292994	-.2967
155	-.39827738E-02	.13263597	.18385955E-02		
156	-.53385230E-02	.15503911	.17237165E-02		

***** POST1 NODAL DISPLACEMENT LISTING *****

LOAD STEP 1 ITERATION= 1 SECTION= 1
TIME= .00000E+00 LOAD CASE= 1

THE FOLLOWING X,Y,Z DISPLACEMENTS ARE IN GLOBAL COORDINATES

NODE	UX	UY	UZ	ROTX	RO
157	-.32969017E-02	.18157941	.64178421E-03	-.19763148	-.3910
158	.53948715E-02	.17281470			
159	.13345669E-01	.15278190			
160	.21382914E-01	.99643346E-01	-.22748280E-02	-.10459307	.2411
161	.18881743E-01	.49458979E-01			
162	.11683410E-01	.20945308E-02			
163	-.33050752E-02	-.56896073E-01	.29737086E-03	.72882379E-01	-.3880
164	.59427965E-03	.33884875E-02	.76405529E-03		
165	.12879708E-02	.50347764E-01	.11135926E-02		
166	.97332652E-04	.98776569E-01	.16446561E-02	-.10361305	-.4545
167	-.45233049E-02	.14914418	.18638337E-02		
168	-.60574174E-02	.17449010	.17537164E-02		

***** POST1 NODAL DISPLACEMENT LISTING *****

LOAD STEP 1 ITERATION= 1 SECTION= 1

TIME= .00000E+00 LOAD CASE= 1

THE FOLLOWING X,Y,Z DISPLACEMENTS ARE IN GLOBAL COORDINATES

NODE	UX	UY	UZ	ROTX	RO
169	-.37061514E-02	.20207986	.65462258E-03	-.19963575	-.4023
170	.60143992E-02	.19227758			
171	.14905493E-01	.16987426			
172	.23890611E-01	.11045491	-.22861736E-02	-.10487819	.2448
173	.21091946E-01	.54350333E-01			
174	.13043779E-01	.14117126E-02			
175	-.37052124E-02	-.64507766E-01	.30353053E-03	.74495183E-01	-.3858
176	.65201819E-03	.28577040E-02	.77692753E-03		
177	.14249418E-02	.55343887E-01	.11243906E-02		
178	.91425761E-04	.10948613	.16439638E-02	-.10388005	-.6975
179	-.50772498E-02	.16580623	.18817067E-02		
180	-.67934387E-02	.19415125	.17760395E-02		

***** POST1 NODAL DISPLACEMENT LISTING *****

LOAD STEP 1 ITERATION= 1 SECTION= 1
TIME= .00000E+00 LOAD CASE= 1

THE FOLLOWING X,Y,Z DISPLACEMENTS ARE IN GLOBAL COORDINATES

NODE	UX	UY	UZ	ROTX	RO
181	-.41335255E-02	.22277947	.66212797E-03	-.20150185	-.4317
182	.66377041E-02	.21191748			
183	.16487524E-01	.18709463			
184	.26433206E-01	.12128114	-.22903238E-02	-.10489986	.2475
185	.23327186E-01	.59174051E-01			
186	.14415844E-01	.61905205E-03			
187	-.40961798E-02	-.72244416E-01	.30714048E-03	.75309627E-01	-.3684
188	.71829817E-03	.22175728E-02	.78495188E-03		
189	.15638353E-02	.60273912E-01	.11321333E-02		
190	.79722962E-04	.12020859	.16409686E-02	-.10389062	-.1874
191	-.56510355E-02	.18258807	.18940032E-02		
192	-.75544340E-02	.21399348	.17914349E-02		

***** POST1 NODAL DISPLACEMENT LISTING *****

LOAD STEP 1 ITERATION= 1 SECTION= 1
TIME= .00000E+00 LOAD CASE= 1

THE FOLLOWING X,Y,Z DISPLACEMENTS ARE IN GLOBAL COORDINATES

NODE	UX	UY	UZ	ROTX	RO
193	-.45952282E-02	.24363684	.66456966E-03	-.20240857	-.4552
194	.72460040E-02	.23169710			
195	.18073674E-01	.20441028			
196	.28994227E-01	.13210418	-.22908718E-02	-.10486173	.2484
197	.25575630E-01	.63937751E-01			
198	.15798809E-01	-.24316643E-03			
199	-.44668315E-02	-.80030944E-01	.30831865E-03	.75521475E-01	-.3545
200	.79957119E-03	.15077144E-02	.78445673E-03		
201	.17059053E-02	.65145619E-01	.11267132E-02		
202	.53196570E-04	.13092748	.16393862E-02	-.10385252	-.2918
203	-.62609979E-02	.19945815	.18936260E-02		

C.1.6 SIG1 and SIG2: Maximum and Minimum Stresses in Wing Beam Elements at End

PRINT ELEMENT STRESS ITEMS PER ELEMENT

***** POST1 ELEMENT STRESS LISTING *****

LOAD STEP 1 ITERATION= 1 SECTION= 1
TIME= .00000E+00 LOAD CASE= 1

ELEM	STR1	STRS
1	-.22618908E+09	-.28040668E+09
2	.23025782E+09	.18410598E+09
3	-.19960055E+09	-.24328425E+09
4	.19443370E+09	.15720218E+09
5	-.17224059E+09	-.21137137E+09
6	.16442113E+09	.13220713E+09
7	-.14790858E+09	-.18118038E+09
8	.13721087E+09	.10986990E+09
9	-.12526659E+09	-.15353005E+09
10	.11280250E+09	89800588.
11	-.10455343E+09	-.12818150E+09
12	90969311.	71927743.
13	-85717416.	-.10517941E+09
14	71641302.	56150810.

***** POST1 ELEMENT STRESS LISTING *****

LOAD STEP 1 ITERATION= 1 SECTION= 1
TIME= .00000E+00 LOAD CASE= 1

ELEM	STR1	STRS
15	-68781327.	-84491692.
16	54722442.	42402040.
17	-53736868.	-66103866.
18	40135703.	30610576.
19	-40576771.	-49999086.
20	27813979.	20718114.
21	-29288952.	-36162771.
22	17701630.	12675145.
23	-19848387.	-24574103.
24	9744300.7	6431845.7
25	-12201789.	-15202410.
26	3875869.4	1924102.3
27	-6283417.4	-8008561.8
28	40698.137	-912818.71

***** POST1 ELEMENT STRESS LISTING *****

LOAD STEP 1 ITERATION= 1 SECTION= 1
TIME= .00000E+00 LOAD CASE= 1

ELEM	STR1	STRS
29	-2106753.2	-3121208.5
30	-1757823.7	-2015210.6
31	-83290.598	-606996.18
32	-700453.58	-1292853.1
33	.00000000E+00	.00000000E+00
34	.00000000E+00	.00000000E+00
35	.00000000E+00	.00000000E+00
36	.00000000E+00	.00000000E+00
37	.00000000E+00	.00000000E+00

38	.00000000E+00	.00000000E+00
39	.00000000E+00	.00000000E+00
40	.00000000E+00	.00000000E+00
41	.00000000E+00	.00000000E+00
42	.00000000E+00	.00000000E+00

***** POST1 ELEMENT STRESS LISTING *****

LOAD STEP 1 ITERATION= 1 SECTION= 1
TIME= .00000E+00 LOAD CASE= 1

ELEM	STR1	STRS
43	.00000000E+00	.00000000E+00
44	.00000000E+00	.00000000E+00
45	.00000000E+00	.00000000E+00
46	.00000000E+00	.00000000E+00
47	.00000000E+00	.00000000E+00
48	.00000000E+00	.00000000E+00
49	20090668.	-11246739.
50	19316278.	-10646252.
51	17341099.	-8969290.2
52	15323348.	-7359129.4
53	13385731.	-5920154.9
54	11621552.	-4724676.7
55	9989956.7	-3712762.3
56	8465536.3	-2842145.2

***** POST1 ELEMENT STRESS LISTING *****

LOAD STEP 1 ITERATION= 1 SECTION= 1
TIME= .00000E+00 LOAD CASE= 1

ELEM	STR1	STRS
57	7040594.0	-2091327.2
58	5716620.2	-1450908.0
59	4497973.5	-917208.38
60	3399174.8	-499530.26
61	2464041.4	-238455.25
62	1781788.7	-220781.66
63	1385709.7	-473135.76
64	1189168.1	-892284.83
65	4007091.5	-15904.756
66	3858390.0	76048.183
67	3848806.4	-27083.535
68	3736569.2	-78223.557
69	3580179.1	-129541.83
70	3360312.2	-153791.30

***** POST1 ELEMENT STRESS LISTING *****

LOAD STEP 1 ITERATION= 1 SECTION= 1
TIME= .00000E+00 LOAD CASE= 1

ELEM	STR1	STRS
71	3095058.4	-160624.85
72	2802407.2	-160124.83
73	2494374.2	-157591.39
74	2178399.4	-155179.07
75	1858740.6	-153330.43
76	1534645.1	-148806.18

77	1196392.0	-130142.88
78	825713.05	-76763.308
79	533648.60	-94718.287
80	389695.05	-246442.95
81	.00000000E+00	.00000000E+00
82	.00000000E+00	.00000000E+00
83	.00000000E+00	.00000000E+00
84	.00000000E+00	.00000000E+00

***** POST1 ELEMENT STRESS LISTING *****

LOAD STEP 1 ITERATION= 1 SECTION= 1
TIME= .00000E+00 LOAD CASE= 1

ELEM	STR1	STRS
85	.00000000E+00	.00000000E+00
86	.00000000E+00	.00000000E+00
87	.00000000E+00	.00000000E+00
88	.00000000E+00	.00000000E+00
89	.00000000E+00	.00000000E+00
90	.00000000E+00	.00000000E+00
91	.00000000E+00	.00000000E+00
92	.00000000E+00	.00000000E+00
93	.00000000E+00	.00000000E+00
94	.00000000E+00	.00000000E+00
95	.00000000E+00	.00000000E+00
96	.00000000E+00	.00000000E+00
97	.00000000E+00	.00000000E+00
98	.00000000E+00	.00000000E+00

***** POST1 ELEMENT STRESS LISTING *****

LOAD STEP 1 ITERATION= 1 SECTION= 1
TIME= .00000E+00 LOAD CASE= 1

ELEM	STR1	STRS
99	.00000000E+00	.00000000E+00
100	.00000000E+00	.00000000E+00
101	.00000000E+00	.00000000E+00
102	.00000000E+00	.00000000E+00
103	.00000000E+00	.00000000E+00
104	.00000000E+00	.00000000E+00
105	.00000000E+00	.00000000E+00
106	.00000000E+00	.00000000E+00
107	.00000000E+00	.00000000E+00
108	.00000000E+00	.00000000E+00
109	.00000000E+00	.00000000E+00
110	.00000000E+00	.00000000E+00
111	.00000000E+00	.00000000E+00
112	.00000000E+00	.00000000E+00

***** POST1 ELEMENT STRESS LISTING *****

LOAD STEP 1 ITERATION= 1 SECTION= 1
TIME= .00000E+00 LOAD CASE= 1

ELEM	STR1	STRS
113	.00000000E+00	.00000000E+00
114	.00000000E+00	.00000000E+00
115	.00000000E+00	.00000000E+00

116	.00000000E+00	.00000000E+00
117	.00000000E+00	.00000000E+00
118	.00000000E+00	.00000000E+00
119	.00000000E+00	.00000000E+00
120	.00000000E+00	.00000000E+00
121	.00000000E+00	.00000000E+00
122	.00000000E+00	.00000000E+00
123	.00000000E+00	.00000000E+00
124	.00000000E+00	.00000000E+00
125	.00000000E+00	.00000000E+00
126	.00000000E+00	.00000000E+00

***** POST1 ELEMENT STRESS LISTING *****

LOAD STEP 1 ITERATION= 1 SECTION= 1
TIME= .00000E+00 LOAD CASE= 1

ELEM	STR1	STRS
127	.00000000E+00	.00000000E+00
128	.00000000E+00	.00000000E+00
129	.00000000E+00	.00000000E+00
130	.00000000E+00	.00000000E+00
131	.00000000E+00	.00000000E+00
132	.00000000E+00	.00000000E+00
133	.00000000E+00	.00000000E+00
134	.00000000E+00	.00000000E+00
135	.00000000E+00	.00000000E+00
136	.00000000E+00	.00000000E+00
137	.00000000E+00	.00000000E+00
138	.00000000E+00	.00000000E+00
139	.00000000E+00	.00000000E+00
140	.00000000E+00	.00000000E+00

***** POST1 ELEMENT STRESS LISTING *****

LOAD STEP 1 ITERATION= 1 SECTION= 1
TIME= .00000E+00 LOAD CASE= 1

ELEM	STR1	STRS
141	.00000000E+00	.00000000E+00
142	.00000000E+00	.00000000E+00
143	.00000000E+00	.00000000E+00
144	.00000000E+00	.00000000E+00
145	.00000000E+00	.00000000E+00
146	.00000000E+00	.00000000E+00
147	.00000000E+00	.00000000E+00
148	.00000000E+00	.00000000E+00
149	.00000000E+00	.00000000E+00
150	.00000000E+00	.00000000E+00
151	.00000000E+00	.00000000E+00
152	.00000000E+00	.00000000E+00
153	.00000000E+00	.00000000E+00
154	.00000000E+00	.00000000E+00

***** POST1 ELEMENT STRESS LISTING *****

LOAD STEP 1 ITERATION= 1 SECTION= 1
TIME= .00000E+00 LOAD CASE= 1

ELEM	STR1	STRS

155	.00000000E+00	.00000000E+00
156	.00000000E+00	.00000000E+00
157	.00000000E+00	.00000000E+00
158	.00000000E+00	.00000000E+00
159	.00000000E+00	.00000000E+00
160	.00000000E+00	.00000000E+00
161	.00000000E+00	.00000000E+00
162	.00000000E+00	.00000000E+00
163	.00000000E+00	.00000000E+00
164	.00000000E+00	.00000000E+00
165	.00000000E+00	.00000000E+00
166	.00000000E+00	.00000000E+00
167	.00000000E+00	.00000000E+00
168	.00000000E+00	.00000000E+00

***** POST1 ELEMENT STRESS LISTING *****

LOAD STEP 1 ITERATION= 1 SECTION= 1
TIME= .00000E+00 LOAD CASE= 1

ELEM	STR1	STRS
169	.00000000E+00	.00000000E+00
170	.00000000E+00	.00000000E+00
171	.00000000E+00	.00000000E+00
172	.00000000E+00	.00000000E+00
173	.00000000E+00	.00000000E+00
174	.00000000E+00	.00000000E+00
175	.00000000E+00	.00000000E+00
176	.00000000E+00	.00000000E+00
177	.00000000E+00	.00000000E+00
178	.00000000E+00	.00000000E+00
179	.00000000E+00	.00000000E+00
180	.00000000E+00	.00000000E+00
181	.00000000E+00	.00000000E+00
182	.00000000E+00	.00000000E+00

***** POST1 ELEMENT STRESS LISTING *****

LOAD STEP 1 ITERATION= 1 SECTION= 1
TIME= .00000E+00 LOAD CASE= 1

ELEM	STR1	STRS
183	.00000000E+00	.00000000E+00
184	.00000000E+00	.00000000E+00
185	.00000000E+00	.00000000E+00
186	.00000000E+00	.00000000E+00
187	.00000000E+00	.00000000E+00
188	.00000000E+00	.00000000E+00
189	.00000000E+00	.00000000E+00
190	.00000000E+00	.00000000E+00
191	.00000000E+00	.00000000E+00
192	.00000000E+00	.00000000E+00
193	.00000000E+00	.00000000E+00
194	.00000000E+00	.00000000E+00
195	.00000000E+00	.00000000E+00
196	.00000000E+00	.00000000E+00

***** POST1 ELEMENT STRESS LISTING *****

LOAD STEP 1 ITERATION= 1 SECTION= 1

TIME= .00000E+00 LOAD CASE= 1

ELEM	STR1	STRS
197	.00000000E+00	.00000000E+00
198	.00000000E+00	.00000000E+00
199	.00000000E+00	.00000000E+00
200	.00000000E+00	.00000000E+00
201	.00000000E+00	.00000000E+00
202	.00000000E+00	.00000000E+00
203	.00000000E+00	.00000000E+00
204	.00000000E+00	.00000000E+00
205	.00000000E+00	.00000000E+00
206	.00000000E+00	.00000000E+00
207	.00000000E+00	.00000000E+00
208	.00000000E+00	.00000000E+00
209	.00000000E+00	.00000000E+00
210	.00000000E+00	.00000000E+00

***** POST1 ELEMENT STRESS LISTING *****

LOAD STEP 1 ITERATION= 1 SECTION= 1
TIME= .00000E+00 LOAD CASE= 1

ELEM	STR1	STRS
211	.00000000E+00	.00000000E+00
212	.00000000E+00	.00000000E+00
213	.00000000E+00	.00000000E+00
214	.00000000E+00	.00000000E+00
215	.00000000E+00	.00000000E+00
216	.00000000E+00	.00000000E+00
217	.00000000E+00	.00000000E+00
218	.00000000E+00	.00000000E+00
219	.00000000E+00	.00000000E+00
220	.00000000E+00	.00000000E+00
221	.00000000E+00	.00000000E+00
222	.00000000E+00	.00000000E+00
223	.00000000E+00	.00000000E+00
224	.00000000E+00	.00000000E+00

***** POST1 ELEMENT STRESS LISTING *****

LOAD STEP 1 ITERATION= 1 SECTION= 1
TIME= .00000E+00 LOAD CASE= 1

ELEM	STR1	STRS
225	.00000000E+00	.00000000E+00
226	.00000000E+00	.00000000E+00
227	.00000000E+00	.00000000E+00
228	.00000000E+00	.00000000E+00
229	.00000000E+00	.00000000E+00
230	.00000000E+00	.00000000E+00
231	.00000000E+00	.00000000E+00
232	.00000000E+00	.00000000E+00
233	.00000000E+00	.00000000E+00
234	.00000000E+00	.00000000E+00
235	.00000000E+00	.00000000E+00
236	.00000000E+00	.00000000E+00
237	.00000000E+00	.00000000E+00
238	.00000000E+00	.00000000E+00

***** POST1 ELEMENT STRESS LISTING *****

LOAD STEP 1 ITERATION= 1 SECTION= 1
TIME= .00000E+00 LOAD CASE= 1

ELEM	STR1	STRS
239	.00000000E+00	.00000000E+00
240	.00000000E+00	.00000000E+00
241	.00000000E+00	.00000000E+00
242	.00000000E+00	.00000000E+00
243	.00000000E+00	.00000000E+00
244	.00000000E+00	.00000000E+00
245	.00000000E+00	.00000000E+00
246	.00000000E+00	.00000000E+00
247	.00000000E+00	.00000000E+00
248	.00000000E+00	.00000000E+00
249	.00000000E+00	.00000000E+00
250	.00000000E+00	.00000000E+00
251	.00000000E+00	.00000000E+00
252	.00000000E+00	.00000000E+00

***** POST1 ELEMENT STRESS LISTING *****

LOAD STEP 1 ITERATION= 1 SECTION= 1
TIME= .00000E+00 LOAD CASE= 1

ELEM	STR1	STRS
253	.00000000E+00	.00000000E+00
254	.00000000E+00	.00000000E+00
255	.00000000E+00	.00000000E+00
256	.00000000E+00	.00000000E+00
257	.00000000E+00	.00000000E+00
258	.00000000E+00	.00000000E+00
259	.00000000E+00	.00000000E+00
260	.00000000E+00	.00000000E+00
261	.00000000E+00	.00000000E+00
262	.00000000E+00	.00000000E+00
263	.00000000E+00	.00000000E+00
264	.00000000E+00	.00000000E+00
265	.00000000E+00	.00000000E+00
266	.00000000E+00	.00000000E+00

***** POST1 ELEMENT STRESS LISTING *****

LOAD STEP 1 ITERATION= 1 SECTION= 1
TIME= .00000E+00 LOAD CASE= 1

ELEM	STR1	STRS
267	.00000000E+00	.00000000E+00
268	.00000000E+00	.00000000E+00
269	.00000000E+00	.00000000E+00
270	.00000000E+00	.00000000E+00
271	.00000000E+00	.00000000E+00
272	.00000000E+00	.00000000E+00
273	.00000000E+00	.00000000E+00
274	.00000000E+00	.00000000E+00
275	.00000000E+00	.00000000E+00
276	.00000000E+00	.00000000E+00
277	.00000000E+00	.00000000E+00
278	.00000000E+00	.00000000E+00

MINIMUMS		
ELEMENT	1	1
VALUE	-.22618908E+09	-.28040668E+09

MAXIMUMS		
ELEMENT	2	2
VALUE	.23025782E+09	.18410598E+09

C.1.7 SXX and SYY: Planar Stresses in Wing Shell Elements

PRINT ELEMENT STRESS ITEMS PER ELEMENT

***** POST1 ELEMENT STRESS LISTING *****

LOAD STEP 1 ITERATION= 1 SECTION= 1
TIME= .00000E+00 LOAD CASE= 1

ELEM	SXX	SYY
1	.00000000E+00	.00000000E+00
2	.00000000E+00	.00000000E+00
3	.00000000E+00	.00000000E+00
4	.00000000E+00	.00000000E+00
5	.00000000E+00	.00000000E+00
6	.00000000E+00	.00000000E+00
7	.00000000E+00	.00000000E+00
8	.00000000E+00	.00000000E+00
9	.00000000E+00	.00000000E+00
10	.00000000E+00	.00000000E+00
11	.00000000E+00	.00000000E+00
12	.00000000E+00	.00000000E+00
13	.00000000E+00	.00000000E+00
14	.00000000E+00	.00000000E+00

***** POST1 ELEMENT STRESS LISTING *****

LOAD STEP 1 ITERATION= 1 SECTION= 1
TIME= .00000E+00 LOAD CASE= 1

ELEM	SXX	SYY
15	.00000000E+00	.00000000E+00
16	.00000000E+00	.00000000E+00
17	.00000000E+00	.00000000E+00
18	.00000000E+00	.00000000E+00
19	.00000000E+00	.00000000E+00
20	.00000000E+00	.00000000E+00
21	.00000000E+00	.00000000E+00
22	.00000000E+00	.00000000E+00
23	.00000000E+00	.00000000E+00
24	.00000000E+00	.00000000E+00
25	.00000000E+00	.00000000E+00
26	.00000000E+00	.00000000E+00
27	.00000000E+00	.00000000E+00
28	.00000000E+00	.00000000E+00

***** POST1 ELEMENT STRESS LISTING *****

LOAD STEP 1 ITERATION= 1 SECTION= 1
TIME= .00000E+00 LOAD CASE= 1

ELEM	SXX	SYY
29	.00000000E+00	.00000000E+00
30	.00000000E+00	.00000000E+00
31	.00000000E+00	.00000000E+00
32	.00000000E+00	.00000000E+00
33	-148250.12	10500122.
34	-84600.641	8854954.5
35	-92419.368	7350585.7
36	-89411.537	6025098.9
37	-88478.115	4845194.9

38	-85338.873	3804865.3
39	-80530.239	2896875.0
40	-74316.091	2115188.6
41	-67072.971	1454275.4
42	-58962.412	909563.39

***** POST1 ELEMENT STRESS LISTING *****

LOAD STEP 1 ITERATION= 1 SECTION= 1
TIME= .00000E+00 LOAD CASE= 1

ELEM	SXX	SYY
43	-49893.869	477340.93
44	-39961.319	154120.28
45	-29019.747	-64182.520
46	-24875.906	-182566.37
47	-8670.5175	-197339.61
48	-121460.74	-103183.76
49	.00000000E+00	.00000000E+00
50	.00000000E+00	.00000000E+00
51	.00000000E+00	.00000000E+00
52	.00000000E+00	.00000000E+00
53	.00000000E+00	.00000000E+00
54	.00000000E+00	.00000000E+00
55	.00000000E+00	.00000000E+00
56	.00000000E+00	.00000000E+00

***** POST1 ELEMENT STRESS LISTING *****

LOAD STEP 1 ITERATION= 1 SECTION= 1
TIME= .00000E+00 LOAD CASE= 1

ELEM	SXX	SYY
57	.00000000E+00	.00000000E+00
58	.00000000E+00	.00000000E+00
59	.00000000E+00	.00000000E+00
60	.00000000E+00	.00000000E+00
61	.00000000E+00	.00000000E+00
62	.00000000E+00	.00000000E+00
63	.00000000E+00	.00000000E+00
64	.00000000E+00	.00000000E+00
65	.00000000E+00	.00000000E+00
66	.00000000E+00	.00000000E+00
67	.00000000E+00	.00000000E+00
68	.00000000E+00	.00000000E+00
69	.00000000E+00	.00000000E+00
70	.00000000E+00	.00000000E+00

***** POST1 ELEMENT STRESS LISTING *****

LOAD STEP 1 ITERATION= 1 SECTION= 1
TIME= .00000E+00 LOAD CASE= 1

ELEM	SXX	SYY
71	.00000000E+00	.00000000E+00
72	.00000000E+00	.00000000E+00
73	.00000000E+00	.00000000E+00
74	.00000000E+00	.00000000E+00
75	.00000000E+00	.00000000E+00
76	.00000000E+00	.00000000E+00

116	-133261.16	30435.261
117	-71751.909	-206649.37
118	-273537.10	-27233.473
119	-322567.38	222917.51
120	-336562.70	-213.80645
121	-320245.81	-37023.252
122	-110868.57	26747.260
123	-55247.176	-173961.19
124	-225712.48	-34900.365
125	-248671.77	209644.83
126	-250309.53	1560.9036

***** POST1 ELEMENT STRESS LISTING *****

LOAD STEP 1 ITERATION= 1 SECTION= 1
TIME= .00000E+00 LOAD CASE= 1

ELEM	SXX	SYY
127	-240328.33	-29227.482
128	-90322.755	23304.539
129	-40539.463	-144956.47
130	-183132.16	-39119.642
131	-186886.42	192871.95
132	-180045.54	2816.7062
133	-176072.45	-22834.526
134	-72185.683	20066.185
135	-27787.215	-119034.28
136	-145410.35	-40508.391
137	-135820.79	173484.08
138	-123806.84	3633.3112
139	-125339.76	-17614.420
140	-56590.583	17029.751

***** POST1 ELEMENT STRESS LISTING *****

LOAD STEP 1 ITERATION= 1 SECTION= 1
TIME= .00000E+00 LOAD CASE= 1

ELEM	SXX	SYY
141	-16679.891	-97050.421
142	-113032.37	-38828.637
143	-96616.563	151538.93
144	-83359.554	3999.5466
145	-90664.473	-13857.923
146	-43722.672	14265.295
147	-6524.4557	-81381.069
148	-87414.760	-33156.684
149	-72521.326	126487.30
150	-63625.732	3831.0537
151	-78540.812	-12334.578
152	-33566.840	11928.941
153	2933.3479	-73616.697
154	-69555.140	-23286.169

***** POST1 ELEMENT STRESS LISTING *****

LOAD STEP 1 ITERATION= 1 SECTION= 1
TIME= .00000E+00 LOAD CASE= 1

ELEM	SXX	SYY

155	-64166.621	98235.175
156	-65019.163	3133.4255
157	-89740.130	-13270.524
158	-25157.180	10110.506
159	11820.530	-64448.307
160	-53511.262	-14887.088
161	-53798.436	72548.530
162	-60869.588	2580.0513
163	-91437.599	-13412.621
164	-15147.776	8497.1301
165	-8510.5324	-31498.889
166	-31641.418	-24408.586
167	10623.480	59273.629
168	32626.553	4162.5194

***** POST1 ELEMENT STRESS LISTING *****

LOAD STEP 1 ITERATION= 1 SECTION= 1
TIME= .00000E+00 LOAD CASE= 1

ELEM	SXX	SYY
169	15963.849	804.45645
170	-18591.522	3809.1469
171	-2984.0924	115453.85
172	72500.319	-90124.539
173	243817.91	111592.92
174	387365.92	10330.305
175	485858.05	46397.777
176	51398.948	-2102.3547
177	236060.89	79583.593
178	344089.99	-271897.30
179	1169351.3	202119.50
180	1690939.1	41404.788
181	1691831.5	148153.41
182	360002.73	-40072.234

***** POST1 ELEMENT STRESS LISTING *****

LOAD STEP 1 ITERATION= 1 SECTION= 1
TIME= .00000E+00 LOAD CASE= 1

ELEM	SXX	SYY
183	1843568.9	8357452.2
184	2879421.7	10914878.
185	3184781.8	12286388.
186	2547616.9	8071492.1
187	1431213.8	4525838.1
188	671168.74	1869343.6
189	1662069.1	7825486.9
190	2537536.0	10333637.
191	2621379.7	10613495.
192	2000817.5	7426342.2
193	1149574.6	4416745.7
194	623616.81	1830944.5
195	1506794.0	7092848.5
196	2216040.1	9155682.5

***** POST1 ELEMENT STRESS LISTING *****

LOAD STEP 1 ITERATION= 1 SECTION= 1

TIME= .00000E+00 LOAD CASE= 1

ELEM	SXX	SYY
197	2173270.6	9018464.0
198	1605558.1	6485860.9
199	928567.50	4081404.8
200	603849.96	1764393.6
201	1347540.7	6282520.7
202	1925385.0	7955447.6
203	1825272.3	7573037.9
204	1326627.9	5524991.6
205	797857.44	3632287.5
206	558495.00	1647812.1
207	1199716.9	5531026.6
208	1670028.8	6834673.0
209	1536280.3	6274793.8
210	1110207.6	4624772.1

***** POST1 ELEMENT STRESS LISTING *****

LOAD STEP 1 ITERATION= 1 SECTION= 1
TIME= .00000E+00 LOAD CASE= 1

ELEM	SXX	SYY
211	708660.72	3164531.7
212	505231.12	1507562.5
213	1056916.5	4816210.3
214	1435754.0	5809132.9
215	1280426.2	5114098.5
216	920807.92	3807488.2
217	628697.82	2713995.1
218	451021.93	1358978.9
219	920137.23	4146453.2
220	1218278.9	4871900.1
221	1047282.2	4080789.4
222	747328.70	3075793.4
223	547894.36	2294219.5
224	397456.42	1208647.3

***** POST1 ELEMENT STRESS LISTING *****

LOAD STEP 1 ITERATION= 1 SECTION= 1
TIME= .00000E+00 LOAD CASE= 1

ELEM	SXX	SYY
225	788578.51	3513964.8
226	1015690.5	4015886.3
227	836021.08	3169474.4
228	589533.39	2427263.9
229	467159.33	1908277.2
230	345198.73	1059497.1
231	663390.59	2921650.4
232	828551.17	3238389.8
233	646932.96	2376130.2
234	448523.28	1859515.2
235	388562.02	1557228.9
236	294705.36	913421.36
237	545120.24	2371553.5
238	656606.30	2539778.5

***** POST1 ELEMENT STRESS LISTING *****

LOAD STEP 1 ITERATION= 1 SECTION= 1
TIME= .00000E+00 LOAD CASE= 1

ELEM	SXX	SYY
239	478703.08	1697833.1
240	322688.45	1371659.2
241	311098.76	1242944.5
242	246420.79	772261.24
243	433956.47	1866713.1
244	498917.81	1924088.6
245	328198.38	1132474.0
246	207625.10	965356.09
247	230833.56	969600.51
248	201105.67	638233.12
249	331869.19	1419861.9
250	357778.49	1402796.7
251	194830.98	679410.78
252	102401.40	646314.90

***** POST1 ELEMENT STRESS LISTING *****

LOAD STEP 1 ITERATION= 1 SECTION= 1
TIME= .00000E+00 LOAD CASE= 1

ELEM	SXX	SYY
253	148185.26	744645.10
254	160442.77	513920.50
255	243146.90	1040554.3
256	245598.11	995757.75
257	96007.641	343324.64
258	28483.472	424173.79
259	88847.129	576558.34
260	127645.51	400907.72
261	175982.72	766774.60
262	192070.15	716220.75
263	84570.467	132866.66
264	59800.055	304260.78
265	131935.51	468647.25
266	97628.455	295593.33

***** POST1 ELEMENT STRESS LISTING *****

LOAD STEP 1 ITERATION= 1 SECTION= 1
TIME= .00000E+00 LOAD CASE= 1

ELEM	SXX	SYY
267	152615.91	523952.44
268	255173.56	519078.95
269	259590.82	65298.831
270	335141.48	263925.93
271	455672.98	381253.43
272	104270.86	186033.14
273	43070.905	200619.73
274	356762.49	121210.89
275	894836.71	155864.47
276	1224845.0	115427.45
277	1218459.8	230783.94
278	218923.62	77840.295

MINIMUMS		
ELEMENT	96	93
VALUE	-676789.91	-328424.96

MAXIMUMS		
ELEMENT	185	185
VALUE	3184781.8	12286388.

C.1.8 SXYY and SZZ: Planar Stresses in Wing Shell Elements

PRINT ELEMENT STRESS ITEMS PER ELEMENT

***** POST1 ELEMENT STRESS LISTING *****

LOAD STEP 1 ITERATION= 1 SECTION= 1
TIME= .00000E+00 LOAD CASE= 1

ELEM	SXYY	SZZ
1	.00000000E+00	.00000000E+00
2	.00000000E+00	.00000000E+00
3	.00000000E+00	.00000000E+00
4	.00000000E+00	.00000000E+00
5	.00000000E+00	.00000000E+00
6	.00000000E+00	.00000000E+00
7	.00000000E+00	.00000000E+00
8	.00000000E+00	.00000000E+00
9	.00000000E+00	.00000000E+00
10	.00000000E+00	.00000000E+00
11	.00000000E+00	.00000000E+00
12	.00000000E+00	.00000000E+00
13	.00000000E+00	.00000000E+00
14	.00000000E+00	.00000000E+00

***** POST1 ELEMENT STRESS LISTING *****

LOAD STEP 1 ITERATION= 1 SECTION= 1
TIME= .00000E+00 LOAD CASE= 1

ELEM	SXYY	SZZ
15	.00000000E+00	.00000000E+00
16	.00000000E+00	.00000000E+00
17	.00000000E+00	.00000000E+00
18	.00000000E+00	.00000000E+00
19	.00000000E+00	.00000000E+00
20	.00000000E+00	.00000000E+00
21	.00000000E+00	.00000000E+00
22	.00000000E+00	.00000000E+00
23	.00000000E+00	.00000000E+00
24	.00000000E+00	.00000000E+00
25	.00000000E+00	.00000000E+00
26	.00000000E+00	.00000000E+00
27	.00000000E+00	.00000000E+00
28	.00000000E+00	.00000000E+00

***** POST1 ELEMENT STRESS LISTING *****

LOAD STEP 1 ITERATION= 1 SECTION= 1
TIME= .00000E+00 LOAD CASE= 1

ELEM	SXYY	SZZ
29	.00000000E+00	.00000000E+00
30	.00000000E+00	.00000000E+00
31	.00000000E+00	.00000000E+00
32	.00000000E+00	.00000000E+00
33	-1083524.8	.00000000E+00
34	-995569.77	.00000000E+00
35	-921282.69	.00000000E+00
36	-854886.36	.00000000E+00
37	-789264.47	.00000000E+00

38	-723069.87	.00000000E+00
39	-656408.18	.00000000E+00
40	-589636.77	.00000000E+00
41	-522916.11	.00000000E+00
42	-456302.10	.00000000E+00

***** POST1 ELEMENT STRESS LISTING *****

LOAD STEP 1 ITERATION= 1 SECTION= 1
TIME= .00000E+00 LOAD CASE= 1

ELEM	SXYY	SZZ
43	-389978.38	.00000000E+00
44	-324490.84	.00000000E+00
45	-260587.48	.00000000E+00
46	-197819.36	.00000000E+00
47	-129873.31	.00000000E+00
48	-45383.317	.00000000E+00
49	.00000000E+00	.00000000E+00
50	.00000000E+00	.00000000E+00
51	.00000000E+00	.00000000E+00
52	.00000000E+00	.00000000E+00
53	.00000000E+00	.00000000E+00
54	.00000000E+00	.00000000E+00
55	.00000000E+00	.00000000E+00
56	.00000000E+00	.00000000E+00

***** POST1 ELEMENT STRESS LISTING *****

LOAD STEP 1 ITERATION= 1 SECTION= 1
TIME= .00000E+00 LOAD CASE= 1

ELEM	SXYY	SZZ
57	.00000000E+00	.00000000E+00
58	.00000000E+00	.00000000E+00
59	.00000000E+00	.00000000E+00
60	.00000000E+00	.00000000E+00
61	.00000000E+00	.00000000E+00
62	.00000000E+00	.00000000E+00
63	.00000000E+00	.00000000E+00
64	.00000000E+00	.00000000E+00
65	.00000000E+00	.00000000E+00
66	.00000000E+00	.00000000E+00
67	.00000000E+00	.00000000E+00
68	.00000000E+00	.00000000E+00
69	.00000000E+00	.00000000E+00
70	.00000000E+00	.00000000E+00

***** POST1 ELEMENT STRESS LISTING *****

LOAD STEP 1 ITERATION= 1 SECTION= 1
TIME= .00000E+00 LOAD CASE= 1

ELEM	SXYY	SZZ
71	.00000000E+00	.00000000E+00
72	.00000000E+00	.00000000E+00
73	.00000000E+00	.00000000E+00
74	.00000000E+00	.00000000E+00
75	.00000000E+00	.00000000E+00
76	.00000000E+00	.00000000E+00

77	.00000000E+00	.00000000E+00
78	.00000000E+00	.00000000E+00
79	.00000000E+00	.00000000E+00
80	.00000000E+00	.00000000E+00
81	.00000000E+00	-.00000000E+00
82	.00000000E+00	-.00000000E+00
83	.00000000E+00	-.00000000E+00
84	.00000000E+00	-.00000000E+00

***** POST1 ELEMENT STRESS LISTING *****

LOAD STEP 1 ITERATION= 1 SECTION= 1
TIME= .00000E+00 LOAD CASE= 1

ELEM	SXYY	SZZ
85	.00000000E+00	-.00000000E+00
86	.00000000E+00	-.00000000E+00
87	-47151.426	.00000000E+00
88	-72666.493	.00000000E+00
89	-28555.144	.00000000E+00
90	19892.519	.00000000E+00
91	16319.430	.00000000E+00
92	12897.116	.00000000E+00
93	-52377.146	.00000000E+00
94	-135346.53	.00000000E+00
95	-43292.820	.00000000E+00
96	32629.498	.00000000E+00
97	46934.644	.00000000E+00
98	52797.144	.00000000E+00

***** POST1 ELEMENT STRESS LISTING *****

LOAD STEP 1 ITERATION= 1 SECTION= 1
TIME= .00000E+00 LOAD CASE= 1

ELEM	SXYY	SZZ
99	-30757.988	.00000000E+00
100	-131633.82	.00000000E+00
101	-49551.266	.00000000E+00
102	36005.094	.00000000E+00
103	52280.836	.00000000E+00
104	62311.746	.00000000E+00
105	-31630.893	.00000000E+00
106	-113553.81	.00000000E+00
107	-45045.985	.00000000E+00
108	31445.283	.00000000E+00
109	45857.930	.00000000E+00
110	57055.143	.00000000E+00
111	-33516.183	.00000000E+00
112	-90759.891	.00000000E+00

***** POST1 ELEMENT STRESS LISTING *****

LOAD STEP 1 ITERATION= 1 SECTION= 1
TIME= .00000E+00 LOAD CASE= 1

ELEM	SXYY	SZZ
113	-38518.230	.00000000E+00
114	25367.809	.00000000E+00
115	36081.157	.00000000E+00

116	46521.290	.00000000E+00
117	-34311.762	.00000000E+00
118	-70908.937	.00000000E+00
119	-32447.050	.00000000E+00
120	19930.479	.00000000E+00
121	27294.483	.00000000E+00
122	36697.173	.00000000E+00
123	-33421.957	.00000000E+00
124	-54694.694	.00000000E+00
125	-27344.018	.00000000E+00
126	15520.181	.00000000E+00

***** POST1 ELEMENT STRESS LISTING *****

LOAD STEP 1 ITERATION= 1 SECTION= 1
TIME= .00000E+00 LOAD CASE= 1

ELEM	SXYY	SZZ
127	20287.357	.00000000E+00
128	28790.641	.00000000E+00
129	-31297.626	.00000000E+00
130	-41389.484	.00000000E+00
131	-22951.903	.00000000E+00
132	11915.629	.00000000E+00
133	14742.406	.00000000E+00
134	22441.425	.00000000E+00
135	-28300.567	.00000000E+00
136	-30515.799	.00000000E+00
137	-19123.181	.00000000E+00
138	8974.1541	.00000000E+00
139	10421.862	.00000000E+00
140	17371.953	.00000000E+00

***** POST1 ELEMENT STRESS LISTING *****

LOAD STEP 1 ITERATION= 1 SECTION= 1
TIME= .00000E+00 LOAD CASE= 1

ELEM	SXYY	SZZ
141	-24219.824	.00000000E+00
142	-22495.280	.00000000E+00
143	-16069.313	.00000000E+00
144	6850.4239	.00000000E+00
145	7598.9332	.00000000E+00
146	13978.237	.00000000E+00
147	-18409.794	.00000000E+00
148	-18602.392	.00000000E+00
149	-14341.499	.00000000E+00
150	5973.2757	.00000000E+00
151	6993.6080	.00000000E+00
152	13226.972	.00000000E+00
153	-10739.293	.00000000E+00
154	-19443.919	.00000000E+00

***** POST1 ELEMENT STRESS LISTING *****

LOAD STEP 1 ITERATION= 1 SECTION= 1
TIME= .00000E+00 LOAD CASE= 1

ELEM	SXYY	SZZ

155	-14154.872	.00000000E+00
156	6486.9537	.00000000E+00
157	8758.7522	.00000000E+00
158	15253.456	.00000000E+00
159	-3318.7097	.00000000E+00
160	-19358.595	.00000000E+00
161	-13346.683	.00000000E+00
162	6577.1320	.00000000E+00
163	9499.7913	.00000000E+00
164	15394.321	.00000000E+00
165	-17017.540	.00000000E+00
166	-1572.0871	.00000000E+00
167	-3130.5238	.00000000E+00
168	-962.66098	.00000000E+00

***** POST1 ELEMENT STRESS LISTING *****

LOAD STEP 1 ITERATION= 1 SECTION= 1
TIME= .00000E+00 LOAD CASE= 1

ELEM	SXYY	SZZ
169	-2022.4724	.00000000E+00
170	90.437667	.00000000E+00
171	-38812.213	.00000000E+00
172	78249.763	.00000000E+00
173	27399.286	.00000000E+00
174	-25630.431	.00000000E+00
175	-50039.475	.00000000E+00
176	-68501.292	.00000000E+00
177	-73212.905	.00000000E+00
178	174710.38	.00000000E+00
179	47118.681	.00000000E+00
180	-65003.523	.00000000E+00
181	-141957.28	.00000000E+00
182	-135153.81	.00000000E+00

***** POST1 ELEMENT STRESS LISTING *****

LOAD STEP 1 ITERATION= 1 SECTION= 1
TIME= .00000E+00 LOAD CASE= 1

ELEM	SXYY	SZZ
183	1555235.7	.00000000E+00
184	1665146.7	.00000000E+00
185	1997344.7	.00000000E+00
186	-645724.04	.00000000E+00
187	-433088.97	.00000000E+00
188	-439731.84	.00000000E+00
189	3445200.5	.00000000E+00
190	3684402.2	.00000000E+00
191	4544135.3	.00000000E+00
192	-2090818.0	.00000000E+00
193	-1472597.7	.00000000E+00
194	-1331418.9	.00000000E+00
195	5116086.0	.00000000E+00
196	5417820.0	.00000000E+00

***** POST1 ELEMENT STRESS LISTING *****

LOAD STEP 1 ITERATION= 1 SECTION= 1

TIME= .00000E+00 LOAD CASE= 1

ELEM	SXYY	SZZ
197	6288152.6	.00000000E+00
198	-3197237.9	.00000000E+00
199	-2495176.6	.00000000E+00
200	-2193472.1	.00000000E+00
201	6572686.2	.00000000E+00
202	6845001.8	.00000000E+00
203	7658380.7	.00000000E+00
204	-3982566.1	.00000000E+00
205	-3298667.7	.00000000E+00
206	-2948390.6	.00000000E+00
207	7712928.9	.00000000E+00
208	7971217.6	.00000000E+00
209	8708281.1	.00000000E+00
210	-4560709.4	.00000000E+00

***** POST1 ELEMENT STRESS LISTING *****

LOAD STEP 1 ITERATION= 1 SECTION= 1
TIME= .00000E+00 LOAD CASE= 1

ELEM	SXYY	SZZ
211	-3928638.2	.00000000E+00
212	-3575790.9	.00000000E+00
213	8571286.8	.00000000E+00
214	8807908.2	.00000000E+00
215	9476289.2	.00000000E+00
216	-4973872.9	.00000000E+00
217	-4401884.2	.00000000E+00
218	-4067106.5	.00000000E+00
219	9166237.0	.00000000E+00
220	9387309.8	.00000000E+00
221	9991743.3	.00000000E+00
222	-5251591.6	.00000000E+00
223	-4739354.5	.00000000E+00
224	-4427748.6	.00000000E+00

***** POST1 ELEMENT STRESS LISTING *****

LOAD STEP 1 ITERATION= 1 SECTION= 1
TIME= .00000E+00 LOAD CASE= 1

ELEM	SXYY	SZZ
225	9543584.0	.00000000E+00
226	9748006.1	.00000000E+00
227	10292070.	.00000000E+00
228	-5415875.9	.00000000E+00
229	-4961706.5	.00000000E+00
230	-4674341.5	.00000000E+00
231	9744209.9	.00000000E+00
232	9932574.1	.00000000E+00
233	10417094.	.00000000E+00
234	-5487263.5	.00000000E+00
235	-5090228.9	.00000000E+00
236	-4828134.8	.00000000E+00
237	9810402.8	.00000000E+00
238	9981361.2	.00000000E+00

***** POST1 ELEMENT STRESS LISTING *****

LOAD STEP 1 ITERATION= 1 SECTION= 1
TIME= .00000E+00 LOAD CASE= 1

ELEM	SXYY	SZZ
239	10406430.	.00000000E+00
240	-5485066.5	.00000000E+00
241	-5145680.3	.00000000E+00
242	-4911390.1	.00000000E+00
243	9781300.7	.00000000E+00
244	9934321.1	.00000000E+00
245	10297050.	.00000000E+00
246	-5425960.6	.00000000E+00
247	-5147360.1	.00000000E+00
248	-4945894.7	.00000000E+00
249	9697699.5	.00000000E+00
250	9825794.7	.00000000E+00
251	10119301.	.00000000E+00
252	-5322177.9	.00000000E+00

***** POST1 ELEMENT STRESS LISTING *****

LOAD STEP 1 ITERATION= 1 SECTION= 1
TIME= .00000E+00 LOAD CASE= 1

ELEM	SXYY	SZZ
253	-5111325.3	.00000000E+00
254	-4949707.8	.00000000E+00
255	9575585.8	.00000000E+00
256	9677581.6	.00000000E+00
257	9887512.4	.00000000E+00
258	-5182335.4	.00000000E+00
259	-5048105.2	.00000000E+00
260	-4929164.7	.00000000E+00
261	9420647.1	.00000000E+00
262	9477822.0	.00000000E+00
263	9603113.7	.00000000E+00
264	-5013680.4	.00000000E+00
265	-4955888.7	.00000000E+00
266	-4868279.9	.00000000E+00

***** POST1 ELEMENT STRESS LISTING *****

LOAD STEP 1 ITERATION= 1 SECTION= 1
TIME= .00000E+00 LOAD CASE= 1

ELEM	SXYY	SZZ
267	9112063.8	.00000000E+00
268	9181577.1	.00000000E+00
269	9249684.9	.00000000E+00
270	-4868584.7	.00000000E+00
271	-4847932.5	.00000000E+00
272	-4718775.4	.00000000E+00
273	8491014.3	.00000000E+00
274	8612829.6	.00000000E+00
275	8830454.4	.00000000E+00
276	-4901726.1	.00000000E+00
277	-4668747.4	.00000000E+00
278	-4446037.5	.00000000E+00

MINIMUMS		
ELEMENT	234	1
VALUE	-5487263.5	.00000000E+00

MAXIMUMS		
ELEMENT	233	1
VALUE	10417094.	.00000000E+00

C.1.9 SIG1, SIG2 and SIG3: Principal Stresses in Wing Shell Elements

PRINT ELEMENT STRESS ITEMS PER ELEMENT

***** POST1 ELEMENT STRESS LISTING *****

LOAD STEP 1 ITERATION= 1 SECTION= 1
TIME= .00000E+00 LOAD CASE= 1

ELEM	SG1	SG2	SG3
1	.00000000E+00	.00000000E+00	.00000000E+00
2	.00000000E+00	.00000000E+00	.00000000E+00
3	.00000000E+00	.00000000E+00	.00000000E+00
4	.00000000E+00	.00000000E+00	.00000000E+00
5	.00000000E+00	.00000000E+00	.00000000E+00
6	.00000000E+00	.00000000E+00	.00000000E+00
7	.00000000E+00	.00000000E+00	.00000000E+00
8	.00000000E+00	.00000000E+00	.00000000E+00
9	.00000000E+00	.00000000E+00	.00000000E+00
10	.00000000E+00	.00000000E+00	.00000000E+00
11	.00000000E+00	.00000000E+00	.00000000E+00
12	.00000000E+00	.00000000E+00	.00000000E+00
13	.00000000E+00	.00000000E+00	.00000000E+00
14	.00000000E+00	.00000000E+00	.00000000E+00

***** POST1 ELEMENT STRESS LISTING *****

LOAD STEP 1 ITERATION= 1 SECTION= 1
TIME= .00000E+00 LOAD CASE= 1

ELEM	SG1	SG2	SG3
15	.00000000E+00	.00000000E+00	.00000000E+00
16	.00000000E+00	.00000000E+00	.00000000E+00
17	.00000000E+00	.00000000E+00	.00000000E+00
18	.00000000E+00	.00000000E+00	.00000000E+00
19	.00000000E+00	.00000000E+00	.00000000E+00
20	.00000000E+00	.00000000E+00	.00000000E+00
21	.00000000E+00	.00000000E+00	.00000000E+00
22	.00000000E+00	.00000000E+00	.00000000E+00
23	.00000000E+00	.00000000E+00	.00000000E+00
24	.00000000E+00	.00000000E+00	.00000000E+00
25	.00000000E+00	.00000000E+00	.00000000E+00
26	.00000000E+00	.00000000E+00	.00000000E+00
27	.00000000E+00	.00000000E+00	.00000000E+00
28	.00000000E+00	.00000000E+00	.00000000E+00

***** POST1 ELEMENT STRESS LISTING *****

LOAD STEP 1 ITERATION= 1 SECTION= 1
TIME= .00000E+00 LOAD CASE= 1

ELEM	SG1	SG2	SG3
29	.00000000E+00	.00000000E+00	.00000000E+00
30	.00000000E+00	.00000000E+00	.00000000E+00
31	.00000000E+00	.00000000E+00	.00000000E+00
32	.00000000E+00	.00000000E+00	.00000000E+00
33	.00000000E+00	-650065.65	-24603176.
34	80452.191	.00000000E+00	-21432799.
35	.00000000E+00	-44235.550	-18587063.
36	.00000000E+00	-9734.2998	-15951439.
37	.00000000E+00	-10061.902	-13524419.

38	.00000000E+00	-4247.7395	-11300422.
39	1236.5300	.00000000E+00	-9279937.3
40	7820.0096	.00000000E+00	-7462444.4
41	14957.078	.00000000E+00	-5847000.1
42	22531.220	.00000000E+00	-4432494.5

***** POST1 ELEMENT STRESS LISTING *****

LOAD STEP 1 ITERATION= 1 SECTION= 1
TIME= .00000E+00 LOAD CASE= 1

ELEM	SG1	SG2	SG3
43	30596.373	.00000000E+00	-3217662.9
44	39585.434	.00000000E+00	-2200461.4
45	49883.477	.00000000E+00	-1377304.0
46	62022.763	.00000000E+00	-745166.81
47	64473.350	.00000000E+00	-305894.38
48	46360.249	.00000000E+00	-74194.590
49	.00000000E+00	.00000000E+00	.00000000E+00
50	.00000000E+00	.00000000E+00	.00000000E+00
51	.00000000E+00	.00000000E+00	.00000000E+00
52	.00000000E+00	.00000000E+00	.00000000E+00
53	.00000000E+00	.00000000E+00	.00000000E+00
54	.00000000E+00	.00000000E+00	.00000000E+00
55	.00000000E+00	.00000000E+00	.00000000E+00
56	.00000000E+00	.00000000E+00	.00000000E+00

***** POST1 ELEMENT STRESS LISTING *****

LOAD STEP 1 ITERATION= 1 SECTION= 1
TIME= .00000E+00 LOAD CASE= 1

ELEM	SG1	SG2	SG3
57	.00000000E+00	.00000000E+00	.00000000E+00
58	.00000000E+00	.00000000E+00	.00000000E+00
59	.00000000E+00	.00000000E+00	.00000000E+00
60	.00000000E+00	.00000000E+00	.00000000E+00
61	.00000000E+00	.00000000E+00	.00000000E+00
62	.00000000E+00	.00000000E+00	.00000000E+00
63	.00000000E+00	.00000000E+00	.00000000E+00
64	.00000000E+00	.00000000E+00	.00000000E+00
65	.00000000E+00	.00000000E+00	.00000000E+00
66	.00000000E+00	.00000000E+00	.00000000E+00
67	.00000000E+00	.00000000E+00	.00000000E+00
68	.00000000E+00	.00000000E+00	.00000000E+00
69	.00000000E+00	.00000000E+00	.00000000E+00
70	.00000000E+00	.00000000E+00	.00000000E+00

***** POST1 ELEMENT STRESS LISTING *****

LOAD STEP 1 ITERATION= 1 SECTION= 1
TIME= .00000E+00 LOAD CASE= 1

ELEM	SG1	SG2	SG3
71	.00000000E+00	.00000000E+00	.00000000E+00
72	.00000000E+00	.00000000E+00	.00000000E+00
73	.00000000E+00	.00000000E+00	.00000000E+00
74	.00000000E+00	.00000000E+00	.00000000E+00
75	.00000000E+00	.00000000E+00	.00000000E+00
76	.00000000E+00	.00000000E+00	.00000000E+00

77	.00000000E+00	.00000000E+00	.00000000E+00
78	.00000000E+00	.00000000E+00	.00000000E+00
79	.00000000E+00	.00000000E+00	.00000000E+00
80	.00000000E+00	.00000000E+00	.00000000E+00
81	.00000000E+00	.00000000E+00	.00000000E+00
82	.00000000E+00	.00000000E+00	.00000000E+00
83	.00000000E+00	.00000000E+00	.00000000E+00
84	.00000000E+00	.00000000E+00	.00000000E+00

***** POST1 ELEMENT STRESS LISTING *****

LOAD STEP 1 ITERATION= 1 SECTION= 1
TIME= .00000E+00 LOAD CASE= 1

ELEM	SG1	SG2	SG3
85	.00000000E+00	.00000000E+00	.00000000E+00
86	.00000000E+00	.00000000E+00	.00000000E+00
87	.00000000E+00	-121470.61	-232037.60
88	388753.13	98174.995	.00000000E+00
89	319483.17	.00000000E+00	-253702.79
90	597984.76	132697.25	.00000000E+00
91	.00000000E+00	-78792.367	-136426.23
92	39182.924	.00000000E+00	-203384.32
93	.00000000E+00	-175971.64	-346419.75
94	552650.96	89949.801	.00000000E+00
95	560253.65	.00000000E+00	-215632.41
96	447465.22	414374.73	.00000000E+00
97	286963.42	.00000000E+00	-73299.354
98	46649.112	.00000000E+00	-220075.87

***** POST1 ELEMENT STRESS LISTING *****

LOAD STEP 1 ITERATION= 1 SECTION= 1
TIME= .00000E+00 LOAD CASE= 1

ELEM	SG1	SG2	SG3
99	.00000000E+00	-126721.94	-321774.74
100	576269.39	90823.813	.00000000E+00
101	625173.48	.00000000E+00	-218025.92
102	536917.69	425112.40	.00000000E+00
103	400337.78	.00000000E+00	-75653.133
104	54779.040	.00000000E+00	-190035.61
105	.00000000E+00	-104728.96	-290954.36
106	514675.91	86728.996	.00000000E+00
107	550557.63	.00000000E+00	-200317.68
108	473051.32	400865.90	.00000000E+00
109	358685.53	.00000000E+00	-77615.858
110	49963.991	.00000000E+00	-171653.98
111	.00000000E+00	-82790.335	-251100.53
112	435842.40	82152.969	.00000000E+00

***** POST1 ELEMENT STRESS LISTING *****

LOAD STEP 1 ITERATION= 1 SECTION= 1
TIME= .00000E+00 LOAD CASE= 1

ELEM	SG1	SG2	SG3
113	448285.23	.00000000E+00	-181868.68
114	394412.50	361624.53	.00000000E+00
115	277283.72	.00000000E+00	-81950.793

116	42732.470	.00000000E+00	-145558.37
117	.00000000E+00	-63526.151	-214875.13
118	364375.22	76672.335	.00000000E+00
119	357086.19	.00000000E+00	-162812.79
120	363684.99	279772.05	.00000000E+00
121	204645.84	.00000000E+00	-83282.183
122	35921.469	.00000000E+00	-120042.78
123	.00000000E+00	-46484.571	-182723.80
124	303747.88	70528.538	.00000000E+00
125	283389.99	.00000000E+00	-144253.19
126	334324.89	211453.26	.00000000E+00

***** POST1 ELEMENT STRESS LISTING *****

LOAD STEP 1 ITERATION= 1 SECTION= 1
TIME= .00000E+00 LOAD CASE= 1

ELEM	SG1	SG2	SG3
127	149435.32	.00000000E+00	-81736.508
128	30183.053	.00000000E+00	-97201.270
129	.00000000E+00	-31877.044	-153618.89
130	251279.34	63753.918	.00000000E+00
131	223197.61	.00000000E+00	-126114.91
132	302176.29	157211.97	.00000000E+00
133	107549.71	.00000000E+00	-77830.478
134	25235.663	.00000000E+00	-77355.162
135	.00000000E+00	-19722.492	-127099.00
136	205450.60	56489.994	.00000000E+00
137	173921.26	.00000000E+00	-108494.21
138	267798.06	114535.07	.00000000E+00
139	76144.178	.00000000E+00	-72043.857
140	20923.062	.00000000E+00	-60483.894

***** POST1 ELEMENT STRESS LISTING *****

LOAD STEP 1 ITERATION= 1 SECTION= 1
TIME= .00000E+00 LOAD CASE= 1

ELEM	SG1	SG2	SG3
141	.00000000E+00	-9945.4860	-103784.83
142	168161.31	48891.093	.00000000E+00
143	138343.17	.00000000E+00	-91732.286
144	231445.77	86643.739	.00000000E+00
145	58492.958	.00000000E+00	-64336.489
146	17458.920	.00000000E+00	-46916.297
147	.00000000E+00	-2241.8688	-85663.656
148	144678.67	41239.701	.00000000E+00
149	124138.49	.00000000E+00	-76466.252
150	193087.46	82182.450	.00000000E+00
151	63354.945	.00000000E+00	-54259.226
152	15494.912	.00000000E+00	-37132.811
153	4411.4356	.00000000E+00	-75094.785
154	137882.78	33898.895	.00000000E+00

***** POST1 ELEMENT STRESS LISTING *****

LOAD STEP 1 ITERATION= 1 SECTION= 1
TIME= .00000E+00 LOAD CASE= 1

ELEM	SG1	SG2	SG3

155	134099.17	.00000000E+00	-63006.765
156	153257.52	103517.20	.00000000E+00
157	93149.504	.00000000E+00	-41804.765
158	15792.330	.00000000E+00	-30839.005
159	11964.666	.00000000E+00	-64592.442
160	129006.03	27112.350	.00000000E+00
161	135732.24	.00000000E+00	-50111.189
162	120642.56	109237.81	.00000000E+00
163	109116.34	.00000000E+00	-30649.666
164	16084.868	.00000000E+00	-22735.514
165	530.93669	.00000000E+00	-40540.358
166	42250.767	20200.999	.00000000E+00
167	861.50723	.00000000E+00	-28550.501
168	84715.730	.00000000E+00	-33511.427

***** POST1 ELEMENT STRESS LISTING *****

LOAD STEP 1 ITERATION= 1 SECTION= 1
TIME= .00000E+00 LOAD CASE= 1

ELEM	SG1	SG2	SG3
169	.00000000E+00	-29777.527	-32779.379
170	3809.5120	.00000000E+00	-18591.887
171	127039.35	.00000000E+00	-14569.602
172	13716.305	.00000000E+00	-246151.49
173	1487.6555	.00000000E+00	-438737.74
174	117862.38	.00000000E+00	-544875.62
175	.00000000E+00	-65991.643	-570192.83
176	98187.568	.00000000E+00	-48890.974
177	264973.61	50670.874	.00000000E+00
178	105221.64	.00000000E+00	-295694.06
179	55841.686	.00000000E+00	-952428.99
180	208498.30	.00000000E+00	-1159403.7
181	.00000000E+00	-193549.67	-1072102.9
182	401380.96	.00000000E+00	-81450.466

***** POST1 ELEMENT STRESS LISTING *****

LOAD STEP 1 ITERATION= 1 SECTION= 1
TIME= .00000E+00 LOAD CASE= 1

ELEM	SG1	SG2	SG3
183	4191751.4	861773.27	.00000000E+00
184	10475294.	2804134.0	.00000000E+00
185	11724297.	3081204.1	.00000000E+00
186	12416391.	2849956.5	.00000000E+00
187	6599950.5	1544026.2	.00000000E+00
188	3809649.9	703336.54	.00000000E+00
189	5865574.6	.00000000E+00	-1147328.7
190	10998869.	990785.14	.00000000E+00
191	12681980.	627478.31	.00000000E+00
192	10928234.	1622828.4	.00000000E+00
193	6774335.4	949830.44	.00000000E+00
194	4209482.8	138773.41	.00000000E+00
195	7346320.7	.00000000E+00	-2978109.3
196	11565743.	.00000000E+00	-940358.39

***** POST1 ELEMENT STRESS LISTING *****

LOAD STEP 1 ITERATION= 1 SECTION= 1

TIME= .00000E+00 LOAD CASE= 1

ELEM	SG1	SG2	SG3
197	12988132.	.00000000E+00	-1492996.6
198	9984809.9	386976.33	.00000000E+00
199	6749466.9	.00000000E+00	-119149.63
200	4718153.6	.00000000E+00	-575259.65
201	8630582.9	.00000000E+00	-4585946.4
202	12028185.	.00000000E+00	-2735849.6
203	13198424.	.00000000E+00	-3365731.6
204	9270174.0	.00000000E+00	-719747.37
205	6718659.1	.00000000E+00	-1072796.9
206	5125789.6	.00000000E+00	-1350094.6
207	9593979.1	.00000000E+00	-5889248.0
208	12380886.	.00000000E+00	-4284214.3
209	13297489.	.00000000E+00	-4943847.9
210	8694963.5	.00000000E+00	-1684001.5

***** POST1 ELEMENT STRESS LISTING *****

LOAD STEP 1 ITERATION= 1 SECTION= 1
TIME= .00000E+00 LOAD CASE= 1

ELEM	SG1	SG2	SG3
211	6691836.9	.00000000E+00	-1910983.4
212	5434994.6	.00000000E+00	-2094416.9
213	10272362.	.00000000E+00	-6916923.8
214	12550164.	.00000000E+00	-5560811.2
215	13268416.	.00000000E+00	-6234444.7
216	8187740.8	.00000000E+00	-2522330.5
217	6640233.1	.00000000E+00	-2624091.5
218	5645699.4	.00000000E+00	-2738046.3
219	10684960.	.00000000E+00	-7685581.3
220	12540546.	.00000000E+00	-6576828.4
221	13093597.	.00000000E+00	-7257124.5
222	7712215.5	.00000000E+00	-3238386.2
223	6542303.4	.00000000E+00	-3218434.8
224	5759499.5	.00000000E+00	-3262324.7

***** POST1 ELEMENT STRESS LISTING *****

LOAD STEP 1 ITERATION= 1 SECTION= 1
TIME= .00000E+00 LOAD CASE= 1

ELEM	SG1	SG2	SG3
225	10878972.	.00000000E+00	-8238973.1
226	12367958.	.00000000E+00	-7363654.1
227	12788391.	.00000000E+00	-8038080.6
228	7253276.1	.00000000E+00	-3828920.1
229	6394532.3	.00000000E+00	-3698456.6
230	5786625.3	.00000000E+00	-3672736.3
231	10897908.	.00000000E+00	-8614955.7
232	12069156.	.00000000E+00	-7954699.6
233	12381045.	.00000000E+00	-8608954.1
234	6809880.8	.00000000E+00	-4294999.2
235	6206214.4	.00000000E+00	-4072709.0
236	5744116.8	.00000000E+00	-3984765.7
237	10786048.	.00000000E+00	-8853625.5
238	11681298.	.00000000E+00	-8384624.7

***** POST1 ELEMENT STRESS LISTING *****

LOAD STEP 1 ITERATION= 1 SECTION= 1
TIME= .00000E+00 LOAD CASE= 1

ELEM	SG1	SG2	SG3
239	11905720.	.00000000E+00	-9003257.8
240	6386861.1	.00000000E+00	-4643874.5
241	5992086.9	.00000000E+00	-4353527.3
242	5652958.1	.00000000E+00	-4216340.6
243	10583971.	.00000000E+00	-8992584.5
244	11243254.	.00000000E+00	-8689062.8
245	11397066.	.00000000E+00	-9253210.8
246	5989111.5	.00000000E+00	-4886351.9
247	5768232.1	.00000000E+00	-4554735.5
248	5536448.7	.00000000E+00	-4384456.3
249	10334440.	.00000000E+00	-9070602.1
250	10796436.	.00000000E+00	-8892280.9
251	10886335.	.00000000E+00	-9383437.5
252	5618744.5	.00000000E+00	-5032346.9

***** POST1 ELEMENT STRESS LISTING *****

LOAD STEP 1 ITERATION= 1 SECTION= 1
TIME= .00000E+00 LOAD CASE= 1

ELEM	SG1	SG2	SG3
253	5550292.2	.00000000E+00	-4686953.3
254	5416035.8	.00000000E+00	-4501574.8
255	10055103.	.00000000E+00	-9102062.4
256	10369768.	.00000000E+00	-9005932.2
257	10398351.	.00000000E+00	-9393962.2
258	5280656.0	.00000000E+00	-5085024.7
259	5354058.9	.00000000E+00	-4750836.2
260	5299051.4	.00000000E+00	-4571042.9
261	9758662.8	.00000000E+00	-9085596.0
262	9985371.0	.00000000E+00	-8982334.0
263	9946320.8	.00000000E+00	-9269890.3
264	4999538.2	.00000000E+00	-5027822.6
265	5192840.0	.00000000E+00	-4725280.1
266	5160674.4	.00000000E+00	-4583553.4

***** POST1 ELEMENT STRESS LISTING *****

LOAD STEP 1 ITERATION= 1 SECTION= 1
TIME= .00000E+00 LOAD CASE= 1

ELEM	SG1	SG2	SG3
267	9320002.7	.00000000E+00	-8905171.6
268	9555338.3	.00000000E+00	-8813792.4
269	9531496.3	.00000000E+00	-8972644.4
270	4886736.2	.00000000E+00	-4850984.9
271	5101865.5	.00000000E+00	-4597020.0
272	4903869.2	.00000000E+00	-4536995.2
273	8582677.3	.00000000E+00	-8399366.1
274	8850343.4	.00000000E+00	-8375731.2
275	9072674.3	.00000000E+00	-8588549.8
276	5216594.6	.00000000E+00	-4588588.5
277	4961516.6	.00000000E+00	-4384082.4
278	4494563.1	.00000000E+00	-4397577.5

MINIMUMS			
ELEMENT	1	33	33
VALUE	.00000000E+00	-650065.65	-24603176.

MAXIMUMS			
ELEMENT	209	185	1
VALUE	13297489.	3081204.1	.00000000E+00

APPENDIX C.2 - ANSYS TAIL DATA

C.2.1 Tail Nodal Locations

PRINT NODE LISTING

***** POST1 NODE LISTING *****

NODE	X	Y	Z	THXY	THY
1	.00000000E+00	.00000000E+00	.00000000E+00	.00000000E+00	.0000
2	.11030704E-01	.10938723E-01	.00000000E+00	.00000000E+00	.0000
3	.36240711E-01	.20943480E-01	.00000000E+00	.00000000E+00	.0000
4	.10310419	.31054370E-01	.00000000E+00	.00000000E+00	.0000
5	.16623887	.27905772E-01	.00000000E+00	.00000000E+00	.0000
6	.22581458	.18849132E-01	.00000000E+00	.00000000E+00	.0000
7	.30000120	.00000000E+00	.00000000E+00	.00000000E+00	.0000
8	.22418722	.49033215E-02	.00000000E+00	.00000000E+00	.0000
9	.16512094	.57736080E-02	.00000000E+00	.00000000E+00	.0000
10	.10419381	.42736020E-02	.00000000E+00	.00000000E+00	.0000
11	.40818560E-01	-.15424590E-02	.00000000E+00	.00000000E+00	.0000
12	.89222055E-02	-.34740705E-02	.00000000E+00	.00000000E+00	.0000
13	.00000000E+00	.00000000E+00	.10132000	.00000000E+00	.0000
14	.11030704E-01	.10938723E-01	.10132000	.00000000E+00	.0000
15	.36240711E-01	.20943480E-01	.10132000	.00000000E+00	.0000

***** POST1 NODE LISTING *****

NODE	X	Y	Z	THXY	THY
16	.10310419	.31054370E-01	.10132000	.00000000E+00	.0000
17	.16623887	.27905772E-01	.10132000	.00000000E+00	.0000
18	.22581458	.18849132E-01	.10132000	.00000000E+00	.0000
19	.30000120	.00000000E+00	.10132000	.00000000E+00	.0000
20	.22418722	.49033215E-02	.10132000	.00000000E+00	.0000
21	.16512094	.57736080E-02	.10132000	.00000000E+00	.0000
22	.10419381	.42736020E-02	.10132000	.00000000E+00	.0000
23	.40818560E-01	-.15424590E-02	.10132000	.00000000E+00	.0000
24	.89222055E-02	-.34740705E-02	.10132000	.00000000E+00	.0000
25	.00000000E+00	.00000000E+00	.20264000	.00000000E+00	.0000
26	.11030704E-01	.10938723E-01	.20264000	.00000000E+00	.0000
27	.36240711E-01	.20943480E-01	.20264000	.00000000E+00	.0000
28	.10310419	.31054370E-01	.20264000	.00000000E+00	.0000
29	.16623887	.27905772E-01	.20264000	.00000000E+00	.0000
30	.22581458	.18849132E-01	.20264000	.00000000E+00	.0000

***** POST1 NODE LISTING *****

NODE	X	Y	Z	THXY	THY
31	.30000120	.00000000E+00	.20264000	.00000000E+00	.0000
32	.22418722	.49033215E-02	.20264000	.00000000E+00	.0000
33	.16512094	.57736080E-02	.20264000	.00000000E+00	.0000
34	.10419381	.42736020E-02	.20264000	.00000000E+00	.0000
35	.40818560E-01	-.15424590E-02	.20264000	.00000000E+00	.0000
36	.89222055E-02	-.34740705E-02	.20264000	.00000000E+00	.0000
37	.00000000E+00	.00000000E+00	.30396000	.00000000E+00	.0000

38	.11030704E-01	.10938723E-01	.30396000	.00000000E+00	.0000
39	.36240711E-01	.20943480E-01	.30396000	.00000000E+00	.0000
40	.10310419	.31054370E-01	.30396000	.00000000E+00	.0000
41	.16623887	.27905772E-01	.30396000	.00000000E+00	.0000
42	.22581458	.18849132E-01	.30396000	.00000000E+00	.0000
43	.30000120	.00000000E+00	.30396000	.00000000E+00	.0000
44	.22418722	.49033215E-02	.30396000	.00000000E+00	.0000
45	.16512094	.57736080E-02	.30396000	.00000000E+00	.0000

***** POST1 NODE LISTING *****

NODE	X	Y	Z	THXY	THY
46	.10419381	.42736020E-02	.30396000	.00000000E+00	.0000
47	.40818560E-01	-.15424590E-02	.30396000	.00000000E+00	.0000
48	.89222055E-02	-.34740705E-02	.30396000	.00000000E+00	.0000
49	.00000000E+00	.00000000E+00	.40528000	.00000000E+00	.0000
50	.11030704E-01	.10938723E-01	.40528000	.00000000E+00	.0000
51	.36240711E-01	.20943480E-01	.40528000	.00000000E+00	.0000
52	.10310419	.31054370E-01	.40528000	.00000000E+00	.0000
53	.16623887	.27905772E-01	.40528000	.00000000E+00	.0000
54	.22581458	.18849132E-01	.40528000	.00000000E+00	.0000
55	.30000120	.00000000E+00	.40528000	.00000000E+00	.0000
56	.22418722	.49033215E-02	.40528000	.00000000E+00	.0000
57	.16512094	.57736080E-02	.40528000	.00000000E+00	.0000
58	.10419381	.42736020E-02	.40528000	.00000000E+00	.0000
59	.40818560E-01	-.15424590E-02	.40528000	.00000000E+00	.0000
60	.89222055E-02	-.34740705E-02	.40528000	.00000000E+00	.0000

***** POST1 NODE LISTING *****

NODE	X	Y	Z	THXY	THY
61	.00000000E+00	.00000000E+00	.50660000	.00000000E+00	.0000
62	.11030704E-01	.10938723E-01	.50660000	.00000000E+00	.0000
63	.36240711E-01	.20943480E-01	.50660000	.00000000E+00	.0000
64	.10310419	.31054370E-01	.50660000	.00000000E+00	.0000
65	.16623887	.27905772E-01	.50660000	.00000000E+00	.0000
66	.22581458	.18849132E-01	.50660000	.00000000E+00	.0000
67	.30000120	.00000000E+00	.50660000	.00000000E+00	.0000
68	.22418722	.49033215E-02	.50660000	.00000000E+00	.0000
69	.16512094	.57736080E-02	.50660000	.00000000E+00	.0000
70	.10419381	.42736020E-02	.50660000	.00000000E+00	.0000
71	.40818560E-01	-.15424590E-02	.50660000	.00000000E+00	.0000
72	.89222055E-02	-.34740705E-02	.50660000	.00000000E+00	.0000

C.2.2 Tail Element Listing

PRINT ELEMENT LISTING

***** POST1 ELEMENT LISTING *****

ELEM	TYPE	STIF	MAT	ESYS	NODES			
1	1	4	3	0	4	16	0	
2	1	4	3	0	16	28	0	
3	1	4	3	0	28	40	0	
4	1	4	3	0	40	52	0	
5	1	4	3	0	52	64	0	
6	1	4	3	0	10	22	0	
7	1	4	3	0	22	34	0	
8	1	4	3	0	34	46	0	
9	1	4	3	0	46	58	0	
10	1	4	3	0	58	70	0	
11	2	41	2	0	10	22	16	4
12	2	41	2	0	22	34	28	16
13	2	41	2	0	34	46	40	28
14	2	41	2	0	46	58	52	40
15	2	41	2	0	58	70	64	52

***** POST1 ELEMENT LISTING *****

ELEM	TYPE	STIF	MAT	ESYS	NODES			
16	1	4	2	0	1	13	0	
17	1	4	2	0	13	25	0	
18	1	4	2	0	25	37	0	
19	1	4	2	0	37	49	0	
20	1	4	2	0	49	61	0	
21	1	4	2	0	7	19	0	
22	1	4	2	0	19	31	0	
23	1	4	2	0	31	43	0	
24	1	4	2	0	43	55	0	
25	1	4	2	0	55	67	0	
26	1	4	2	0	6	18	0	
27	1	4	2	0	18	30	0	
28	1	4	2	0	30	42	0	
29	1	4	2	0	42	54	0	
30	1	4	2	0	54	66	0	

***** POST1 ELEMENT LISTING *****

ELEM	TYPE	STIF	MAT	ESYS	NODES			
31	2	41	3	0	1	12	24	13
32	2	41	3	0	12	11	23	24
33	2	41	3	0	11	10	22	23
34	2	41	3	0	10	9	21	22
35	2	41	3	0	9	8	20	21
36	2	41	3	0	8	7	19	20
37	2	41	3	0	13	24	36	25
38	2	41	3	0	24	23	35	36
39	2	41	3	0	23	22	34	35
40	2	41	3	0	22	21	33	34

41	2	41	3	0	21	20	32	33
42	2	41	3	0	20	19	31	32
43	2	41	3	0	25	36	48	37
44	2	41	3	0	36	35	47	48
45	2	41	3	0	35	34	46	47

***** POST1 ELEMENT LISTING *****

ELEM	TYPE	STIF	MAT	ESYS	NODES			
46	2	41	3	0	34	33	45	46
47	2	41	3	0	33	32	44	45
48	2	41	3	0	32	31	43	44
49	2	41	3	0	37	48	60	49
50	2	41	3	0	48	47	59	60
51	2	41	3	0	47	46	58	59
52	2	41	3	0	46	45	57	58
53	2	41	3	0	45	44	56	57
54	2	41	3	0	44	43	55	56
55	2	41	3	0	49	60	72	61
56	2	41	3	0	60	59	71	72
57	2	41	3	0	59	58	70	71
58	2	41	3	0	58	57	69	70
59	2	41	3	0	57	56	68	69
60	2	41	3	0	56	55	67	68

***** POST1 ELEMENT LISTING *****

ELEM	TYPE	STIF	MAT	ESYS	NODES			
61	2	41	2	0	1	2	12	12
62	2	41	2	0	2	3	11	12
63	2	41	2	0	3	4	10	11
64	2	41	2	0	4	5	9	10
65	2	41	2	0	5	6	8	9
66	2	41	2	0	6	7	8	8
67	2	41	2	0	13	14	24	24
68	2	41	2	0	14	15	23	24
69	2	41	2	0	15	16	22	23
70	2	41	2	0	16	17	21	22
71	2	41	2	0	17	18	20	21
72	2	41	2	0	18	19	20	20
73	2	41	2	0	25	26	36	36
74	2	41	2	0	26	27	35	36
75	2	41	2	0	27	28	34	35

***** POST1 ELEMENT LISTING *****

ELEM	TYPE	STIF	MAT	ESYS	NODES			
76	2	41	2	0	28	29	33	34
77	2	41	2	0	29	30	32	33
78	2	41	2	0	30	31	32	32
79	2	41	2	0	37	38	48	48
80	2	41	2	0	38	39	47	48
81	2	41	2	0	39	40	46	47
82	2	41	2	0	40	41	45	46

83	2	41	2	0	41	42	44	45
84	2	41	2	0	42	43	44	44
85	2	41	2	0	49	50	60	60
86	2	41	2	0	50	51	59	60
87	2	41	2	0	51	52	58	59
88	2	41	2	0	52	53	57	58
89	2	41	2	0	53	54	56	57
90	2	41	2	0	54	55	56	56

***** POST1 ELEMENT LISTING *****

ELEM	TYPE	STIF	MAT	ESYS	NODES			
91	2	41	2	0	61	62	72	72
92	2	41	2	0	62	63	71	72
93	2	41	2	0	63	64	70	71
94	2	41	2	0	64	65	69	70
95	2	41	2	0	65	66	68	69
96	2	41	2	0	66	67	68	68

APPENDIX C.2.3 - TAIL GEOMETRY DATA

STIF4; 3-Dimensional Beam Elements:

Part	NSET	Area (m^2) R1	I_{zz} (m^4) R2	I_{yy} (m^4) R3	Z-thk. (m) R4	Y-thk. (m) R5
Carbon Spar Cap	1	$7.85e^{-7}$	$4.91e^{-14}$	$4.91e^{-14}$	.001	.001
Leading Edge	3	$8.84e^{-5}$	$1.24e^{-9}$	$1.24e^{-9}$	.015	.015
Trailing Edge	4	$9.45e^{-5}$	$3.82e^{-9}$	$3.82e^{-9}$	.027	.007

STIF41; 4 Node Shell Element:

Part	NSET	Thickness (m) R1
Spar Web	2	.00158
Ribs	3	.00158
Mylar	4	.00003

C.2.4 Tail Nodal Displacements

PRINT NODAL DISPLACEMENTS

***** POST1 NODAL DISPLACEMENT LISTING *****

LOAD STEP 1 ITERATION= 1 SECTION= 1
TIME= .00000E+00 LOAD CASE= 1

THE FOLLOWING X,Y,Z DISPLACEMENTS ARE IN GLOBAL COORDINATES

NODE	UX	UY	UZ	ROTX	RO
1	.00000000E+00	.00000000E+00	.00000000E+00	.00000000E+00	.0000
2	.00000000E+00	.00000000E+00	.00000000E+00	.00000000E+00	.0000
3	.00000000E+00	.00000000E+00	.00000000E+00	.00000000E+00	.0000
4	.00000000E+00	.00000000E+00	.00000000E+00	.00000000E+00	.0000
5	.00000000E+00	.00000000E+00	.00000000E+00	.00000000E+00	.0000
6	.00000000E+00	.00000000E+00	.00000000E+00	.00000000E+00	.0000
7	.00000000E+00	.00000000E+00	.00000000E+00	.00000000E+00	.0000
8	.00000000E+00	.00000000E+00	.00000000E+00	.00000000E+00	.0000
9	.00000000E+00	.00000000E+00	.00000000E+00	.00000000E+00	.0000
10	.00000000E+00	.00000000E+00	.00000000E+00	.00000000E+00	.0000
11	.00000000E+00	.00000000E+00	.00000000E+00	.00000000E+00	.0000
12	.00000000E+00	.00000000E+00	.00000000E+00	.00000000E+00	.0000

***** POST1 NODAL DISPLACEMENT LISTING *****

LOAD STEP 1 ITERATION= 1 SECTION= 1
TIME= .00000E+00 LOAD CASE= 1

THE FOLLOWING X,Y,Z DISPLACEMENTS ARE IN GLOBAL COORDINATES

NODE	UX	UY	UZ	ROTX	RO
13	.19659007E-06	.33036236E-04	.28255177E-06	-.61838739E-03	-.8921
14	.10543241E-05	.32170093E-04			
15	.19031590E-05	.30115734E-04			
16	.29691020E-05	.23985568E-04	-.60084893E-05	-.43708731E-03	.5450
17	.27538498E-05	.17299595E-04			
18	.17346854E-05	.10380600E-04	.00000000E+00	-.18926695E-03	.3205
19	-.55147986E-06	.14884607E-05	.12433339E-06	-.27803555E-04	-.9237
20	.59801140E-07	.10573933E-04	.88237128E-06		
21	.24907567E-06	.17421343E-04	.21961139E-05		
22	.31355515E-06	.23842725E-04	.53420121E-05	-.43481694E-03	.4281
23	.13269640E-07	.29722807E-04	.36276579E-05		
24	-.77020102E-07	.32342173E-04	.29691003E-05		

***** POST1 NODAL DISPLACEMENT LISTING *****

LOAD STEP 1 ITERATION= 1 SECTION= 1
TIME= .00000E+00 LOAD CASE= 1

THE FOLLOWING X,Y,Z DISPLACEMENTS ARE IN GLOBAL COORDINATES

NODE	UX	UY	UZ	ROTX	RO
25	-.53313603E-06	.11850217E-03	.53216018E-06	-.10352000E-02	-.1221
26	.31320099E-05	.11481161E-03			
27	.65771407E-05	.10627375E-03			
28	.10378885E-04	.82686969E-04	-.98596502E-05	-.69994239E-03	.8929
29	.94410273E-05	.59106197E-04			
30	.60474620E-05	.35584716E-04	.00000000E+00	-.29656570E-03	.5082
31	-.16871017E-05	.52772281E-05	.23452406E-06	-.45040068E-04	-.1300

32	.35465854E-06	.36245408E-04	.17307739E-05		
33	.91696947E-06	.59526103E-04	.41233934E-05		
34	.65488369E-06	.82266061E-04	.86253400E-05	-.69656114E-03	.2263
35	-.11270486E-05	.10469313E-03	.65019865E-05		
36	-.16988279E-05	.11552622E-03	.50243806E-05		

***** POST1 NODAL DISPLACEMENT LISTING *****

LOAD STEP 1 ITERATION= 1 SECTION= 1
TIME= .00000E+00 LOAD CASE= 1

THE FOLLOWING X,Y,Z DISPLACEMENTS ARE IN GLOBAL COORDINATES

NODE	UX	UY	UZ	ROTX	RO
37	-.21088081E-05	.23681132E-03	.72407023E-06	-.12744215E-02	-.1849
38	.57315515E-05	.22891485E-03			
39	.12982615E-04	.21077725E-03			
40	.20600186E-04	.16185987E-03	-.12014505E-04	-.84548539E-03	.1103
41	.18471768E-04	.11449564E-03			
42	.11695275E-04	.68563660E-04	.00000000E+00	-.34722171E-03	.5956
43	-.31341024E-05	.10280270E-04	.31998751E-06	-.52354264E-04	-.1521
44	.74620450E-06	.69838189E-04	.24348437E-05		
45	.16325429E-05	.11533732E-03	.53777908E-05		
46	.76384488E-06	.16103273E-03	.10367297E-04	-.84101927E-03	-.2847
47	-.32729763E-05	.20745895E-03	.81587829E-05		
48	-.45983453E-05	.23043219E-03	.62981694E-05		

***** POST1 NODAL DISPLACEMENT LISTING *****

LOAD STEP 1 ITERATION= 1 SECTION= 1
TIME= .00000E+00 LOAD CASE= 1

THE FOLLOWING X,Y,Z DISPLACEMENTS ARE IN GLOBAL COORDINATES

NODE	UX	UY	UZ	ROTX	RO
49	-.42722380E-05	.37248312E-03	.84309964E-06	-.13872764E-02	-.2449
50	.85481906E-05	.35956313E-03			
51	.20314686E-04	.32998658E-03			
52	.32356646E-04	.25113386E-03	-.12968664E-04	-.90568683E-03	.1200
53	.28723879E-04	.17610463E-03			
54	.17960178E-04	.10482085E-03	.00000000E+00	-.36457120E-03	.6363
55	-.46780355E-05	.15706851E-04	.37352021E-06	-.54355243E-04	-.1469
56	.12098532E-05	.10677497E-03	.28620166E-05		
57	.23189443E-05	.17743649E-03	.60702572E-05		
58	.64752460E-06	.24983038E-03	.11073466E-04	-.90080036E-03	-.2469
59	-.61051585E-05	.32460522E-03	.89937106E-05		
60	-.83418879E-05	.36203679E-03	.68903630E-05		

***** POST1 NODAL DISPLACEMENT LISTING *****

LOAD STEP 1 ITERATION= 1 SECTION= 1
TIME= .00000E+00 LOAD CASE= 1

THE FOLLOWING X,Y,Z DISPLACEMENTS ARE IN GLOBAL COORDINATES

NODE	UX	UY	UZ	ROTX	RO
61	-.69858122E-05	.51519310E-03	.88305551E-06	-.14191230E-02	-.2792
62	.11233865E-04	.49684179E-03			
63	.27912834E-04	.45485822E-03			
64	.44686167E-04	.34381205E-03	-.13204980E-04	-.91921825E-03	.1224

65	.39412333E-04	.23951121E-03			
66	.24499007E-04	.14194963E-03	.00000000E+00	-.36739035E-03	.6498
67	-.60912293E-05	.21240350E-04	.39157313E-06	-.54743500E-04	-.1357
68	.18085483E-05	.14460270E-03	.29668311E-05		
69	.30137666E-05	.24137009E-03	.62148874E-05		
70	.29604436E-06	.34200435E-03	.11226399E-04	-.91419667E-03	-.3968
71	-.95356748E-05	.44725479E-03	.91994440E-05		
72	-.12769733E-04	.50034749E-03	.70773111E-05		

MAXIMUMS

NODE	64	61	64	61	64
VALUE	.44686167E-04	.51519310E-03	-.13204980E-04	-.14191230E-02	.1224

C.2.5 SIG1 and SIG2: Maximum and Minimum Stresses in Tail Beam Elements at End

PRINT ELEMENT STRESS ITEMS PER ELEMENT

***** POST1 ELEMENT STRESS LISTING *****

LOAD STEP 1 ITERATION= 1 SECTION= 1
TIME= .00000E+00 LOAD CASE= 1

ELEM	STR1	STR2
1	-114456.13	-316077.15
2	-76447.388	-199504.33
3	-39148.892	-115255.40
4	-15384.538	-52984.993
5	-2743.5687	-14189.459
6	264228.23	118549.19
7	159376.01	75888.107
8	88260.406	36558.070
9	37869.664	12730.305
10	10288.421	669.83116
11	.00000000E+00	.00000000E+00
12	.00000000E+00	.00000000E+00
13	.00000000E+00	.00000000E+00
14	.00000000E+00	.00000000E+00

***** POST1 ELEMENT STRESS LISTING *****

LOAD STEP 1 ITERATION= 1 SECTION= 1
TIME= .00000E+00 LOAD CASE= 1

ELEM	STR1	STR2
15	.00000000E+00	.00000000E+00
16	357916.66	-322923.97
17	262717.85	-231805.04
18	162293.26	-138526.12
19	84994.923	-70253.698
20	35241.898	-30293.553
21	26607.026	-11208.928
22	15411.136	-1764.5458
23	10472.981	111.26102
24	5002.4774	1627.2925
25	3151.3374	-915.56836
26	127620.38	-127620.38
27	77955.661	-77955.661
28	39138.596	-39138.596

***** POST1 ELEMENT STRESS LISTING *****

LOAD STEP 1 ITERATION= 1 SECTION= 1
TIME= .00000E+00 LOAD CASE= 1

ELEM	STR1	STR2
29	16030.821	-16030.821
30	3868.3038	-3868.3038
31	.00000000E+00	.00000000E+00
32	.00000000E+00	.00000000E+00
33	.00000000E+00	.00000000E+00
34	.00000000E+00	.00000000E+00
35	.00000000E+00	.00000000E+00
36	.00000000E+00	.00000000E+00
37	.00000000E+00	.00000000E+00

77	.00000000E+00	.00000000E+00
78	.00000000E+00	.00000000E+00
79	.00000000E+00	.00000000E+00
80	.00000000E+00	.00000000E+00
81	.00000000E+00	.00000000E+00
82	.00000000E+00	.00000000E+00
83	.00000000E+00	.00000000E+00
84	.00000000E+00	.00000000E+00

***** POST1 ELEMENT STRESS LISTING *****

LOAD STEP 1 ITERATION= 1 SECTION= 1
TIME= .00000E+00 LOAD CASE= 1

ELEM	STR1	STR2
85	.00000000E+00	.00000000E+00
86	.00000000E+00	.00000000E+00
87	.00000000E+00	.00000000E+00
88	.00000000E+00	.00000000E+00
89	.00000000E+00	.00000000E+00
90	.00000000E+00	.00000000E+00
91	.00000000E+00	.00000000E+00
92	.00000000E+00	.00000000E+00
93	.00000000E+00	.00000000E+00
94	.00000000E+00	.00000000E+00
95	.00000000E+00	.00000000E+00
96	.00000000E+00	.00000000E+00

MINIMUMS		
ELEMENT	1	16
VALUE	-114456.13	-322923.97

MAXIMUMS		
ELEMENT	16	6
VALUE	357916.66	118549.19

C.2.6 SIG1, SIG2 and SIG3: Principal Stresses in Tail Shell Elements

PRINT ELEMENT STRESS ITEMS PER ELEMENT

***** POST1 ELEMENT STRESS LISTING *****

LOAD STEP 1 ITERATION= 1 SECTION= 1
TIME= .00000E+00 LOAD CASE= 1

ELEM	SG1	SG2	SG3
1	.00000000E+00	.00000000E+00	.00000000E+00
2	.00000000E+00	.00000000E+00	.00000000E+00
3	.00000000E+00	.00000000E+00	.00000000E+00
4	.00000000E+00	.00000000E+00	.00000000E+00
5	.00000000E+00	.00000000E+00	.00000000E+00
6	.00000000E+00	.00000000E+00	.00000000E+00
7	.00000000E+00	.00000000E+00	.00000000E+00
8	.00000000E+00	.00000000E+00	.00000000E+00
9	.00000000E+00	.00000000E+00	.00000000E+00
10	.00000000E+00	.00000000E+00	.00000000E+00
11	339339.53	.00000000E+00	-15647.732
12	214253.95	.00000000E+00	-7327.3720
13	118630.07	.00000000E+00	-8060.5804
14	54702.744	.00000000E+00	-7899.7845

***** POST1 ELEMENT STRESS LISTING *****

LOAD STEP 1 ITERATION= 1 SECTION= 1
TIME= .00000E+00 LOAD CASE= 1

ELEM	SG1	SG2	SG3
15	18277.505	.00000000E+00	-6047.1556
16	.00000000E+00	.00000000E+00	.00000000E+00
17	.00000000E+00	.00000000E+00	.00000000E+00
18	.00000000E+00	.00000000E+00	.00000000E+00
19	.00000000E+00	.00000000E+00	.00000000E+00
20	.00000000E+00	.00000000E+00	.00000000E+00
21	.00000000E+00	.00000000E+00	.00000000E+00
22	.00000000E+00	.00000000E+00	.00000000E+00
23	.00000000E+00	.00000000E+00	.00000000E+00
24	.00000000E+00	.00000000E+00	.00000000E+00
25	.00000000E+00	.00000000E+00	.00000000E+00
26	.00000000E+00	.00000000E+00	.00000000E+00
27	.00000000E+00	.00000000E+00	.00000000E+00
28	.00000000E+00	.00000000E+00	.00000000E+00

***** POST1 ELEMENT STRESS LISTING *****

LOAD STEP 1 ITERATION= 1 SECTION= 1
TIME= .00000E+00 LOAD CASE= 1

ELEM	SG1	SG2	SG3
29	.00000000E+00	.00000000E+00	.00000000E+00
30	.00000000E+00	.00000000E+00	.00000000E+00
31	50661.871	.00000000E+00	-15829.582
32	133473.50	21885.110	.00000000E+00
33	169268.34	26649.204	.00000000E+00
34	206452.89	39967.904	.00000000E+00
35	87053.060	14097.838	.00000000E+00
36	40368.108	.00000000E+00	-1268.4769
37	99024.264	.00000000E+00	-74353.044

38	148092.99	.00000000E+00	-48069.048
39	193526.62	.00000000E+00	-63143.750
40	151587.40	.00000000E+00	-13844.074
41	93963.549	.00000000E+00	-13086.769
42	59861.685	.00000000E+00	-23874.275

***** POST1 ELEMENT STRESS LISTING *****

LOAD STEP 1 ITERATION= 1 SECTION= 1
TIME= .00000E+00 LOAD CASE= 1

ELEM	SG1	SG2	SG3
43	129544.53	.00000000E+00	-114821.11
44	157978.06	.00000000E+00	-103045.44
45	182469.32	.00000000E+00	-118794.53
46	116659.93	.00000000E+00	-56046.425
47	89073.577	.00000000E+00	-48301.082
48	73153.831	.00000000E+00	-44407.980
49	144782.41	.00000000E+00	-137651.35
50	156557.72	.00000000E+00	-134185.11
51	169891.91	.00000000E+00	-144916.16
52	94505.951	.00000000E+00	-78414.974
53	84652.154	.00000000E+00	-68254.136
54	77633.835	.00000000E+00	-60260.355
55	145140.84	.00000000E+00	-143138.48
56	150021.88	.00000000E+00	-143995.06

***** POST1 ELEMENT STRESS LISTING *****

LOAD STEP 1 ITERATION= 1 SECTION= 1
TIME= .00000E+00 LOAD CASE= 1

ELEM	SG1	SG2	SG3
57	156823.13	.00000000E+00	-152151.74
58	87478.225	.00000000E+00	-84668.567
59	80321.127	.00000000E+00	-75390.857
60	74242.627	.00000000E+00	-68623.303
61	.00000000E+00	.00000000E+00	.00000000E+00
62	.00000000E+00	.00000000E+00	.00000000E+00
63	.00000000E+00	.00000000E+00	.00000000E+00
64	.00000000E+00	.00000000E+00	.00000000E+00
65	.00000000E+00	.00000000E+00	.00000000E+00
66	.00000000E+00	.00000000E+00	.00000000E+00
67	.00000000E+00	-1183.1255	-4423.1214
68	10023.239	480.84135	.00000000E+00
69	14545.709	.00000000E+00	-3310.7380
70	10790.667	5107.1019	.00000000E+00

***** POST1 ELEMENT STRESS LISTING *****

LOAD STEP 1 ITERATION= 1 SECTION= 1
TIME= .00000E+00 LOAD CASE= 1

ELEM	SG1	SG2	SG3
71	2010.5922	.00000000E+00	-164.29972
72	460.72165	.00000000E+00	-2011.1873
73	.00000000E+00	-332.46256	-7538.1193
74	15991.957	684.55541	.00000000E+00
75	23584.165	.00000000E+00	-3085.4002
76	21603.539	2415.4067	.00000000E+00

77	14290.554	900.59542	.00000000E+00
78	948.83483	.00000000E+00	-3082.1157
79	1248.6589	.00000000E+00	-6655.6354
80	14573.620	676.11902	.00000000E+00
81	21981.065	.00000000E+00	-2640.0079
82	21334.203	1962.4192	.00000000E+00
83	16511.648	771.72085	.00000000E+00
84	1344.6206	.00000000E+00	-2454.3932

***** POST1 ELEMENT STRESS LISTING *****

LOAD STEP 1 ITERATION= 1 SECTION= 1
TIME= .00000E+00 LOAD CASE= 1

ELEM	SG1	SG2	SG3
85	1757.6581	.00000000E+00	-3212.9683
86	7785.5734	460.03797	.00000000E+00
87	11822.150	.00000000E+00	-1634.5269
88	10112.699	2053.6752	.00000000E+00
89	5884.9047	5.3745550	.00000000E+00
90	563.79095	47.287043	.00000000E+00
91	5499.6376	.00000000E+00	-2125.4494
92	4250.9604	1718.9284	.00000000E+00
93	.00000000E+00	-456.31200	-2268.9476
94	4684.0920	.00000000E+00	-5351.0495
95	.00000000E+00	-2756.5921	-5321.3903
96	6369.5407	.00000000E+00	-435.09798

MINIMUMS			
ELEMENT	1	95	57
VALUE	.00000000E+00	-2756.5921	-152151.74

MAXIMUMS			
ELEMENT	11	34	1
VALUE	339339.53	39967.904	.00000000E+00

C.2.7 SIG1, SIG2 and SIG3: Principal Nodal Tail Stresses

PRINT PRIN NODAL STRESSES PER NODE

***** POST1 NODAL STRESS LISTING *****

LOAD STEP 1 ITERATION= 1 SECTION= 1
TIME= .00000E+00 LOAD CASE= 1
SHELL STRESSES ARE AT MIDDLE

NODE	SIG1	SIG2	SIG3	SI	S
1	25330.935	.21491473E-06	-7914.7910	33245.726	30079
2	.00000000E+00	.00000000E+00	.00000000E+00	.00000000E+00	.0000
3	.00000000E+00	.00000000E+00	.00000000E+00	.00000000E+00	.0000
4	709.37484	.24096576E-04	-127096.37	127805.75	12745
5	.00000000E+00	.00000000E+00	.00000000E+00	.00000000E+00	.0000
6	.00000000E+00	.00000000E+00	.00000000E+00	.00000000E+00	.0000
7	10840.262	.10016136E-06	-4869.5891	15709.851	13928
8	21509.757	2103.1028	-317.11923	21826.877	20779
9	46998.711	11717.124	.41777536E-06	46998.711	42530
10	153688.68	14930.958	-3129.5464	156818.22	14891
11	80839.384	12878.204	.78127218E-06	80839.384	75231
12	64017.030	7593.4932	.84655791E-06	64017.030	60641
13	49688.987	-394.37517	-31724.598	81413.585	71522

***** POST1 NODAL STRESS LISTING *****

LOAD STEP 1 ITERATION= 1 SECTION= 1
TIME= .00000E+00 LOAD CASE= 1
SHELL STRESSES ARE AT MIDDLE

NODE	SIG1	SIG2	SIG3	SI	S
14	5011.6195	-351.14208	-2211.5607	7223.1802	6878.
15	9917.7258	1336.5014	-1655.3690	11573.095	10516
16	11109.620	2134.3896	-156944.03	168053.65	16471
17	8021.9012	.00000000E+00	-1157.0354	9178.9366	8659.
18	2621.9671	.00000000E+00	-1492.5818	4114.5489	3807.
19	21985.358	.20862490E-06	-15718.152	37703.511	32929
20	35243.086	554.85126	-10566.851	45809.937	42137
21	65700.068	4671.9320	-11718.690	77418.758	72324
22	168189.98	6161.2775	-16224.778	184414.76	17643
23	114163.80	4951.7641	-22880.329	137044.13	12713
24	90168.653	3576.4067	-19410.868	109579.52	10140
25	75980.075	-110.82085	-65782.256	141762.33	12324
26	7995.9787	176.04642	-3769.0597	11765.038	11519

***** POST1 NODAL STRESS LISTING *****

LOAD STEP 1 ITERATION= 1 SECTION= 1
TIME= .00000E+00 LOAD CASE= 1
SHELL STRESSES ARE AT MIDDLE

NODE	SIG1	SIG2	SIG3	SI	S
27	16751.319	2086.3106	-1542.7001	18294.019	16947
28	15414.326	737.80385	-97007.653	112421.98	10966
29	20505.834	450.29771	-695.10237	21200.937	20652
30	12368.082	.00000000E+00	-2665.3017	15033.384	14318
31	35284.342	.33787617E-06	-30862.880	66147.223	57403
32	45642.470	-364.71425	-30857.295	76499.765	67638
33	66765.637	-237.30517	-34953.438	101719.08	91912
34	123843.43	.25978344E-06	-40175.016	164018.45	15143

35	119040.87	-516.27044	-60406.539	179447.41	15997
36	99066.113	-55.410426	-54257.017	153323.13	13598
37	91932.224	.88471039E-06	-86300.800	178233.02	15457
38	7911.1396	338.05951	-3327.8177	11238.957	10803
39	15691.969	1736.5343	-1320.0039	17011.973	15824

***** POST1 NODAL STRESS LISTING *****

LOAD STEP 1 ITERATION= 1 SECTION= 1
TIME= .00000E+00 LOAD CASE= 1
SHELL STRESSES ARE AT MIDDLE

NODE	SIG1	SIG2	SIG3	SI	S
40	14982.769	596.01265	-51952.512	66935.281	64373
41	21259.990	385.86042	-521.39103	21781.381	21342
42	13928.232	.00000000E+00	-2344.0142	16272.246	15516
43	44349.254	.42440245E-06	-41028.723	85377.977	73981
44	51326.550	-364.65579	-43770.097	95096.647	83141
45	62486.579	-176.81110	-50339.176	112825.76	99278
46	92596.116	.68630494E-06	-57065.499	149661.62	13318
47	114373.29	-434.53394	-86919.735	201293.02	17563
48	103756.23	.99431010E-06	-80783.081	184539.31	16084
49	97434.064	.93635383E-06	-94456.981	191891.05	16621
50	4771.6158	230.01899	-1606.4841	6378.0999	5965.
51	8454.7101	730.48206	-817.26344	9271.9736	8627.
52	9422.1961	786.62767	-21714.198	31136.394	28992

***** POST1 NODAL STRESS LISTING *****

LOAD STEP 1 ITERATION= 1 SECTION= 1
TIME= .00000E+00 LOAD CASE= 1
SHELL STRESSES ARE AT MIDDLE

NODE	SIG1	SIG2	SIG3	SI	S
53	9040.9440	2.6872775	-412.03239	9452.9764	9255.
54	4873.1717	23.643521	-436.09107	5309.2627	5094.
55	48170.368	15.762348	-45333.891	93504.259	81007
56	52624.609	-126.39041	-46714.432	99339.041	86288
57	59003.861	-140.57049	-52430.384	111434.24	97019
58	73491.846	.67789105E-06	-61212.255	134704.10	11763
59	107509.54	-272.98741	-96821.780	204331.32	17729
60	102173.58	.98335911E-06	-92639.682	194813.26	16895
61	75205.041	.70052190E-06	-72748.168	147953.21	12823
62	4875.2990	859.46422	-1062.7247	5938.0237	5259.
63	1785.3846	-228.15600	-3706.1275	5491.5121	4833.
64	5106.9127	.29196846E-07	-8978.1123	14085.025	12692
65	.00000000E+00	-1642.2492	-6850.5867	6850.5867	6369.

***** POST1 NODAL STRESS LISTING *****

LOAD STEP 1 ITERATION= 1 SECTION= 1
TIME= .00000E+00 LOAD CASE= 1
SHELL STRESSES ARE AT MIDDLE

NODE	SIG1	SIG2	SIG3	SI	S
66	4210.8727	.00000000E+00	-6528.7510	10739.624	10180
67	40441.505	.36018392E-06	-34388.762	74830.267	65176
68	49534.402	524.55900	-33614.119	83148.521	72976
69	58386.801	.45057354E-06	-36059.628	94446.429	83310
70	63886.365	1846.2536	-45403.803	109290.17	95217

71	84917.209	.76802675E-06	-72511.084	157428.29	13694
72	77521.367	310.01284	-71017.633	148539.00	12874

MINIMUMS					
NODE	2	65	16	2	2
VALUE	.00000000E+00	-1642.2492	-156944.03	.00000000E+00	.0000

MAXIMUMS					
NODE	22	10	12	59	59
VALUE	168189.98	14930.958	.84655791E-06	204331.32	17729

APPENDIX C.3 - ANSYS FUSELAGE DATA

C.3.1 Fuselage Element Listing

LIST ALL SELECTED ELEMENTS. (LIST NODES)

ELEM	MAT	TYP	REL	ESYS	NODES	
1	1	1	1	0	2	4
2	1	1	1	0	1	3
3	1	1	1	0	4	6
4	1	1	1	0	3	5
5	1	1	1	0	6	8
6	1	1	1	0	5	7
7	1	1	1	0	8	10
8	1	1	1	0	7	9
9	1	1	1	0	10	11
10	1	1	1	0	9	12
11	1	1	1	0	11	13
12	1	1	1	0	12	14
13	1	1	1	0	13	15
14	1	1	1	0	14	16
15	1	1	1	0	15	17
16	1	1	1	0	16	17
17	1	2	2	0	1	2
18	1	2	2	0	2	3
22	1	2	2	0	3	4
23	1	2	2	0	4	5

ELEM	MAT	TYP	REL	ESYS	NODES	
24	1	2	2	0	5	6
25	1	2	2	0	6	7
26	1	2	2	0	7	8
27	1	2	2	0	8	9
28	1	2	2	0	9	10
29	1	2	2	0	9	11
30	1	2	2	0	11	12
31	1	2	2	0	12	13
32	1	2	2	0	13	14
33	1	2	2	0	14	15
34	1	2	2	0	15	16
35	1	1	1	0	19	21
36	1	1	1	0	18	20
37	1	1	1	0	21	23
38	1	1	1	0	20	22
39	1	1	1	0	23	25
40	1	1	1	0	22	24
41	1	1	1	0	25	27
42	1	1	1	0	24	26
43	1	1	1	0	27	28

ELEM	MAT	TYP	REL	ESYS	NODES	
44	1	1	1	0	26	29
45	1	1	1	0	28	30
46	1	1	1	0	29	31
47	1	1	1	0	30	32
48	1	1	1	0	31	33
49	1	1	1	0	32	34
50	1	1	1	0	33	34
51	1	2	2	0	18	19
52	1	2	2	0	19	20

53	1	2	2	0	20	21
54	1	2	2	0	21	22
55	1	2	2	0	22	23
56	1	2	2	0	23	24
57	1	2	2	0	24	25
58	1	2	2	0	25	26
59	1	2	2	0	26	27
60	1	2	2	0	26	28
61	1	2	2	0	28	29
62	1	2	2	0	29	30
63	1	2	2	0	30	31

ELEM	MAT	TYP	REL	ESYS	NODES	
64	1	2	2	0	31	32
65	1	2	2	0	32	33
66	1	2	2	0	2	19
67	1	2	2	0	19	4
68	1	2	2	0	4	23
69	1	2	2	0	23	8
70	1	2	2	0	8	27
71	1	2	2	0	27	10
72	1	2	2	0	27	11
73	1	2	2	0	11	30
74	1	2	2	0	30	15
75	1	2	2	0	15	34
76	1	2	2	0	34	17
77	1	2	2	0	2	21
78	1	2	2	0	21	6
79	1	2	2	0	6	25
80	1	2	2	0	25	10
81	1	2	2	0	10	28
82	1	2	2	0	28	13
83	1	2	2	0	13	32

ELEM	MAT	TYP	REL	ESYS	NODES	
84	1	2	2	0	32	17
85	1	2	2	0	1	18

C.3.2 STRS: Maximum and Minimum Stresses in Fuselage Truss Elements at End

PRINT ELEMENT STRESS ITEMS PER ELEMENT

***** POST1 ELEMENT STRESS LISTING *****

LOAD STEP 1 ITERATION= 1 SECTION= 1
TIME= .00000E+00 LOAD CASE= 1

ELEM	STRS
1	-213812.45
2	.10712259E-07
3	2599229.1
4	-1270833.3
5	4557516.9
6	-3734623.0
7	6959156.7
8	-6198412.7
9	-9324.9627
10	-7146607.2
11	-23133.815
12	-7144282.1
13	-11891.085
14	-7157325.3

***** POST1 ELEMENT STRESS LISTING *****

LOAD STEP 1 ITERATION= 1 SECTION= 1
TIME= .00000E+00 LOAD CASE= 1

ELEM	STRS
15	26501.808
16	-7192386.9
17	.00000000E+00
18	-55067.344
22	1742162.4
23	-1742162.4
24	1742162.4
25	-1742162.4
26	1742162.4
27	-1543075.4
28	1801766.7
29	-4856.1775
30	6420.6665
31	2743.9961

***** POST1 ELEMENT STRESS LISTING *****

LOAD STEP 1 ITERATION= 1 SECTION= 1
TIME= .00000E+00 LOAD CASE= 1

ELEM	STRS
32	-4489.0300
33	9416.2146
34	-36168.061
35	-213564.43
36	.53561295E-07
37	2599973.2
38	-1115079.4
39	4558757.0
40	-3423115.1

```
   41     3072680.9
   42    -2546897.4
   43    -5150.5174
   44    -2941544.5
   45    -9941.9572

      ***** POST1 ELEMENT STRESS LISTING *****

LOAD STEP     1  ITERATION=     1  SECTION=  1
TIME=    .00000E+00     LOAD CASE=  1

ELEM        STRS
   46    -2940587.9
   47    -4863.6773
   48    -2945957.9
   49     12032.213
   50    -2960389.2
   51    -25958.995
   52     36711.562
   53     1088018.5
   54    -1088018.5
   55     1088018.5
   56    -1088018.5
   57     1088018.5
   58    -963684.32
   59     1121221.8

      ***** POST1 ELEMENT STRESS LISTING *****

LOAD STEP     1  ITERATION=     1  SECTION=  1
TIME=    .00000E+00     LOAD CASE=  1

ELEM        STRS
   60    -2996.6782
   61     3964.2622
   62     1694.7584
   63    -2772.5336
   64     5815.6820
   65    -22332.643
   66    -41497.496
   67     90038.929
   68    -90038.929
   69     90038.929
   70    -41562.188
   71     .00000000E+00
   72    -1068.4487
   73     1913.9842

      ***** POST1 ELEMENT STRESS LISTING *****

LOAD STEP     1  ITERATION=     1  SECTION=  1
TIME=    .00000E+00     LOAD CASE=  1

ELEM        STRS
   74    -1913.9842
   75     1632.5762
   76     .00000000E+00
   77     144415.53
   78    -144415.53
   79     144415.53
```

C.4 CONFIGURATION 1 TOP VIEW

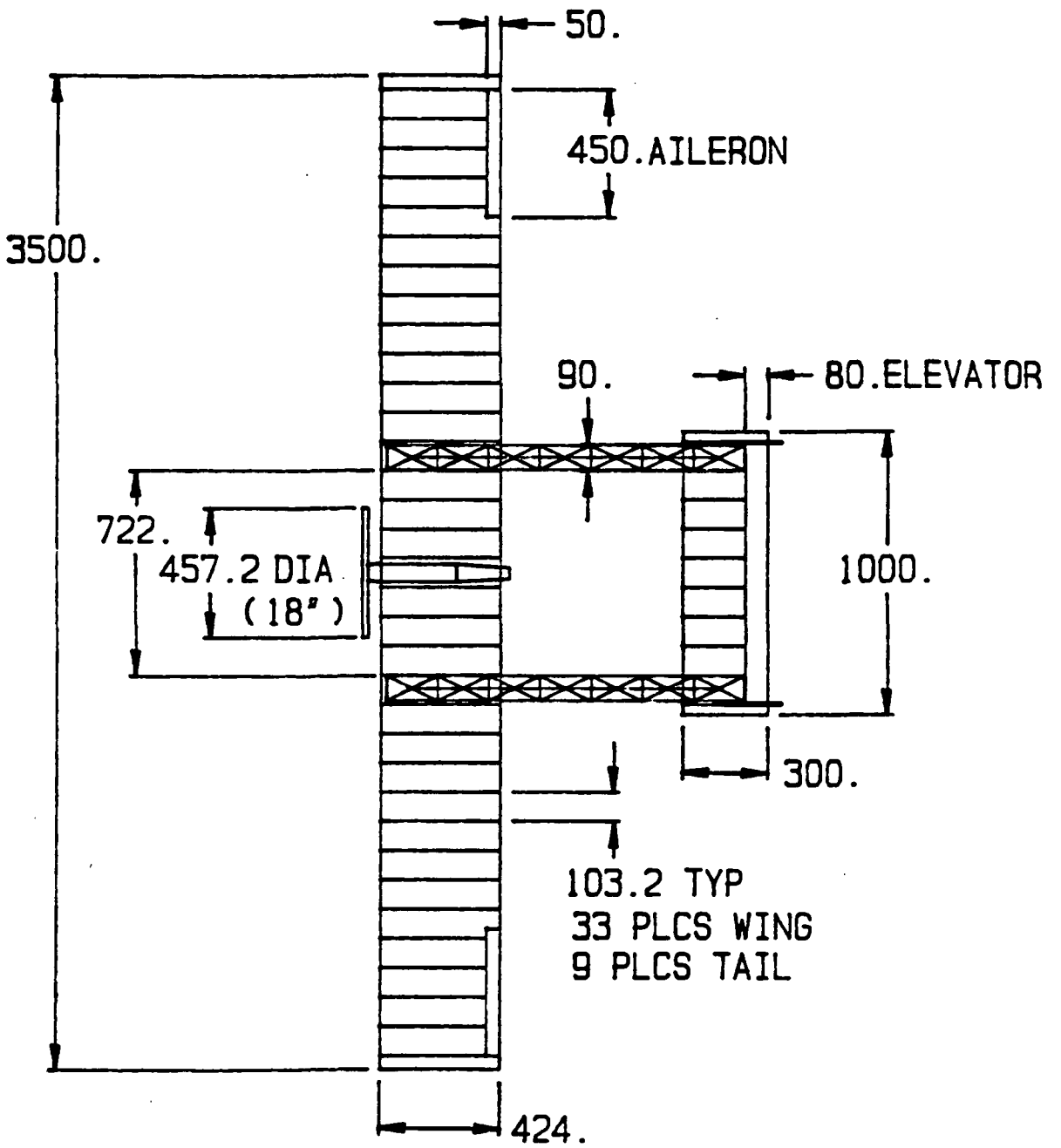

NOTES:
ALL DIMS IN mm.
SOLAR CELLS NOT SHOWN

WPI	Date:11-30-91	Title: DESIGN 1 - TOP VIEW
	Scale: 1 : 25	Drawn by: D. MARSHALL

C.5 CONFIGURATION 2 TOP VIEW

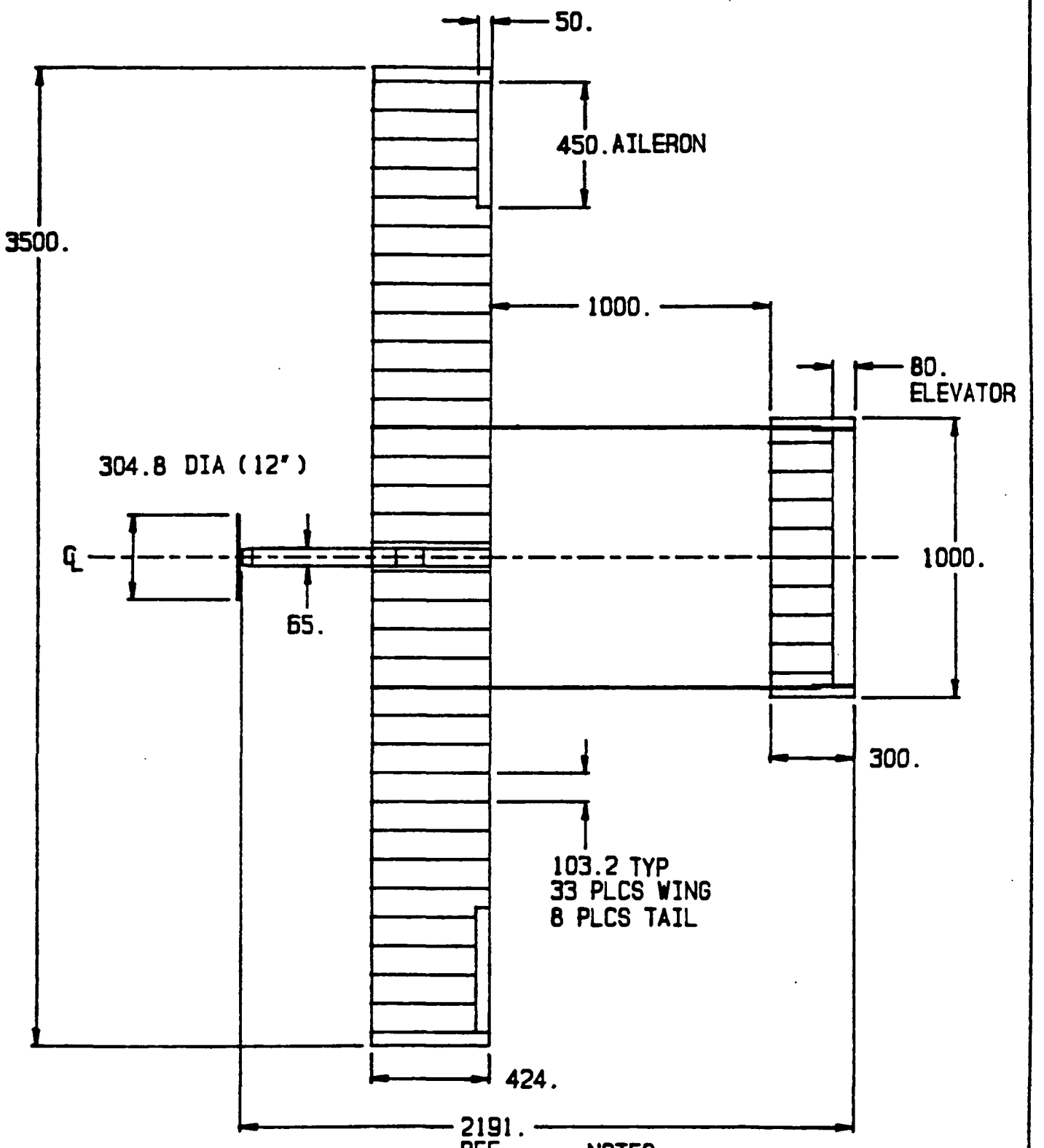

NOTES:
ALL DIMENSIONS ARE IN mm.
SOLAR CELLS NOT SHOWN

WPI	Date: 1 - 5 - 91	Title: DESIGN 2 - TOP VIEW
	Scale: 1 : 20	Drawn by: D. MARSHALL

C.6 CONFIGURATION 2 SIDE VIEW

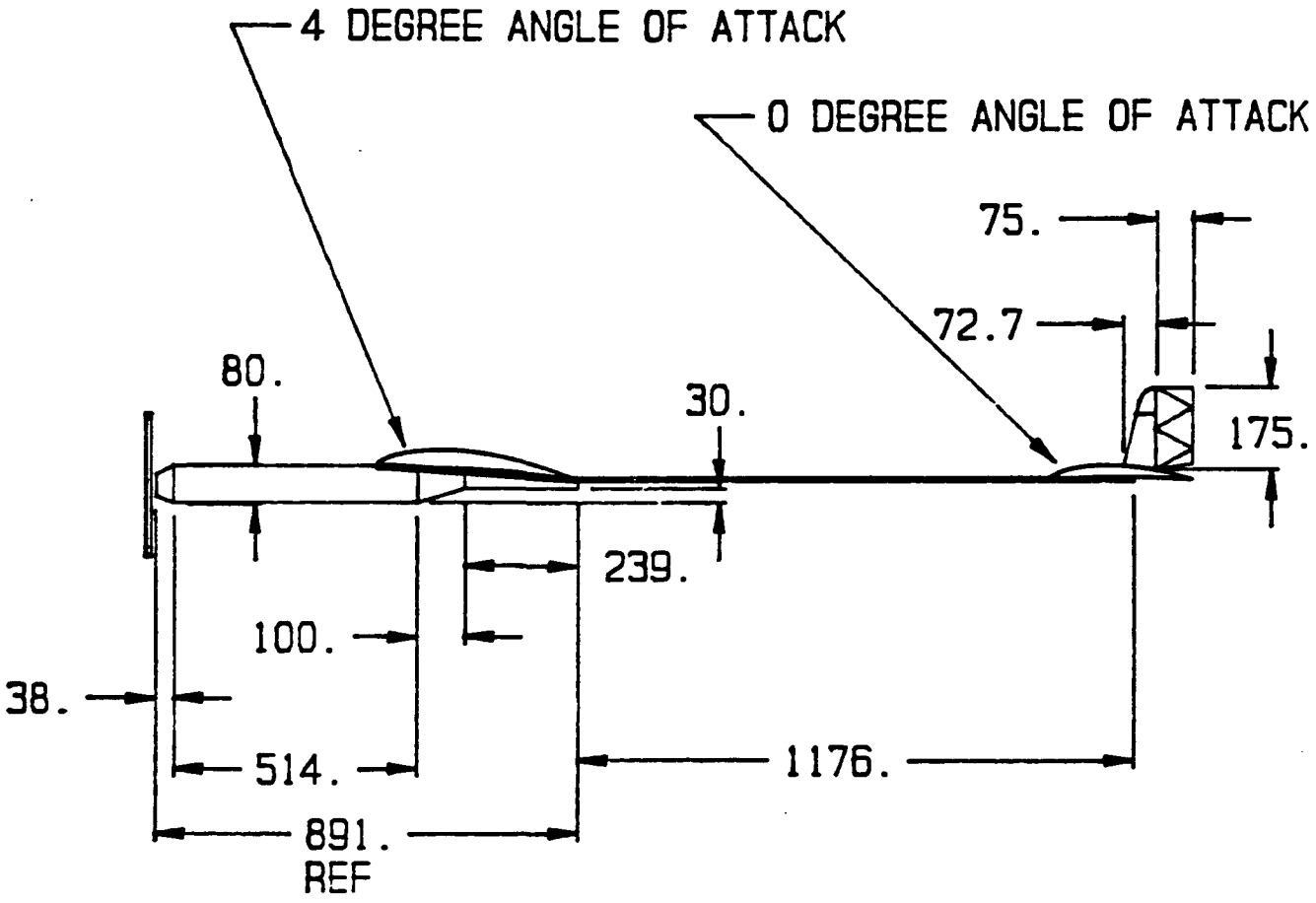

NOTES:
ALL DIMENSIONS ARE IN mm.

WPI	Date: 1 - 5 - 91	Title: DESIGN 2 - SIDE VIEW
	Scale: 1 : 16	Drawn by: D. MARSHALL

C.9 FINAL CONFIGURATION TOP VIEW

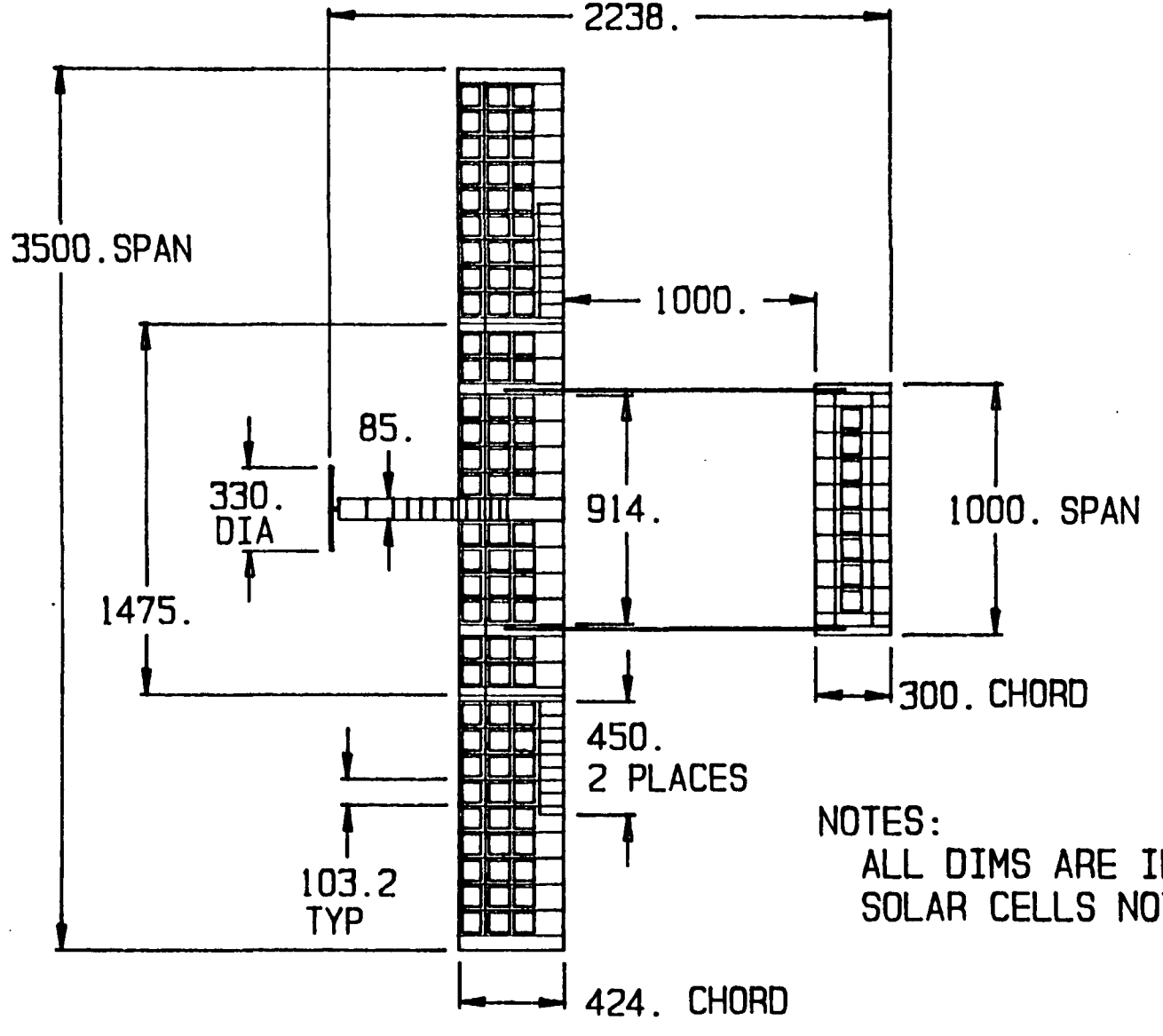

NOTES:
ALL DIMS ARE IN mm.
SOLAR CELLS NOT TO SCALE

WPI	Date: 4-10-91	Title: FINAL DESIGN TOP VIEW
	Scale: .0375 : 1	Drawn by: D. MARSHALL

C.10 FINAL CONFIGURATION ISOMETRIC

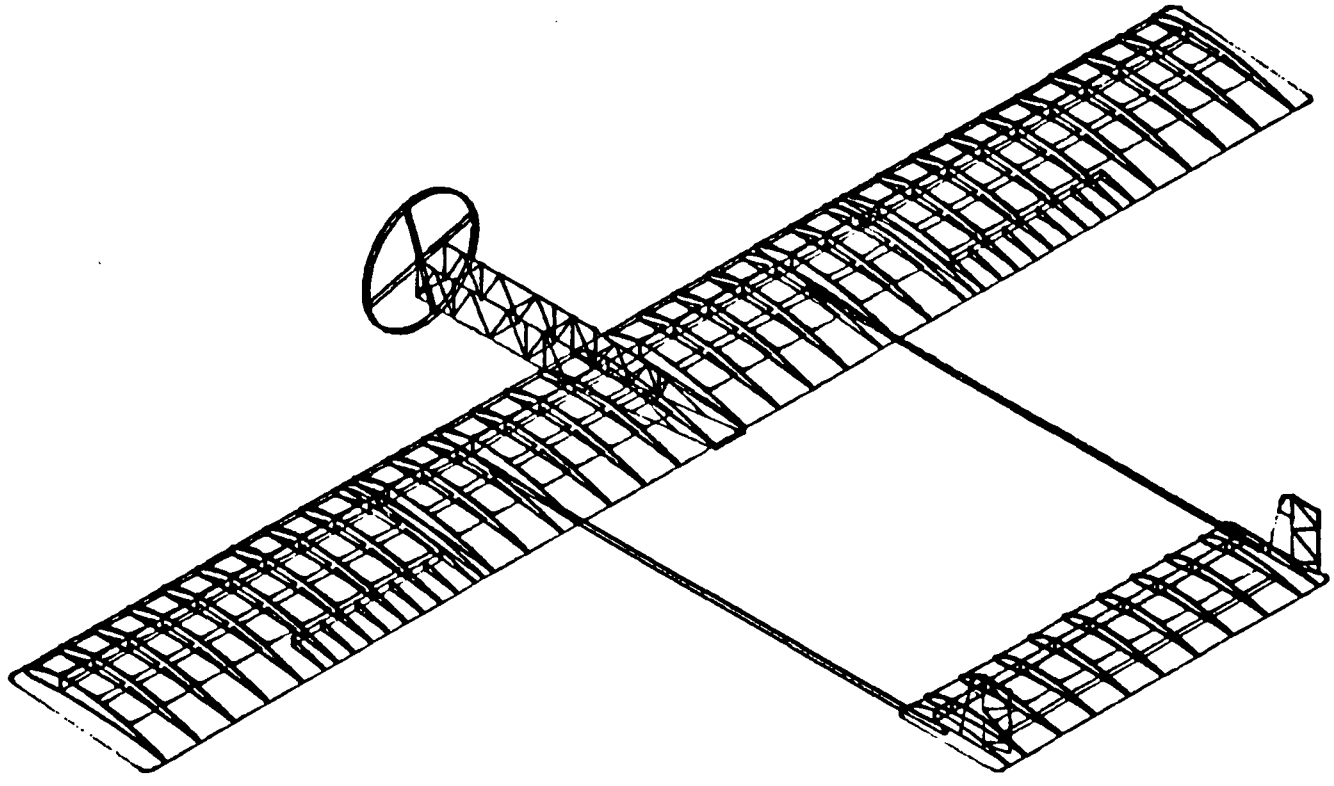

WPI	Date: 4-10-91	Title: FINAL DESIGN ISOMETRIC
	Scale: 1 : 16	Drawn by: D. MARSHALL

C.11 WING RIB CELL PLACEMENT DETAIL - SIDE VIEW

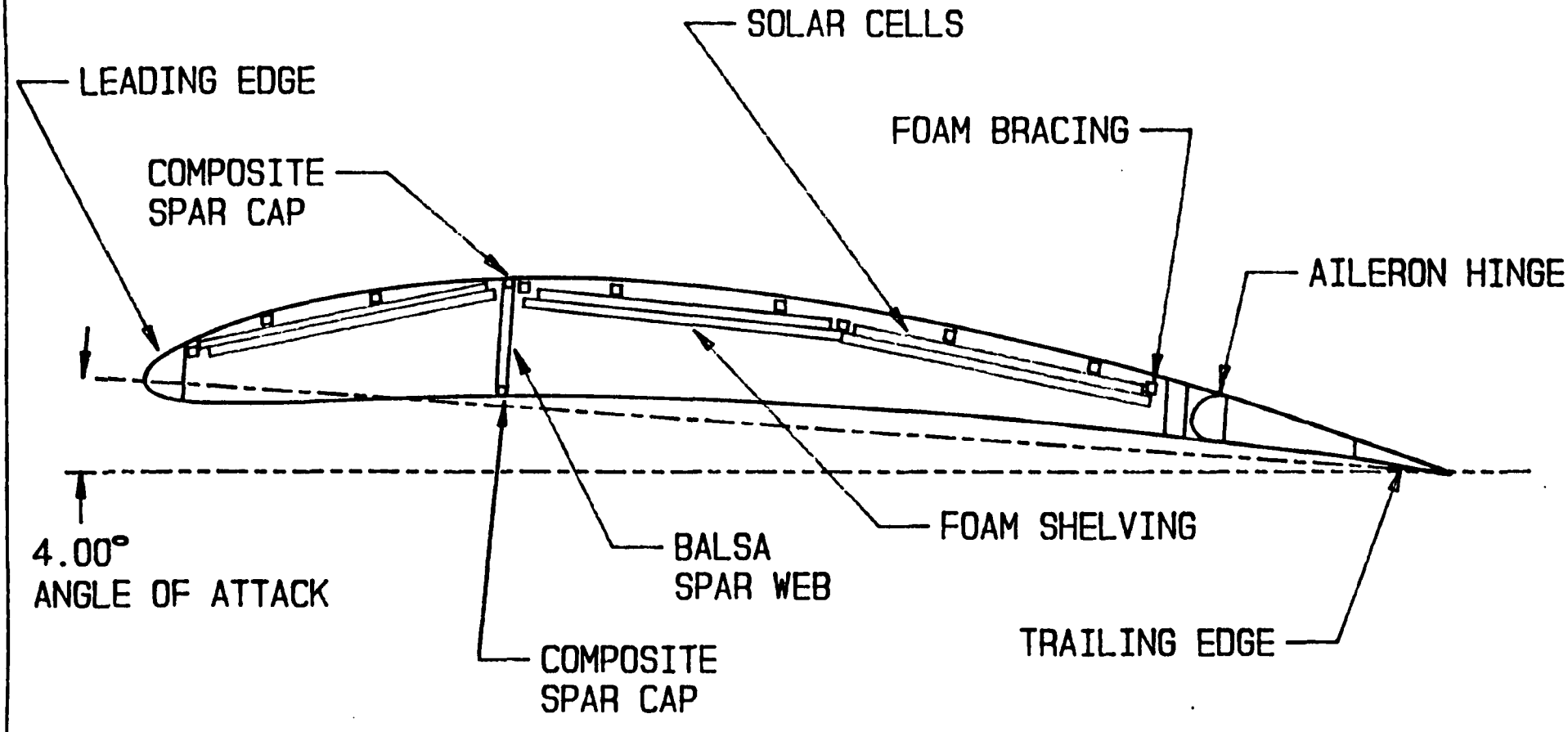

WPI	Date: 4-10-91	Title: WING RIB SIDE DETAIL
	Scale: 1 : 2	Drawn by: D. MARSHALL

C.12 WING RIB/TUBE CONNECTION DETAIL - SIDE VIEW

C.13 TAIL RIB/TUBE CONNECTION DETAIL - SIDE VIEW

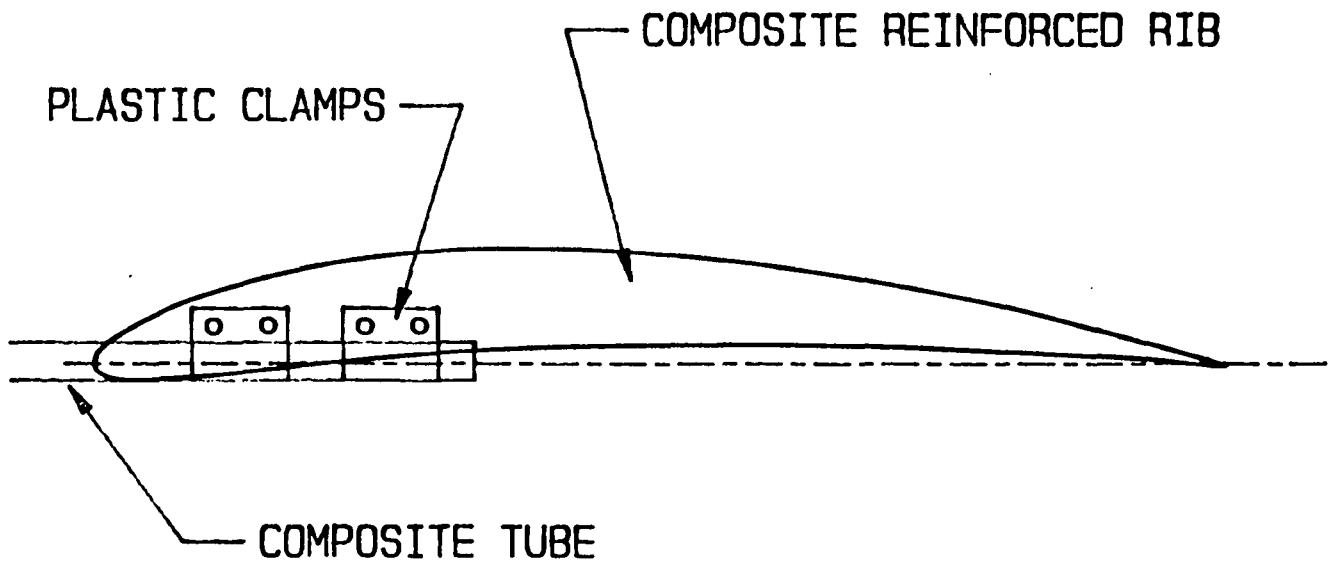

WPI	Date: 4-10-91	Title: TAIL CLAMP SIDE DETAIL
	Scale: 1 : 2	Drawn by: D. MARSHALL

APPENDIX D

CONTROLS & INTERFACE

APPENDIX D.1

SOLAR ARRAY DATA

CONSTANTS

Solar Time:	12.119	hr (decimal)
Day:	110	
Rated Efficiency:	0.125	
-After losses:	0.102624	percent
Area/cell:	0.009073	m^2
# of Cells		
Front of Wing:	30	@ 13 deg tilt
Back of Wing:	60	@ -7 deg tilt
Tail:	8	@ 0 deg tilt

Latitude:	0.735656	rad
Azimith angle:	0	rad
Hr. angle:	0.031154	rad
Decline angle:	0.195936	rad
Zenith angle:	0.540406	rad
Transmit. (air):	0.633530	percent

Mar. 16-75 Apr. 20-110

MACRO DEFINITIONS FOR THIS DATABASE

Auto Graph (Alt-G) {MENU}GP

Tilt (deg)	(rad)	Incidence (rad)	Solar Rad (W/m^2)	Earth Rad (W/m^2)	Power per cell (W)
-27	-0.47123	1.011158	710.760946	450.2886	0.419269
-26	-0.45378	0.993716	730.441229	462.7567	0.430878
-25	-0.43633	0.976275	749.899014	475.0838	0.442356
-24	-0.41887	0.958834	769.128371	487.2662	0.453699
-23	-0.40142	0.941393	788.123445	499.3001	0.464904
-22	-0.38397	0.923952	806.878449	511.1820	0.475968
-21	-0.36651	0.906512	825.387670	522.9081	0.486886
-20	-0.34906	0.889072	843.645469	534.4750	0.497656
-19	-0.33161	0.871632	861.646286	545.8791	0.508274
-18	-0.31415	0.854193	879.384638	557.1169	0.518738
-17	-0.29670	0.836754	896.855120	568.1850	0.529044
-16	-0.27925	0.819316	914.052411	579.0800	0.539188
-15	-0.26179	0.801878	930.971274	589.7986	0.549168
-14	-0.24434	0.784441	947.606553	600.3375	0.558981
-13	-0.22689	0.767004	963.953182	610.6936	0.568624
-12	-0.20943	0.749568	980.006182	620.8637	0.578094
-11	-0.19198	0.732133	995.760662	630.8446	0.587387
-10	-0.17453	0.714698	1011.21182	640.6334	0.596501
-9	-0.15707	0.697264	1026.35496	650.2270	0.605434
-8	-0.13962	0.679831	1041.18546	659.6226	0.614182
-7	-0.12217	0.662399	1055.69880	668.8173	0.622744
-6	-0.10471	0.644968	1069.89057	677.8082	0.631115
-5	-0.08726	0.627537	1083.75644	686.5926	0.639295
-4	-0.06981	0.610108	1097.29218	695.1679	0.647279
-3	-0.05235	0.592681	1110.49368	703.5315	0.655067
-2	-0.03490	0.575254	1123.35692	711.6807	0.662654
-1	-0.01745	0.557829	1135.87797	719.6132	0.670040
0	0	0.540406	1148.05302	727.3265	0.677222
1	0.017453	0.522984	1159.87836	734.8182	0.684198
2	0.034906	0.505565	1171.35039	742.0861	0.690965
3	0.052359	0.488147	1182.46561	749.1279	0.697522
4	0.069813	0.470732	1193.22065	755.9415	0.703866
5	0.087266	0.453320	1203.61222	762.5249	0.709996
6	0.104719	0.435911	1213.63715	768.8760	0.715910
7	0.122173	0.418505	1223.29240	774.9929	0.721605
8	0.139626	0.401103	1232.57503	780.8737	0.727081
9	0.157079	0.383706	1241.48220	786.5167	0.732335
10	0.174532	0.366313	1250.01120	791.9201	0.737366
11	0.191986	0.348927	1258.15944	797.0822	0.742173
12	0.209439	0.331547	1265.92443	802.0016	0.746753
13	0.226892	0.314175	1273.30380	806.6766	0.751106
14	0.244346	0.296812	1280.29532	811.1060	0.755231
15	0.261799	0.279460	1286.89685	815.2883	0.759125
16	0.279252	0.262121	1293.10637	819.2222	0.762788
17	0.296705	0.244798	1298.92200	822.9066	0.766218
18	0:314159	0.227494	1304.34197	826.3403	0.769415
19	0.331612	0.210215	1309.36462	829.5223	0.772378
20	0.349065	0.192966	1313.98843	832.4516	0.775106
21	0.366519	0.175757	1318.21198	835.1273	0.777597
22	0.383972	0.158602	1322.03399	837.5487	0.779852
23	0.401425	0.141518	1325.45330	839.7149	0.781869
24	0.418879	0.124536	1328.46887	841.6254	0.783648
25	0.436332	0.107704	1331.07976	843.2795	0.785188
26	0.453785	0.091105	1333.28520	844.6767	0.786489
27	0.471238	0.074895	1335.08451	845.8166	0.787550

Attack (deg)	Power Front (W)	Toward Power Back (W)	Tail Power (W)	Total Power (W)	Attack (deg)	Power Front (W)	Away Power Back (W)	Tail Power (W)	Total Power (W)
27	15.56215	0	3.354155	18.91631	-27	0	32.35132	3.354155	35.70547
26	15.87132	0	3.447029	19.31835	-26	0	32.95013	3.447029	36.39716
25	16.17566	0	3.538852	19.71451	-25	0	33.53891	3.538852	37.07776
24	16.47506	0	3.629597	20.10466	-24	0	34.11747	3.629597	37.74707
23	16.76945	0	3.719237	20.48869	-23	0	34.68564	3.719237	38.40487
22	17.05873	0	3.807744	20.86648	-22	ERR	35.24324	3.807744	ERR
21	17.34282	0	3.895091	21.23791	-21	ERR	35.79011	3.895091	ERR
20	17.62162	ERR	3.981251	ERR	-20	ERR	36.32607	3.981251	ERR
19	17.89505	ERR	4.066199	ERR	-19	ERR	36.85097	4.066199	ERR
18	18.16303	ERR	4.149908	ERR	-18	12.57808	37.36465	4.149908	54.09264
17	18.42548	ERR	4.232353	ERR	-17	12.92635	37.86694	4.232353	55.02565
16	18.68232	25.15616	4.313509	48.15200	-16	13.27069	38.35770	4.313509	55.94191
15	18.93347	25.85271	4.393351	49.17954	-15	13.61099	38.83677	4.393351	56.84112
14	19.17885	26.54139	4.471855	50.19210	-14	13.94714	39.30402	4.471855	57.72301
13	19.41838	27.22198	4.548996	51.18936	-13	14.27904	39.75929	4.548996	58.58733
12	19.65201	27.89428	4.624752	52.17104	-12	14.60659	40.20245	4.624752	59.43380
11	19.87964	28.55808	4.699099	53.13682	-11	14.92969	40.63337	4.699099	60.26216
10	20.10122	29.21318	4.772014	54.08642	-10	15.24824	41.05191	4.772014	61.07217
9	20.31668	29.85938	4.843477	55.01955	-9	15.56215	41.45794	4.843477	61.86357
8	20.52595	30.49649	4.913463	55.93591	-8	15.87132	41.85134	4.913463	62.63613
7	20.72897	31.12431	4.981953	56.83523	-7	16.17566	42.23200	4.981953	63.38961
6	20.92567	31.74265	5.048926	57.71725	-6	16.47506	42.59979	5.048926	64.12378
5	21.11600	32.35132	5.114360	58.58168	-5	16.76945	42.95461	5.114360	64.83842
4	21.29989	32.95013	5.178237	59.42827	-4	17.05873	43.29634	5.178237	65.53331
3	21.47730	33.53891	5.240536	60.25675	-3	17.34282	43.62488	5.240536	66.20824
2	21.64817	34.11747	5.301239	61.06688	-2	17.62162	43.94013	5.301239	66.86300
1	21.81244	34.68564	5.360327	61.85841	-1	17.89505	44.24200	5.360327	67.49739
0	21.97006	35.24324	5.417782	62.63109	0	18.16303	44.53040	5.417782	68.11122
-1	22.12100	35.79011	5.473588	63.38470	1	18.42548	44.80522	5.473588	68.70430
-2	22.26520	36.32607	5.527725	64.11900	2	18.68232	45.06640	5.527725	69.27646
-3	22.40261	36.85097	5.580179	64.83377	3	18.93347	45.31386	5.580179	69.82751
-4	22.53320	37.36465	5.630933	65.52879	4	19.17885	45.54751	5.630933	70.35729
-5	22.65693	37.86694	5.679972	66.20385	5	19.41838	45.76728	5.679972	70.86565
-6	22.77375	38.35770	5.727281	66.85874	6	19.65201	45.97312	5.727281	71.35241
-7	22.88364	38.83677	5.772845	67.49326	7	19.87964	46.16495	5.772845	71.81744
-8	22.98656	39.30402	5.816651	68.10723	8	20.10122	46.34272	5.816651	72.26060
-9	23.08247	39.75929	5.858685	68.70045	9	20.31668	46.50637	5.858685	72.68174
-10	23.17136	40.20245	5.898934	69.27275	10	20.52595	46.65585	5.898934	73.08074
-11	23.25318	40.63337	5.937386	69.82394	11	20.72897	46.79113	5.937386	73.45748
-12	23.32792	41.05191	5.974030	70.35386	12	20.92567	46.91215	5.974030	73.81185
-13	23.39556	41.45794	6.008854	70.86236	13	21.11600	47.01888	6.008854	74.14373
-14	23.45607	41.85134	6.041848	71.34927	14	21.29989	47.11129	6.041848	74.45303
-15	23.50944	42.23200	6.073001	71.81444	15	21.47730	47.18934	6.073001	74.73965
-16	23.55564	42.59979	6.102305	72.25774	16	21.64817	47.25303	6.102305	75.00350
-17	23.59467	42.95461	6.129749	72.67903	17	21.81244	47.30232	6.129749	75.24451
-18	23.62651	43.29634	6.155326	73.07818	18	21.97006	47.33720	6.155326	75.46259
-19	23.65116	43.62488	6.179029	73.45507	19	22.12100	47.35766	6.179029	75.65769
-20	23.66860	43.94013	6.200849	73.80958	20	22.26520	47.36370	6.200849	75.82975
-21	23.67883	44.24200	6.220781	74.14162	21	22.40261	47.35530	6.220781	75.97870
-22	23.68185	44.53040	6.238817	74.45106	22	22.53320	47.33249	6.238817	76.10451
-23	23.67765	44.80522	6.254953	74.73783	23	22.65693	0	6.254953	28.91188
-24	23.66624	45.06640	6.269184	75.00184	24	22.77375	0	6.269184	29.04294
-25	0	45.31386	6.281505	51.59536	25	22.88364	0	6.281505	29.16514
-26	0	45.54751	6.291913	51.83942	26	22.98656	0	6.291913	29.27847
-27	0	45.76728	6.300404	52.06769	27	23.08247	0	6.300404	29.38288

	Voltage		Current (A)		Power (VxI) in Watts		
	Test	Estimate	Test	Estimate	Test	Estimate	
Cell Test------>	0		0.878		0		
Jan 27, 1991	0.385		0.702		0.27027		
5 deg C	0.467		0.665		0.310555		----- Maximum Power Point
1:27 PM	0.54		0.149		0.08046		
	0.548		0.141		0.077268		MPP after array
	0.554		0.085		0.04709		and wiring losses:0.677222
	0.555		0.061		0.033855		
	0.566		0.021		0.011886		Theoretical Power based
	0.568		0.012		0.006816		on 12.5% efficiency
	0.566		0.008		0.004528		for day 110: 0.824879
	0.565		0.007		0.003955		
	0.564		0.006		0.003384		New Solar Cell
	0.563		0.005		0.002815		Efficiency: 0.102624
	0.562		0.004		0.002248		
	0.563		0.003		0.001689		
	0.562		0.002		0.001124		
	0.568		0		0		
	0		2.259884		0		
	0.350735		1.806877		0.633735		
	0.425437		1.711643		0.728196	<-------	
	0.49194		0.383511		0.188664		
	0.499228		0.362919		0.181179		
	0.504694		0.218781		0.110417		
	0.505605		0.157007		0.079383		
	0.515626		0.054051		0.027870		
	0.517448		0.030886		0.015982		
	0.515626		0.020591		0.010617		
	0.514715		0.018017		0.009273		
	0.513804		0.015443		0.007934		
	0.512893		0.012869		0.006600		
	0.511982		0.010295		0.005271		
	0.512893		0.007721		0.003960		
	0.511982		0.005147		0.002635		
	0.517448		0		0		

APPENDIX D.2

MOTOR SPECIFICATIONS & EVALUATION

MECHANICAL SPECIFICATIONS

ASTRO MOTOR	MOTOR DIA	MOTOR LENGTH	MOTOR WEIGHT	MOUNTING HOLES	SHAFT DIA	PROP SHAFT	GEAR RATIO
COBALT 020	1.25 in	1.75 in	3.5 oz	2x4-40	0.125 in	3/16 in	2.4
COBALT 035	1.25 in	2.00 in	4.5 oz	2x4-40	0.125 in	3/16 in	2.4
COBALT 05	1.25 in	2.25 in	6.5 oz	2x4-40	0.156 in	1/4 in	2.2
COBALT 05FAI	1.25 in	2.25 in	6.5 oz	2x4-40	0.156 in	1/4 in	2.2
COBALT 15	1.31 in	2.25 in	7.5 oz	2x4-40	0.156 in	1/4 in	2.2
COBALT 25	1.62 in	2.50 in	11.0 oz	2x6-32	0.250 in	5/16 in	1.7
COBALT 40	1.62 in	2.75 in	13.0 oz	2x6-32	0.250 in	5/16 in	1.7
COBALT 60	1.62 in	2.75 in	20.0 oz	4x6-32	0.250 in	5/16 in	None

ELECTRICAL SPECIFICATIONS

ASTRO MOTOR	LEAD BATTERY	SYSTEM WEIGHT	POWER OUTPUT	DIRECT DRIVE PROP @ RPM	GEARED DRIVE PROP @ RPM
COBALT 020	4x 800 mA	9 oz	50 watts	6x4 @ 10,000	10x6 @ 4,500
COBALT 035	5x 800 mA	11 oz	90 watts	6x4 @ 12,500	10x6 @ 5,500
COBALT 05	7x 900 mA	16 oz	125 watts	7x4 @ 14,500	11x7 @ 6,000
COBALT 05FAI	7x1,200 mA	20 oz	200 watts	7x6 @ 14,000	12x6 @ 6,000
COBALT 15	12x 900 mA	25 oz	200 watts	7x4 @ 16,000	11x7 @ 7,500
COBALT 25	14x1,200 mA	38 oz	300 watts	9x5 @ 10,000	13x8 @ 5,800
COBALT 40	18x1,200 mA	47 oz	450 watts	10x5 @ 11,500	13x8 @ 6,600
COBALT 60	28x1,200 mA	74 oz	1,200 watts	13x8 @ 9,000	Not Available

ASTRO BATTERY CHARGERS

4005B	AC/DC Auto Charger (4-7 Cells)	$ 74.95
102	DC/DC Super Charger (1-28 Cells)	$119.95
103	DC/DC Variable Charger (4-7 Cells)	$ 39.95
4005C	DC/DC Six/Seven Cell Charger	$ 29.95

MOTOR ACCESSORIES

200	Electronic Speed Control (35A)	$ 69.95
202	Electronic Speed Control (60A)	$ 99.95
4023	Electronic On-Off Control	$ 39.95
4032	Micro Switch	$ 5.95
4033	Gear Box for Cobalt 05/15	$ 34.95
4041	Gear Box for Cobalt 25/40	$ 39.95
4046	Gear Box for Cobalt 020/035	$ 34.95
4039	Super Flex Wire	$ 2.50
5021	Propeller Adaptor for 020/035	$ 4.95
5022	Propeller Adaptor for 05/15	$ 4.95
5023	Propeller Adaptor for 25/40	$ 5.95

ASTRO ELECTRIC POWERED AIRPLANE KITS

1015	Partenavia P-68 Victor (05 Twin Engine)	$ 79.95
1018	Porterfield Collegiate (15/25)	$ 79.95
1019	Astro Sport (020 to 05)	$ 79.95
1020	Challenger Sailplane (05, 05 Geared)	$ 49.95
1021	Viking Old Timer (05, 05 Geared)	$ 49.95

Evaluation of Astro-05 Cobalt D.C. Motor 11/13/90

Stall Test

Current X-axis	Voltage Y-axis
5.1	0.31
7.3	0.46
18.4	1
20.6	1.1
22.6	1.2

Regression Output:

Constant	0.074344	Intercept
Std Err of Y Est	0.017028	
R Squared	0.998650	
No. of Observations	5	
Degrees of Freedom	3	
X Coefficient(s)	0.049976	slope (Ra)
Std Err of Coef.	0.001060	

****

No load test

voltage	current	speed X-axis	K (motor constant)	Torque Y-axis
0.16	1.72	0		0.016090
0.93	1.9	88	0.009436	0.017774
2.08	2.2	213	0.009267	0.020580
3.37	2.5	352	0.009222	0.023387
5.2	2.6	534	0.009493	0.024322

		K(avg):	0.009354	

Regression Output:

Constant	0.016591	intercept (Tf)
Std Err of Y Est	0.000941	
R Squared	0.946607	
No. of Observations	5	
Degrees of Freedom	3	
X Coefficient(s)	0.000016	slope (B) damping coefficient
Std Err of Coef.	0.000002	

Stall Test - 11/13/90

Astro Flight Cobalt-05 D.C. Motor

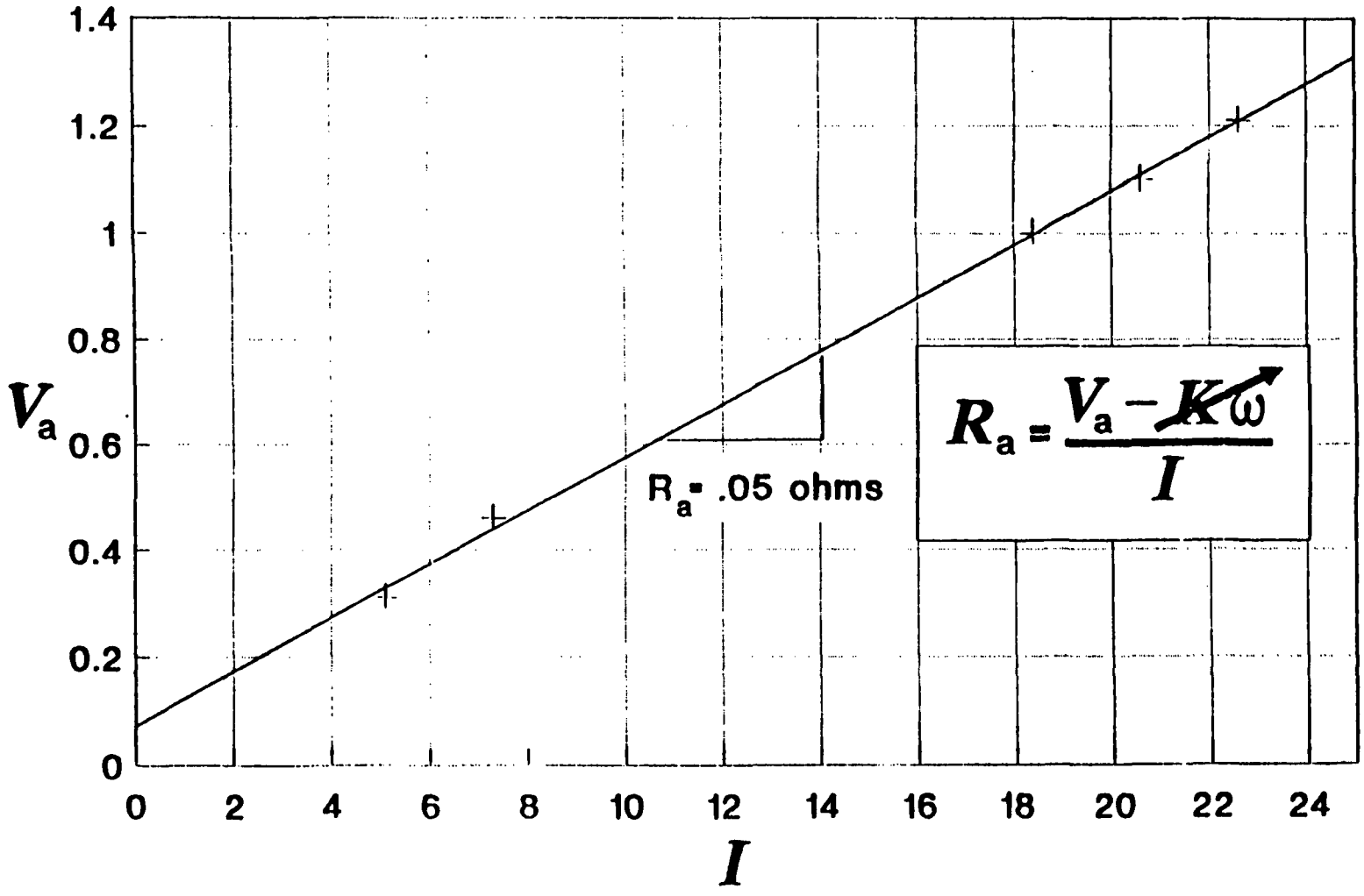

No-Load Test 11/13/90

Astro Flight Cobalt-05 D.C. Motor

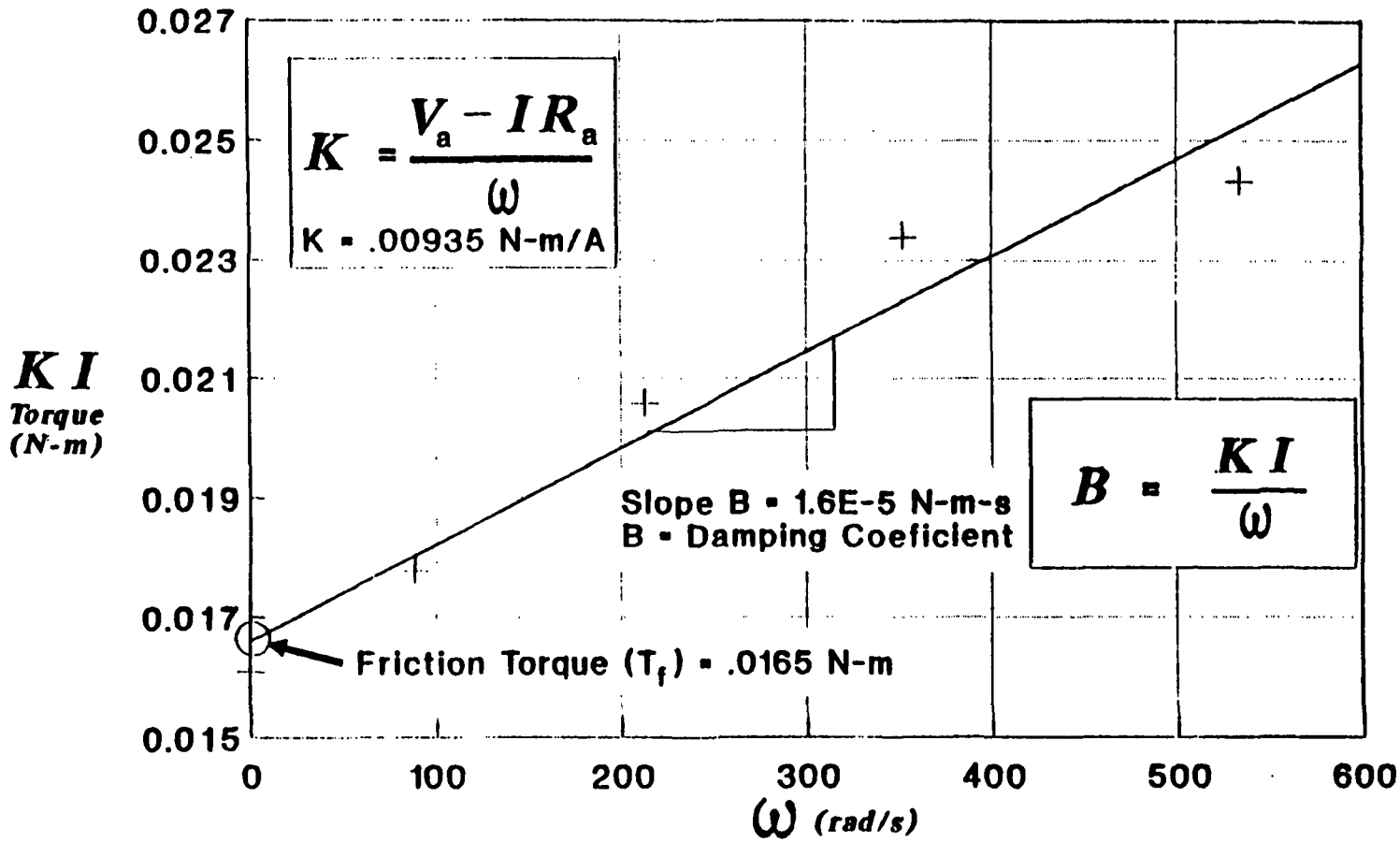

APPENDIX D.3

PROPELLER EFFICIENCY DATA

Efficiency Tests 2/17/91 using a folding Aero-Haute 13"x6.5" propeller

Trial	Delta(P)	Voltage (V)	Current (A)	RPM	Thrust (N)	Torque (N-m)
Trial 1	29	0	0	0	0	0
	29					
	29	2	3.61	1900	0.08	0.01
	29	3	6.48	2800	0.87	0.03
	29	4	9.9	3650	2.36	0.06
	29	5	13.58	4350	3.98	0.096
	30	6	17.58	5100	6.23	0.133
	30	7	21.97	5750	8.43	0.175
	29.250					
Trial 2	44	0	0	0	0	0
	44					
	44					
	44	3	3.62	2940	0.15	0.011
	44	4	7.11	3730	0.67	0.039
	45	5	10.93	4450	2.2	0.074
	45	6	15.88	5160	4.33	0.119
	45	7	20.88	5800	6.45	0.165
	44.375					

Efficiency Tests 2/

Trial	Velocity	P in (W)	P out motor (W)	P out prop (W)	Emotor	Epropeller	Epropulsi
		V x I	Torque x RPM	Thrust x vel.			
Trial 1	7.001	0.000	0.000	0.000	0.000	0.000	0.000
	7.001	7.220	1.990	0.560	0.276	0.281	0.078
	7.001	19.440	8.796	6.090	0.452	0.692	0.313
	7.001	39.600	22.934	16.521	0.579	0.720	0.417
	7.001	67.900	43.731	27.862	0.644	0.637	0.410
	7.120	105.480	71.031	44.359	0.673	0.624	0.421
	7.120	153.790	105.374	60.023	0.685	0.570	0.390
	7.035 Average						
Trial 2	8.623	0.000	0.000	0.000	0.000	0.000	0.000
	8.623	10.860	3.387	1.293	0.312	0.382	0.119
	8.623	28.440	15.234	5.777	0.536	0.379	0.203
	8.720	54.650	34.484	19.185	0.631	0.556	0.351
	8.720	95.280	64.302	37.759	0.675	0.587	0.396
	8.720	146.160	100.217	56.247	0.686	0.561	0.385
	8.672 Average						

Efficiency Tests 11/17/90 using a folding 12"x7" propeller

Trial	Delta(P)	Voltage (V)		Current (A)	RPM	Thrust (N)	Torque (N-m)
Trial 1	23	9	0	0	0	0	0
	23	9					
	23	9	2	2.53	1870	0.07	0.014
	23	9	3	4.75	2820	0.5	0.025
	23	9	4	7.5	3695	1.65	0.043
	24	10	5	10.1	4425	3.15	0.062
	24	10	6	12.7	5200	4.5	0.083
	23	9	7	15.6	5950	6.03	0.111
	23	9	8	19.32	6600	7.84	0.14
Average	23.22222						
Trial 2	29	15	0	0	0	0	0
	29	15					
	29	15	2.5	2.78	2400	0.08	0.018
	29	15	3	4.04	2865	0.14	0.026
	29	15	4	6.77	3740	1.05	0.043
	30	16	5	9.98	4450	2.65	0.068
	30	16	6	13.09	5230	4.27	0.098
	30	16	7	16.15	5950	5.7	0.122
	30	16	8	20	6650	7.7	0.148
Average	29.44444						
Trial 3	34	20	0	0	0	0	0
	34	20					
	34	20					
	34	20	3	3.5	2885	0.08	0.012
	34	20	4	6.31	3745	0.6	0.03
	34	20	5	9.73	4450	2.13	0.057
	35	21	6	13.08	5225	3.76	0.088
	35	21	7	16.18	5900	5.72	0.116
	34	20	8	20.2	6600	7.18	0.15
Average	34.22222						
Trial 4	44	30	0	0	0	0	0
	44	30					
	44	30					
	44	30	3.5	4.24	3390	0	0.024
	44	30	4	5.67	3820	0.2	0.033
	44	30	5	8.93	4410	1.2	0.055
	44	30	6	12.67	5225	3.11	0.087
	44	30	7	16.36	5950	4.82	0.119
	45	31	8	21.65	6775	6.72	0.158
Average	44.11111						
Trial 5	54	40	0	0	0	0	0
	54	40					
	54	40					
	55	41					
11/6/90/A	55	41	4	5.58	3950	0.03	0.032
11/6/90B	55	41	5	8.4	4600	0.93	0.055
	56	42	6	12.63	5360	2.7	0.092
	55	41	7	16.48	6050	4.5	0.123
	56	42	8	21.7	6750	6.45	0.159
	54.88888						

Efficiency Tests 11

Trial	Velocity	P in (W) V x I	P out motor (W) Torque x RPM	P out prop (W) Thrust x vel.	Emotor	Epropeller	Epropulsive
Trial 1	6.234	0.000	0.000	0.000	ERR	ERR	ERR
	6.234						
	6.234	5.060	2.742	0.436	0.542	0.159	0.086
	6.234	14.250	7.383	3.117	0.518	0.422	0.219
	6.234	30.000	16.638	10.287	0.555	0.618	0.343
	6.368	50.500	28.730	20.061	0.569	0.698	0.397
	6.368	76.200	45.197	28.658	0.593	0.634	0.376

Efficiency Tests 11

Trial	Velocity	P in (W) V x I	P out motor (W) Torque x RPM	P out prop (W) Thrust x vel.	Emotor	Epropeller	Epropulsive
	6.234	109.200	69.162	37.593	0.633	0.544	0.344
	6.234	154.560	96.761	48.878	0.626	0.505	0.316
Average	6.264						
Trial 2	7.001	0.000	0.000	0.000	ERR	ERR	ERR
	7.001						
	7.001	6.950	4.524	0.560	0.651	0.124	0.081
	7.001	12.120	7.801	0.980	0.644	0.126	0.081
	7.001	27.080	16.841	7.351	0.622	0.436	0.271
	7.120	49.900	31.688	18.868	0.635	0.595	0.378
	7.120	78.540	53.673	30.403	0.683	0.566	0.387
	7.120	113.050	76.016	40.585	0.672	0.534	0.359
	7.120	160.000	103.065	54.825	0.644	0.532	0.343
Average	7.054						
Trial 3	7.580	0.000	0.000	0.000	ERR	ERR	ERR
	7.580						
	7.580						
	7.580	10.500	3.625	0.606	0.345	0.167	0.058
	7.580	25.240	11.765	4.548	0.466	0.387	0.180
	7.580	48.650	26.562	16.145	0.546	0.608	0.332
	7.691	78.480	48.150	28.917	0.614	0.601	0.368
	7.691	113.260	71.670	43.991	0.633	0.614	0.388
	7.580	161.600	103.673	54.425	0.642	0.525	0.337
Average	7.605						
Trial 4	8.623	0.000	0.000	0.000	ERR	ERR	ERR
	8.623						
	8.623						
	8.623	14.840	8.520	0.000	0.574	0.000	0.000
	8.623	22.680	13.201	1.725	0.582	0.131	0.076
	8.623	44.650	25.400	10.348	0.569	0.407	0.232
	8.623	76.020	47.603	26.817	0.626	0.563	0.353
	8.623	114.520	74.147	41.563	0.647	0.561	0.363
	8.720	173.200	112.097	58.601	0.647	0.523	0.338
Average	8.634						
Trial 5	9.553	0.000	0.000	0.000	ERR	ERR	ERR
	9.553						
	9.553						
	9.641						

Efficiency Tests 2/17/91 using a wood Zinger 14"x8" propeller

Trial	Delta(P)	Voltage (V)	Current (A)	RPM	Thrust (N)	Torque (N
Trial 1	15	0	0	0	0	0
	15					
	15	2	6.62	1725	0.61	0.039
	15	3	12.3	2460	2.28	0.088
	15	3.5	14.81	2820	3.53	0.118
	15	4	18.22	3145	4.6	0.145
	15	4.5	20.65	3415	5.43	0.17
	15	5	24.17	3725	6.69	0.204
Trial 2	30	0	0	0	0	0
	30					
	30	2.5	6.82	2235	0.17	0.042
	30	3	9.88	2545	0.96	0.07
	30	3.5	12.73	2845	1.95	0.096
	30	4	15.85	3135	2.7	0.126
	30	4.5	19.44	3450	3.77	0.159

Efficiency Tests 2/

Trial	Velocity	P in (W) V x I	P out motor (W) Torque x RPM	P out prop (W) Thrust x vel.	Emotor	Epropeller	Epropulsi
Trial 1	5.035	0.000	0.000	0.000	0.000	0.000	0.000
	5.035	13.240	7.045	3.071	0.532	0.436	0.232
	5.035	36.900	22.670	11.479	0.614	0.506	0.311
	5.035	51.835	34.847	17.773	0.672	0.510	0.343
	5.035	72.880	47.755	23.160	0.655	0.485	0.318
	5.035	92.925	60.795	27.339	0.654	0.450	0.294
	5.035	120.850	79.577	33.682	0.658	0.423	0.279
Trial 2	7.120	0.000	0.000	0.000	0.000	0.000	0.000
	7.120	17.050	9.830	1.210	0.577	0.123	0.071
	7.120	29.640	18.656	6.835	0.629	0.366	0.231
	7.120	44.555	28.601	13.884	0.642	0.485	0.312
	7.120	63.400	41.365	19.225	0.652	0.465	0.303
	7.120	87.480	57.444	26.843	0.657	0.467	0.307